Analysis of the topology of premixed swirl-stabilized confined flames

Thibault Guiberti

École Centrale Paris

THÈSE

présentée par

Thibault F. Guiberti

pour l'obtention du

GRADE de DOCTEUR

Formation doctorale : Énergétique

Laboratoire d'accueil : Laboratoire d'Énergétique Moléculaire et Macroscopique, Combustion (EM2C) du CNRS et de l'ECP

Analyse de la topologie des flammes prémélangées swirlées confinées

Soutenue le 4 Février 2015

Jury :	MM	Escudié	D.	Rapporteur	DR au CNRS/CETHIL
		Cessou	A.	Rapporteur	DR au CNRS/CORIA
		Sotton	J.	Examinateur	MCF (HDR) à l'ENSMA
		Bruneaux	G.	Examinateur	IFPEN
		Poinsot	T.	Examinateur	DR au CNRS/IMFT
		Schuller	T.	Directeur de thèse	Prof. à l'ECP
		Durox	D.	Co-Directeur	IR au CNRS/EM2C

École Centrale des Arts et Manufactures
Grand Établissement sous tutelle
du Ministère de l'Éducation Nationale
Grande Voie des Vignes
92295 Châtenay-Malabry Cedex
Tél : 33 (1) 41 13 10 00
Télex : 634 991 F EC PARIS

Laboratoire d'Énergétique Moléculaire et Macroscopique, Combustion (E.M2.C.)
UPR 288, CNRS et École Centrale Paris
Tél : 33 (1) 41 13 10 31
Fax : 33 (1) 47 02 80 35

2015EOAP0014

Remerciements

Je tiens à remercier dans un premier temps mon directeur de thèse Thierry Schuller pour m'avoir permis de réaliser ma thèse au laboratoire EM2C dans d'excellentes conditions. Je le remercie également pour sa très grande disponibilité et sa gentillesse. Il est agréable d'avoir un directeur de thèse dont on a le sentiment qu'il travail au moins aussi dur, sinon plus, que nous. Je remercie également mon co-directeur Daniel Durox dont la très grande expérience fut un véritable atout. J'ai particulièrement apprécié sa gentillesse ainsi que toutes nos discussions autour d'un repas et fut très heureux de l'avoir à mes cotés jusqu'au dernier jour de ma thèse.

Mes remerciements vont également aux membres de mon jury et plus particulièrement à mes rapporteurs, Dany Escudié et Armelle Cessou, pour leurs remarques et questions qui m'ont permises d'améliorer mon manuscrit.

Je remercie également l'Ecole Normale Supérieure de Cachan pour m'avoir financé au travers d'une Allocation Spécifique aux Normaliens.

Je tiens aussi à remercier l'ensemble de l'équipe technique du laboratoire EM2C, plus particulièrement Yannick Le Teno et Sid Bouamama, sans qui ma thèse, à dominante expérimentale, n'aurait pas pris la même tournure. Je tiens également à remercier les filles du service administratif, Nathalie Rodrigues, Anne-Cécile Aiach et Brigitte Llobel, pour leur gentillesse et leur disponibilité sans faille.

Pour toutes nos discussions et leur aide sur certaines des expériences, je remercie Deanna Lacoste et Laurent Zimmer. Sans eux mon SNR en OH-PLIF n'aurait pu être à deux chiffres. Je remercie également Benjamin Robbes et Salma Bejaoui pour les moments partagés avec eux en salle de manip.

J'ai également une pensé pour mes chers co-bureau Renaud Mercier, Maria Castela et Florence Drui qui, à l'heure où j'écris ces lignes, travaillent dur comme fer à l'obtention de leur grade sacré de docteur. Je remercie également les autres doctorants, Clément Mirat, Raphaël Baudoin et bien d'autres, pour tous ses moments partagés à EM2C et ailleurs.

Il est également important de mentionner la très assidue team course à pied, Deanna Lacoste, Florent Sainct, Diane Rusterholtz, Matthieu Boileau, Aymeric Vié, Adam Larat... Grâce à eux, je fais maintenant parti de la longue mais prestigieuse liste des marathoniens de thèse.

J'en termine par le plus important, mes parents, qui m'ont toujours permis de poursuivre mes études dans les meilleures conditions. Sans eux rien de cela ne serait possible, et je les en remercie infiniment.

Abstract

This work deals with the stabilization of premixed turbulent swirling flames of methane/hydrogen/air combustible mixtures with different dilution rates of nitrogen and carbon dioxide. A central bluff body helps stabilizing the flames at low swirl numbers. The flame tip eventually impinges the combustor peripheral wall. The general objective is to gain understanding of the mechanisms governing the stabilization and the topology of these flames. It is found that the swirl number, the combustible mixture composition, the geometry of the combustor, and the thermal boundary conditions have a strong impact on the shape taken by these flames. The experimental setup used to characterize flame topologies is first described. Flames prone to topology bifurcations are selected and are studied for different arrangements of the combustor when the combustion chamber shape and size, the injection tube diameter, and swirl number are varied. One operating condition is fully characterized under non-reactive and reactive conditions using Planar Hydroxyl Laser Induced Fluorescence (OH-PLIF), Particle Imaging Velocimetry (PIV), and Laser Induced Phosphorescence of thermographic phosphors (LIP) to generate a detailed database of the flow and the corresponding boundary conditions. An analysis is then conducted to understand the mechanisms controlling shape bifurcations when the flame interacts with the combustor peripheral wall. Effects of the combustible mixture composition, the bulk flow velocity, and the swirl number are analyzed. It is shown that the transition from a V to an M shaped flame is triggered by a flashback of the V flame tip along the boundary layer of the combustor peripheral wall. Dimensionless numbers controlling these transitions are identified and a simplified model is developed to help the prediction of the flame shapes. The physics of these shape bifurcations differs when the flame does not interact with the combustor wall. The influence of hydrogen enrichment in the fuel blend on the shape taken by the flame is emphasized using flame chemiluminescence and OH-PLIF. LIP and thermocouple measurements demonstrate that the thermal boundary conditions also have a strong impact on the flame topology. The combined effects of strain and heat losses are investigated using joint OH-PLIF and PIV experiments. It is shown that flammability limits of premixed flames are reduced due to heat losses and the transitions from M to V shaped flames is consecutive to localized extinctions of flame front elements located in the outer shear layer of the jet flow that are submitted to large strain rates. These exper-

iments are completed by an analysis of the dynamics of methane/hydrogen/air flames at a low swirl number. It is shown that low frequency and high amplitude velocity modulations generated by a loudspeaker alter the shape taken by these flames. The stabilization of these flames diluted by nitrogen and carbon dioxide is finally examined. It was possible to stabilize swirled flames featuring important dilution rates due to the presence of the bluff body, installed on the axis of the injection tube. The recirculation zone behind this element supplies hot burnt gases to the flame anchoring point. Using OH* chemiluminescence imaging, it is shown than increasing the molar fraction of diluent in the fuel reduces the light emission from excited OH* radicals. The influence of dilution on the flame chemistry is emphasized with experiments conducted at a fixed thermal power and fixed adiabatic flame temperature. It is also demonstrated that the composition of the diluent has a strong influence on the temperature field of the burnt gases and of the combustor wall surfaces. Dilution with carbon dioxide increases radiative heat losses from the burnt gases in comparison to dilution with nitrogen. This penalizes the combustor efficiency equipped with four transparent quartz walls. The experiments conducted in this work reveal that heat losses strongly alter the topology of swirling flames.

Résumé

Ce travail porte sur la stabilisation de flammes prémélangées et swirlées de mélanges combustibles méthane/hydrogène/air avec différents taux de dilution d'azote et de dioxyde de carbone. Une tige centrale permet de stabiliser des flammes pour de faibles nombres de swirl. Le sommet de la flamme interagît éventuellement avec les parois de la chambre de combustion. L'objectif de ces travaux est d'améliorer la connaissance des mécanismes qui gouvernent la stabilisation et la topologie de ces flammes. Ces travaux démontrent que le nombre de swirl, la composition du mélange combustible, la géométrie de la chambre de combustion ainsi que les conditions aux limites thermiques ont une grande influence sur la forme prise par la flamme. Le dispositif expérimental permet de modifier la forme et la taille de la chambre de combustion, le diamètre du tube d'injection et le nombre de swirl. Des conditions opératoires propices aux transitions de forme de flamme sont ensuite étudiées pour différentes configurations de brûleur. Une caractérisation expérimentale fouillée d'un point de fonctionnement est réalisée grâce à la Fluorescence Induite par Laser sur le radical Hydroxyle (OH-PLIF), la Vélocimétrie par Images de Particules (PIV) et la Phosphorescence Induite par Laser de phosphores sensibles à la température (LIP). Une base de donnée de l'écoulement et des conditions aux limites associées est obtenue sans et avec combustion. Les mécanismes qui contrôlent les transitions de forme de flamme sont ensuite analysés lorsque la flamme interagît avec les parois de la chambre de combustion. L'influence de la composition du mélange combustible, de la vitesse débitante et du nombre de swirl est caractérisée. Il est démontré que la transition d'une flamme en V vers une flamme en M est déclenchée par un retour de flamme dans la couche limite le long d'une des parois latérales de la chambre de combustion. Les nombres sans dimension contrôlant ces transitions sont identifiés et un modèle de prévision de la forme de ces flammes est développé. La physique déterminant les transitions de forme de flammes est différente lorsque celles-ci n'interagissent pas avec les parois de la chambre de combustion. En utilisant le signal de chimiluminescence OH* et la OH-PLIF, il est montré que la teneur en hydrogène dans le combustible a une grande influence sur la forme de flamme. L'utilisation de la LIP et de thermocouples a également permis de montrer que les conditions aux limites thermiques jouent un rôle prépondérant sur la forme de flamme. Les effets combinés de l'étirement et des pertes thermiques sont examinés par l'utilisation

conjointe de la PIV et de la OH-PLIF. Il est montré que les limites d'extinction de flammes pauvres prémélangées sont réduites par les pertes thermiques et que la transition d'une flamme en M vers une flamme en V est consécutive à l'extinction du front de flamme situé dans la couche de cisaillement externe du jet soumis à un étirement trop important. Ces expériences sont complétées par une analyse de la dynamique de ces flammes. Des modulations de la vitesse débitante à basse fréquence et à haute amplitude modifient la forme de flamme. La stabilisation de flammes CH_4/H_2/air diluées par du N_2 ou du CO_2 est finalement examinée. La zone de recirculation produite par la tige centrale permet d'alimenter la base de la flamme avec des gaz brûlés chauds et de stabiliser des flammes fortement diluées. Augmenter la fraction molaire de diluant dans le combustible réduit l'intensité de la lumière émise par le radical OH*. Il est également montré que la composition du diluant a un impact sur le champ de température des gaz brûlés et des surfaces de la chambre de combustion. La dilution par du CO_2 augmente les pertes thermiques par rayonnement des gaz brûlés. Cela réduit l'efficacité de la chambre de combustion équipée de quatre parois transparentes. Les expériences conduites dans ces travaux révèlent que les pertes thermiques modifient fortement la forme des flammes swirlées.

Contents

Introduction

Context

In many combustion-based industrial systems, injectors put the flow into rotation to create a swirl motion that helps to stabilize combustion in turbulent flows. Swirled burners are used in industrial boilers and furnaces. The Pillard GRC 70 MW burner shown in Fig. 1, the John Zink Co. 12 MW burner in Fig. 2a, or the Proyce S.A. TENOX 17 MW burner in Fig. 2b are examples of different technologies. Swirled burners are also used in gas turbines for power generation. The GT26 turbine is powered with the Alstom EV combustor shown in Fig. 3a. The Siemens G30 DLE combustor drawn in Fig. 3b is installed on the 13 MW SGT-400 turbine. Aircraft propulsion is also powered with engines equipped with air and fuel swirling injectors. The Rolls-Royce Trent 900 equipping the Airbus A380 and the General Electric GEnx installed in the Boeing 787 are two famous examples.

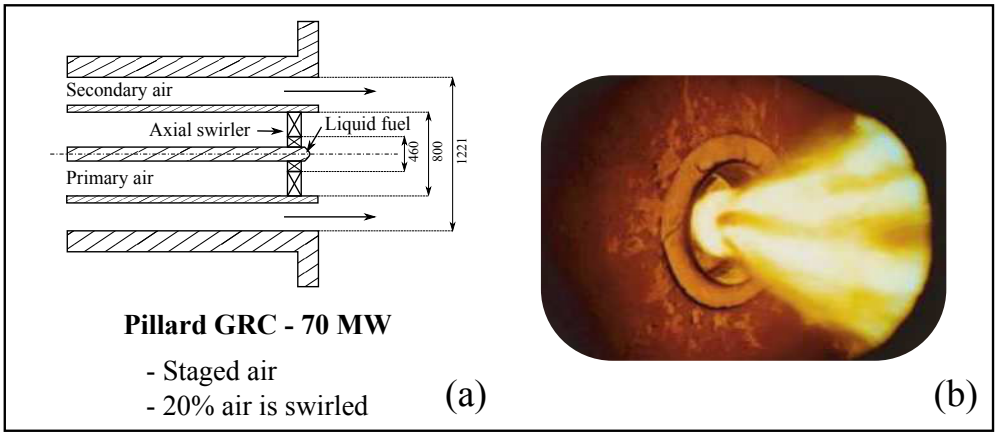

Figure 1: *(a) Schematics of the Pillard GRC burner. Adapted from Mirat (2015). (b) Typical non-premixed flame stabilized in the Pillard GRC burner (Commercial documentation from Pillard).*

In most of these systems, only a fraction of the fuel and air flows is swirled. In the Pillard GRC burner, schematically drawn in Fig. 1a, air is injected at

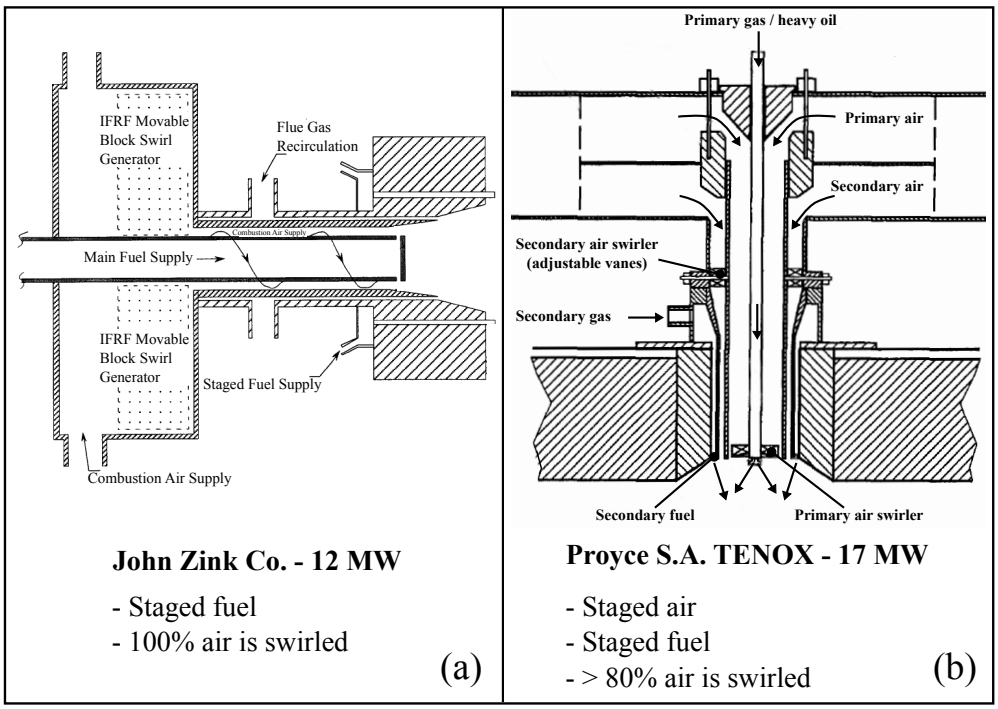

Figure 2: *Schematics of two different burners powering industrial boilers. (a) The John Zink Co. burner. Adapted from Hsieh et al. (1998). (b) The Proyce S.A. TENOX burner. Adapted from Ballester et al. (1997).*

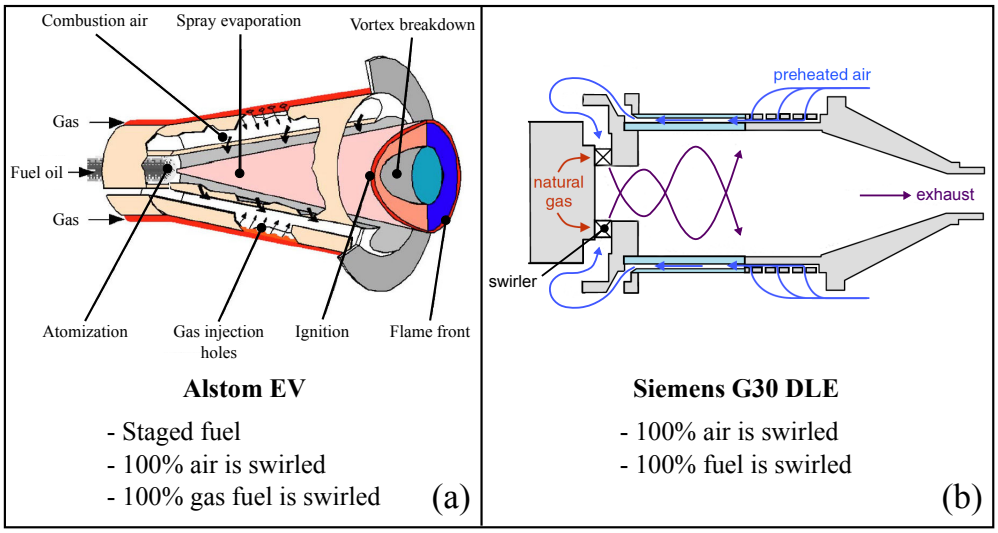

Figure 3: *Schematics of two different burners equipping gas turbines for power generation. (a) The Alstom EV combustor. Adapted from Döbbeling et al. (2005). (b) The Siemens G30 DLE combustor. Adapted from Stopper et al. (2010).*

two different locations (primary and secondary air) and only the primary air, which roughly represents 20% of the total air mass flow rate injected, passes through the swirler. The liquid fuel injected in the center of the burner is not swirled. In the burner shown in Fig. 2a, all the air is put into rotation and the fuel, injected at two different locations (main fuel and staged fuel), is not swirled. In the Proyce S.A. TENOX burner shown in Fig. 2b, both air and fuel are staged and approximately 80% of the injected air flow rate passes though a swirler.

For safety reasons, the fuel and air are injected separately and mixing, which is realized at the outlet of the injector, is more difficult. It means that air and fuel are not perfectly mixed before the combustion reaction. Combustion takes place in a non-premixed or partially premixed mode. These modes generally yield low quality combustion and produce unburned hydrocarbons, soot, and important pollutant emissions (Glassman (1996a) and Glassman (1996b)). Figure 1b shows one example of a typical non-premixed flame stabilized in the Pillard GRC burner powered with heavy fuel. The bright yellow color is due to the gray-body thermal radiation from soots. For these reasons, the latest industrial burners that were developed are operated closer to the premixed mode such as in the Alstom EV combustor (see Fig. 3a) or the Siemens G30 DLE combustor (see Fig. 3b). In both systems, air and gaseous fuels are premixed within or upstream the swirler. This also reduces the complexity of injectors design.

Lean premixed combustion a promising technology for aircraft propulsion and is already widely used for electricity production with ground gas turbines. In the premixed mode, an homogeneous mixture of air and fuel enters the combustion chamber and it is possible to adjust the flame temperature by modifying the equivalence ratio ϕ of the combustible mixture. There is an optimum for low emissions of carbon monoxide CO and nitric oxides NOx (see Fig. 4) (Brown (1995), Docquier and Candel (2002)) pollutants when the burner is operated at lean conditions ($\phi < 1$).

Burner designs based on lean premixed swirl combustion technologies are also a promising option for the optimization of industrial furnaces in the glass or steel-industry. In the steel industry, gaseous by-products like the Blast Furnace Gas (BFG) or the Coke Oven Gas (COG) can be valorized to reduce operational costs and pollutant emissions. These gaseous mixtures feature some interesting properties which will be analyzed in Ch.1.3 but they are also more difficult to burn because of their low heat value (Gicquel et al. (2003), Paubel et al. (2007), Paubel (2007)). It is interesting to analyze the structure of swirl flows and the main features of lean premixed flames to understand the key mechanisms controlling the stabilization of these flames. A brief overview of these problems is conducted in the following.

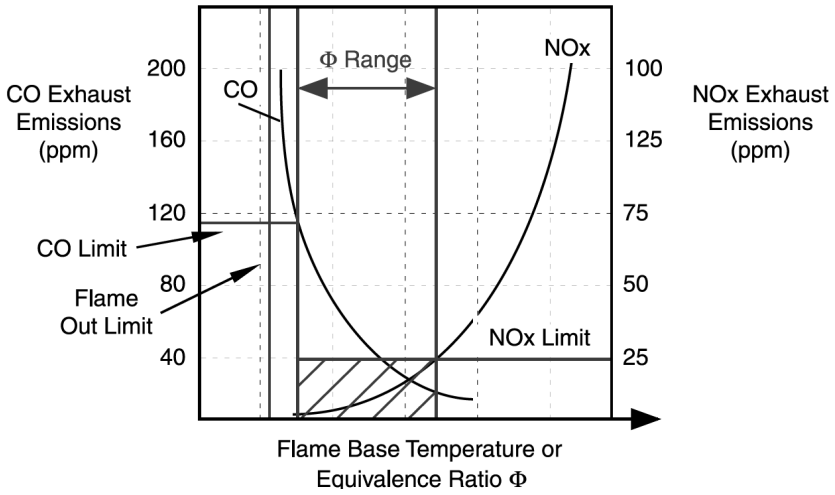

Figure 4: *CO and NOx production from lean premixed combustion. Reproduced from Docquier and Candel (2002). Adapted from Brown (1995).*

The structure of swirl flows

Swirl flows have two advantageous features. They allow the stabilization of flames in high Reynolds number flows and yield compact flames. The first feature allows to increase the combustion power and the second allows to reduce the size of the combustion chamber. The flow downstream swirled injectors is controlled by the intensity of swirl *i.e.* the rate of rotation of the flow which is generally characterized by the swirl number S. For a cylindrical or annular swirled injector and without considering pressure effects (Gupta et al. (1984)), the swirl number is given by:

$$\mathrm{S} = \frac{\int_0^{R_i} v_\theta v_z r^2 dr}{R_i \int_0^{R_i} v_z^2 r dr} \tag{1}$$

where R_i denotes the injection tube radius and r represents the radial distance to the burner axis. The quantities v_z and v_θ stand for the axial and azimuthal velocities at the outlet of the injector. Figure 5 shows the topology of a confined isothermal flow downstream an annular swirled injector for low $\mathrm{S} < 0.5$ and high $\mathrm{S} > 0.6$ swirl numbers. In both cases, the flow features an Outer Recirculation Zone (ORZ) in the corner of the combustion chamber dump plane and the combustor peripheral wall. In this region, the flow is recirculating in the reverse direction of the injected flow due to the sudden expansion of the cross-section behind the backward step. In the low swirl case, a small Inner

Recirculation Zone (IRZ) with flow reversal is also created in the wake of the central bluff-body. When the swirl number S is increased above a critical value, typically $S_c \simeq 0.6$, a vortex breakdown phenomenon takes place yielding a large reverse flow along the centerline of the combustor (Gupta et al. (1984)). This large vortex bubble is not the consequence of the wake of the bluff-body but results from an hydrodynamic instability of the flow (Gupta et al. (1984)). This yields an IRZ featuring large reverse axial velocities. In a reacting flow, this region helps stabilizing the flame because it features low velocities and continuously supplies hot burnt gases that ignite the fresh stream fed by the injector. Flames stabilized in the central recirculation flow region away from the central bluff-body are said aerodynamically stabilized. Figure 6 shows the structure of the flow of an aerodynamically stabilized premixed flame.

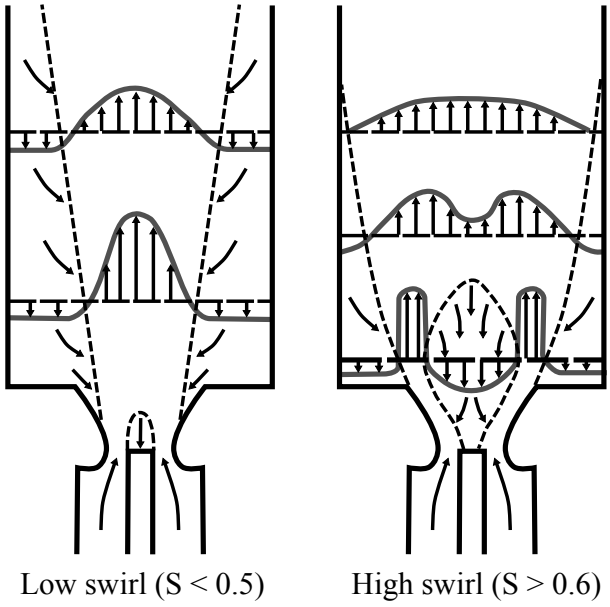

Figure 5: *Flow patterns observed for swirling jets exhausting from divergent nozzles for two different swirl numbers $S < 0.5$ (left) and $S > 0.6$ (right). Reproduced from Beér and Chigier (1972).*

The phenomenon causing the reverse flow for a sufficiently high swirl number is called vortex breakdown (Lucca-Negro and O'Doherty (2001)). Figure 7 shows a schematic diagram explaining the IRZ formation due to vortex breakdown. Close to the injector, the azimuthal velocity produces a centrifugal pressure gradient that causes a pressure drop along the central axis of the combustor. The azimuthal component of the velocity decays when the distance to the injector increases meaning that the pressure along the combustor axis increases with the distance to the injector. This axial pressure gradient causes the reverse flow generating the IRZ.

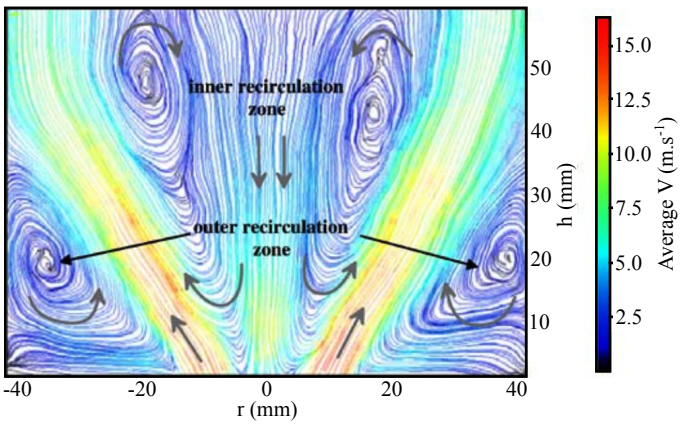

Figure 6: *Time averaged streamlines of the flow field of an aerodynamically stabilized premixed methane/air flame. Adapted from Sadanandan et al. (2008).*

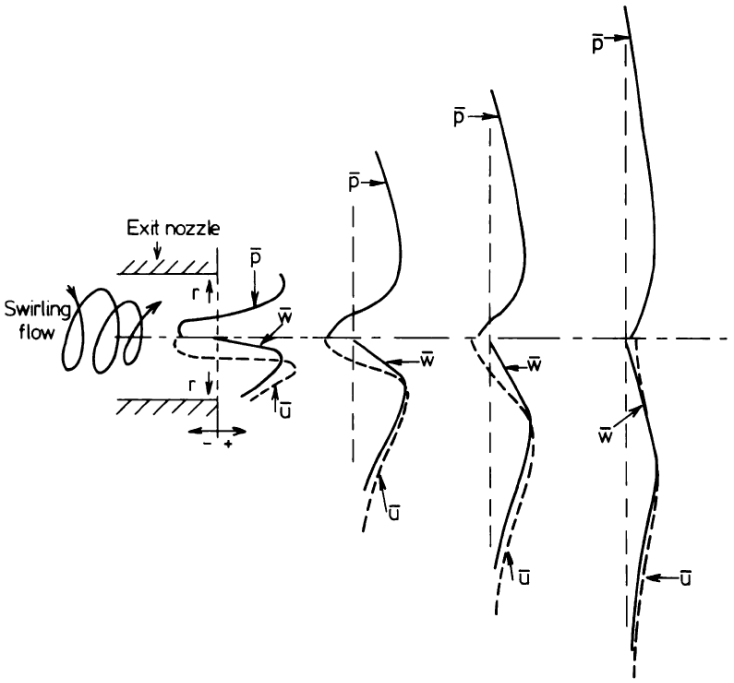

Figure 7: *Schematic diagram of the vortex breakdown mechanism leading to the formation of an IRZ. $\bar{u}$, $\bar{w}$, and $\bar{p}$ respectively stand for the axial velocity, the azimuthal velocity, and the pressure. Reproduced from Gupta et al. (1984).*

Vortex breakdown usually gives rise to hydrodynamic flow instabilities such as the Precessing Vortex Core (PVC). This instability, which has been the topic of a review by Syred (2006) for combustion systems, is shown in Fig. 8. This he-

lical structure develops along the Inner Shear Layer (ISL) located between the swirling jet of reactants and the Inner Recirculation Zone (IRZ). It was demonstrated that the PVC influences the stabilization of swirled flames (Stöhr et al. (2011), Steinberg et al. (2013), and Terhaar et al. (2014)).

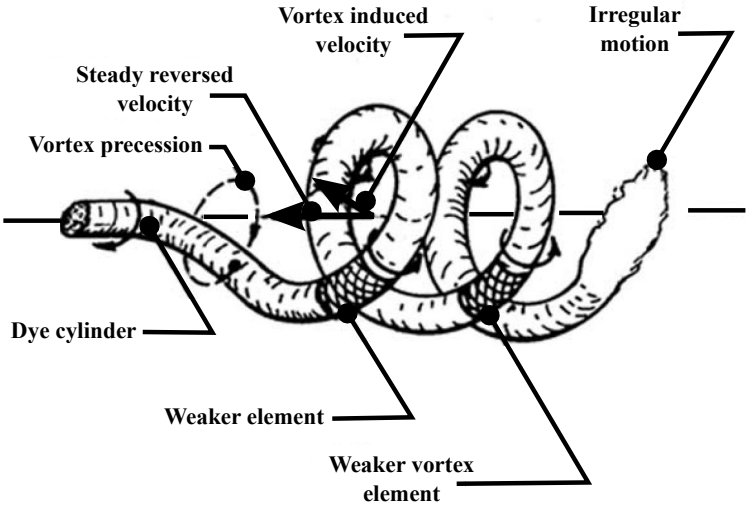

Figure 8: *Structure of a PVC. Adapted from Chanaud (1965).*

If the swirl number is lower than the critical value for vortex breakdown, the IRZ does not exist. In this situation, stabilization of the flame is more difficult. A possible way to improve stabilization is to add a bluff-body on the center of the injection tube to generate an IRZ in the wake of the solid element. Figure 9 shows an example of reverse flow in the wake of a bluff-body when the swirl number is lower than the threshold value for vortex breakdown $S = 0.316 < 0.6$. In this situation, the flame is said bluff-body stabilized.

Lean premixed combustion

Lean premixed combustion is an efficient way to reduce pollutant emissions (see Fig. 4) but this combustion mode is more sensitive to turbulence and flow perturbations. Lean premixed combustion with swirled injectors raises issues in terms of flame stabilization and dynamic stability. The dynamics of lean premixed swirled flames is one of the main concerns for gas turbine and jet engine manufacturers (see the review articles from Huang and Yang (2009) and Candel et al. (2014) or the textbook from Lieuwen and Yang (2005)). This problem is out of the scope of this work that deals with the stabilization of theses flames. Lean premixed flames are particularly sensitive to flashback, blow-off, and topology transitions.

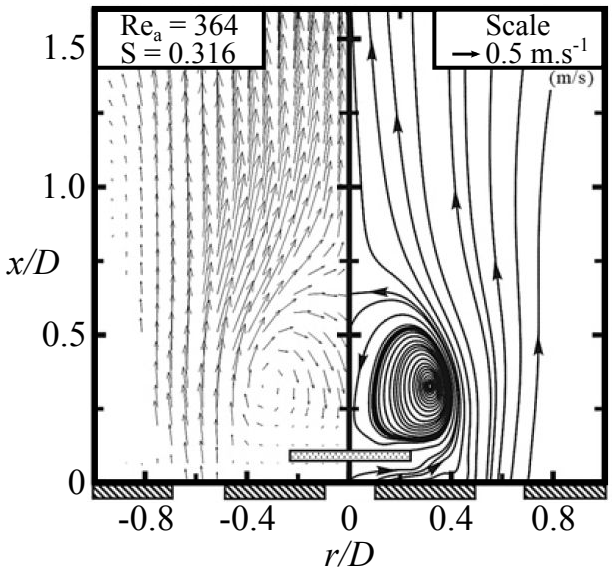

Figure 9: *Velocity vectors and streamlines in the wake of a bluff-body for Re* = 364 *and S* = 0.316. *Adapted from Huang and Yen (2008).*

Flashback: Because a flammable mixture exists upstream the combustion chamber, flashback may occur in the injector of premixed swirled combustors. This phenomenon is associated to a flame protruding suddenly or progressively within the injector and heating up dangerously the metallic pieces of the injectors. Different mechanisms leading to flashback were identified in turbulent swirling flows. Sommerer et al. (2004) list five possibilities: flashback by autoignition, flashback in the boundary layer, turbulent flame propagation in the core flow, combustion instabilities leading to flashback and flashback induced by vortex breakdown. Flashback is still the topic of numerous experimental and numerical studies, especially when the fuel blend includes hydrogen (Kurdyumov et al. (2000), Heeger et al. (2010), Eichler and Sattelmayer (2011), Syred et al. (2012), Gruber et al. (2012)).

Lean blow-off: Lean premixed flames are also more susceptible to blow-off as reviewed by Shanbhogue et al. (2009). Blow-off of lean premixed flames generally starts by the apparition of local extinctions along the flame sheet where the local strain rate exceeds the extinction limit. The flame resistance to strain is reduced when lean mixtures are burnt (Mastorakos et al. (1995)). Close to blow-off, the flame front survives in a shear layer because hot burnt gases recirculating in the IRZ rapidly mixes with incoming cold reactants and autoignition occurs (Kariuki et al. (2012)). The flame front near lean blow-off is unstable and features frequent extinctions and reignitions. Ultimately, lean flame blow-off occurs if the time delay before reignition takes place exceeds

a critical value. Stöhr et al. (2011) demonstrated that the PVC can have a positive effect on the flame stability. The PVC delays the lean blow-off because it yields local vortical structures with low strain rates and accelerate the mixing between hot burned gases and cold reactants. Mechanisms leading to lean blow-off are still the topic of many investigations for swirling flows.

Lean swirl flames stabilized aerodynamically or stabilized in the wake of a bluff-body are also sensitive to topology changes. There have been relatively few studies on this topic in comparison to studies on flashback and blow-off. This problem is the main topic of this thesis. The analysis of the current state of knowledge on the topology of swirl flames is the subject of the following section.

Topologies of swirl flames

This work is concerned with the stabilization of swirl flames for operating conditions away from flashback in the injection tube and away from the lean blow-off limit.

Lean premixed swirl-stabilized flames generally take a V or an M shape. Figures 10 and Fig. 11 show examples of V and M flames. The main characteristics of the topology of these flames and the associated flow structures are synthesized in Fig. 12. In premixed combustors with swirled injectors, flames generally have a V shape if the combustion reaction only takes place at the boundaries of the internal shear layer (ISL) of the swirling jet of reactants in contact with the hot internal recirculation zone (IRZ) filled with burnt products (Fig. 12a-b). If combustion also takes place between the outer shear layer (OSL) of the jet and the external recirculation zone (ORZ) of burnt gases, the flame stabilizes with an M shape (Fig. 12a-c).

The shape taken by the flame in a steady operating combustor is an important feature that controls the uniformity of the temperature field in the burnt gases at the combustor outlet. This is the main feature that controls the process. It also alters the heat fluxes to the combustor walls and to the injector, which determine the lifetime of the combustor. Topological changes of the flame shape are known to alter the performance of the combustor and pollutant emissions (Schmitt et al. (2007)). It is now also admitted that the shape of the flame has a strong influence on its dynamics and in particular on its sensitivity to thermo-acoustic instabilities (Huang and Yang (2004), Kim and Hochgreb (2011), Durox et al. (2013)). As an illustration, Kim et al. (2010) reported that the supplemental anchorage of M flames allow them to damp flow perturbations more efficiently than V flames.

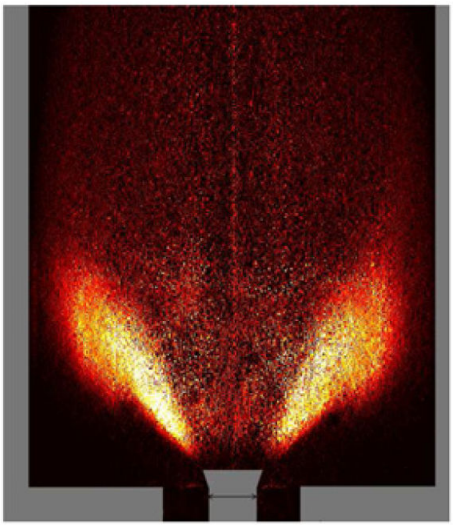

Figure 10: *Example of an atmospheric methane/air V flame with an equivalence ratio of* $\phi = 0.7$*, a bulk flow injection velocity* $U = 2.67\ \mathrm{m \cdot s^{-1}}$*, and a swirl number* $S = 0.55$*. The image is shown after Abel inversion (Poularikas (2010)). Adapted from Palies et al. (2010).*

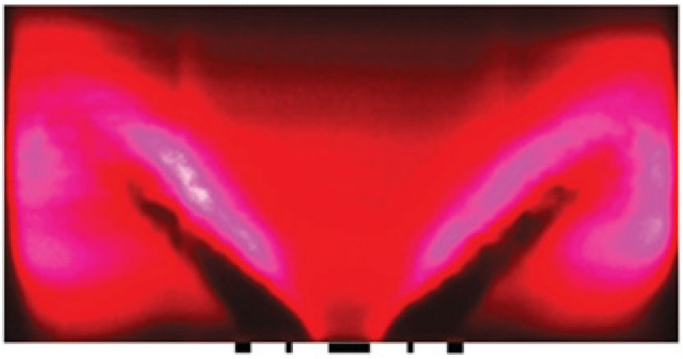

Figure 11: *Example of mean OH-PLIF image of an atmospheric stratified methane/air swirling M flame with a global equivalence ratio* $\phi = 0.55$ *and a bulk flow injection velocity* $U = 5\ \mathrm{m \cdot s^{-1}}$*. Adapted from Kim and Hochgreb (2012).*

Sudden changes of the shape taken by swirled flames are observed in all combustion chambers when the fuel and air flowrates, the injection temperature, or the pressure operating condition are modified (see for examples the studies from Durbin et al. (1996), Terhaar et al. (2014), Chterev et al. (2014)). Chterev et al. (2014) reported that increasing the equivalence ratio or the temperature of the stream of gases at injection benefits the stabilization of M flames (Fig. 13). It is also possible to observe topological transitions even if the operating conditions are not modified (Moeck et al. (2012), Ketelheun et al. (2013)). Ketelheun et al. (2013) emphasized the strong influence of the thermal

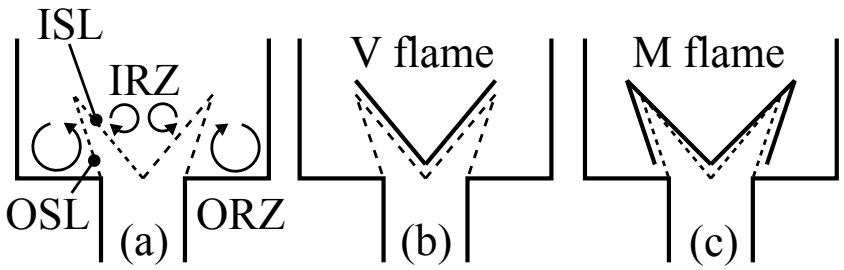

Figure 12: *(a) Schematic of a swirling jet flow in a combustion chamber with its inner (ISL) and outer (OSL) shear layers and the inner (IRZ) and outer (ORZ) recirculation zones. (b) V flame. (c) M flame.*

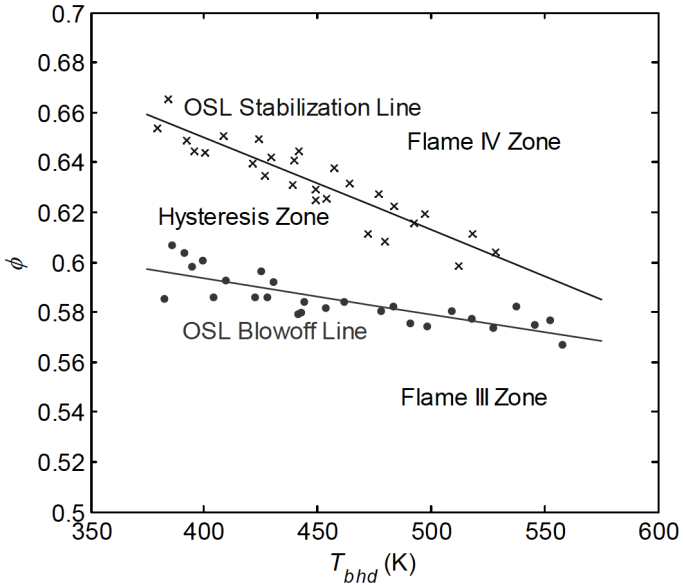

Figure 13: *Typical flame topology chart within a swirl combustor operated at atmospheric pressure and fed with a preheated mixture of natural gas and air at a temperature T_{bhd}. Reproduced from Chterev et al. (2014). Flame III refers to a V flame and flame IV corresponds to an M flame.*

boundary conditions of the combustion chamber on the flame topology. This indicates that topological changes may occur during the thermal transient of the combustor or when heat transfers to the burner or to the combustion chamber boundaries are modified. For a fixed equivalence ratio and a fixed bulk flow injection velocity, Moeck et al. (2012) observed a flapping combustion mode shown in Fig. 14 where the shape of the flame fluctuates with time between V and M states as shown in Fig. 15. It is thus important to identify and sort out the parameters controlling the flame topology in combustors operated with swirl burners.

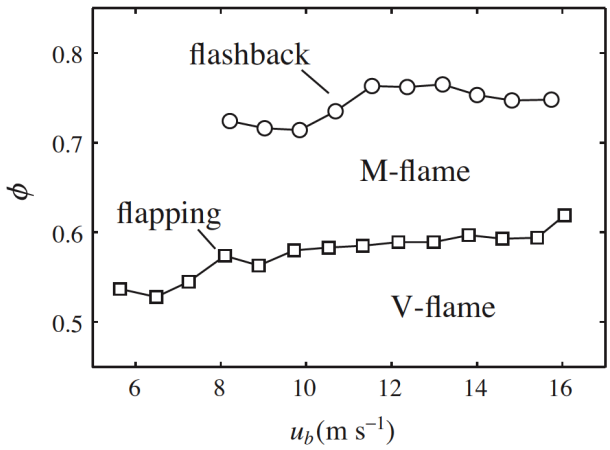

Figure 14: *Typical flame topology chart in a laboratory scale swirl combustor operated at atmospheric pressure and fed with a mixture of methane and air. Reproduced from Moeck et al. (2012).*

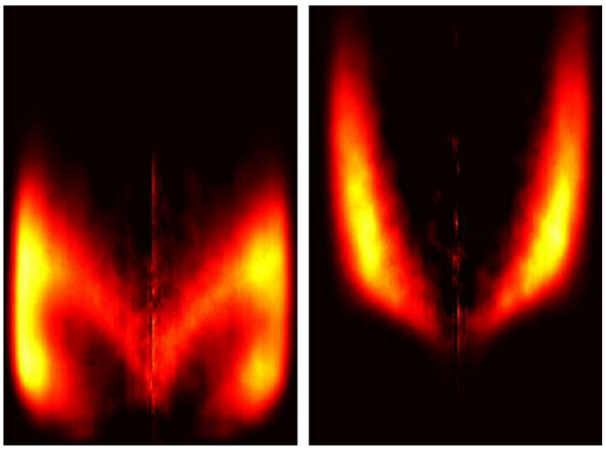

Figure 15: *Typical V and M swirling methane/air flames for two different operating conditions. left:* $\phi = 0.62$ *and* $U = 12.2\,\mathrm{m\cdot s^{-1}}$. *Right:* $\phi = 0.57$ *and* $U = 12.1\,\mathrm{m\cdot s^{-1}}$. *Reproduced from Moeck et al. (2012).*

Before considering effects of swirl, it is worth examining in more details previous studies considering the stabilization of V and M flames. The shape taken by a laminar premixed flame stabilized in the wake of a solid surface results from a competition between the local flow velocity, the stretched flame speed and heat losses to the burner. Many studies have focused on the stabilization of laminar V flames (Lewis and Von Elbe (1987), Edmondson and Heap (1970), Kawamura et al. (1979), Treviño et al. (1991), Sung et al. (1992)). Simultaneous analyses of the stabilization of laminar V and M flames are more scarce (Kawamura et al. (1979), Mallens et al. (1997)). It was found that these different shapes can be obtained for the same flow conditions by modifying the

ignition location (Schuller et al. (2003)) (see Fig. 16). Kawamura et al. (1979) and Mallens et al. (1997) studied experimentally and numerically V and M flame shape transitions on a laminar unconfined burner. By increasing the flow velocity they found that the M to V shape transition is reached for a critical velocity gradient in the jet flow lower than the value necessary to reach the V flame blow-off limit.

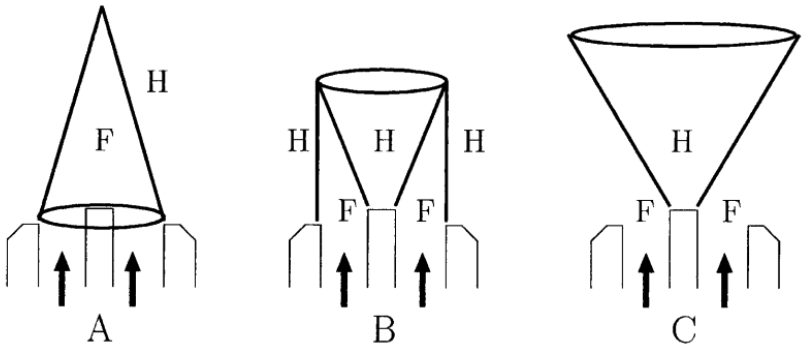

Figure 16: *Shapes taken by a laminar flame above a burner depending on the location of the ignition point. Ignition is realized near the burner rim (B) or near the rod (C). Capital letters F and H respectively refer to fresh gases and hot burnt gases. Reproduced from Schuller et al. (2003).*

In turbulent configurations, unconfined flames are often stabilized by a bluff body (Esquiva-Dano et al. (2001) and Kariuki et al. (2012)) or by imparting swirl to the flow (Lilley (1977), Gupta et al. (1984)). For a sufficiently high swirl, vortex breakdown occurs resulting in the formation of an IRZ (Lucca-Negro and O'Doherty (2001)) that continuously provides hot burnt gases to the flame root and help stabilizing the reaction. Unconfined flames generally take a V shape and it is difficult to identify situations with unconfined M flames fed by hydrocarbon combustible mixtures. For high injection Reynolds numbers, the strain rate in the OSL and ambient air entrainment diluting the reactive stream of gases are generally too important to stabilize a reaction layer in this region (Zukoski and Marble (1956), Longwell et al. (1949), Kariuki et al. (2012)), even in strongly swirling flows (Syred and Beér (1974)). By confining the flame, the ORZ of hot burnt gases generated in the corners of the injection plane and chamber walls benefits to the stabilization of M flames (Nogenmyr et al. (2013)).

A large number of parameters alters the topology of swirling flames in turbulent combustors. The hierarchy between parameters affecting chemistry, aerodynamics, and heat-transfers is not clear. Kim et al. (2010) reported effects of chemistry by changing the composition of the combustible mixture. They observed that increasing the concentration of hydrogen H_2 in a CH_4/H_2/air

combustible mixture benefits to M flames as shown in Fig. 17. Terhaar et al. (2014) studied the topologies of CH_4/H_2/air flames diluted with steam. These authors list three possible flame shapes depending on the steam dilution rate and hydrogen enrichment. Dry flames or steam diluted flames featuring high hydrogen enrichment exhibit a V shape. Trumpet-like flames are found for intermediate steam dilution rates. At high steam dilution rates, flames stabilize with an annular shape. Kim and Hochgreb (2012) analyzed effects of stratification of the fuel on the stabilization of CH_4/air swirling flames. They reported that modifying the radial distribution of the fuel alters the shape taken by the flame as shown in Fig. 18. This emphasizes effects of the flow field and mixing on flame topology. By modifying the blades angle of a radial swirler installed in a laboratory scale burner, Durox et al. (2013) observed effects of the swirl number on the topology of premixed lean CH_4/air flames as shown in Fig. 19.

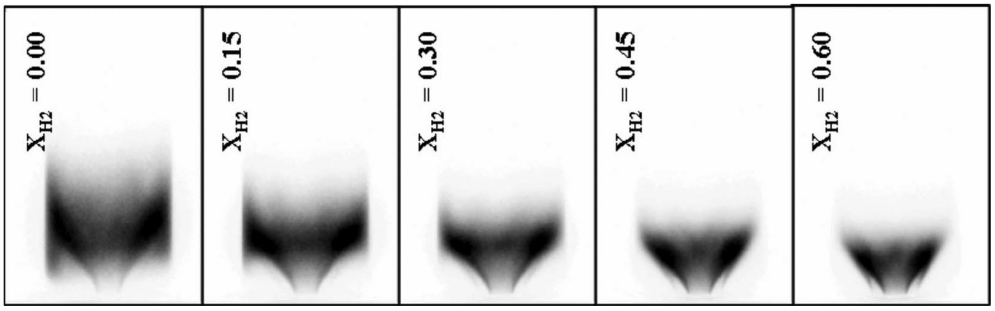

Figure 17: *CH^* chemiluminescence images of CH_4/H_2/air flames at atmospheric pressure for different H_2 molar fractions in the fuel mixture, a fixed equivalence ratio $\phi = 0.60$, and a bulk flow velocity $U = 60\ \mathrm{m \cdot s^{-1}}$. The combustible mixture is preheated to $T_{in} = 473\ \mathrm{K}$. Reproduced from Kim et al. (2010).*

During experiments in a pressurized model combustor, Seo (1999) observed a transition from a V to an M flame when the temperature of the injected CH_4/air combustible mixture was increased from $T_{in} = 570\ \mathrm{K}$ to $T_{in} = 660\ \mathrm{K}$ (Fig. 20). This indicates that the temperature of unburnt gases and the temperature of the whole combustion chamber is susceptible to affect the flame topology. These studies highlight parameters altering flame topologies but the governing mechanisms driving changes of the flame topology in a swirled combustor are not well understood. Further insight may be obtained by examining results of simulations.

Huang and Yang (2004) conducted Large Eddy Simulation (LES) calculations of the experiments of Seo (1999). Starting from a stabilized V flame, they increased the temperature of the injected gases and, as in the experiments, they observed a transition from a V to an M flame. Figure 21 shows a sequence of 2-D temperature fields in the central longitudinal plane of the combustor

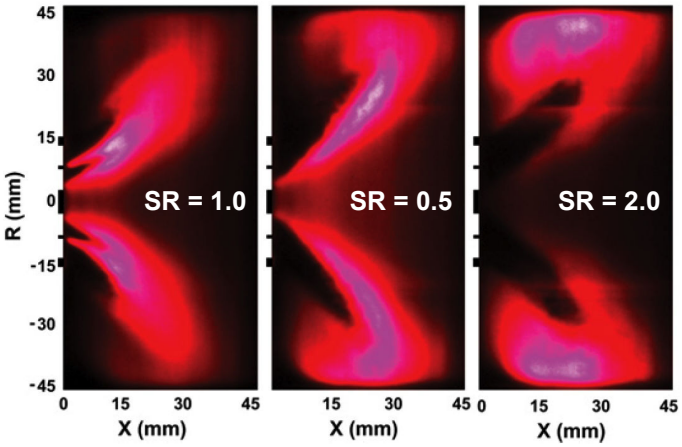

Figure 18: *Time-averaged OH-PLIF distribution of atmospheric CH_4/air flames featuring different stratification ratios SR defined by the ratio of the inner stream equivalence ratio to the outer stream equivalence ratio. The global equivalence ratio and the bulk flow velocity are fixed to $\phi = 0.60$ and $U = 5\ \mathrm{m \cdot s^{-1}}$. Adapted from Kim and Hochgreb (2012).*

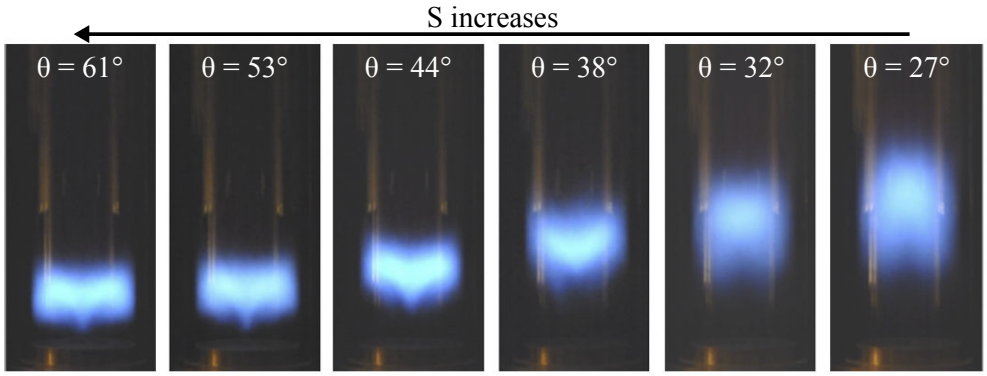

Figure 19: *Images of premixed CH_4/air flames in an atmospheric laboratory scale burner operated at an equivalence ratio $\phi = 0.70$ and a bulk flow injection velocity $U = 11.0\ \mathrm{m \cdot s^{-1}}$ for different swirler blade angles. Adapted from Durox et al. (2013).*

during the V to M transition. Initially, the V flame tip interacts with the combustor peripheral wall and it is clear that the shape transition is triggered by a flashback of the flame in the boundary layer of the combustor peripheral wall. Authors explain that increasing the inlet gas temperature increases the laminar burning velocity of the combustible mixture until favorable conditions are met for flashback. This transition from a V to an M flame by flashback in the boundary layer of the combustor peripheral wall is only possible if the V flame tip impinges the combustor wall.

Using simulations based on a Reynolds-Averaged Navier-Stokes (RANS) de-

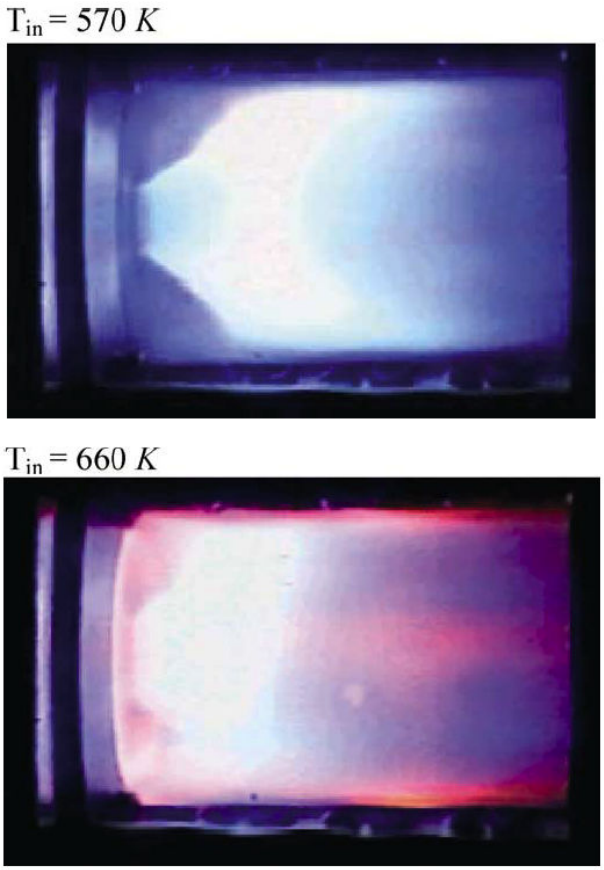

Figure 20: *Images of V and M CH_4/air flames at p = 0.463 MPa for a swirl number S = 0.76, an equivalence ratio ϕ = 0.60, and a bulk flow injection velocity U = 86.6 m · s^{-1}. Reproduced from Seo (1999).*

scription of the reacting flow, Tay Wo Chong et al. (2009) calculated the shape taken by a swirl flame in a model combustor from TU München. Results from adiabatic simulations were compared to chemiluminescence images from the experiments. Figure 22 shows that adiabatic simulations predict an M flame while in the experiments the swirl flame has a V shape. The correct V shape of the flame was roughly captured when the authors conducted simulations accounting for the combined effects of strain rate and heat losses. The supplemental flame front of an M flame is located in the OSL, *i.e.* in a region of the flow featuring high levels of strain. These results indicate that M to V shape transitions might be triggered by localized extinctions of flame elements located in the OSL due to combined effects of strain rate and heat losses.

Influence of strain rate on the extinction limits of premixed laminar flames was demonstrated in a large number of numerical studies conducted with planar flames stabilized in counter-flows (Giovangigli and Smooke (1987), Giovangigli

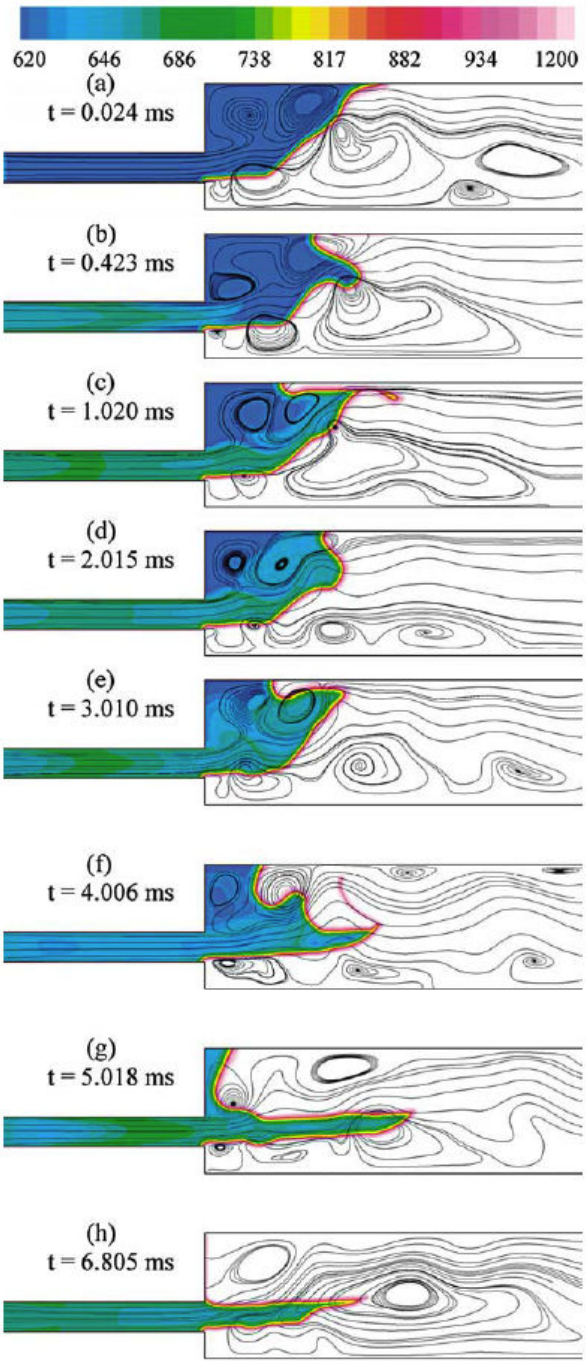

Figure 21: *Transition from a V to an M swirling CH_4/air flame with increased inlet temperature (top color bar) captured by LES. Reproduced from Huang and Yang (2004).*

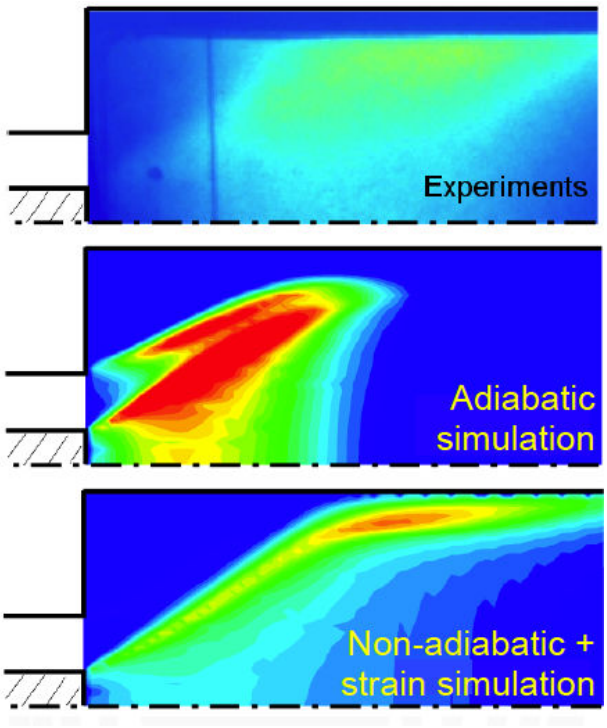

Figure 22: *Spatial distribution of heat release rate for the same flow injection conditions of a natural gas/air swirling flame with a thermal power P = 70 kW and an equivalence ratio ϕ = 0.71. (top) OH* chemiluminescence experiments, (middle) adiabatic RANS, (bottom) RANS accounting for heat-losses and strain rate. Adapted from Tay Wo Chong et al. (2009).*

and Smooke (1989), Sanchez et al. (2000)) and experiments (Wu and Law (1985), Law et al. (1988), Egolfopoulos et al. (1997), Ren et al. (2001)). In many applications, the flows considered feature high Reynolds numbers and efforts were made to investigate effects of strain on turbulent flames. Experiments and simulations were conducted on counter-flow configurations with turbulent flames stabilized in a diffusion mode (Mastorakos et al. (1995), Geyer et al. (2005), and Coppola et al. (2009)) or in a premixed mode (Bray et al. (1991), Kostiuk et al. (1993a), Kostiuk et al. (1993b), Escudié and Haddar (1993), Mastorakos et al. (1995), Bray et al. (1996), Escudié et al. (1999), Coriton et al. (2010), Coriton et al. (2011), and Coriton et al. (2013)). Mastorakos et al. (1995) determined experimentally that the leanest equivalence ratio ϕ for stable operation in a counter-flow configuration increases when the temperature T of the gaseous stream opposing a stream of lean natural gas and air is reduced. The effect is only visible if $T < 1450$ K. More recently, Coriton et al. (2013) investigated the cross effects of strain rate, turbulence and heat losses under comparable conditions. They demonstrated that, at a fixed strain rate, increasing the enthalpy defect in the stream of burnt gases impinging a

$CH_4/O_2/N_2$ combustible mixture increases the probability of localized extinctions of the flame front.

Changes of the flame shape occur in a wide variety of combustors. It is however possible to define two distinct situations where the physical mechanisms driving transitions of the flame shape differ. Figure 23 shows a schematics of these two different possibilities. Situation A refers to a case where the flame tip impinges the combustor peripheral wall. In this configuration, the strong interaction taking place between the flame and the solid wall is an important element controlling changes of the flame topology. If the combustion chamber cross section is increased or if the flame becomes more compact, situation B may arise. In this configuration, there is no direct interaction between the flame tip and the wall. The physics behind transitions taking place in this configuration differs from the previous case. As an illustration, the V to M flame transition triggered by a flashback along the boundary layer of the combustor peripheral wall (Seo (1999), Huang and Yang (2004)) is no longer possible in situation B. Both situations A and B are of practical interest and the mechanisms at the origin of flame shape modifications for these two distinct situations need to be elucidated.

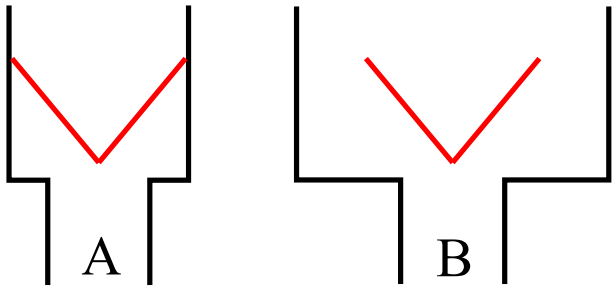

Figure 23: *Schematics of a flame in configuration A featuring a strong direct flame/wall interaction and in configuration B featuring no direct flame/wall interaction.*

Thesis objectives and contents

This work is part of a more extensive project dealing with the stabilization of turbulent flames from low heat value combustible mixtures. The project is financed by l'Agence Nationale de la Recherche, VALOGAZ (ANR-10-EESI-0005). This thesis began with an extensive phase of design and setup of a 26 m^2 room split into a control room and a room dedicated to experiments. The control room includes the systems enabling to control the experimental setup. The lab room includes all fluid and electricity supplies, the test rig and

an exhaust system. Efforts were made to meet the handling and safety regulations concerning harmful gases, lasers, and electrical devices. A schematic showing the facilities of the lab room is shown in appendix A.

The present research focuses on the topology of premixed swirling flames of CH_4/H_2/air eventually diluted with CO_2 or N_2. The objective of this work are:

- Design a well instrumented test-rig for the characterization of swirling flame stabilization mechanisms.
- Conduct a comprehensive parametric study to identify the main mechanisms controlling modifications of the flame shape when the flame is in contact with the combustor peripheral wall (situation A in Fig. 23).
- Analyze the combined effects of strain rate and heat losses on the topology of swirling flames when there is no direct flame wall interaction (situation B in Fig. 23).
- Understand the dynamics of perturbed CH_4/H_2/air swirling flames and effects of mass flow rate perturbations on changes of the flame topology.
- Stabilize CH_4/H_2/air swirling flames with high dilution rates of N_2 and CO_2 far from the solid peripheral wall of the combustor.

These elements are needed to improve our understanding of the stabilization mechanisms of swirling flames. This work comprises two main parts and seven chapters described in the block-diagram in Fig. 24. The content of the seven chapters is briefly described in what follows.

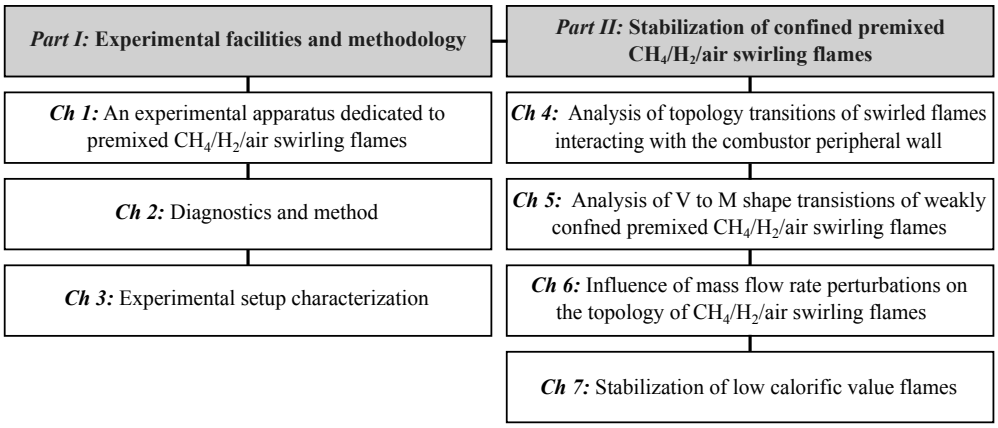

Figure 24: *Block-diagram of the thesis manuscript.*

Part I: Experimental facilities and methodology

The first part of this manuscript includes the description of the experimental setup and the operating conditions that were selected. The diagnostics and a

detailed characterization of the experimental setup operated with or without flames are then presented.

The operating conditions selected for our studies are described in **chapter 1**. The experimental setup which has been developed to stabilize the swirling flames of interest is then presented including the fluid supply hardware and the burner dedicated to the combustion of $H_2/CH_4/N_2/CO_2$/air mixtures. The diagnostics are described in **chapter 2**. We used Laser Doppler Velocimetry (LDV), Hot Wire anemometry (HW), and Particle Image Velocimetry (PIV) to study the velocity field in the combustor. We also used flame chemiluminescence imaging and Planar laser-Induced Fluorescence of the Hydroxyl radical (OH-PLIF) to analyze the topology of the swirling flames and of the flow of the burnt products. Temperature measurements were carried out with thermocouples to measure solid and gas temperatures and Laser Induced Phosphorescence (LIP) of thermographic phosphors to determine surface temperatures of the combustor walls. In **chapter 3** the flow in the combustor under non-reactive and reactive conditions is analyzed in details for a reference flow condition. The flow through the swirler is analyzed in the first section. In a second stage, the flow within the combustion chamber operated under non-reactive conditions is analyzed using PIV. Then, the thermal behavior of the combustor is analysed by LIP and thermocouple measurements conducted during the thermal transient after ignition and at steady-state. Finally, a reference flame is defined for which detailed measurements were carried out with chemiluminescence, PIV, and OH-PLIF.

Part II: Stabilization of confined premixed CH_4/H_2/air swirling flames

The second part of this manuscript describes the results obtained on the mechanisms of stabilization of confined premixed CH_4/H_2/air swirling flames.

Chapter 4 describes effects of swirl, mixture composition, injection velocity, and flame anchoring on topological bifurcations of premixed flames interacting with the combustion chamber peripheral wall. Mechanisms controlling flashback of the tip of swirled flames along a solid wall are rapidly reviewed in section 4.1. The experimental setup and the diagnostics used to examine V/M flame topology transitions are presented in section 4.2. Structures of V and M stable flames are presented in section 4.3 for two configurations of the injector. A model for determining the boundary of V to M flame topology bifurcation is proposed in section 4.4. Predictions are compared to measurements in section 4.5 for two different injection systems by varying the swirling rate, combustible mixture injection velocity, equivalence ratio and hydrogen enrichment in the

combustible mixture.

The physics driving topology transitions in a swirled combustor when the flame does not interact with the combustor peripheral walls is analyzed in **chapter 5**. Effects of the combustible mixture, heat losses, and strain rate are examined. The experimental setup used for this purpose, the diagnostics, and the flow conditions are presented in section 5.1. The impact of the H_2 concentration in the fuel is analyzed in section 5.2, before considering the influence of the thermal boundaries of the combustor in section 5.3. Finally, the combined effects of the heat losses and strain rate are analyzed experimentally and numerically.

In **chapter 6** the influence of mass flow rate perturbations on the topology of CH_4/H_2/air swirling flames is examined for different modulation frequencies and amplitudes. The flame transfer function of a reference CH_4/H_2/air flame is first measured for two different perturbation amplitudes. Two modulation frequencies are then selected and further experiments are conducted using joint OH-PLIF/PIV/chemiluminescence measurements. Interactions of the flame front and burnt gases with vortices detached from the injector rim during a modulation period are analyzed in details. Finally, the response of two CH_4/H_2/air flames, featuring different hydrogen enrichments, to a low frequency and high amplitude modulation is analyzed. Changes of the unsteady flame topology are described using joint OH-PLIF/chemiluminescence measurements.

The stabilization of CH_4/H_2/air swirled flames diluted with N_2 or CO_2 is finally examined in **chapter 7**. A CH_4/H_2/air reference flame with $X_{H_2}/(X_{H_2} + X_{CH_4}) = 0.60$, $\phi = 0.70$, and $P = 4\,\text{kW}$ is first selected. The molar fraction of the diluent (N_2 or CO_2) is increased to analyze effects of dilution on the flame topology. The laminar burning velocities S_L and the adiabatic flame temperatures T_{ad} of these flames are then examined using 1-D laminar direct simulations. The chemiluminescence signal of these diluted flames is then analyzed to infer effects of dilution on the flame topology and on the intensity of the light emitted by the flame. Finally, thermocouple measurements are used to determine the combustor thermal efficiency when the diluent concentration and composition are varied.

Part I

Experimental facilities and methodology

Chapter 1

An experimental apparatus dedicated to premixed CH_4/H_2/air swirling flames

The operating conditions selected for our studies are described in this chapter. The experimental setup which has been developed to stabilize the swirling flames of interest is then presented with the fluid supply hardware and the burner dedicated to the combustion of $H_2/CH_4/N_2/CO_2$/air mixtures. Details are given on the different combustion chambers and swirler geometries used in this work.

1.1 Selection of operating conditions

Large amounts of gaseous by-products are generated during the steel production process. These gas mixtures, of various compositions, include combustible gases such as methane (CH_4), hydrogen (H_2) or carbon monoxide (CO). The Coke Oven Gas (COG) and the Blast Furnace Gas (BFG) are the two main gaseous by-products generated (Modesto and Nebra (2009), Chen et al. (2011)). Valorization of these by-products is an efficient way to reduce the consumption of fuel and to minimize the pollutant emissions from the steel production plant. One possibility is to use these mixtures for in-situ combustion in the various ovens from the plant.

The composition of these gaseous by-products change with time. It also depends on the origin of the raw materials and the specific process from the steel plant (Chen et al. (2011)). Table 1.1 shows typical compositions of COG and BFG. Both COG and BFG gases are produced in the same plant but their compositions highly differ. The COG has a calorific value per unit of mass comparable to that of natural gas (NG) and belongs to the family of High Calorific Value (HCV) gases. Conversely, BFG can be defined as a Low Calorific Value

(LCV) fuel due to the high fractions of inert species like nitrogen or carbon dioxide in its composition. Table. 1.2 summarizes the molar and mass Lower Calorific Values for NG, COG, and BFG mixtures.

Table 1.1: *Typical compositions in mass and molar fractions of Coke Oven Gas (COG) and Blast Furnace Gas (BFG) (Chen et al. (2011)).*

Species	COG		BFG	
Fraction	molar X_k	mass Y_k	molar X_k	mass Y_k
N_2	0.04	0.125	0.55	0.501
CO_2	0.02	0.098	0.22	0.315
CO	0.06	0.188	0.20	0.182
H_2	0.63	0.141	0.03	0.002
CH_4	0.25	0.448	0	0

Table 1.2: *Molar and mass Lower Calorific Values for NG, COG, and BFG mixtures.*

Lower Calorific Value	NG (CH_4)	COG	BFG
mass ($MJ \cdot kg^{-1}$)	50.1	41.4	2.2
molar ($MJ \cdot m^{-3}$)	33.3	15.4	2.8

1.1.1 Operating conditions

We first focus on the combustion of COG. This gaseous mixture has a large content of hydrogen which is a highly reactive species. This facilitates the stabilization of flames (Chomiak et al. (1989)). Secondly, as only water vapor is produced by the combustion of hydrogen, hydrogen-based fuels are very promising in terms of cuts in carbon dioxide emissions. In this section, a HCV reference flame featuring a composition representative of COG will be defined. The HCV reference mixture is then diluted with inert species such as nitrogen and carbon dioxide to study the stabilization of LCV flames.

Noting the small concentration of carbon monoxide in the composition of COG (Tab. 1.1), it has been decided to exclude CO from the composition of the reference flame to reduce the complexity of handling such component (Paubel (2007), Bouvet (2009)). The traces of N_2 and CO_2 are not considered as well to simplify the combustible mixture composition. The reference combustible mixture is then only composed of CH_4 and H_2. An analysis based on the laminar burning velocity S_L and adiabatic flame temperature T_{ad} is used in the following to select a composition representative of COG mixtures.

The laminar burning velocity S_L and adiabatic flame temperature T_{ad} are calculated by computing 1-D freely propagating flames using the REGATH solver

developed at the EM2C laboratory (Candel et al. (2011)). For that purpose, the detailed chemistry mechanism from Lindstedt (1998) is used without accounting for the NOx chemistry leading to 29 species and 141 reactions. This chemistry scheme was validated by many comparisons with experiments and simulations for hydrocarbon mixtures (Sick et al. (1998), Juchmann et al. (1998), Gibaud et al. (2005), and Panoutsos et al. (2009)). Different fresh gas combustible compositions were explored by varying both the equivalence ratio ϕ and the fuel composition. Figures 1.1 and 1.2 show the laminar burning velocity S_L and the adiabatic flame temperature T_{ad} of CH_4/H_2/air mixtures as a function of the H_2 molar fraction in the fuel $X_{H_2}^{fuel}$. This concentration goes from 0.0 (pure methane case) to 1.0 (pure hydrogen case). Calculations are carried out for equivalence ratios $0.7 \leq \phi \leq 1$. The laminar burning velocity S_L and the adiabatic flame temperature T_{ad} of COG/air flames are respectively superimposed in Figs. 1.1 and 1.2 to ease the reading. The COG composition taken for these calculations is indicated in Tab. 1.1.

Figure 1.1 indicates that a molar fraction of hydrogen $X_{H_2}^{fuel} \simeq 0.70$ in the reference combustible mixture is needed to reach the same laminar burning velocity as for the combustion of COG. This remains true for equivalence ratios ranging from $\phi = 0.7$ to 1. Results slightly differ for the adiabatic flame temperatures presented in Fig. 1.2. The value of $X_{H_2}^{fuel}$ in the combustible mixture allows to reproduce the adiabatic temperature of COG/air flame changes with the equivalence ratio. Hydrogen enrichments ranging from $X_{H_2}^{fuel} = 0.60$ to $X_{H_2}^{fuel} = 0.70$ are used to represent the combustion of COG when the equivalence ratio varies from $\phi = 0.7$ to 1. A combustible mixture with an equivalence ratio of $\phi = 0.7$, an hydrogen enrichment $X_{H_2}^{fuel} = 0.70$ reproduces the laminar burning velocity S_L and adiabatic flame temperature T_{ad} of a COG/air flame featuring the same equivalence ratio. At this low equivalence ratio, the adiabatic flame temperature is limited and NOx production is reduced (Brown (1995), Docquier and Candel (2002)). This operating condition is thus of specific interest.

The composition of COG can vary with time and with the raw material feeding the plant. Flames with different hydrogen enrichments are thus studied to account for this variability. Table 1.3 summarizes the operating conditions chosen for the CH_4/H_2/air flames investigated in this work. To comply with the optimal range of the experimental setup that will be fully described in the following sections of this chapter, the thermal power P must be adjusted to the range within $2\,\text{kW} \leq P \leq 6\,\text{kW}$. The majority of the flames considered in this work are stabilized with a thermal power $P \simeq 4\,\text{kW}$. Hydrogen enrichments ranging from $X_{H_2}^{fuel} = 0$ to $X_{H_2}^{fuel} = 0.86$ are used to account for the COG composition variability. The case $X_{H_2}^{fuel} = 0$ corresponds to a combustible mixture with pure methane. Flames with varying equivalence ratios ($0.5 \leq \phi \leq 1.0$) are studied to analyze the effect of this parameter on flame stabilization.

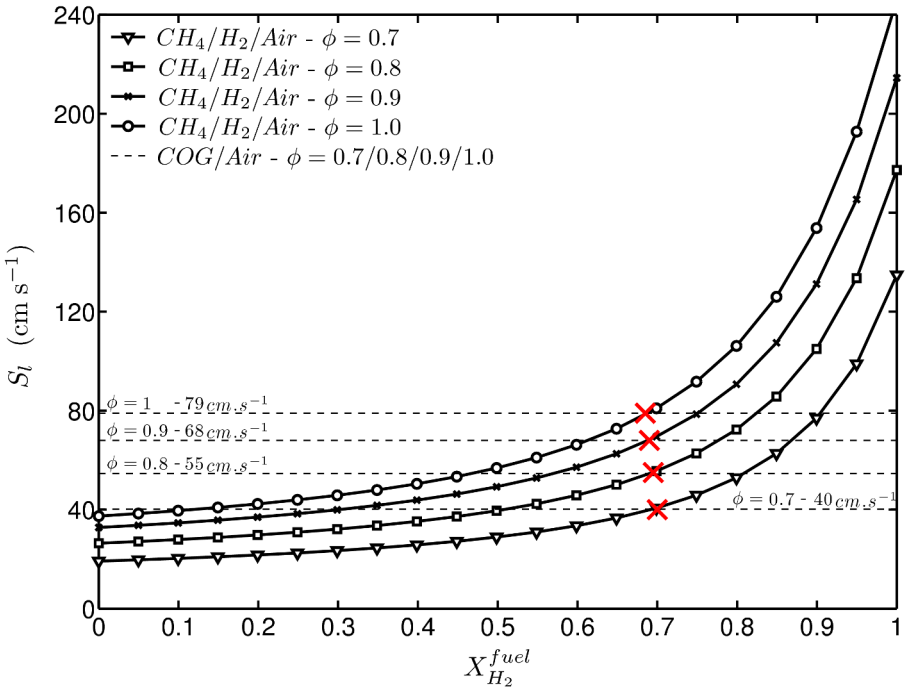

Figure 1.1: *Laminar burning velocity S_L of H_2/CH_4/air mixtures for increasing H_2 molar fractions in the fuel $X_{H_2}^{fuel}$ ranging from 0 to 1 at fixed equivalence ratios of ϕ = 0.7, 0.8, 0.9, 1.0. Values are superimposed to those found for the laminar burning velocity of COG/air mixtures at the same equivalence ratios. Red crosses show the H_2 molar fraction in the fuel of the H_2/CH_4/air mixtures having the same laminar burning velocities as the COG/air mixture at a given equivalence ratio. The detailed chemistry mechanism due to Lindstedt (1998) is used for these calculations. The pressure is set to 101325 Pa and the fresh gas temperature is T_u = 298 K.*

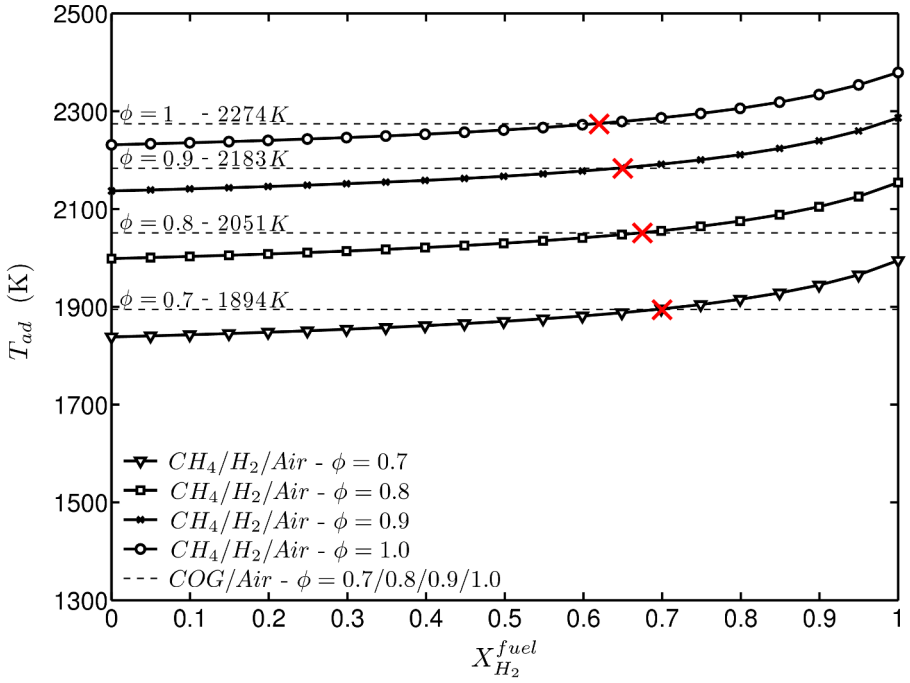

Figure 1.2: *Adiabatic flame temperature T_{ad} of $H_2/CH_4/air$ mixtures for increasing H_2 molar fractions in the fuel $X_{H_2}^{fuel}$ ranging from 0 to 1 at fixed equivalence ratios of ϕ = 0.7, 0.8, 0.9, 1.0. Values are superimposed to those found for the adiabatic flame temperature of COG/air mixtures at the same equivalence ratios. Red crosses show the H_2 molar fraction in the fuel of the $H_2/CH_4/air$ mixtures having the same adiabatic flame temperature as the COG/air mixture at a given equivalence ratio. The detailed chemistry mechanism due to Lindstedt (1998) is used for these calculations. The pressure is set to 101325 Pa and the fresh gas temperature is T_u = 298 K.*

Table 1.3: *Ranges of operating conditions covered for experiments with CH_4/H_2/air flames.*

P (kW)	ϕ	$X_{H_2}^{fuel}$	S_L ($cm \cdot s^{-1}$)	T_{ad} (K)
2 – 6	0.5 – 1.0	0 – 0.86	$\simeq$ 10 – 70	$\simeq$ 1500 – 2200

We also studied the stabilization of LCV flames diluted by N_2 and CO_2. Two different sets of experiments with LCV flames are conducted. The impact of the dilution with N_2 on a reference CH_4/H_2/air flame defined by $X_{H_2}^{fuel}$ = 0.60, ϕ = 0.7, and P = 4 kW is first examined. In a second time, CO_2 is used to dilute the flames. These experiments are conducted at fixed thermal power and hydrogen enrichment in the fuel blend and for different equivalence ratios. Figures 1.3a and 1.3c show the evolution of the laminar burning velocity and adiabatic flame temperature of $H_2/CH_4/N_2$/air mixtures for increasing N_2 molar fractions in the fuel $X_{N_2}^{fuel}$ ranging from 0 to 0.8 at fixed equivalence ratios ϕ = 0.7, 0.8, and 0.9. These figures show that the flames with $X_{N_2}^{fuel} \simeq 0.60$ have the same laminar burning velocity and adiabatic flame temperature as 0.3COG/0.7BFG/air (molar fractions) flames. Figures 1.3b and 1.3d show the evolution of the laminar burning velocity and adiabatic flame temperature of $H_2/CH_4/CO_2$/air mixtures for increasing CO_2 molar fractions in the fuel $X_{CO_2}^{fuel}$ ranging from 0 to 0.8 at fixed equivalence ratios of ϕ = 0.7, 0.8, 0.9. These figures show that the flames with $X_{CO_2}^{fuel} \simeq 0.45$ have the same laminar burning velocity and adiabatic flame temperature as 0.3COG/0.7BFG/air flames. Table 1.4 summarizes the operating conditions chosen for the study of LCV flames.

Table 1.4: *Ranges of operating conditions covered for experiments with CH_4/H_2/air flames diluted by N_2 or CO_2.*

P (kW)	ϕ	X_{H_2} in the CH_4/H_2 mixture	$X_{N_2}^{fuel}$	$X_{CO_2}^{fuel}$
4	0.7 – 0.9	0.60	0 – 0.60	0 – 0.50

1.1.2 Requirements of the experimental setup

Based on the operating conditions described in Tabs. 1.3 and 1.4, an experimental apparatus dedicated to the combustion of $CH_4/H_2/N_2/CO_2$/air swirling mixtures was designed and built. The different maximum flow rates of fluids flowing through the burner are summarized in the following list:

- Air (combustion) - $\simeq$ 200 $NL \cdot min^{-1}$
- CH_4 - $\leq$ 10 $NL \cdot min^{-1}$
- H_2 - $\leq$ 20 $NL \cdot min^{-1}$
- N_2 - $\leq$ 30 $NL \cdot min^{-1}$

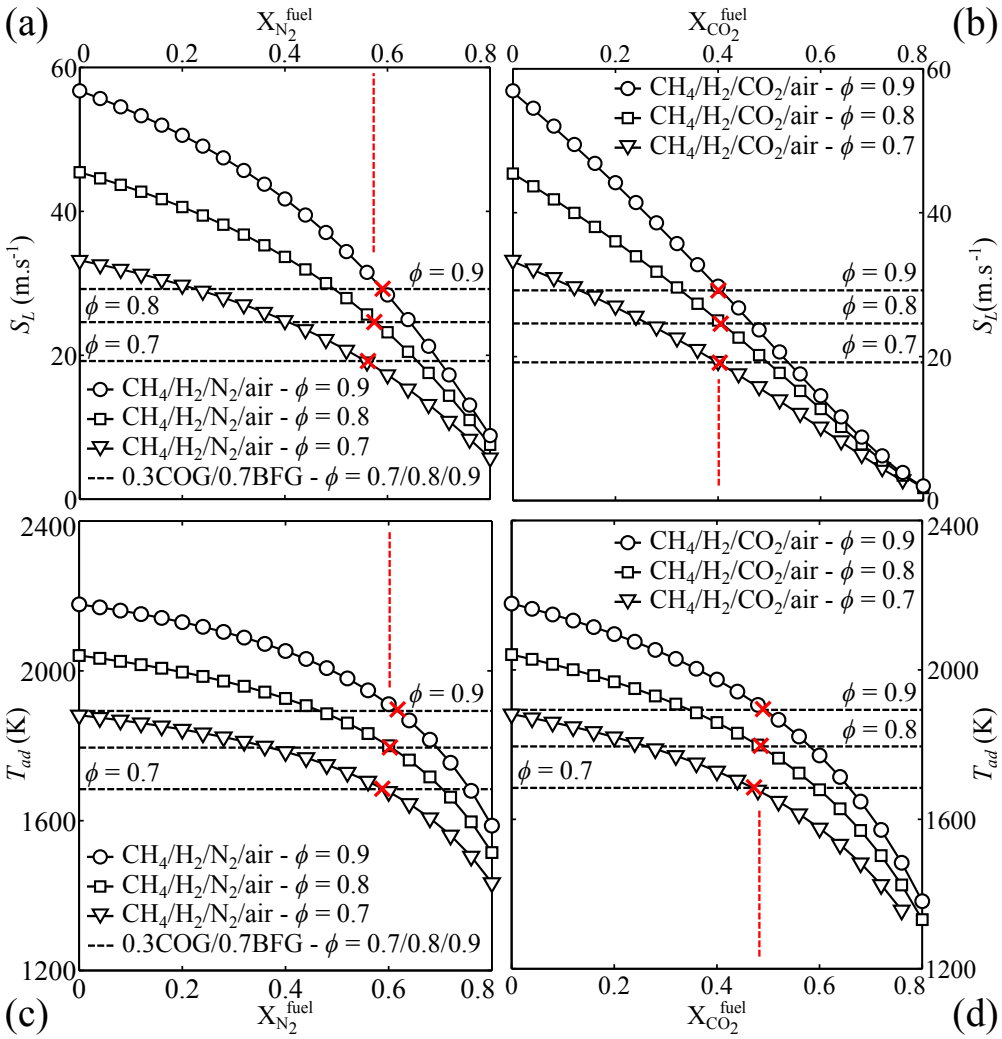

Figure 1.3: *Laminar burning velocity S_L (a)-(b) and adiabatic flame temperature (c)-(d) of $H_2/CH_4/N_2$/air mixtures with $X_{H_2}/(X_{H_2}+X_{CH_4})$ = 0.60 when the molar fraction of N_2 (left column) and CO_2 (right column) in the fuel increases from $X_{diluent}^{fuel}$ = 0 to 0.8. Results are shown for three different equivalence ratios ϕ = 0.7, 0.8, and 0.9. Values are superimposed to those found for 0.3COG/0.7BFG/air (molar fractions) mixtures at the same equivalence ratios. Red crosses show the diluent molar fraction in the fuel of the mixtures having the same laminar burning velocities or adiabatic flame temperature as the 0.3COG/0.7BFG/air mixture. The detailed chemistry mechanism from Lindstedt (1998) is used for calculations.*

- CO_2 - $\leq 30\ \mathrm{NL \cdot min^{-1}}$

Additional air and liquid water supply lines were developed for the thermal management of the combustor and lasers:

- Air (miscellaneous) - $\leq 100\ \mathrm{NL \cdot min^{-1}}$
- Liquid water (burner cooling) - $\leq 2\ \mathrm{L \cdot min^{-1}}$
- Liquid water (lasers cooling) - $\leq 50\ \mathrm{L \cdot min^{-1}}$

A high-voltage spark igniter (7 kV and 30 mA) is used to initiate combustion. Figure 1.4 shows a simplified schematics of the experimental setup with the network of fluid supply used to produce the combustible mixture with the desire composition, the water cooling system, and the ignition electrodes. Pure gaseous species (CH_4, H_2, N_2, and CO_2) and filtered air are supplied to the experimental room by a network of pipes connected to pressurized gas cylinders and an air compressor located outside. Five thermal mass flow controllers (MFC) (see Sec. 1.1.3 for details) are used to produce the desired combustible mixture in a mixing box. The mixture is then fed to the burner (see Sec. 1.2 for details) where a swirling flame is stabilized. Water-cooling of the burner is used to limit the temperatures reached in the injector. The water mass flow rate through the burner is manually adjusted to reach the desired operating temperature of the metallic pieces. Flames are ignited by a spark generated between two electrodes separated by a 3 mm gap and located few millimeters above the burner exhaust. The 7 kV voltage difference between the two electrodes is generated by a high voltage transformer (Siemens, ZE 30/7). A more detailed version of the schematics describing the experimental setup is produced in appendix A.

1.1.3 Mass-flow regulation

The mass flow rates of the different gases injected are regulated by thermal mass flow controllers (MFC) (Bronkhorst F-Series). These MFC were carefully calibrated using real gases (TrigasFI GmbH) or with nitrogen. In the latter case, correction coefficients from Bronkhorst were used. To reduce imprecisions, MFC are used at flow rates larger than 10% of their respective full scales. When a large range of mass flow rates is required, different MFC featuring different full scales are used to inject the same gas. These precautions lead to a relative precision of 1.5% of the set operating point for each gas mass flow rate. In the case of CH_4/H_2/air combustible mixture, the composition and mass flow rate are known with a relative precision always better than 4.5%. For $CH_4/H_2/N_2/CO_2$/air mixtures, the relative precision drops to 7.5%.

For a CH_4/air mixture, a thermal power P and an equivalence ratio ϕ are se-

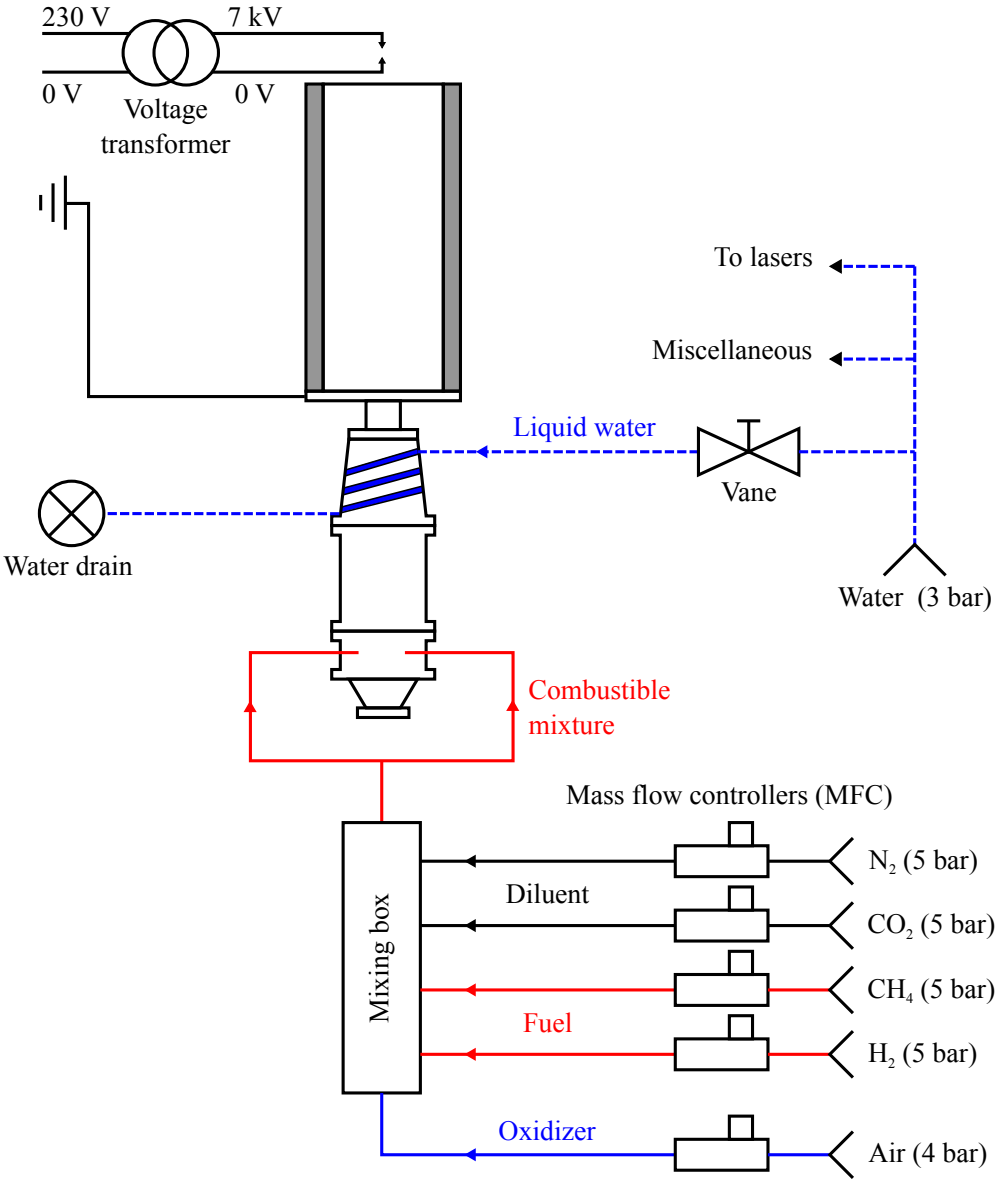

Figure 1.4: *Simplified schematics of the experimental setup including the production of the combustible mixture, the water cooling system, and the ignition electrodes.*

lected to calculate the two species mass fractions and the total mass flow rate and, therefore, produce the mixture of interest using two MFC. To produce CH_4/H_2/air mixtures, the mass flow rates of methane $\dot{m}_{CH_4}$, hydrogen $\dot{m}_{H_2}$, and air $\dot{m}_{air}$ need to be fixed. This was realized by selecting a thermal power P, an equivalence ratio ϕ, and an hydrogen molar enrichment in the fuel blend $X_{H_2}^{fuel}$. With these operating parameters, it is for example possible to stabilize and compare flames featuring the same thermal power and equivalence ratio, but different hydrogen enrichments in the fuel blend.

It is shown in chapter 4 that the laminar burning velocity S_L is a key parameter for the stabilization of swirling flames interacting with the combustor peripheral walls. To analyze the influence of this parameter, it is useful to stabilize and compare flames featuring the same thermal power and laminar burning velocity but different hydrogen enrichments in the fuel. Both equivalence ratio and hydrogen enrichment in the fuel varies in this case.

An automated method for the control of mass flow controllers was developed. This method allows to produce $CH_4/H_2/N_2/CO_2$/air mixtures while controlling a wide range of input parameters such as the thermal power, the equivalence ratio, the hydrogen enrichment, the fraction of diluent species, the laminar burning velocity, the adiabatic flame temperature, *etc.* This method is briefly described here. The laminar burning velocity S_L and the adiabatic flame temperature T_{ad} of $CH_4/H_2/N_2/CO_2$/air mixtures are first computed over wide ranges of equivalence ratio, hydrogen enrichment, nitrogen enrichment, and carbon dioxide enrichment. This is achieved with the REGATH flame solver. As an illustration, Fig. 1.5a shows the evolution of the adiabatic flame temperature T_{ad} for $CH_4/H_2/N_2$/air mixtures with equivalence ratios ranging from $\phi = 0.70$ to $\phi = 0.94$ and nitrogen enrichment in the fuel ranging form $X_{N_2}^{fuel} = 0$ to $X_{N_2}^{fuel} = 0.8$. The hydrogen enrichment is fixed to $X_{H_2}^{fuel} = 0.6$ in Fig. 1.5a. It is clear that, at a fixed nitrogen enrichment, increasing the equivalence ratio increases the adiabatic flame temperature. Conversely, at a fixed equivalence ratio, increasing the nitrogen enrichment decreases the adiabatic flame temperature. For each nitrogen enrichment in the range $0 \leq X_{N_2}^{fuel} \leq 0.8$, there is an equivalence ratio yielding a given adiabatic flame temperature. The case where $T_{ad} = 1900$ K is selected as an example and is shown in Fig. 1.5a.

Figure 1.5b shows the evolution of the equivalence ratio of $CH_4/H_2/N_2$/air mixtures as a function of both the nitrogen enrichment and the adiabatic flame temperature. Using these calculations, we can produce and stabilize $CH_4/H_2/N_2$/air flames featuring fixed adiabatic flame temperatures. We can do the same for $CH_4/H_2/N_2$/air flames featuring fixed laminar burning velocities. When the input parameters are chosen, an home-made LabVIEW routine, fed with all the results from the REGATH calculations, computes the thermal power, the equivalence ratio, and the $H_2/N_2/CO_2$ enrichments. This

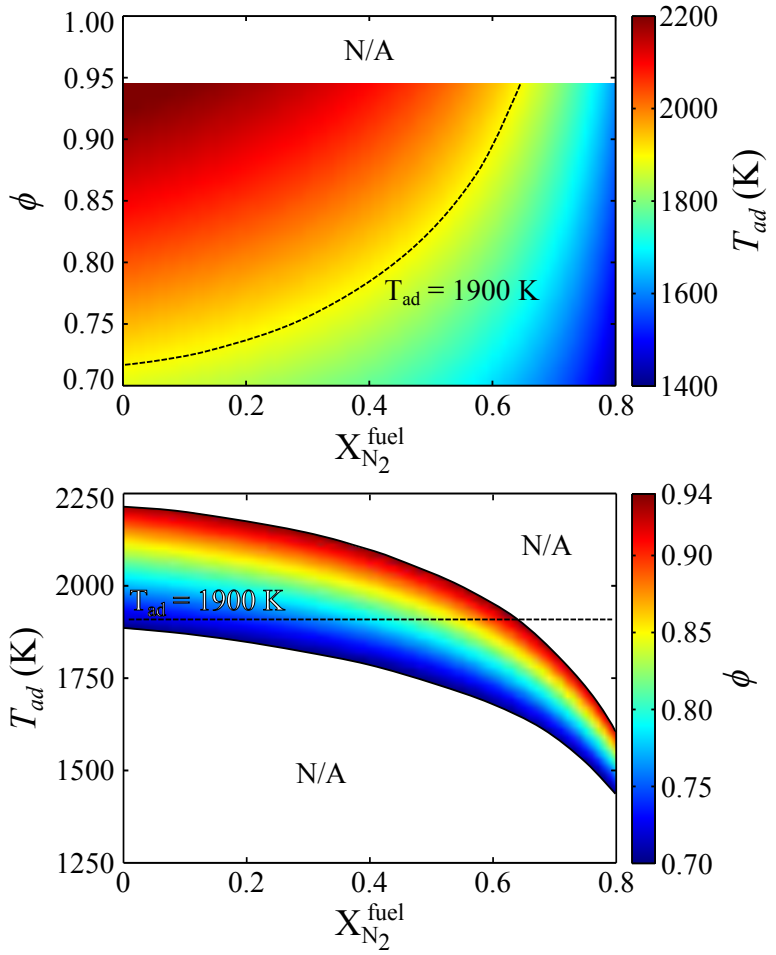

Figure 1.5: *(a) Adiabatic flame temperature T_{ad} as a function of the nitrogen enrichment in the fuel $X_{N_2}^{fuel}$ and the equivalence ratio ϕ with $X_{H_2}/(X_{H_2} + X_{CH_4}) = 0.60$. (b) Equivalence ratio ϕ as a function of the nitrogen enrichment in the fuel $X_{N_2}^{fuel}$ and the calculated adiabatic flame temperature T_{ad} with $X_{H_2}/(X_{H_2} + X_{CH_4}) = 0.60$.*

program then computes the corresponding species mass fractions and the operating mass flow rates. Finally, these instructions are sent to the mass flow controllers. This flexible and automated method helps to conduct parametric analyses very rapidly with a high repeatability and precision.

1.2 Burner

When the combustible mixture of interest flows out of the mixing box, it enters the burner. The burner drawn in Fig. 1.6 is comparable to that used by Palies et al. (2010) and Palies et al. (2011b) for the investigation of linear and nonlinear dynamics of swirling flames submitted to acoustic forcing. This burner is fed by mixtures of methane, hydrogen and air diluted by nitrogen or carbon dioxide, and includes a cylindrical injection tube with a 14 mm exit diameter. The flow is put in rotation by a radial swirling vane located upstream of the injection tube. Details on the radial swirl vane are given in Sec. 1.3. A 6 mm diameter central rod installed on the burner axis helps anchoring the flame at the injection unit outlet 2 mm above the combustion chamber dump plane. The presence of the central rod reduces the degrees of freedom of the system because all flames stabilized with this setup feature a flame root anchored on this element.

The mixture enters the burner through a plenum and subsequently passes through a set of grid/honeycomb/grid arrangement before entering a water-cooled convergent nozzle to reach a nearly uniform top hat velocity profile at the entrance of the swirler. The flames are stabilized in the combustion chamber which, in the schematics presented in Fig. 1.6, features four 250 mm (height) × 92 mm (width) × 12 mm (thickness) quartz windows. We chose a combustion chamber featuring a squared cross section for two reasons. First it is more representative of the geometry of typical industrial furnaces such as those found in the steel-industry. Secondly, laser-based optical diagnostics are facilitated when the combustion chamber windows are flat. Laser reflections and light scattering problems are limited compared to chambers equipped with cylindrical windows. If required, one quartz window can be replaced by a water-cooled stainless-steel wall. This element, presented in Fig. 1.7, is used to modify the wall temperature of the combustion chamber by adjusting the water mass flow rate, $\dot{m}_{water}$, through the cooling channels. The section expansion ratio at the injection tube outlet is quite large $S_1/S_0 = 62.9$, where S_0 and S_1 denote the sections of the injection tube and the combustion chamber, respectively. This is a deliberate choice that is again representative of the targeted industrial furnaces. In this configuration, flames do not interact directly with the combustion chamber walls as the flame tip lies far away from these walls. To prevent ambient air intrusion at the combustor outlet a convergent exhaust is

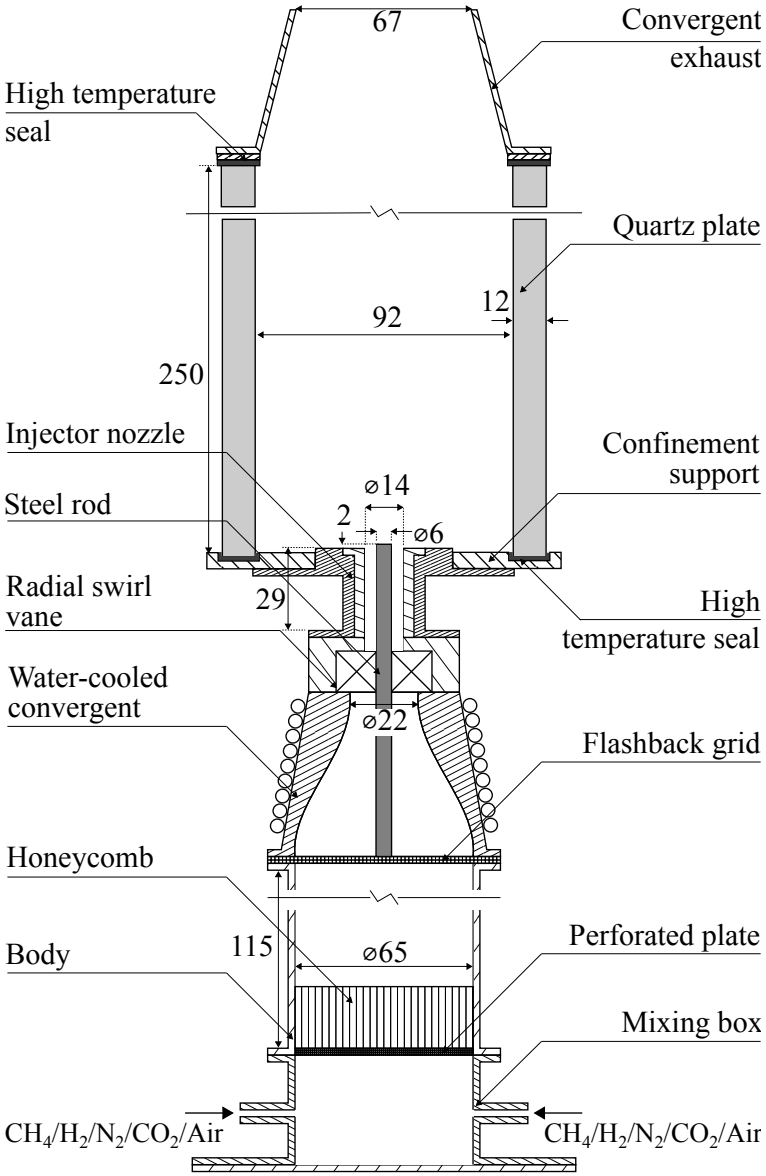

Figure 1.6: *Schematics of the burner showing the different pieces and the main dimensions (in mm).*

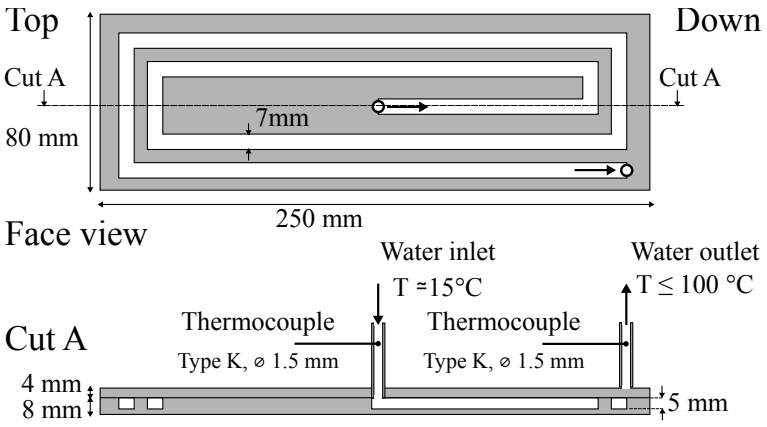

Figure 1.7: *Schematics of the water-cooled stainless-steel combustor wall.*

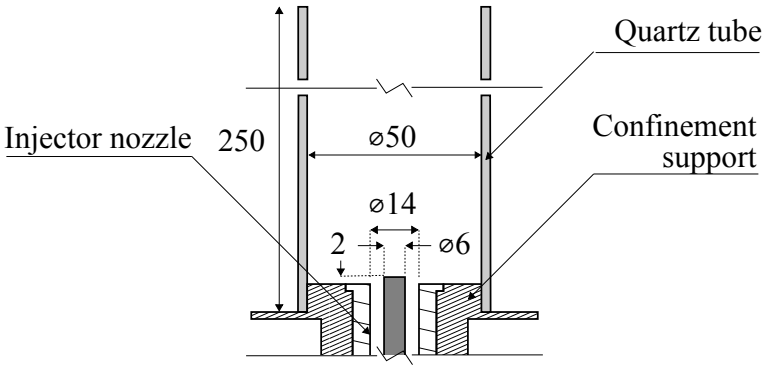

Figure 1.8: *Schematics of the burner equipped with a* 50 mm *diameter cylindrical confinement chamber. Dimensions are in mm.*

added on the top of the chamber to accelerate the outgoing flow. This nozzle features an outlet section contraction ratio of 0.45.

It is also possible to replace the squared combustion chamber by a cylindrical quartz tube as shown in Fig. 1.8. This tube features an internal diameter of 50 mm which yields a reduced section expansion ratio of $S_1/S_0 = 15.6$ between the injection tube and the combustion chamber. In this configuration, flames strongly interact with the combustor peripheral wall and stabilization is altered. This configuration is closer to that of combustion chambers equipping gas turbines for energy production or aircraft engines for propulsion.

1.3 Swirlers

A swirl flow is generated to facilitate the stabilization of lean premixed flames. Upstream the injector, the flow is put in rotation by a radial swirl vane (also

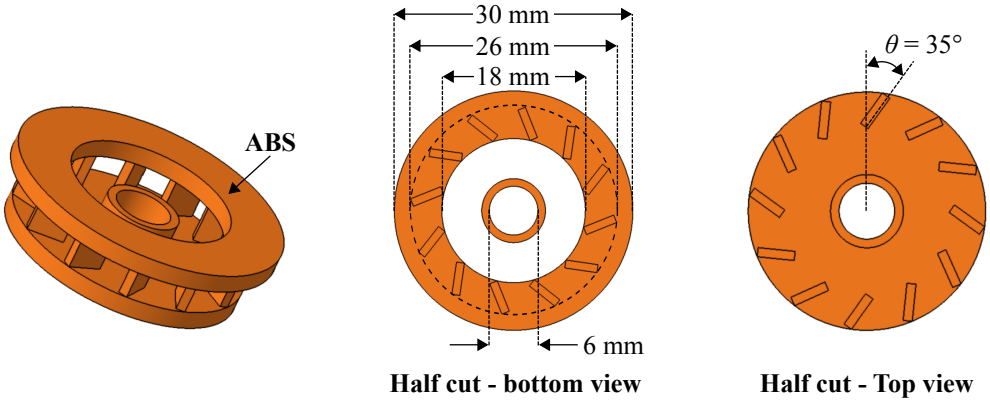

Figure 1.9: *Schematics of the radial swirl vane featuring a fixed vane angle* $\theta = 35°$ *with the main dimensions.*

called swirler) as the one presented in Fig. 1.9. With this device, the gaseous flow is forced to pass through an arrangement of 12 inclined blades and streamlines are bent in the azimuthal direction. The resulting rotating flow is characterized by the swirl number S. The largest deviation is obtained for the largest swirl number. The swirl number depends on the swirl vane geometry (Galley et al. (2011)):

$$S = \frac{1}{1-\psi}\tan(\theta)\frac{R}{2L}\left[1-\left(\frac{R_p}{R}^2\right)\right] \tag{1.1}$$

where ψ is the blockage factor (Beér and Chigier (1972)), R_p denotes the radius of the central rod, R indicates the radius of the injection tube, L is the blade span, *i.e* the height of the blade in the axial direction of the burner, and θ stands for the blade angle. The two main parameters affecting the swirl number are the blade angle θ and the blade span L. If the blade angle θ is increased, the swirl number increases. Conversely, if the span is increased the streamlines deviation is reduced and the swirl number decreases.

The amount of swirl that is required for flame stabilization depends on a large number of parameters such as the composition of the combustible mixture, the bulk flow velocity at the injection tube outlet, and the presence or absence of a central rod. It was difficult to select *a priori* the swirler geometry that is the best adapted to our needs. We decided to build an important number of swirlers featuring different blade angles θ or blade span L. Selection of the optimal swirler design was made empirically by igniting flames at the operating conditions described in Tab. 1.3 and analyzing the stabilization of the flames for different swirler geometries. The swirler featuring a blade angle $\theta = 35°$ and a blade span $L = 4$ mm was found to be well suited for the stabilization of lean CH_4/H_2/air flames at a $P = 4$ kW thermal power. This swirler is characterized

by a geometric swirl number S = 0.5 calculated with Eq.(1.1).

Swirlers were executed with fast prototyping. Swirlers are made of ABS (Acrylonitrile butadiene styrene) and it is possible to produce more than 20 different swirler geometries in one batch. It takes approximately one day to design and produce a swirler with this technique. It has however few drawbacks. ABS is a thermoplastic meaning that it is fragile and very sensitive to heat. One flashback event in the injection tube may be sufficient to deteriorate the swirler. After such an event, it is necessary to replace this element by a new one using the same CAO, but slight changes in the final geometry executed by the machine may occur due to the non-perfect repeatability of the process. As an illustration, the machine that we used features a precision of 2/10 mm. This value must be compared to the smallest dimension of our swirler geometry which is the blade thickness of 1 mm. The relative precision is not very good. This can have severe consequences on the resulting swirling flow (Bourgouin et al. (2013)). Consequently, we were very careful concerning flashback events when using swirlers made with ABS and all experiments at fixed swirl numbers were conducted using the same swirlers. The study of the flow patterns generated by the swirler as well as the determination of the swirl number S are described in chapters 3 and 4.

Another system with movable radial blades was also used to easily change the swirl number. Different values of swirl number S can be set using a remote step motor controlling the trailing edge blades angle θ of the swirler with respect to the radial direction. Figure 1.10 shows top views of the swirler for two distinct vane angles and a schematic of the main dimensions of this device. With this system, fully described in Durox et al. (2013), it is possible to vary continuously the swirl number during experiments. This system also comes with a serious drawback. The repeatability in the blade angle is not guaranteed due to eventual failures of the step motor. When changes in the swirl number are not needed, fixed radial swirl vanes were used to ensure a perfect repeatability of the injections conditions.

Both fixed and adjustable swirl vanes can be used either with the squared or the cylindrical combustion chamber and with the 14 mm injection tube equipped with the central rod. When the adjustable swirl vane is used, it is also possible to remove the central rod and decrease the injection tube diameter to 12 mm. This is used to achieve higher swirl numbers as shown in chapter 5. In this case, flames are no longer anchored at the central rod tip but they are aerodynamically stabilized away from solid elements. This stabilization mode is possible when the swirl number exceeds a certain threshold value associated to a vortex breakdown of the flow along the burner axis (Gupta et al. (1984)). More details are provided in Sec. 3. The two injector configurations are shown in Fig. 1.11. Configuration A refers to the 14 mm annular injection tube equipped with the

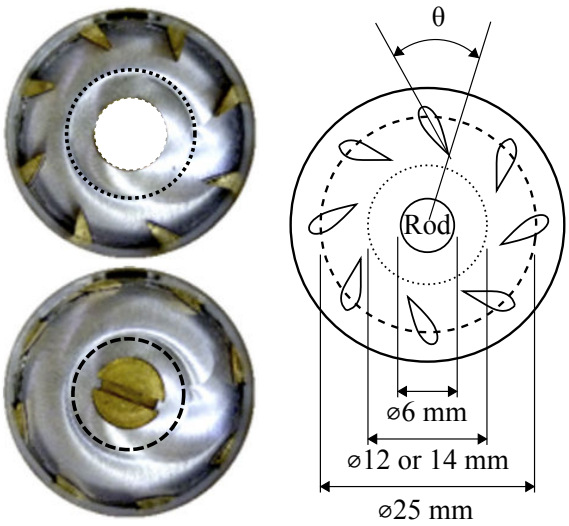

Figure 1.10: *Left: top views of the adjustable swirler for a blade angle $\theta = 23°$ (top) and $\theta = 61°$ (bottom) (Durox et al. (2013)). The black dotted and dashed circles represent the 14 mm (configuration A) and 12 mm (configuration B) injection tube diameters respectively. The central hole is crossed by the rod in configuration A and obstructed by a screw in configuration B. Right: Schematic with the main dimensions of the swirler.*

central rod. Configuration B refers to the 12 mm cylindrical injection tube without central rod.

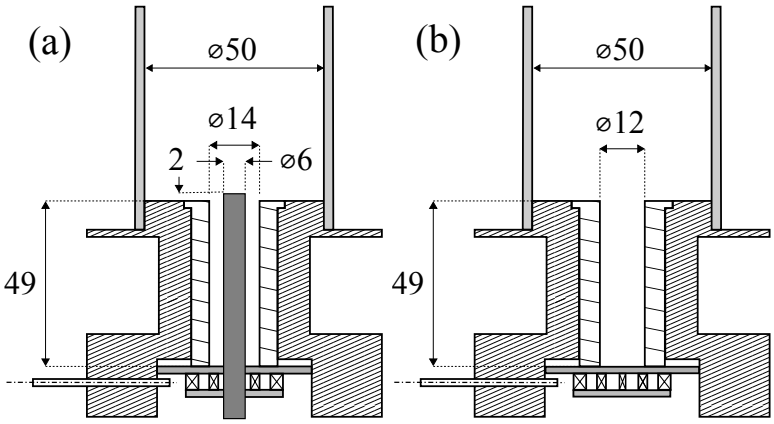

Figure 1.11: *(a) Injector with the central rod (configuration A). (b) Injector without central rod (configuration B). Dimensions are in mm.*

Chapter 2

Diagnostics and methods

The different diagnostics that were used in this work are described in this chapter. We used Laser Doppler Velocimetry (LDV), Hot Wire anemometry (HW), and Particle Image Velocimery (PIV) to study the velocity field in the combustor. We also used flame chemiluminescence imaging and Planar Laser-Induced Fluorescence of the Hydroxyl radical (OH-PLIF) to analyze the topology of the flame and of the burnt gases. Thermocouples were used to measure solid and gas temperatures and Laser Induced Phosphorescence (LIP) of thermographic phosphors was applied for the determination of surface temperatures.

The degree of personal implication and the additional developments of the diagnostics that were necessary to fulfil the scientific objectives are variable and depend on the technique. This dictates the level of details that is given in the different sections of this chapter. For example, we conducted LDV measurements on a well known configuration and did not bring any improvement to the initial setup. Conversely, the LIP technique was not available at EM2C and we had to develop a LIP setup based on a detailed examination of the current state of the art and helpful discussions with research teams outside of the lab.

2.1 Laser Doppler Velocimetry (LDV)

As mentioned in Sec. 1.3, the burner that is used in these studies is equipped with a radial swirl vane in order to help the stabilization of flames. Different swirl vanes were used. The geometry of the radial swirler has a strong influence on the downstream flow topology that was characterized by LDV.

The LDV system is similar to the one used by Ducruix (1999), Schuller (2003), Birbaud (2006), Noiray (2007), Palies (2010), and Boudy (2012) for the analysis of the dynamics of laminar premixed conical flames, laminar V-flames, or swirling flames and the reader is referred to these previous studies for details

on the setup. Only settings that are specific to our study are described in the following. The LDV system is operated with a green CW (Continuous Wave) argon laser (2 W at λ = 514 nm). This light is scattered by micrometric oil droplets (D_{10} = 2.5 µm and D_{32} = 5 µm) seeded into the flow by a nebulizer fully described by Durox et al. (1999). The scattered Mie signal is collected by a photomultiplier with a narrow-band interference filter center on λ = 514 nm. A frequency counter is associated to deduce the velocity from Doppler bursts. The flow through the nebulizer is partly by-passed to ensure a data rate comprised between 40 kHz and 60 kHz for the injection velocities explored. The validation rate is better than 50% for these settings. A 5 MHz Bragg frequency shift module is used to discriminate negative and positive velocities. In our experiments, the analog signal delivered by the frequency counter is sampled at 16384 Hz during 2 s. It has been checked that this acquisition rate and duration yields fully converged mean and root-mean-square (rms) values for the different components of the velocity for for the different flow operating conditions explored.

The setup that is used allows to measure only one component of the 3-D velocity during a given experiment. The laser optics are rotated and the photomultiplier is realigned on the interference fringes to measure another velocity component during a following experiment. It was then possible to measure the mean and rms values for the axial u_z, azimuthal u_θ, and radial u_r velocities at the injector outlet. Due to the rotational symmetry of the injection tube, we assumed that a complete characterization of the swirl is obtained by measuring only one 2-D velocity profile along the radial coordinate. Measurements were conducted as close as possible to the injector rim, 2 mm above the injection plane or 1 mm above the central rod tip when this element is installed. The distance between two measurement points in the radial direction is set to 0.5 mm and velocity profiles were measured for radial distances $|r| < 7.5$ mm above the injection hole. Data are recorded using an automated control for displacement and acquisition of the signals. Velocity profiles are presented in Sec. 3.1 where the different radial swirl vanes used are fully characterized.

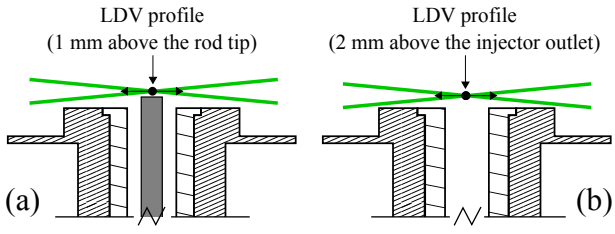

Figure 2.1: *Schematic of the injector showing the position of the LDV measurements with the injector set in configuration A (a) and B (b).*

2.2 Hot wire anemometry (HW)

LDV measurements are limited to the regions of the flow downstream the injector tube outlet within regions with optical access. Measurements of the velocity upstream the injector, inside the injection tube, were realized with a Hot Wire (HW). A hole of few millimeters diameter is drilled in the burner to introduce the probe. These measurements were used to analyze the dynamics of CH_4/H_2/air flames that are presented in Ch. 6.6. After a brief description of the principle of this measurement technique, the following sections describe the impact of the gas composition on the measurements.

2.2.1 Measurement principle

Hot wire anemometry relies on the cooling effect of a gaseous or liquid flow surrounding a heated solid body. Assuming that the flow velocity is large enough, a regime of forced convection between the gaseous flow and the solid element may be reached (Incropera and Witt (1990)). In this case, the thermal power extracted from the solid by forced convection and dissipated into the fluid is a monotonous function of the fluid velocity. The higher is the fluid velocity, the higher is the convective heat flux. Assuming that the relation between the convective heat flux and the velocity is known with precision, it is possible to deduce the flow velocity by measuring the convective heat flux through the heated solid surface.

Figure 2.2 shows a schematic of a HW probe and its electronics for signal conditioning. The hot wire probe used here consists in a tungsten wire featuring a large aspect ratio $L/D >> 1$ between its length $L = 1$ mm and its diameter $D = 5$ µm. This wire is placed in the fluid of interest, where the velocity measurement is needed. One considers a one-dimensional gaseous flow characterized by a velocity u, a temperature T, a thermal conductivity k, and a kinetic viscosity ν. The wire that features an electric resistance R_{HW} is crossed by a current I_{HW}. Due to the Joule effect, the wire delivers a thermal power $P = R_{HW} I_{HW}^2$ and heats up to a temperature T_{HW} higher than the gas temperature T. Consequently, a convective heat flux Q is transferred from the wire to the gas and at steady state one has $P = Q$. Therefore if the gas velocity is modified, the convective heat flux will change and the thermal equilibrium will cease.

When operated as a Constant Temperature Anemometer (CTA), the temperature of the wire is maintained constant (Bruun (1995)). When Q is increased due to a velocity increase, the temperature of the wire decreases because $P < Q$ and the wire resistance R_{HW} decreases. In this case the current supplied to the wire, which is regulated by a specific circuit, increases so that the thermal power produced from the Joule effect rises and compensates the convective heat

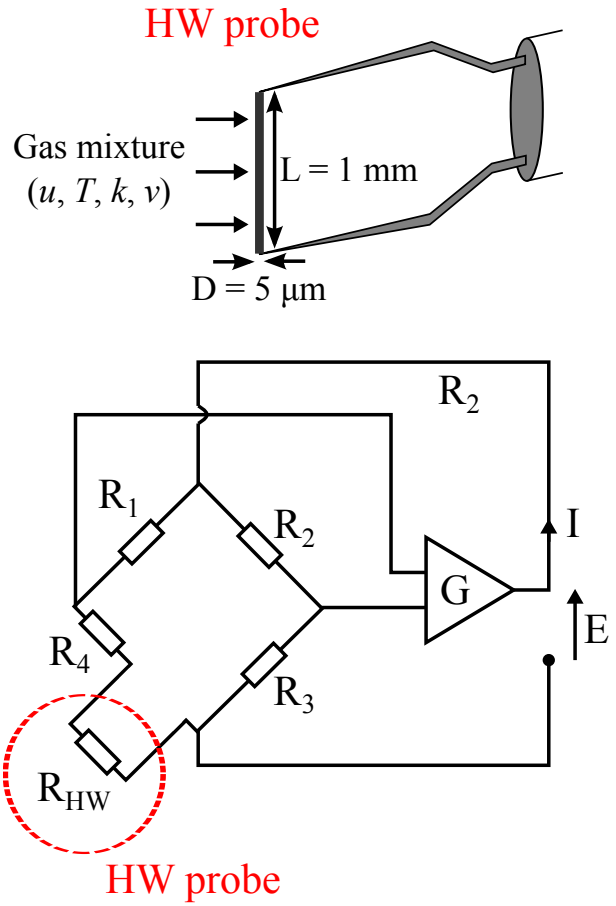

Figure 2.2: *Schematic of a hot wire probe (top) and control electronics (bottom). The surrounding gas mixture features a velocity u, a temperature T, a thermal conductivity k, and a kinetic viscosity ν. The capital letters L and D respectively stand for the length and diameter of the hot wire. In the bottom schematic, load resistors are denoted by a capital R. E and I respectively stand for the output voltage and the current supplied to the Wheatstone bridge.*

flux. The wire temperature remains thus constant. From the Ohm's law, one can deduce that the voltage difference between the two extremities of the hot wire, $U_{HW} = R_{HW} I_{HW}$, also increases. Assuming that the output voltage of the system E is proportional to U_{HW}, it is possible to detect changes in the gas velocity by monitoring the output voltage. As it is operated at a fixed temperature, a CTA is not affected by the thermal inertia of the wire and features an high frequency bandwidth. We use a CTA purchased from Dantec Dynamics (Mini CTA 54T30 and probe 55P11) with a typical cut-off frequency higher than 5 kHz .

2.2.2 Theoretical elements

In a CTA, the flow velocity u is deduced from the measurement of the output voltage E which is a monotonous function of the thermal power P produced in the wire due to the Joule effect at thermal steady state (Bruun (1995)). Therefore, the relation between P (which equals Q) and u is needed. The objective of this subsection is to introduce the main equations for the determination of this relation.

At thermal steady state, the energy balance $P = Q$ is verified which leads to the following expression:

$$\frac{U_{HW}^2}{R_{HW}} = P = Q = hA(T_{HW} - T) = hA\Delta T \tag{2.1}$$

where h stands for the convective heat transfer coefficient at the wire surface and A is the wire surface area ($A = \pi DL$). In our experiments, the wire temperature is fixed to $T_{HW} = 573\,\mathrm{K}$ and the gas temperature is close to $T = 298\,\mathrm{K}$. The convective heat transfer coefficient h is given by the Nusselt number which is a function of the flow Reynolds Re and Prandtl Pr numbers (Incropera and Witt (1990)):

$$\mathrm{Nu} = \frac{hD}{k} = f(\mathrm{Re})g(\mathrm{Pr}) \tag{2.2}$$

One should note that in this equation, the mixture properties k and ν must be evaluated at the the film temperature defined as $T_f = \frac{1}{2}(T_{HW} + T)$. As an example, the empirical correlation due to Hilpert (1933) yields the Nusselt number as $\mathrm{Nu} = \mathrm{CRe^m Pr^{\frac{1}{3}}}$ where C and m are constants that depend on the Reynolds number Re. For gases, the Prandtl number is a weak function of the fluid composition and temperature and it is possible to simplify Eq. 2.2 as follows:

$$\mathrm{Nu} = \frac{hD}{k} = f_1(\mathrm{Re}) = f_1\left(\frac{uD}{\nu}\right) \tag{2.3}$$

Consequently, the following expression can be written for a fixed wire geometry:

$$\frac{U_{HW}^2}{R_{HW}} = f_2\left(\frac{u}{\nu}\right)k\Delta T \tag{2.4}$$

The electrical resistance of the wire R_{HW} is only a function of its temperature T_{HW} which is kept constant. The gas temperature is also constant in our experiments. One can then also write:

$$U_{HW}^2 = f_3\left(\frac{u}{\nu}\right)k \tag{2.5}$$

Finally, as the output voltage E is a known function of the voltage difference between the two extremities of the wire U_{HW}, one can write:

$$\frac{E^2}{k} = f_4\left(\frac{u}{\nu}\right) \tag{2.6}$$

or for a fixed gas composition:

$$E^2 = f_5(u) \tag{2.7}$$

The velocity u can thus be deduced from the voltage E if the function f_4 in Eq. 2.6 or f_5 in Eq. 2.7 is known without ambiguity. Correlations for the heat transfer coefficient are only approximates and it is difficult to determine the degree of confidence of the measured velocity when these correlations are used. Therefore a calibration step is required to obtain a precise relation between E and u.

2.2.3 Calibration of hot wire probes

The calibration of hot wire probes was carried out by measuring the output voltage E as a function of the gas velocity u in a setup where u can be varied and is known with a precision better than 3%. Figure 2.3 shows a schematic of this setup. A laminar and one-dimensional gaseous flow is generated through a brass converging nozzle with a contraction ratio $\sigma = 21$ and featuring a 12 mm outside diameter. The gas composition and bulk flow velocity are adjusted using different thermal mass-flow controllers (see Sec. 1.1.3) for air, methane, and hydrogen. The hot wire is installed 1 mm above the nozzle outlet section where the velocity profile is flat and the velocity u is known with a precision better than 3%. The velocity is deduced from the indications of the mass-flow controllers. The whole setup was calibrated with LDV measurements. At this step, one must be careful to orientate the wire orthogonal to the flow. The hot wire probe is inclined at 45° with respect to the horizontal plane to minimize perturbations from the wake of the probe.

Figure 2.4 shows the square value of output voltage E as a function of the velocity u at the nozzle exit for $0\ \mathrm{m \cdot s^{-1}} < u \leq 10\ \mathrm{m \cdot s^{-1}}$. One should note that Eq. 2.7 is valid only when the Richardson number Ri of the flow surrounding the hot wire is lower than unity. This criterion $\mathrm{Ri} << 1$ corresponds to a regime of forced convection where the relation shown in Eq. 2.2 is valid. In our experiments, the Richardson number is $\mathrm{Ri} = 0.01$ for a flow velocity $u = 5.6\ \mathrm{cm \cdot s^{-1}}$. Velocities below this value $u = 5.6\ \mathrm{cm \cdot s^{-1}}$ cannot be measured precisely with our CTA because natural convection can no longer be neglected.

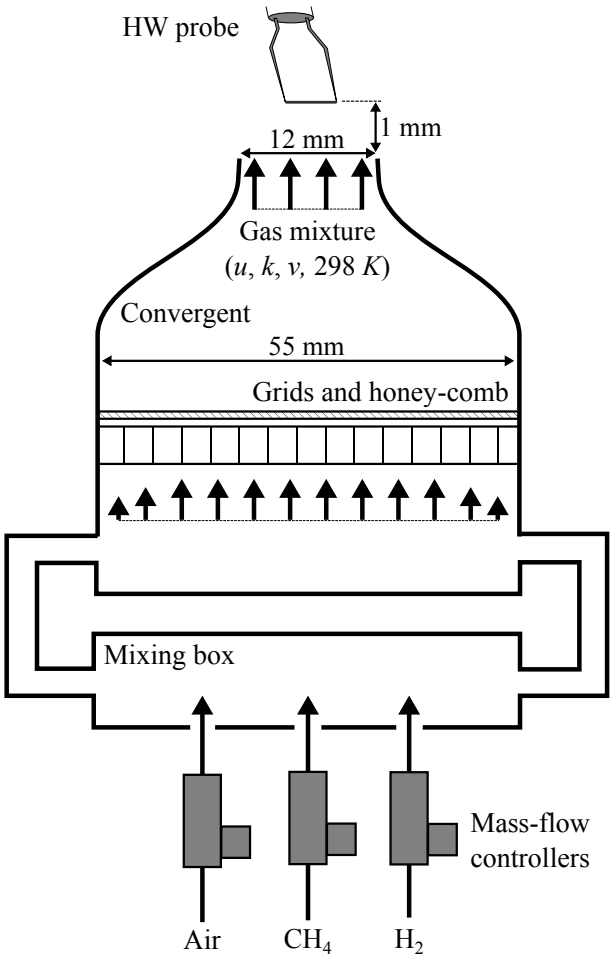

Figure 2.3: *Schematic of the hot wire calibration setup.*

Experiments presented in Fig. 2.4 are repeated for five mixtures of CH_4/H_2/air with different compositions. In all cases, the square value of the output voltage E increases with the incoming gas velocity u. These measurements however also show that the function f_5 in Eq. 2.7 is valid only for a fixed gas composition. Consequently, the calibration curve differs for the five mixtures of interest. This demonstrates that one should be careful to calibrate the hot wire using the same mixture as the mixture in which velocity measurements are needed.

It is now interesting to examine an alternative way of determining the calibration curve of the hot wire that may be used to infer the response for mixtures with different compositions. By exploiting Eq. 2.6, it is possible to infer the calibration curve of a different mixture if the calibration curve of a reference mixture was previously measured. The ratio $\left(E^2/k\right)/\left(u/\nu\right)$ is independent of the mixture composition and is only a function of the incoming velocity u.

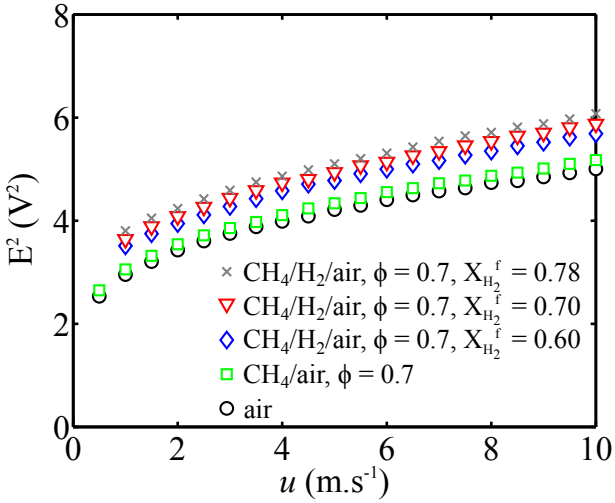

Figure 2.4: *Square values of the output voltage E as a function of the velocity u at the convergent exit for $0\,\mathrm{m\cdot s^{-1}} < u \leq 10\,\mathrm{m\cdot s^{-1}}$ and for five different mixtures of $CH_4/H_2/air$.*

Mejia (2014) used this technique to calibrate a hot wire with pure air mixtures and realize experiments with CH_4/air mixtures. He chose to correct hot wire measurements for variations in the fuel-mass fraction by calculating the mixture kinetic viscosity ν and the thermal conductivity k using the reduced form of the calibration curved defined by Eq. 2.6. With the same technique, Hultmark and Smits (2010) corrected hot wire measurement for gas temperature modifications. This is possible because the evolution of ν and k with temperature are well known (Sutherland (1893), Kannuluik and Carman (1951)). Mejia (2014) used the following simplified expressions to determine the CH_4/air mixtures kinetic viscosity and thermal conductivity:

$$\nu = \mathrm{Y}_{\mathrm{CH_4}}\nu_{\mathrm{CH_4}} + \mathrm{Y}_{\mathrm{air}}\nu_{\mathrm{air}} \tag{2.8}$$

$$k = \mathrm{Y}_{\mathrm{CH_4}}k_{\mathrm{CH_4}} + \mathrm{Y}_{\mathrm{air}}k_{\mathrm{air}} \tag{2.9}$$

where Y_k is the mass fraction of the k_{th} species featuring a thermal conductivity k_k and a kinetic viscosity ν_k. This method is also retained here and designated by method 1. Figure 2.5a shows the evolution of E^2/k as a function of u/ν for the same operating conditions as in Fig. 2.4 and using method 1 for the determination of the mixture kinetic viscosity and thermal conductivity.

One can see that the expressions used for the calculation of the mixture properties do not yield a satisfactory collapse of all the experimental data. The

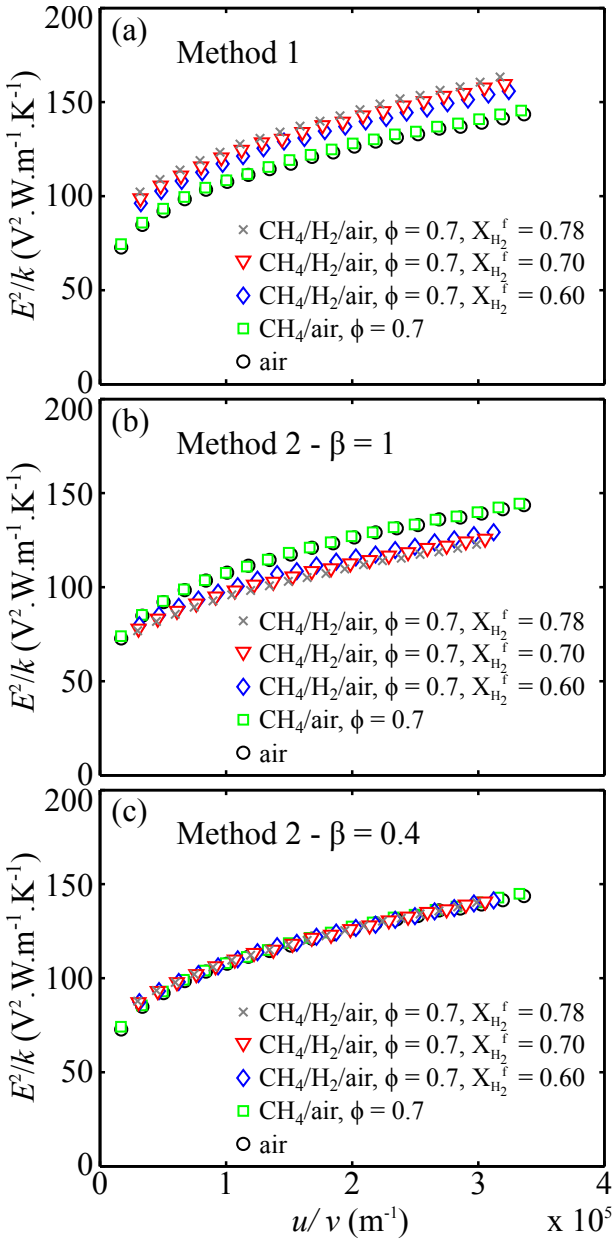

Figure 2.5: *Ratio E^2/k as a function of the ratio u/ν at the convergent exit for $0\ \mathrm{m\cdot s^{-1}} < u \leq 10\ \mathrm{m\cdot s^{-1}}$ and for five different mixtures of $CH_4/H_2/air$. (a) The thermal conductivity and kinetic viscosity are calculated using method 1 (Eqs. 2.8 and 2.9). (b) The thermal conductivity and kinetic viscosity are calculated using method 2 (CHEMKIN method) with $\beta = 1$ or (c) $\beta = 0.4$.*

CH_4/air and air calibration curves are nearly superimposed. This is attributed to the small mass fraction of methane in our lean CH_4/air mixture but also to the fact that the kinetic viscosity and the thermal conductivity of methane and

air are very close (Incropera and Witt (1990)). Small differences in the determinations of the mixture thermal conductivity and kinetic viscosity have a reduced effect. This is not the case for CH_4/H_2/air mixtures because the physical properties of hydrogen strongly differ from the ones of air or CH_4. As an illustration, $\nu_{H_2} = 21.8 \times 10^{-5}$ m$^2 \cdot$s^{-1} at $T = 435$ K while $\nu_{CH_4} = 3.5 \times 10^{-5}$ m$^2 \cdot$s^{-1} and $\nu_{air} = 2.9 \times 10^{-5}$ m$^2 \cdot$s^{-1} at the same temperature.

It is then necessary to come up with better expressions for the calculation of the mixtures kinetic viscosity ν and the thermal conductivity k. We chose the expressions used in the flame solver CHEMKIN (Kee et al. (1992)) which have been validated by numerous comparisons with experiments. In this code, the mixture viscosity is computed from the Wilke formula (Wilke (1950)) that is not reproduced here. The mixture thermal conductivity is calculated using the formula from Mathur et al. (1967):

$$k = \frac{1}{2}\left(\beta \sum_{i=1}^{n} X_i k_i + (2-\beta)\frac{1}{\sum_{i=1}^{n} X_i/k_i}\right) \tag{2.10}$$

where, the subscript i stands for species i out of n species, X represents the molar fraction, and β is a weighting factor that is taken to $\beta = 1$ in CHEMKIN. Figure 2.5b shows the evolution of E^2/k as a function of u/ν for the same operating conditions than in Fig. 2.5b and using the same formula as in CHEMKIN for the determination of the mixture kinetic viscosity and thermal conductivity. This method is designated as method 2. While CH_4/air and air curves are still well superimposed, results were not drastically improved. One should note that the CH_4/H_2/air curves now stand below the air curve in Fig. 2.5b. Finally, another attempt is made by changing the weighting factor to $\beta = 0.4$. Results are presented in Fig. 2.5c. Using this new value, all data collapse on the same curve indicating that the mixture properties are correctly evaluated.

It is however difficult to say if the value $\beta = 0.4$ will remain optimum for mixtures not covered by the five operating conditions considered. The main conclusion from that analysis is that it is risky to use a single calibration curve (obtained with air for example) and use it to measure the velocity of mixtures with hydrogen. Hot wire measurements with CH_4/H_2/air mixtures were thus always calibrated with real gases in this work.

2.3 Flame chemiluminescence

Different radical species are produced or consumed during the elementary reactions taking place in the combustion process. Radical species feature short life times and are generally absent or in very low concentrations in the burnt gases, but the combustion process highly depends on these intermediate species.

The Hydroxide radical (OH), the Methylidyne radical (CH), and the Diatomic carbon radical (C_2) are intermediate species present within the reaction front of hydrocarbon flames. Figure. 2.6 shows the calculated normalized molar fractions of OH, CH, and C_2 as a function of the distance to a one-dimensional premixed laminar flame front of a CH_4/H_2/air mixture calculated with $X_{H_2}^{fuel} = 0.60$ and $\phi = 0.70$ at $T_u = 300$ K and $P = 101325$ Pa. We used the REGATH solver (Candel et al. (2011)) and the detailed chemistry mechanism from Lindstedt (1998). The OH, CH, and C_2 radicals are produced at different locations. One can see that CH and C_2 radicals feature a similar but short life time in comparison to the OH radical. The maximum concentration of these different radicals strongly differs. The molar fraction of OH is here 5 orders of magnitude larger than the CH concentration which is already 7 orders of magnitude larger than the molar fraction of C_2. The conditions explored here are lean with $\phi = 0.7 < 1$. The C_2 radical would be produced in larger quantities in rich hydrocarbon flames. Moreover, we use large concentrations of hydrogen in our combustible mixture ($X_{H_2}^{fuel} = 0.60$ in Fig. 2.6). The concentration of CH is low in comparison to OH due to the low content of carbon atoms in the combustible mixture.

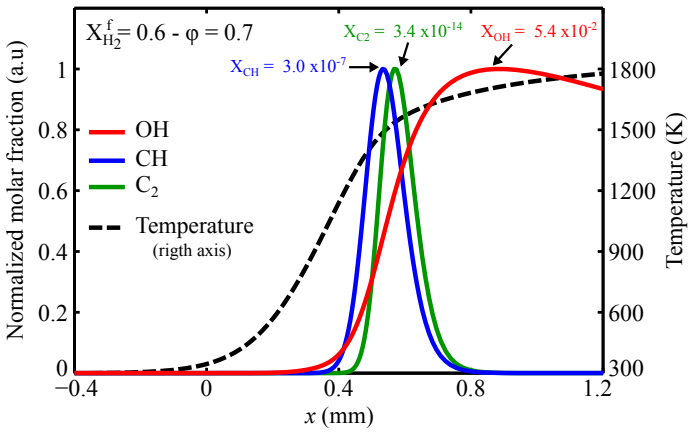

Figure 2.6: *Normalized molar fractions of OH, CH, and C_2 as a function of the distance to a one-dimensional laminar flame front of a CH_4/H_2/air flame ($X_{H_2}^{fuel} = 0.60$ and $\phi = 0.70$). right-axis: Evolution of the gas temperature. The REGATH solver (Candel et al. (2011)) was used with the detailed chemistry mechanism from Lindstedt (1998).*

Figure. 2.6 also shows the evolution of the gas temperature in the flame (right axis). The OH, CH, and C_2 radicals are present in high temperature zones where $T > 1300$ K. This means that a high fraction of these molecules populate excited states (Gaydon (1957)). Excited radical are represented by the superscript * in the following. These excited molecules emit light when they transit back to the ground state. It is then possible to detect the presence of

these molecules by detecting the light spontaneous emission (flame chemiluminescence) and infer the presence of a reactive flame front.

Due to the discrete values of possible energy levels, radical species emit light at specific wavelengths that depend on the molecule structure. Figure. 2.7 shows the simulated emission spectra of OH* and CH* radicals at P = 101325 Pa and T = 1850 K. This temperature is close to the adiabatic flame temperature T_{ad} = 1882 K for a $X_{H_2}^{fuel}$ = 0.60 and ϕ = 0.70 mixture . Simulations are conducted using the LIFBASE software from Luque and Crosley (1999) and spectra are here convoluted using a 1 nm coarse slit function to only retain the main features of the emission. The maximum of emission for the OH* radical is in the UV, at 309 nm. The maximum of emission for the CH* radical is in the visible range, at 431 nm.

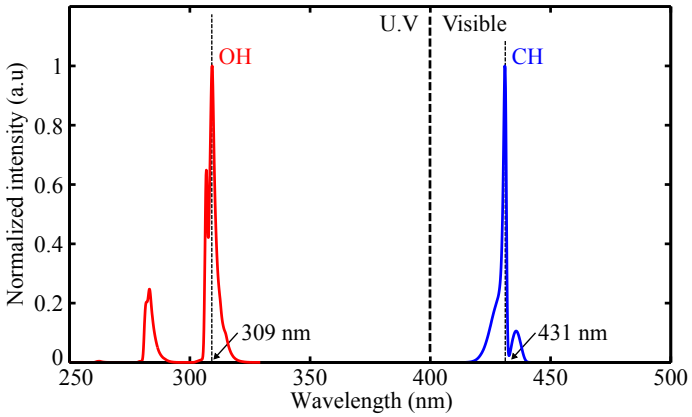

Figure 2.7: *Simulated emission spectra of OH* and CH* radicals at* P = 101325 Pa *and* T = 1850 K *using LIFBASE (Luque and Crosley (1999)). Spectra are convoluted using a* 1 nm *coarse slit function.*

In the flames of interest, the light intensity spontaneously emitted by OH* is expected to be much larger than the one emitted by CH*. In practice, due to the reduced sensitivity of the collection optics and CCD chips of regular cameras in the UV, the signal intensity collected by the measurement devices is of the same order of magnitude for OH* and CH* and both radicals will be used for the study of flame chemiluminescence.

2.3.1 Chemiluminescence imaging using CCD cameras

CCD cameras are used to collect the flame chemiluminescence and infer the position of the reactive region. Narrow-bandpass filters can be placed in front of the camera to select only one radical of interest. Filters featuring a Full Width at Half Maximum (FWHM) lower than 20 nm are used. Filters centered at

310 nm (for example Asahi Spectra Co., ZBPA310) are used for the detection of OH*. Filters centered at 431 nm are also used for the detection of CH*. The broadband chemiluminescence, without filter in front of the glass lens, was also recorded on a 752(H)x582(V) pixels^2 interlaced CCD camera (Pulnix TMC-6 color) operated at a frame rate of 50 images per second. If a higher repetition rate is required, we use a high speed CMOS camera (FASTCAM ultima APX i^2) with a glass lens that can be operated at a frame rate of few thousand images per second. When a higher sensitivity is required, the chemiluminescence from OH* is imaged on a 1024(H)x1024(V) pixels^2 (or 512(H)x512(V)) ICCD camera (Princeton Instruments, PIMax) equipped with a UV lens (UV-NIKKOR, 105 mm, f/4.5).

Figure 2.8a shows an example of the OH* chemiluminescence signal recorded with the ICCD camera when $X_{H_2}^{fuel} = 0.60$ and $\phi = 0.70$. To reach statistical convergence of the mean image, it is generally needed that the gate of the ICCD camera stays open during few milliseconds. The minimum integration time needed to obtain a sufficient signal intensity for instantaneous shots depends on the flame of interest and on the camera sensitivity and is generally close to few hundreds of microseconds.

It is worth recalling that the chemiluminescence signal is integrated in the line of sight. Assuming that the flame is axisymmetric in average, an Abel deconvolution can be applied to the mean chemiluminescence images to project the axially symmetric flame emission onto the plane of symmetry of the flame (Poularikas (2010)). We use an home-made Matlab® routine to compute Abel transforms. Figure 2.8b shows the Abel deconvoluted image of the mean flame presented in Fig. 2.8a. This is the trace of the flame front in the symmetry plane of the burner. Abel transforms can only be applied on mean chemiluminescence images as instantaneous images of turbulent flames are typically three dimensional and feature no symmetries. Figure 2.8b shows high levels of noise along the central axis. This is due to the mathematical formalism of the Abel transform that yields a singularity at the axis for $r = 0$, r being the coordinate along the radial direction (Poularikas (2010)).

2.3.2 Chemiluminescence analysis using a PMT

Another way of taking advantage of the flame chemiluminescence is to examine its temporal evolution rather that its spatial distribution. For that, we use photosensor modules (PMT) featuring a 20 kHz bandwidth and a strong spectral response from 200 nm to 600 nm (Hamamatsu, H5784-06). Using an adequate set of collimation optics, the broadband chemiluminescence emission of OH* or CH* is integrated over the whole flame region. Its evolution can be analyzed with a high temporal resolution. The PMT is equipped with a

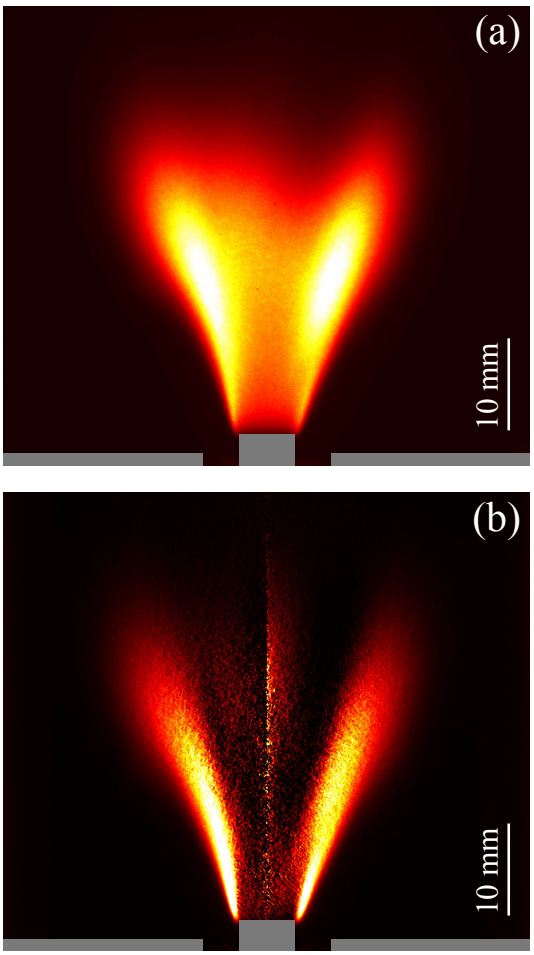

Figure 2.8: *(a) Mean chemiluminescence of OH* for a flame at* $X_{H_2}^{fuel} = 0.60$, $\phi = 0.70$, *and* $U = 14\ \mathrm{m \cdot s^{-1}}$. *(b) Abel transform applied to the OH* chemiluminescence image presented in (a).*

10 nm bandpass filter (CVI, F10–307.1–4–25.0M) centered at 307 nm for OH* analysis. For CH*, the PMT is equipped with a 10 nm bandpass filter (CVI, F10–430.0–4–25.0M) centered at 430 nm.

Figure 2.9a shows the temporal evolution of the OH* chemiluminescence collected with the PMT during a 4 s experiment conducted with a turbulent CH_4/H_2/air flame obtained for $X_{H_2}^{fuel} = 0.60$, $\phi = 0.70$, and $U = 14\ \mathrm{m \cdot s^{-1}}$. These data are used to calculate the Power-Spectral-Density (PSD) of this signal and analyze the spectral response of the flame. The dynamics of CH_4/H_2/air swirling flames is analyzed in chapter 6. Figure 2.9b shows the evolution of the OH* chemiluminescence intensity collected with the PMT when the flame shown in Fig. 2.9a is submitted to harmonic flowrate modulations at $f = 160$ Hz

with a loudspeaker placed at the bottom of the burner. One can see that the OH* chemiluminescence signal features a strong sinusoidal response at this frequency.

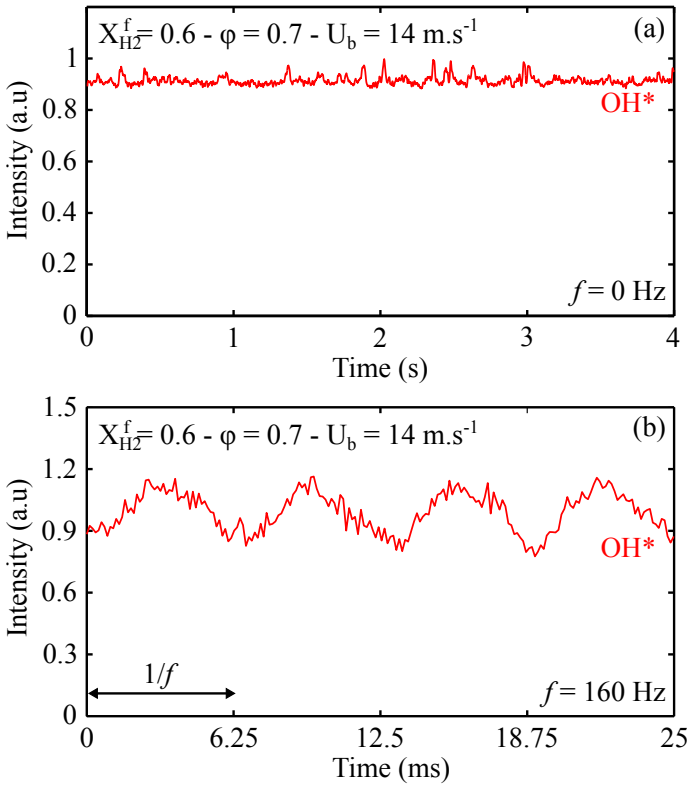

Figure 2.9: *(a) Normalized intensity of the OH* chemiluminescence integrated over the whole flame region as a function of time for* $X_{H_2}^{fuel}$ = 0.60, ϕ = 0.70, *and* U = 14 m · s^{-1}. *(b) Same but for the flame forced at a frequency* f = 160 Hz.

2.4 Planar Hydroxyl Laser Induced Fluorescence (OH-PLIF)

Analysis of flame stabilization processes requires information on the flame topology. The chemiluminescence imaging technique presented in Sec. 2.3 yields an information integrated in the line of sight. It is difficult to discriminate the contribution of flame fronts located at different depths with this technique. A possible way to circumvent this problem is to apply an Abel transformation (Poularikas (2010)) but this mathematical operation is limited to axisymmetric configurations and consequently cannot be applied to examine instantaneous images of turbulent flames. Planar Laser Induced Fluorescence (PLIF) is used for this purpose. This technique and its implementation in the present study

are described in this section.

2.4.1 Generalities on OH-PLIF

Laser Induced Fluorescence (LIF) allows to detect a chemical species, that may be an atom or a molecule, stimulated by a laser source. There are many references where this technique is described for use as a diagnostics for combustion analysis (see for example Daily (1997) and Eckbreth (1996)). Basics aspects that lead to practical choices for the selection of appropriate devices and settings are synthesized in the following.

LIF consists in the observation of the spontaneous emission of atoms or molecules populating unstable states after being excited by a tuned laser radiation. Figure 2.10 shows a schematic of a simplified model describing fluorescence processes for an atom. The two-level atom model only considers transitions between a fundamental level, Level 1, and an excited level, Level 2. In the presence of a laser radiation tuned to the transition, atoms in the Level 1 absorb part of the energy and transit to Level 2. The excited atoms can then leave this unstable state following three different processes:

- Induced emission occurring in the presence of a radiation field that forces the atoms to transit back to a lower energy state. Consequently, the induced emission ceases when the laser radiation is turned off.
- Spontaneous emission deriving from the natural instability of excited states.
- Quenching characterizing non-radiative relaxations of atoms by collision processes.

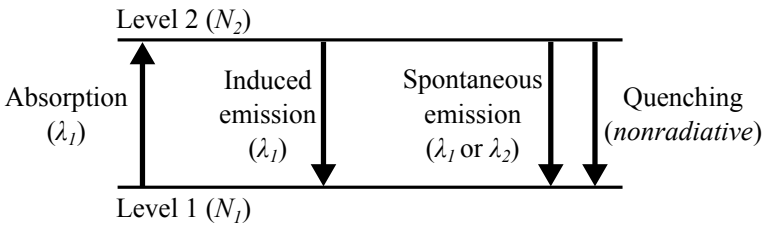

Figure 2.10: *Schematic of the simplified two-level atom model for fluorescence. N_1 and N_2 stand for the populations of Levels 1 and 2. The wavelength of the photon emitted (or absorbed) is denoted by λ. Adapted from Daily (1997).*

In a two-level description, induced and spontaneous emissions release photons at a similar wavelength λ_1 that the laser radiation. Excitation and fluorescence happen at the same wavelength and laser scattering can interfere with the signal of interest. In reality, LIF processes are more complex, especially for heavy atoms and molecules. In many cases, spontaneous emission does take place between the excited state and the laser tuned ground state but at a

state of lower or higher energy. This phenomenon is called direct line fluorescence. Other fluorescence mechanisms are described by Daily (1997). It is then possible to isolate the collected signal using an adequate interferometric filter to collect this spontaneous emission and remove laser interferences. Another possibility to increase the signal to noise ratio is to temporally decorrelate the excitation and the collection of fluorescence. Figure 2.11, adapted from Daily (1997), shows the temporal evolutions of the populations N_1 and N_2, of Level 1 and Level 2, during and after a laser radiation. The simplified two-level atom model is used here for the sake of simplicity. A pulsed laser radiation is applied to atoms initially populating Level 1. Consequently, the population N_2 increases while the population N_1 decreases because $N_1 + N_2 = 1$. A steady state establishes if the duration of the laser pulse is long enough. When the laser source ceases, unstable atom populating Level 2 relax either via spontaneous emission or quenching and the population N_1 increases to the detriment of the population N_2. After a few tens of nanosecond equilibrium is reached and $N_2 = 0$. Assuming that signal collection (camera aperture) starts for $t > \tau_p$, the fluorescence signal recorded is not polluted by the laser excitation.

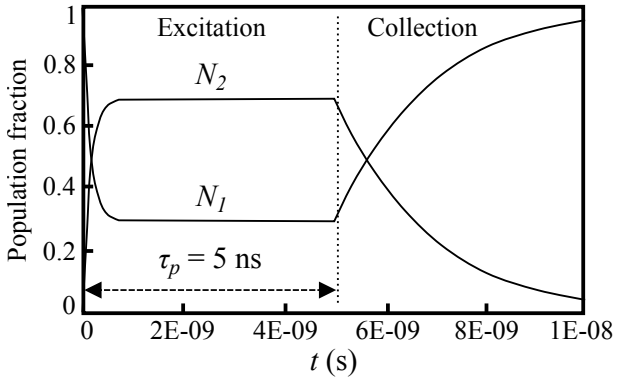

Figure 2.11: *Temporal evolutions of the population of Level 1 (N_1) and Level 2 (N_2) after a pulsed laser radiation using the two-level atom model. The duration of the laser pulse (τ_p = 5 ns which is common for Nd:YAG pumped dye lasers) is here sufficient to reach steady state.*

2.4.2 Selection of the excitation line

Regardless of the fluorescence model, the laser excitation must be tuned to an authorized transition of the atom or molecule of interest. The hydroxyl radical (OH) is a good fluorescent flame front marker (Cessou and Stepowski (1996), Daily (1997), Augé (2005), Coppola et al. (2009), Stöhr et al. (2011), Coriton et al. (2011), Chterev et al. (2014)). It was shown in Fig. 2.6 that the OH molar fraction in the reactive layer of CH_4/H_2/air lean flames exceeds the molar fraction of the other radicals CH and C_2 which benefits the

intensity of the fluorescence. In many studies (Daily (1997), Augé (2005), Sadanandan et al. (2008), Coppola et al. (2009), Stöhr et al. (2011), Coriton et al. (2011), Coriton et al. (2013), Sainct (2014), Chterev et al. (2014)), the following transition between two vibrational bands is used to excite the OH molecule: $(X^2\Pi, v" = 0) \rightarrow (A^2\Sigma^+, v' = 1)$. This transition is usually labelled $A^2\Sigma - X^2\Pi(1,0)$. As a consequence, the emitted fluorescence signal may be collected in the following vibrational bands $A^2\Sigma - X^2\Pi(1,1)$ and $A^2\Sigma - X^2\Pi(0,0)$. Figure 2.12 shows the excitation and collection spectra, including every rotational transitions possible for the vibrational bands considered, and convoluted using a 1 nm coarse slit function. This figure, realized by calculating the absorption [280 nm - 290 nm] and emission [300 nm - 320 nm] spectra of the OH radical using LIFBASE (Luque and Crosley (1999)), clearly shows that excitation and collection spectra are not overlapped.

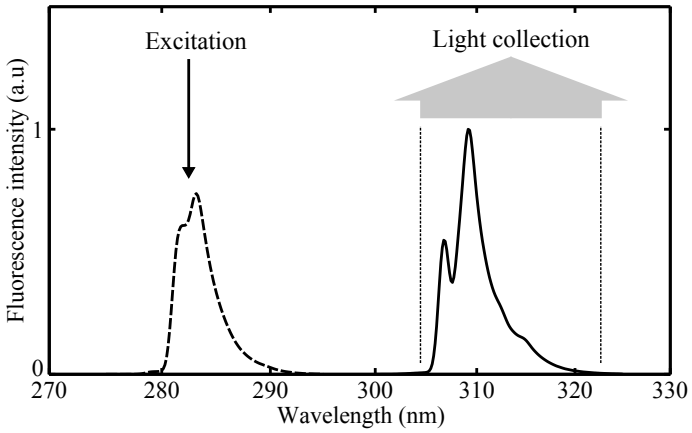

Figure 2.12: *Normalized absorption* [280 nm - 290 nm] *and emission* [300 nm - 320 nm] *spectra of the OH radical convoluted with a* 1 nm *coarse slit function using LIFBASE (Luque and Crosley (1999)).*

It is then necessary to select a proper rotational transition for the OH excitation. There are many possibilities but all the rotational transitions do not yield similar fluorescence properties (Daily (1997)). Figure 2.13 shows the OH absorption spectrum in the $A^2\Sigma - X^2\Pi(1,0)$ band between 280 nm and 290 nm for a simulated temperature $T = 2000$ K assuming a thermalized system. In these calculations a refined 0.01 nm slit function is used to properly separate absorption lines. One can note that the two higher peaks belong to the Q branch: the $Q_1(6)$ and $Q_1(9)$ rotational transitions at 282.93 nm and 293.93 nm respectively. At 2000 K, choosing one of these two excitation line allows to maximize the signal level. However, optimizing the signal to noise ratio is not the only criterion for the selection of the excitation line. Croonenbroek (1996) and Augé (2005) explain that the selected line needs to comply with the following criteria:

- Isolated line to prevent inaccurate laser selectivity.

- Elevated absorption to increase the signal to noise ratio.
- Temperature independent population to mitigate signal variation in case of medium temperature fluctuations.
- Excitation and emission spectrally shifted to prevent laser interferences during collection.

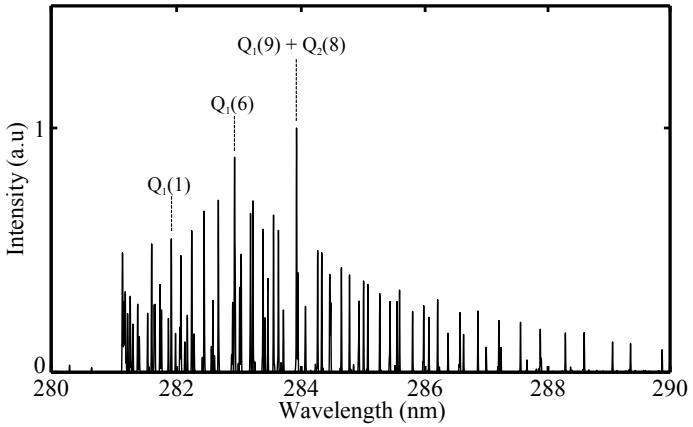

Figure 2.13: *Absorption spectrum of the OH radical convoluted with a* 0.01 nm *slit function using the LIFBASE software from Luque and Crosley (1999). The spectrum is calculated assuming a thermalized system at* T = 2000 K.

The spectral shift condition is automatically satisfied when exciting the $A^2\Sigma - X^2\Pi(1,0)$ band and collecting light from the $A^2\Sigma - X^2\Pi(1,1)$ and $A^2\Sigma - X^2\Pi(0,0)$ bands as shown in Fig. 2.12. The $Q_1(6)$ and $Q_1(9)$ transitions yield high absorption coefficients at T = 2000 K. It is then interesting to use one of these line to study the fluorescence of the OH radical from CH_4/H_2/air flames. However, in the case of flame/wall interaction, the burnt gas temperature differs from the flame adiabatic temperature, T_{ad}, and reaches much lower values. In addition, the OH radical may persist in the burnt gases as shown in Fig. 2.6. Thus, using a line with a strong absorption coefficient at moderate temperatures is an interesting alternative to detect the position of burnt gases of a flame interacting with a wall. The intensities of the $Q_1(1)$ (281.91 nm), $Q_1(6)$ (282.93 nm), and $Q_1(9)$ (283.93 nm) are compared as a function of the temperature in Fig. 2.14. The temperature T = 1882 K corresponds to a reference flame, thoroughly examined in this study, at $X_{H_2}^{fuel}$ = 0.60, $X_{CH_4}^{fuel}$ = 0.40 and ϕ = 0.70. It is clear that the $Q_1(6)$ and $Q_1(9)$ lines are well suited for investigations at high temperatures close to the adiabatic flame temperature. For lower temperatures when T < 1250 K, the $Q_1(1)$ line becomes interesting and its use may be considered. The isolated line criterion is considered satisfied for $Q_1(1)$ and $Q_1(6)$ transitions because lines are well separated. Conversely, $Q_1(9)$ and $Q_2(8)$ lines are very close which is a possible source of imprecisions (see Fig. 2.13). For this reason the $Q_1(9)$ line is excluded from this study as in the previous work of Augé (2005) or Sainct (2014). As a conclusion, the $Q_1(6)$

line will be used here for OH-PLIF measurements as in Stepowski et al. (1994) and Cessou et al. (2004) except in the case of strong flame/wall interactions where the the $Q_1(1)$ line is preferred (see chapter 4).

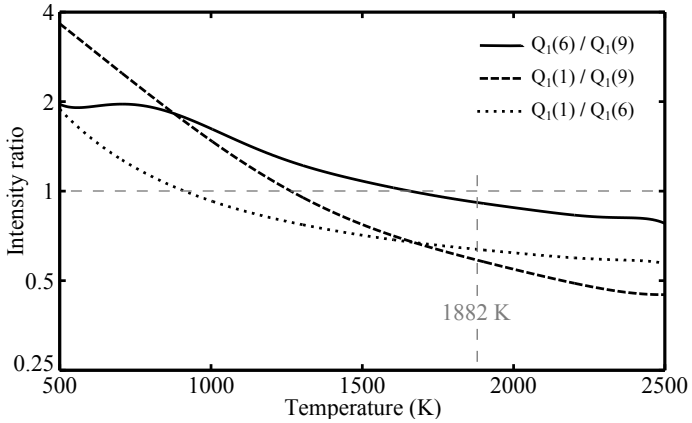

Figure 2.14: *Evolutions of the absorption intensity ratios $Q_1(6)/Q_1(9)$, $Q_1(1)/Q_1(9)$, and $Q_1(1)/Q_1(6)$ for the OH radical as a function of temperature. Data were calculated with the LIFBASE software from Luque and Crosley (1999). The temperature of* 1882 K *corresponds to the adiabatic flame temperature of a reference case obtained for $X_{H_2}^{fuel} = 0.60$, $X_{CH_4}^{fuel} = 0.40$ and $\phi = 0.70$.*

2.4.3 OH-PLIF setup

The OH radicals located in the flame front and burnt gases are excited using a laser sheet that crosses the flame in the region of interest. This technique yields information in a plane. Images were realized in longitudinal and transverse planes.

2.4.3.1 OH-PLIF in longitudinal planes

Figure 2.15 shows a schematic of the OH-PLIF setup with a longitudinal plane. The OH-PLIF system comprises a Continuum ND6000 dye laser with Rhodamine 590 dye diluted in ethanol solvent and pumped by a Continuum Precision Nd:YAG laser cadenced at 10 Hz. The pulse has a temporal Full Width at Half Maximum close to FWHM = 6 ns (Sainct (2014)). The diameter of the laser beam in the UV is 5 mm approximately. The laser was tuned to excite the $Q_1(6)$ (or $Q_1(1)$ for the investigation of flame/wall interactions) transition of the (1,0) band of the $A^2\Sigma - X^2\Pi(1,0)$ system of OH at 282.93 nm. Fluorescence from the $A^2\Sigma - X^2\Pi(1,1)$ and $A^2\Sigma - X^2\Pi(0,0)$ bands was collected with a UV lens (UV-NIKKOR, 105 mm, f/4.5) and imaged onto a 512(H)x512(V) pixels^2 ICCD camera (Princeton Instruments, PIMax) equipped with a 40 nm bandpass filter (Semrock, FF01-320/40) centered at 320 nm or a 10 nm bandpass

filter (Asahi Spectra Co., ZBPA310) centered at 310 nm. Figure 2.16 shows the transmittance spectrum of this interference filter that overlaps the OH fluorescence spectrum. The filter is used to avoid recording the fluorescence signals from solid surfaces (quartz, steel,...) or the fluorescence of other molecules than OH. The temporal shift between the laser radiation and the collection window is small enough to reduce direct laser interferences. In addition, the very short aperture time used (< 50 ns) is sufficient to neglect the chemiluminescence contribution of radicals present in the flame front like OH*, CH* or C_2*.

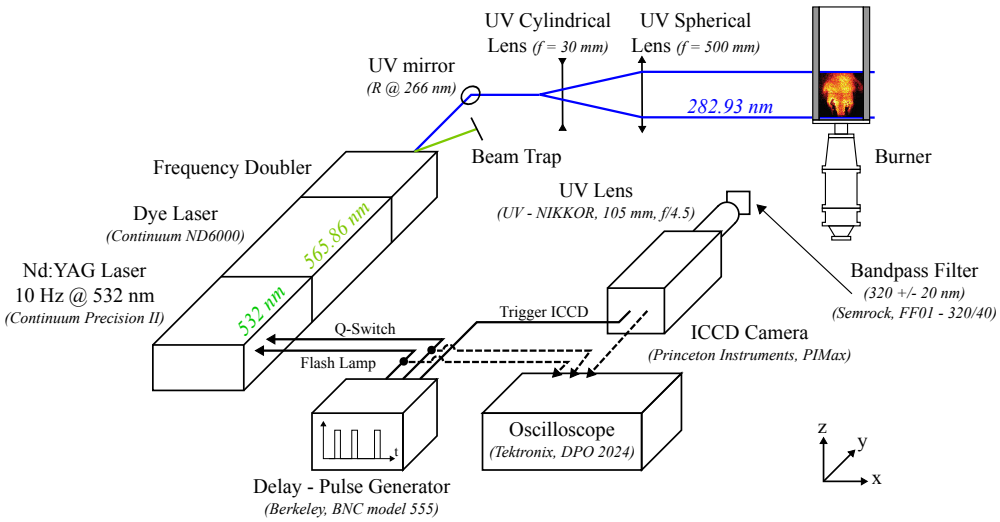

Figure 2.15: *Schematic of the longitudinal OH-PLIF setup.*

The vertical laser sheet is produced with the combination of a plano-concave cylindrical lens (f_{cyl} = 30 mm) and a 75 mm diameter plano-convex spherical lens (f_{sph} = 500 mm). The height of the laser sheet is 83 mm. This value slightly exceeds the spherical lens diameter and a fraction of the laser light is lost because it does not impact the lens. In practice, the vertical laser sheet his reduced to a 50 mm height and a 0.5 mm thickness (at the burner center). Black thermal tape is used to remove the extremities xith insufficient energy. Due to the important volume of the laser sheet, OH-PLIF measurements are conducted in the linear regime and the collection intensity depends on the laser pulse energy (Daily (1997), Sainct (2014)). This is considered acceptable here as we do not intend to infer quantitative information on OH concentration with this technique. However, efforts are made to conduct experiments with roughly constant energy pulses of 10 mJ.

Temporal synchronization between the laser and the ICCD camera is achieved using a Delay - Pulse Generator (Berkeley, BNC model 555). Settings of this device are gathered in the timetable shown in Fig. 2.17. The Flash-lamp/Q-

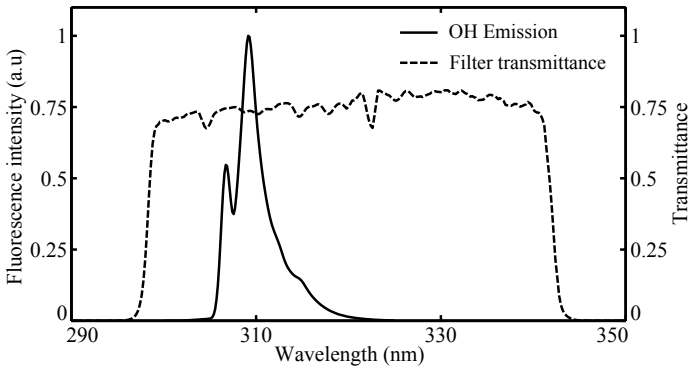

Figure 2.16: *Transmittance spectra of the interference filter used for OH-PLIF experiments (Semrock, FF01-320/40). The transmitted zone overlaps the emission spectrum of the OH radical convoluted with a* 1 nm *coarse slit function using LIFBASE (Luque and Crosley (1999)).*

switch delay for the Nd:YAG laser is fixed to 284 µs to maximize the pulse energy while the ICCD camera gate delay and gate width are adjusted to isolate the OH fluorescence signal. Finally, a high cadence oscilloscope is used to monitor the later settings during experiments.

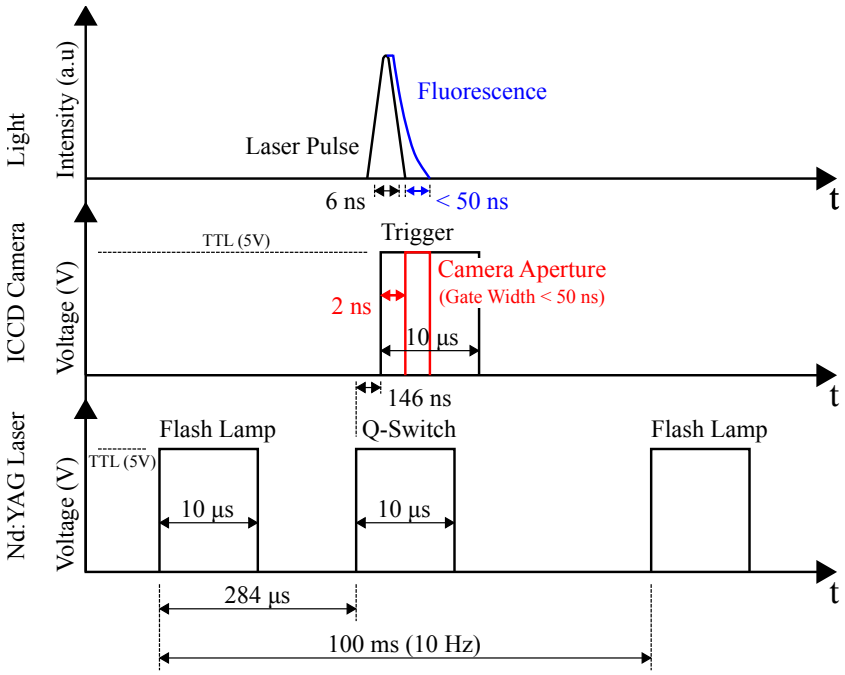

Figure 2.17: *Timetable of the Nd:YAG laser and ICCD camera settings. Parameters are adjusted to optimize the detection of the decaying fluorescence signal from the OH radical.*

2.4.3.2 OH-PLIF in transverse planes

Figure 2.18 shows a schematic of the experimental setup for OH-PLIF measurements in transverse planes. This setup has many similarities with the longitudinal setup but the cylindrical lens is here rotated by a 90° angle to generate a horizontal laser sheet. Due to the hot gases exhausting the combustion chamber at the burner exhaust, it is not possible to place the ICCD camera directly above the burner to detect the fluorescence signal. One possible way would be to use a 45° water-cooled mirror with an important reflectivity in the UV. This solution was not retained. Instead, we decided to install the ICCD camera obliquely away from the hot gas stream. The focus on the horizontal laser sheet is harder because the Plane of Sharp Focus (PoSF) is perpendicular to the ICCD lens axis. A Scheimpflug adapter is used to rotate the PoSF and make it to coincide with the horizontal laser sheet. Figure 2.19 describes the Scheimpflug adapter setup. The ICCD UV lens is no longer fixed to the ICCD camera body and can be rotated. The rotation angle is adjusted until the lens plane and the ICCD plane intercept in a line located in the PoSF.

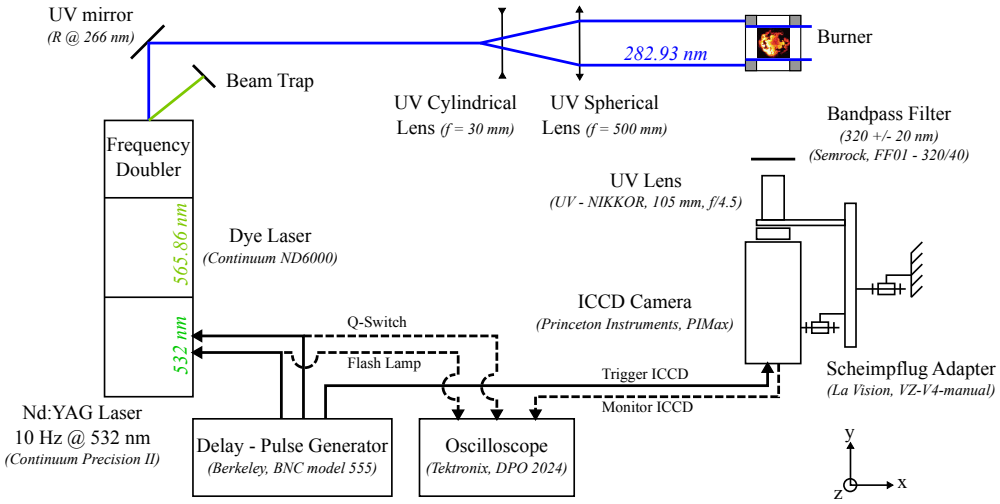

Figure 2.18: *Schematic of the transverse OH-PLIF setup.*

This operation yields geometrical distortions that need to be corrected. Figure 2.20a shows the image of a square target coinciding with the PoSF. The dimensions of the resulting quadrangle ($b/10\,\mathrm{px}\cdot\mathrm{mm}^{-1}$ on the Y axis and $a/10\,\mathrm{px}\cdot\mathrm{mm}^{-1}$ on the X axis) are not the same. Moreover, parallelism in the direction X is not conserved in this projection. It is then necessary to transform transverse OH-PLIF images to correct these geometrical distortions. We use a Matlab® home made script for this purpose. The Matlab® script includes the functions *cpselect* and *cp2tform* to produce the image transformation based on the square target image shown in Fig. 2.20a. This transformation is a combina-

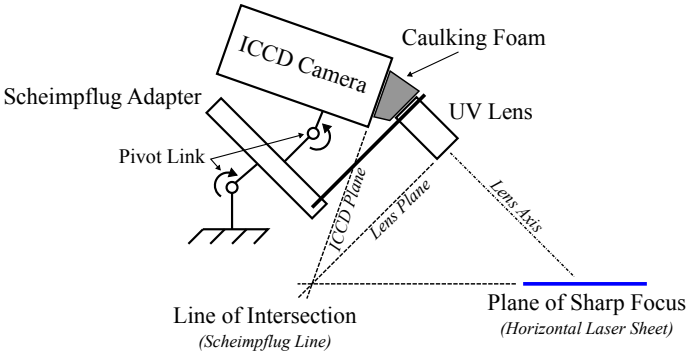

Figure 2.19: *Schematic of the Scheimpflug setup used to adjust the Plane of Sharp Focus (PoSF) to the horizontal laser sheet during transverse OH-PLIF experiments.*

tion of translation, rotation, and scaling. The transformation is then applied to the raw OH-PLIF images using the function *imtransform*. Figure 2.20b shows the transformed target image. After transformation, dimensions in the X and Y directions are the same and parallelism is conserved. This transformation is then applied on all transverse OH-PLIF images. An example is shown in Fig. 2.20c and d for a flame.

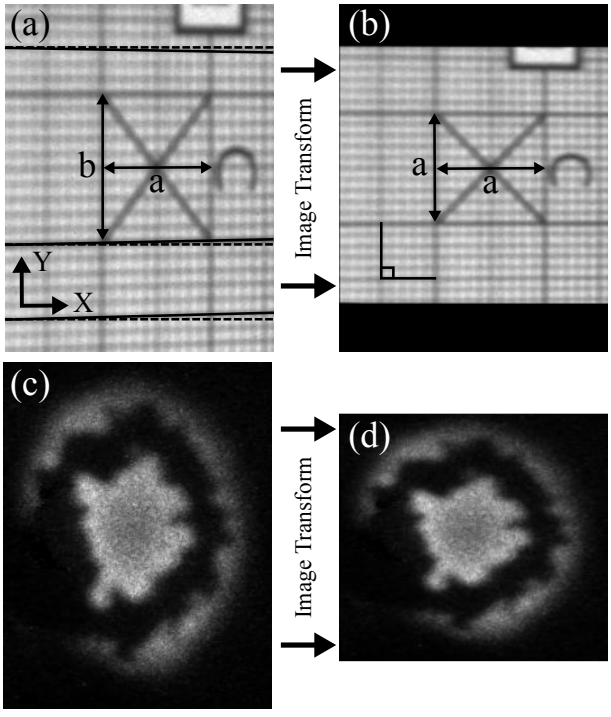

Figure 2.20: *Raw (a) and transformed (b) calibration image used to correct geometrical distortions resulting from the Scheimpflug setup for transverse OH-PLIF. Examples of instantaneous transverse OH-PLIF image before (c) and after (d) transformation.*

2.4.3.3 Wavelength calibration

The laser source for OH-PLIF is tuned to the $Q_1(6)$ (282.93 nm) or $Q_1(1)$ (281.91 nm) rotational bands of OH. The accurate selection of the laser output wavelength is achieved with a step motor. However, the correspondence between the laser wavelength and motor step can be lost due to unwanted events (shocks, vibrations, power cuts, mistaken shutdown procedure...). Accordingly, a calibration procedure is necessary to ensure proper laser selectivity. This can be done with a lambda-meter featuring a 1/100 nm precision to examine the wavelength shift between the dye laser settings and the actual output wavelength. Unfortunately, this device was not available for these experiments. We decided to use another method that does not require additional hardware. A fluorescence spectrum is measured, by varying the wavelength of excitation of the OH present in a flame, and compared to a fluorescence spectrum calculated with LIFBASE (Luque and Crosley (1999)) under similar conditions. The experimental spectrum is produced by plotting the mean fluorescence intensity detected over a predefined Region of Interest (RoI) of the ICCD chip as a function of the excitation wavelength. We chose to use the Inner Recirculation Zone (IRZ) which is detected on all transverse OH-PLIF images as it is only composed of burnt gases. Fluctuations due to turbulence and/or laser pulse energy variations are mitigated by averaging the measurements over 50 images. Examples of calibration spectra are presented in Fig. 2.21a and b for the $Q_1(1)$ and $Q_1(6)$ bands respectively. In both cases, measured and calculated spectra are normalized and base lines are artificially superimposed. The measured spectrum is horizontally shifted with respect to the wavelength indicated on the Dye laser software to optimize the fit. It was necessary to select an horizontal shift of 1.10 nm to tune the laser wavelength to the line $Q_1(1)$ and a 0.02 nm shift was needed for $Q_1(6)$. The difference between these two values may be linked to the multiple laser displacements between experiments using $Q_1(1)$ and $Q_1(6)$ as excitation bands.

The peaks relative intensities, that are reasonably well captured for $Q_1(6)$ but not for $Q_1(1)$, are not important here. The wavelength distribution of a group of five or six peaks is sufficient to deduce the corresponding band with confidence.

2.4.3.4 Typical OH-PLIF results and post-processing

After proper hardware adjustment and calibration, it is possible to obtain instantaneous OH-PLIF images in longitudinal or transverse planes at different locations in the burner. Figure 2.22 shows examples of results. These images are used to delineate the flame front position and help understanding flame stabilization mechanisms.

Images describing the mean structure of the flow are also constructed by determining the probability of being in the burnt gases. We do not calculate the

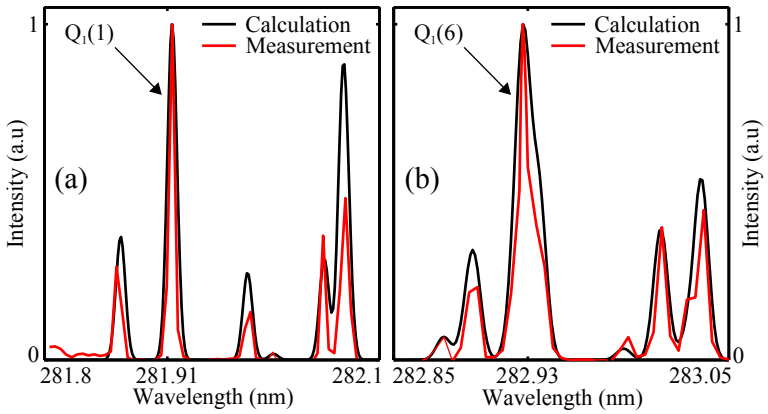

Figure 2.21: *Measured (red) and calculated (black) fluorescence spectra centered at the $Q_1(1)$ (a) and $Q_1(6)$ (b) rotational bands. Measured spectra are obtained by averaging the fluorescence intensity in the IRZ and over 50 images. Calculations are performed with LIFBASE (Luque and Crosley (1999)) and convoluted with a* 0.01 nm *slit function for a temperature* T = 1882 K.

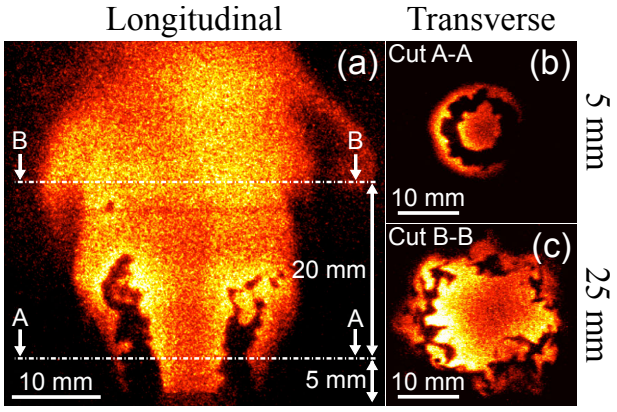

Figure 2.22: *Typical instantaneous OH-PLIF images in a longitudinal (a) plane and transverse planes located at two different heights (b)* = 5 mm *and (c)* = 25 mm *above the central rod tip.*

mean OH molar fraction at a given location but the probability to see OH *i.e* burnt gases at this location. The method used for the calculation of probability for OH detection is described in Fig. 2.23. Instantaneous snapshots are first binarized to separate zones filled with hot burnt gases from cooler regions of the flow. Due to noise and external perturbations, regions without OH may feature a background signal. An intensity threshold is applied to remove these pixels as described in Fig. 2.23b. The probability of OH presence at each location is obtained by summing N $n \times m$ pixels^2 binarized OH-PLIF images and finally dividing each pixel value by N. The resulting image is a $n \times m$ pixels^2 binary image where a pixel value of 1 means that the corresponding region is always filled with burnt gases. A value of 0 indicates a region filled with fresh reac-

tants. Results are presented in terms of a percentage as shown in Fig. 2.23c. To achieve a satisfying convergence of the probabilities, N is always larger than 400 in these experiments.

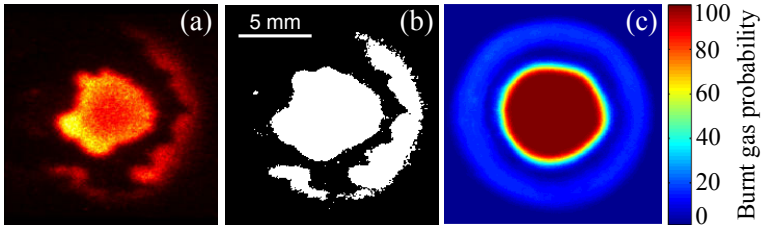

Figure 2.23: *(a): Typical instantaneous transverse OH-PLIF image. (b): Binarized image using a fixed threshold (12% of the image maximum pixel intensity). (c): Average over 500 binarized images giving the probability (between 0 and 100) to have burnt gases.*

Figure 2.24a shows another example of instantaneous OH-PLIF image. A 1-D profile of the normalized pixel intensity is plotted along the red dashed line in Fig. 2.24b (black dashed curve). The region between $x = -2$ mm and $x = 2$ mm features a strong OH-PLIF signal. The pixel intensity along the red dashed line is also plotted for the corresponding images binarized with intensity thresholds fixed to 10% (black), 12% (red), 14% (green), and 16% (blue). The threshold level intensity is defined with respect to the maximum intensity in the image to account for possible laser energy fluctuations. The region featuring a delectable OH-PLIF signal is satisfyingly captured using these different threshold values. With an intensity threshold at fixed 10% of the maximum pixel intensity, the flame front is positioned at $x = 2.05$ mm. With an intensity threshold at 16%, it is positioned at $x = 1.9$ mm. As long as the intensity threshold is comprised between 10% and 16%, the error in the detection of the OH-PLIF signal position is lower than 0.2 mm.

2.5 Particle Imaging Velocimetry (PIV)

Particle Image Velocimetry (PIV) is used to provide instantaneous 2-D velocity fields in a plane. PIV is widely used in combustion and the basics of this technique are not described in this document. A comprehensive description of this technique can be found for example in Raffel et al. (2007). Only the specific settings of our setup are described here.

2.5.1 PIV setup

The PIV setup is presented in Fig. 2.25 in a configuration where two components of the velocity are measured in a central longitudinal plane.

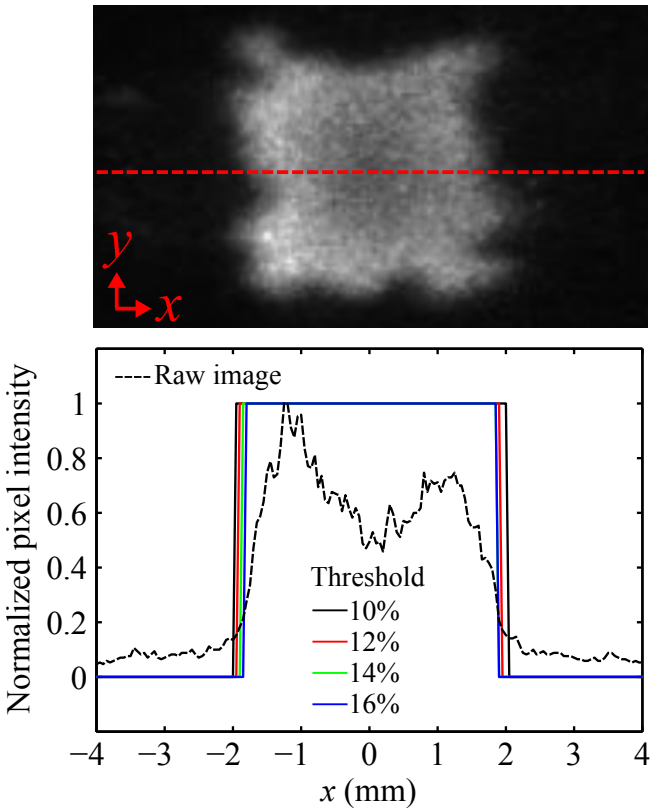

Figure 2.24: *(a) Typical instantaneous transverse OH-PLIF image. (b) Normalized pixel intensity plotted along the red dashed line for the raw OH-PLIF image (black dashed line) and the corresponding image binarized with an intensity threshold of 10% (black), 12% (red), 14% (green), and 16% (blue) of the maximum pixel intensity.*

The PIV apparatus features a 2×400 mJ Nd:YAG laser doubled at 532 nm operated at 10 Hz (Continuum, Powerlite SL3-PIV) and a 1600(H)x1200(V)-pixels^2 dual-shot CCD camera (Dantec Dynamics, Flow Sense). To reduce interfering reflections from the laser light, the flame chemiluminescence, or the ambient light, a 10 nm bandpass filter centered at 532 nm was placed in front of the camera lens. The laser sheet produced a vertical plane has a 50 mm height and a relatively wide thickness of 2 mm to minimize out of sheet particle displacements of the swirling flow between the two laser pulses separated by a time duration Δt. The optimal duration Δt depends on the maximum velocity that one wishes to measure (Raffel et al. (2007)) and ranges from $5\ \mu s \leq \Delta t \leq 40\ \mu s$ in our experiments. This delay is adapted to obtain a maximum particle displacement in the images comprised between 6 and 8 pixels. We used the Dantec Dynamics software for images acquisition and images correlations. A three passes window deformation technique comprising 128×128, 64×64 and finally 32×32 pixels^2 interrogation areas, is applied for correlations

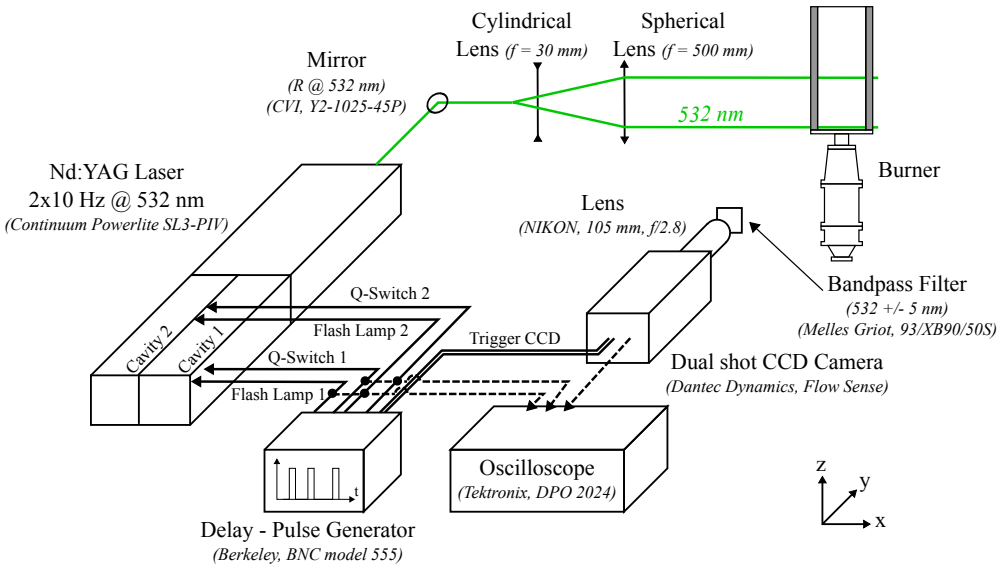

Figure 2.25: *Schematic of the longitudinal PIV setup.*

of the images. This leads to a vector spacing of a few hundreds of μm in both directions. PIV algorithms account for the subpixel displacement of particles. The typical precision is 0.1 pixel, which corresponds to a maximum precision on velocity measurements of $0.25\ \mathrm{m \cdot s^{-1}}$.

2.5.2 Seeding of the flow

PIV relies on the detection of the Mie scattering of light due to the presence of small particles seeded into the flow. Therefore, PIV measures the velocity of these particles which is close to the fluid velocity if the Stokes number Stk of the particles is small. The Stokes number Stk depends on a wide range of parameters, but it mainly depends on the characteristic size of the particles and the density of the material used. Small particles are convected at a velocity close to the flow velocity (Stk << 1) but sufficiently large particles are required to obtain sufficient Mie signal intensity. The selection of the particles is a matter of compromise. Based on these considerations, the typical characteristic size of the particles used in our experiment is of few micrometers.

PIV measurements are conducted in the combustion chamber under non-reactive and reactive conditions. Measurements require a sufficient particle density in the whole measurement domain. This means that under reactive conditions particles should resist to high temperatures. Liquid particles can only be used to infer the flow velocity field in regions of temperature lower than the vaporization temperature of the liquid. For that reason, solid particles are preferred under reactive conditions.

PIV in flames if often achieved with TiO_2 (Titanium dioxide) or ZrO_2 (Zirconium dioxide) particles. Titanium dioxide particles melt at 2128 K while ZrO_2 particles melt at 2988 K. These values are larger than the adiabatic flame temperatures of interest. We chose to use ZrO_2 particles (Fisher Scientific Zirconium (IV) oxyde, Z/1850/50). With solid seeding, it is difficult to obtain an homogeneous particles distribution. Particles also often deposit in the inner parts of the burner and feeding lines. It is necessary to regularly clean and/or change pieces after PIV campaigns conducted under reactive conditions. For that reason and when only non-reactive conditions are studied, liquid droplets are preferred.

In non-reactive cases the flow is seeded with the same oil particles as the ones that were used for LDV measurements (see Sec.2.1). Under reactive conditions, seeding is achieved using an home made cyclonic chamber where solid particles are advected in the injected air flow. The cyclonic chamber is partially bypassed to adjust the air flow injected in this device and optimize the quantity of particles transported by the flow. This is necessary to obtain a satisfying particle density in the combustion chamber for a wide range of operating conditions.

2.5.3 PIV in transverse planes

PIV measurements were also conducted in transverse planes. The PIV setup for experiments in transverse planes is similar to the one presented in Fig. 2.25. The main difference is that the cylindrical and spherical lenses forming the laser sheet are rotated by 90° to obtain a horizontal laser sheet. As for OH-PLIF experiments, the plane of sharp focus of the CCD chip must coincide with the laser sheet. Under non-reactive conditions, we used a mirror, installed above the combustion chamber and oriented with a 45° angle with respect to the horizontal plane. The CCD camera is installed horizontally. The angle of the mirror needs to be close to 45° to prevent geometrical distortions of the Mie images.

For measurements with combustion, we use the same technique as for transverse OH-PLIF experiments (see Sec. 2.4.3.2). The camera is installed with a 45° angle with respect to the horizontal axis. The rotation needed for precise sharp focused image acquisition is achieved using a Scheimpflug adapter.

Unfortunately, PIV post-processing is more complicated when the CCD array is not parallel to the laser sheet. Figure 2.26 shows a diagram of a particle displacement in the laser sheet between the two laser pulses and its image on the CCD chip. At a given time t, a particle is at position A which yields an

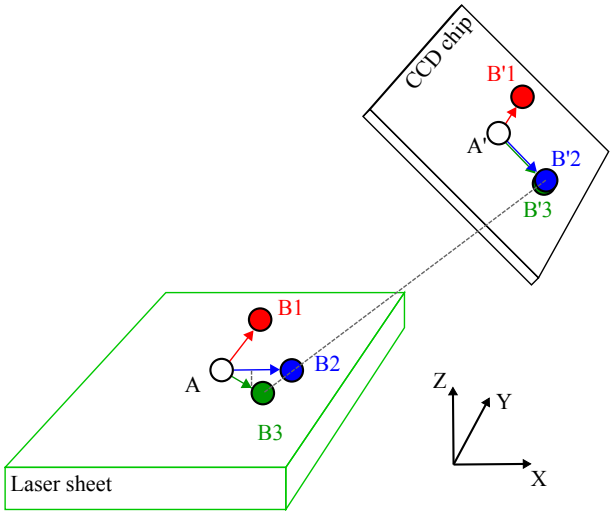

Figure 2.26: *Schematic for transverse plane measurements.*

image at a position A' on the CCD chip. If during a time step Δt the particle moves along the Y axis, *i.e.* an axis parallel to the rotation axis of the camera and lens, to a new position B1, a non ambiguous image B'1 is produced on the CCD chip. But if during the same time step Δt the particle moves along the X axis orthogonal to the Y axis to a new position B2, an ambiguous image B'2 is produced on the CCD chip. The same image B'2 could be obtained on the CCD chip with another displacement of the particle from A to position B3. In this case, the displacement along the X axis is shorter but there is an additional short displacement along the Z axis in Fig. 2.26. It is worth noting that this particle would still be illuminated by the laser and detected by the CCD due to the finite thickness of the laser sheet. The motion A-B2 and A-B3 would output a similar velocity magnitude along the X coordinate while, in fact, the displacement of the particle differs along this axis.

A possible way to remove this ambiguity is to use an additional PIV camera imaging the same region and located at a different position. This technique called Stereo-PIV (Raffel et al. (2007)) yields the three velocity components at each measurement point in the laser sheet. This technique is more difficult to settle. Most of the PIV experiments were conducted here in parallel to OH-PLIF experiments (see Sec. 2.5.5) leading to a relatively heavy setup. For these reasons, no additional PIV camera was used in our experiments and only the velocity component along the Y axis, *i.e* the axis parallel to the rotation axis of the mirror, is measured during transverse PIV experiments conducted in transverse planes. The velocity along the X axis and in the symmetry plane of the combustor is determined by longitudinal PIV. Therefore the loss of information is limited to a fraction of the combustor which is of limited interest for the purpose of these investigations.

The combustor was mounted on a two-dimensional mechanical translation system. It was then possible to independently move the combustor along the X and Z directions and conduct PIV measurements in longitudinal planes at different positions and in transverse planes at different heights above the injection tube outlet.

2.5.4 Examples of Mie scattering images

A few examples of Mie scattering images obtained with the PIV setup in the longitudinal and transverse configurations are presented. Figure 2.27 shows examples of Mie scattering images obtained under non-reactive conditions and using oil as seeding. Under these conditions, it is possible to achieve a very satisfying seeding with a sufficient particle density and a good homogeneity of the particle distribution within the different regions of the flow. Moreover, the particle size distribution obtained with this nebulizer is narrow (Durox et al. (1999)). However, important perturbations due to laser reflections on the combustor walls are visible in transverse images (Fig. 2.27b). A background subtraction method is then applied to increase the signal to noise ratio (Fig. 2.27c).

Figure 2.28a shows an example of a Mie scattering image obtained under non-reactive conditions but using ZrO_2 particles as seeding. This figure shows that while the seeding is still dense and homogeneous, the particle size distribution widens. One can observe small white dots, corresponding to small particles, but also bigger spots that are due to bigger particles and to agglomerates of particles. A wider size distribution does not raises difficulties for image correlations but it implies that a fraction of the particles may not follow the gaseous flow if the condition $Stk << 1$ is not satisfied. It is possible to reduce the fraction of big spots by drying and stirring the ZrO_2 mixture.

Figure 2.28b shows an example of a Mie scattering image obtained under reactive conditions and using ZrO_2 particles as seeding. In this picture, the seeding quality is considered good as the particles density is sufficient and not a lot of big spots are detectable. However, the seeding density is not homogeneous. This is attributed to the non-uniformity of the temperature field in the combustion chamber due to the flame. The jet of fresh gases features a high density of particles while the Inner Recirculation Zone (IRZ) filled with burnt gases shows a reduced density. In a first approximation, the particle density ratio across the flame is equal to the gas density ratio which is itself inversely proportional to the gas temperature ratio. The seeding density is reduced in the hot regions of the flow, *i.e.* in the Inner Recirculation Zone and Outer Recirculation Zone, due to the gas thermal expansion. This is a problem as it is difficult to obtain a good seeding for images post-processing in the hot regions of the flow for

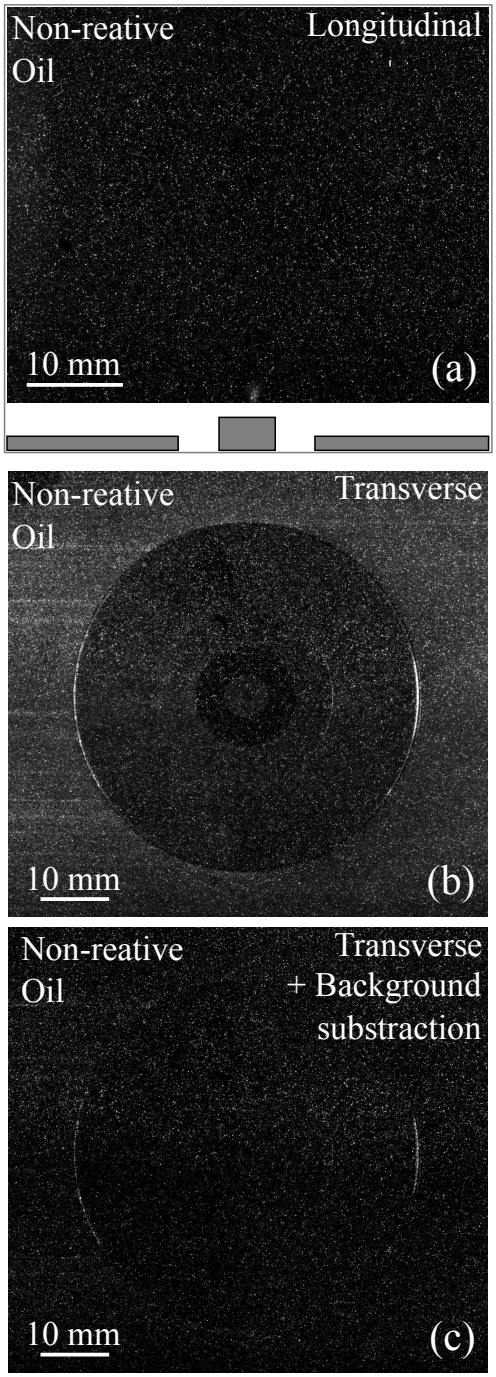

Figure 2.27: *Examples of Mie scattering images obtained under non-reactive conditions and using oil as a seeding agent in a longitudinal (a) or a transverse plane (b) and (c). A background subtraction is applied on (c). See the electronic version of this document for a better image definition.*

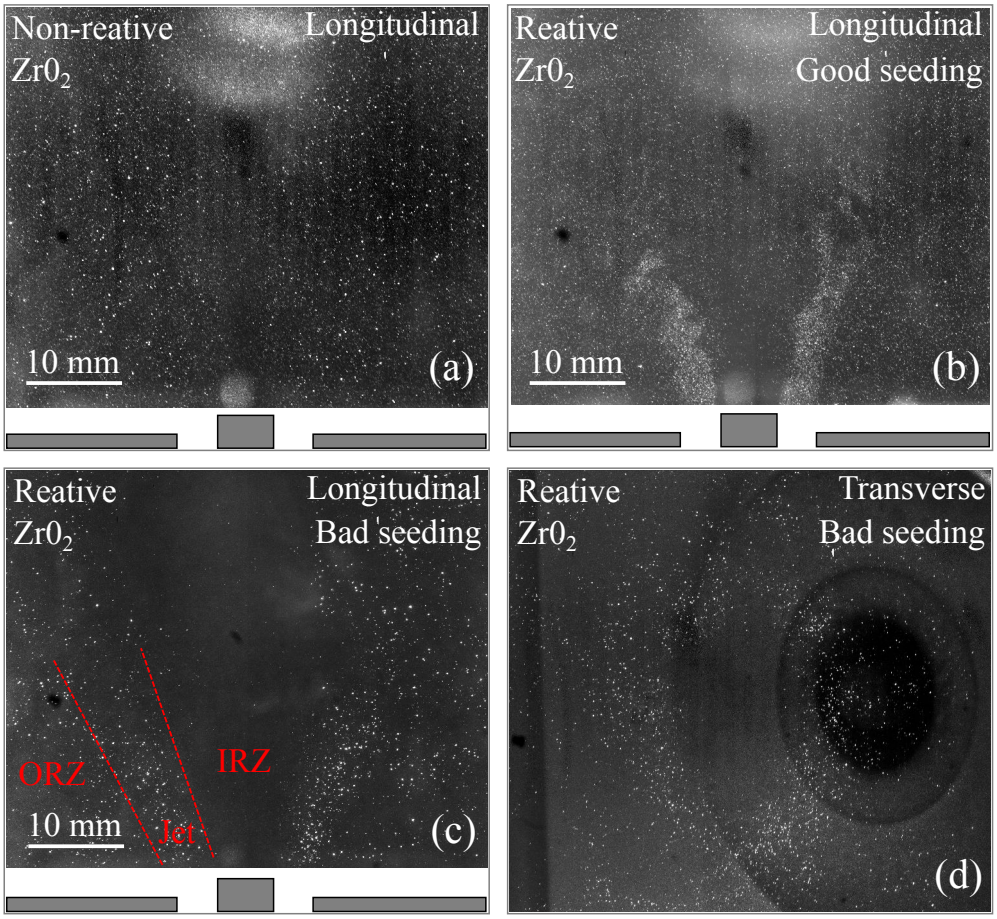

Figure 2.28: *Examples of Mie scattering images obtained under non-reactive (a) and reactive ((b)-(d)) conditions and using ZrO_2 as seeding in a longitudinal or a transverse plane. See the electronic version of this document for a better image definition.*

certain flow operating conditions.

Figure 2.28c shows another example of a Mie scattering image obtained under reactive conditions and using ZrO_2 particles as seeding. In this image, the seeding quality is not sufficient and the IRZ is nearly empty of particles. Images correlation does not yield the correct velocity in this region. The difficulty to seed the IRZ is enhanced by the fact that this region cannot be directly seeded due to the presence of the central rod tip. Particles featuring too high Stokes numbers cannot follow the rapid deviation of the streamlines through the flame and do not penetrate the IRZ. The seeding quality is also emphasized by Fig 2.28d where large holes without seeding are visible in these transverse planes. Ensuring a sufficient seeding quality was the main challenge of the reactive PIV experiments presented in this work.

2.5.5 Synchronized OH-PLIF/PIV setup

In numerous cases, the simultaneous knowledge of the flame front position and the corresponding velocity field is needed. Therefore, PIV experiments and OH-PLIF experiments were conducted simultaneously as often as possible. Synchronized OH-PLIF/PIV experiments numerous equipments, great care in laser alignment, and generate a lot of exploitable data. The synchronized OH-PLIF/PIV setup, methods, and post-processing conducted in this work are now described. Figure 2.29 shows a schematic of this setup. The PIV and OH-PLIF apparatus are similar to the ones used for separate OH-PLIF and PIV experiments. A beam splitter (CVI, BSR-25-1025) has been added in the setup to superimpose PIV and OH-PLIF laser lines before the optics producing the laser sheets. In addition, the OH-PLIF ICCD camera and the PIV CCD camera are installed on each side of the burner and are facing each other.

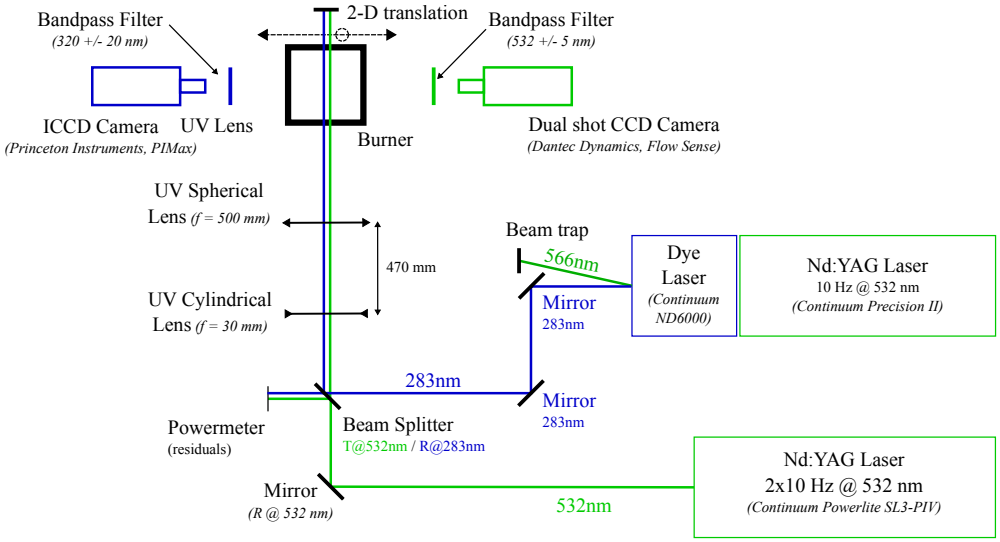

Figure 2.29: *Schematic of the synchronized OH-PLIF/PIV setup.*

2.5.5.1 Temporal synchronization

In the synchronized setup, lasers and cameras are triggered with the same material. The synchronization chart of each device is not reproduced here. When PIV and OH-PLIF measurements are conducted simultaneously, one must be careful that the velocity field obtained by PIV corresponds to the OH distribution obtained by OH-PLIF. The PIV and OH-PLIF lasers sheets must be superimposed and lasers pulses must be triggered at similar times. Figure 2.30 shows a chronograph for the synchronization of PIV and OH-PLIF laser pulses.

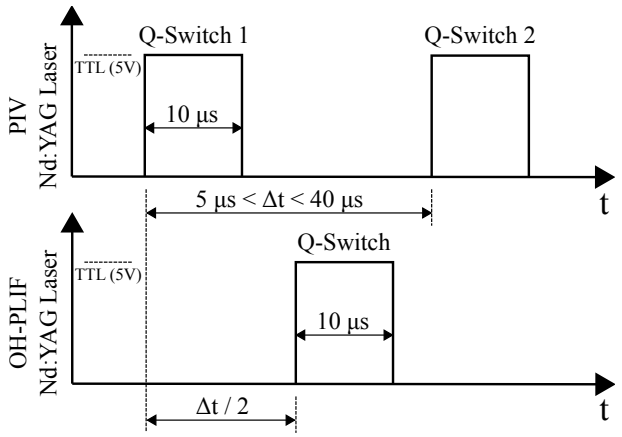

Figure 2.30: *Chronograph of the temporal synchronization of the PIV and OH-PLIF lasers Q-switches.*

In our experiments, the two Q-switch to Flash lamp delays of the two cavities of the PIV Nd:YAG laser are adjusted to obtain sufficient and equivalent energy for the two consecutive laser pulses. Triggering of the two Flash lamps is then adjusted to obtain a time interval Δt between the two laser pulses adapted to the flow velocity. The Q-switch to Flash lamp delay of the OH-PLIF Nd:YAG laser is adjusted for maximum pulse energy. Finally, the delay between the trigger of the Flash lamp of the OH-PLIF laser and the trigger of the Flash lamp of the first PIV cavity is adjusted so that the OH-PLIF laser fires at a time $\Delta t/2$ after the first PIV laser. This means that the LIF image is taken between the two PIV shots.

2.5.5.2 Spatial synchronization

As shown by Fig. 2.29, the two cameras are not located at the same position. Moreover, they are not equipped with the same lenses and feature two different magnifications. Finally, the PIV camera has a 1600(H)x1200(V)-pixels^2 CCD array while the OH-PLIF camera has a 512(H)x512(V)-pixels^2 or a 1024(H)x1024(V)-pixels^2 ICCD array. The field of view of the PIV CCD camera is 51×38 mm^2 and the field of view of the OH-PLIF ICCD camera is 46×46 mm^2. Therefore, PIV/OH-PLIF images are post-processed to superimpose the velocity field and the OH field. The OH-PLIF images are flipped horizontally as both cameras are facing each other. Then the OH-PLIF images are cropped and resized to generate a 1600(H)x1200(V)-pixels^2 image. The operation that allows to superimpose the modified OH-PLIF images and the PIV images is a combination of translation, rotation, and scaling. However, it is very difficult to obtain an analytical expression of this transformation due to the relative positions of the cameras and lenses settings. We use an empirical

method for the determination of this transformation.

The objective is to image a non-ambiguous pattern on both CCD and ICCD chips at the same time. For that, we remove the combustion chamber and inject ZrO2 particles in a pure air stream at the burner outlet. The triggering signal of the ICCD camera used for OH-PLIF experiments is adjusted so that the ICCD camera gate opens at exactly the same time as the first PIV shot. Thus, the image of the light scattered by the particles at 532 nm is visible on both PIV CCD and OH-PLIF ICCD cameras. Both cameras see the same particles, at the same instant. To do so, the bandpass filter equipping the OH-PLIF camera is removed and the PIV laser pulse energy is lowered. Figure 2.31 shows examples of raw Mie scattering images captured on the CCD and ICCD chips.

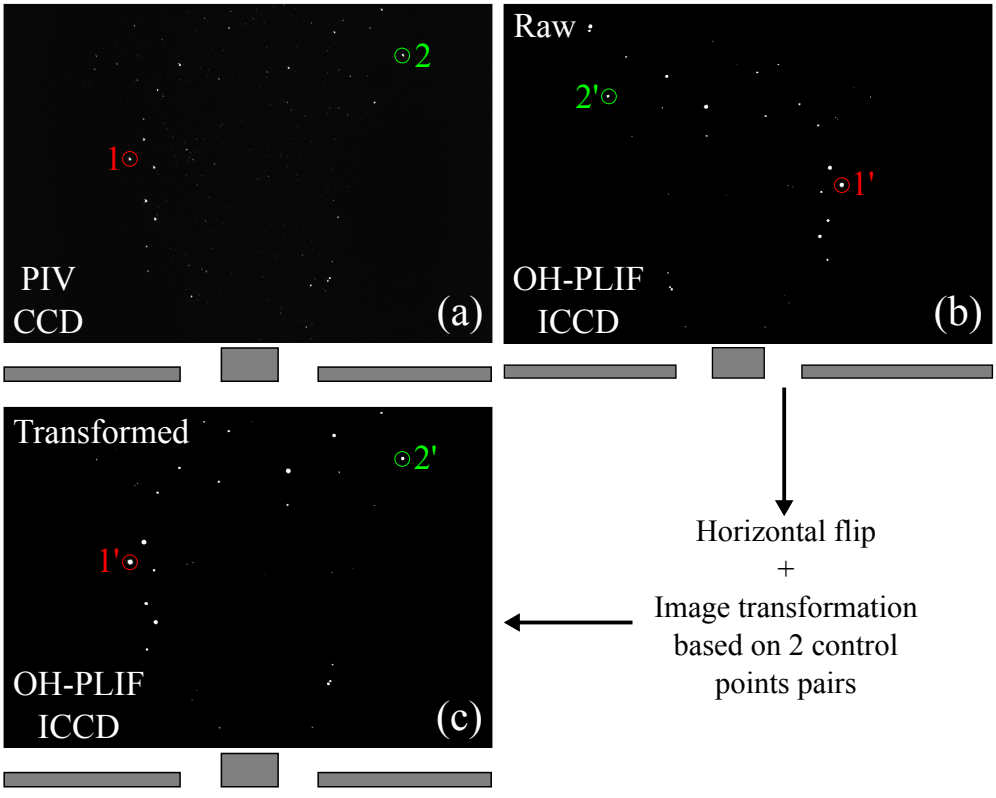

Figure 2.31: *(a) Mie scattering image of ZrO_2 particles imaged onto the PIV CCD under-non-reactive conditions. (b) Image of the same particles with the OH-PLIF ICCD at the same instant. (c) Corrected OH-PLIF image. See the electronic version of this document for a better image definition.*

The Mie signal captured by the PIV CCD camera is shown in Fig. 2.31a. Figure 2.31b shows the image captured by the OH-PLIF camera. The PIV image stands as the reference image. The OH-PLIF image is the target image. It

is possible to select control points on the reference image and seek for their correspondence on the target image. Selecting control points featuring high intensities (ZrO_2 particles) is very handy. Figures 2.31a and 2.31b show that it is possible to select two control/target point pairs without ambiguity. As the images are only distorted by a combination of translation, rotation, and scaling between the two cameras, two pairs are sufficient to determine the transformation for OH-PLIF images correction. This operation is realized with Matlab® using the *cp2tform* function fed by the control and target images as well as the two or more control/target points pairs obtained with the *cpselect* function.

It is finally possible to apply the correction on the raw OH-PLIF image (target image) with the *imtransform* function and verify that the target points on the corrected images coincide with the control points. Figure 2.31c shows the resulting OH-PLIF image after post-processing with Matlab®. One can see that the result is very satisfying when comparing Figs. 2.31a and 2.31c. The accuracy in the positioning of the corrected target point is always better than 2 pixels. This is acceptable because the spacing of the PIV vectors grid is 16 pixels. This operation can then be generalized on OH-PLIF images obtained in experiments under reactive conditions. We assume that the combustion chamber walls and the bandpass filters have negligible effects on the quality of the images correction. Figure 2.32 shows an example of OH-PLIF image before and after correction.

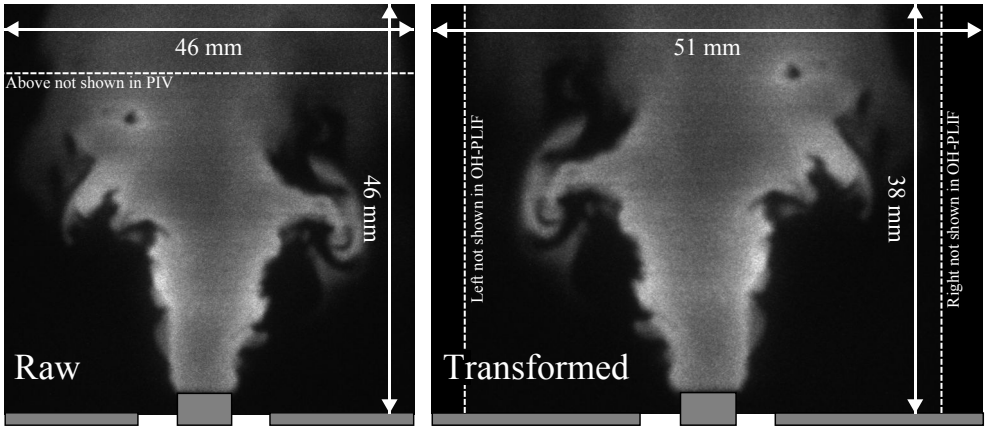

Figure 2.32: *Raw and corrected typical OH-PLIF images obtained under reactive conditions.*

2.6 Laser Induced Phosphorescence (LIP)

In many applications it is useful to know the combustor wall temperatures. These walls are subjected to convective and radiative heat fluxes from the

flame and hot gases. Depending on heat-losses, the wall temperatures take values ranging from the ambient temperature to the adiabatic temperature of the flame stabilized in the combustor. In many cases a fraction of the heat stored in the burnt gases is used to heat a solid load like steel or glass. Too high temperatures may damage the installations. A precise target temperature of the load may also be needed to optimize the process. The thermal state of the combustor can also affect flame stabilization.

While techniques dedicated to gas temperature measurements are numerous (thermocouples (Francois et al. (1997) and Hindasageri et al. (2013)), emission (Gaydon (1957), Lo et al. (2014)), absorption (Arroyo and Hanson (1993)), Raman spectroscopy (Lo et al. (2014)) or Laser Induced Fluorescence of species (Cattolica (1981), Eckbreth (1996), Devillers et al. (2008), Strozzi et al. (2009), and Tea et al. (2011))), the technologies dedicated to the measurement of surface temperatures are relatively limited. The easiest way is to equip the combustor walls with thermocouples. Thermocouples are cheap and yield a very satisfying precision. However, thermocouple positions must be planned during the combustor design and it is not possible to use thermocouples in the transparent and fragile quartz walls that are used for direct visualization of the flame and laser diagnostics. Another well known possibility is to measure the surface temperature using infrared pyrometry. This technique relies on the detection of the radiative flux emitted in the infrared by a hot surface. Using the Stefan-Boltzmann law one can deduce the surface temperature (Cetas (1978)). However, the precision of this technique depends on the precision on the knowledge of the surface material emissivity. When surfaces with different materials are used or when the surface properties varies with time (metal corrosion, particle deposition...), this emissivity is difficult to determine. Moreover, for transparent or semi-transparent materials interferences may arise from the infrared emission of gaseous species present in the burnt gases of the flames (H_2O for example, Gaydon (1957)). Consequently, we decided to use another diagnostic to measure the temperatures reached at the wall surfaces of our combustor: the Laser Induced Phosphorescence (LIP). The objective of this section is to describe how we applied LIP in a small scale non-adiabatic combustor.

2.6.1 Generalities on LIP

LIP is based on the use of thermographic phosphors that are mainly composed of ceramic materials doped with rare earth elements or transition metals. These materials are luminescent as they have the property to emit visible light after being excited with short wavelength light, usually ultraviolet. The energy absorbed by the thermographic phosphors during excitation must be released. Return to the ground state takes place by radiative and non-radiative transfers. The radiative transfer is related to the spontaneous emission of photons (generally visible light) while non-radiative processes depend only on internal energy

transfers. The LIP for surface temperature measurement relies on the fact that non-radiative transfers in thermographic phosphors are temperature dependent (Brübach et al. (2013)). Internal energy transfers are enhanced when the temperature is increased. This phenomenon is called thermal quenching. Thus, the fraction of energy remaining available for radiative transfers is reduced at high temperatures.

If a thermographic phosphor layer is deposited on a surface of interest and excited with an ultraviolet light source, collecting the subsequent visible luminescence provides an information on the surface temperature. More details on fundamental properties of phosphors are provided by Shionoya et al. (2012) and Brübach et al. (2013). They use the following simplified model for the luminescence of thermographic phosphors. If $t = 0$ corresponds to the end of the light excitation, the subsequent luminescence intensity $I(t)$ decays exponentially:

$$I(t) = I_0 \exp\left(-\frac{t}{\tau}\right) \tag{2.11}$$

where I_0 is the light intensity at $t = 0$ and τ stands for the lifetime of the phosphorescence signal also called decay time. An evaluation of τ can be derived from the differential equation describing the population of the excited state $N^*(t)$:

$$\frac{\mathrm{d}N^*(t)}{\mathrm{d}t} = -(R_R + R_{NR})N^*(t) \tag{2.12}$$

where R_R and R_{NR} denote the rates of radiative and non-radiative transfer processes. The solution of this equation is:

$$N^*(t) = N_0^* \exp(-(R_R + R_{NR})t) \tag{2.13}$$

where N_0^* stands for the excited population at $t = 0$. Assuming that the emitted light is proportional to the excited population, one deduces the decay time τ:

$$\tau = \frac{1}{R_R + R_{NR}} \tag{2.14}$$

The decay time depends on the radiative and non-radiative energy transfer rates and consequently also on temperature. Figure 2.33 shows examples of normalized phosphorescence signals collected with a photomultiplier tube (PMT) for the $Mg_{3.5}FGeO_5$:Mn thermographic phosphor at different temperatures. In all cases the luminescence signal decays exponentially with time and the decay time strongly decreases when temperature increases.

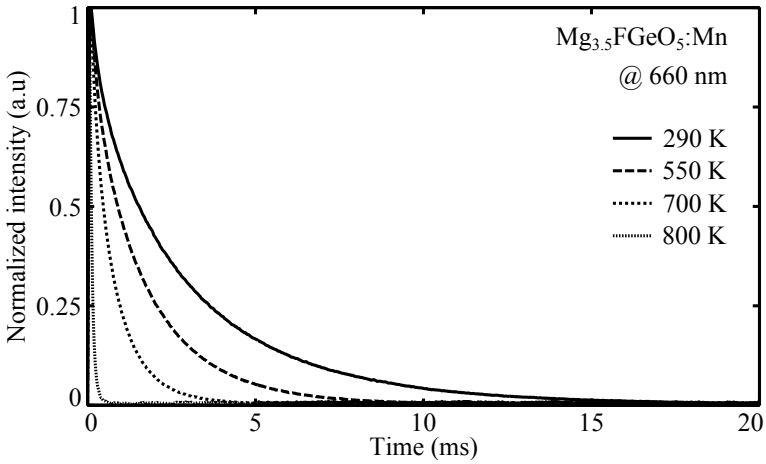

Figure 2.33: *Examples of time resolved phosphorescence signals obtained after excitation of $Mg_{3.5}FGeO_5$:Mn using a* 266 nm *pulsed laser. Results are shown for different temperatures. The light emission decay is collected by a photomultiplier tube (PMT) equipped with a* 10 nm *bandpass interferometric filter centered at* 660 nm.

In most cases, a given thermographic phosphor emits visible light at different wavelengths. For that reason, a temperature/decay time couple is valid at a very specific wavelength. Figure 2.34, taken from Allison and Gillies (1997), shows two examples of emission spectra for the La_2O_2S:Eu phosphor at 4.5 °C and 36 °C. These spectra feature multiple emission lines with different intensities. Moreover, intensity ratios of certain line pairs are drastically altered by temperature (see the pair 468.4 nm/538.2 nm for example). It is then also possible to deduce the temperature using the intensity ratio of properly selected emission lines.

2.6.2 Measurement strategies

Two different techniques were developed for measurements of surface temperatures with thermographic phosphors. The first one exploits the lifetime of the signal and the second one uses the intensity ratio of different emission bands. The objective of this section is to provide information to help the selection of the method best suited to our case. For this purpose, we will focus on a single phosphor, $Mg_{3.5}FGeO_5$:Mn, and compare both methods using the data available in the literature. Figure 2.35, reproduced from Brübach et al. (2013), shows the evolution of the lifetime and the intensity ratio (633 nm/660 nm) as a function of the temperature for the $Mg_{3.5}FGeO_5$:Mn phosphor. In the following, we will call this type of curve "calibration curve". Fig. 2.35 shows that both calibration curves vary monotonously with the temperature. Thus, the temperature can be obtained with both methods. The sensitivity of the measurement is a function of the stiffness of the curves as small variations of

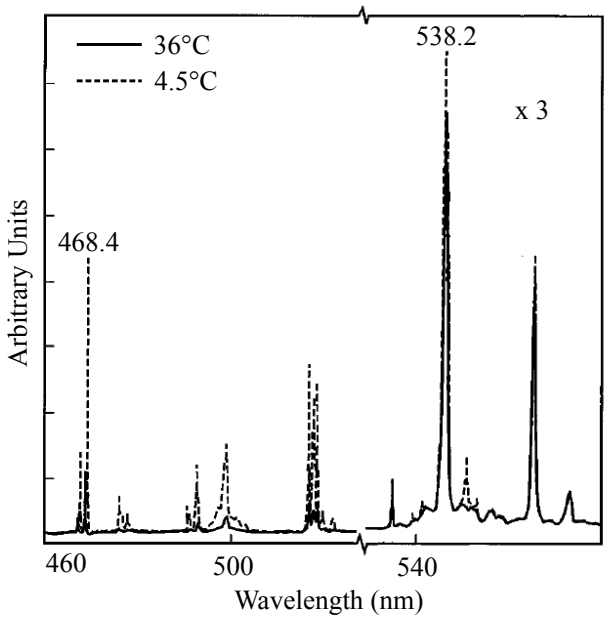

Figure 2.34: *Emission spectra of La_2O_2S:Eu at* 4.5 °C *and* 36 °C *showing the effect of temperature. From Allison and Gillies (1997).*

temperatures yield strong variations of the measured value (lifetime or intensity ratio) in regions where the slope is high. Consequently, the lifetime method features a poor sensitivity for temperatures T = 300 K – 650 K but a very high sensitivity for temperatures comprised between T = 650 K and T = 900 K. In contrast, the intensity ration method has a good sensitivity if T < 600 K.

Figure 2.36a and b, also from Brübach et al. (2013), plot the normalized temporal and spatial standard deviations of the mean measurements shown in Fig. 2.35 as a function of temperature for both methods. It is shown than the lifetime method is better if T > 500 K. This is emphasized when comparing the spatial standard deviation only, where the lifetime method yields better results in the whole temperature range. This behavior can be attributed to the higher number of parameters that affect the spectral transfer function of the detection system in comparison to the temporal transfer function. As an example, the spectral transfer function strongly depends on the quality of the optical alignment of the system. Using Figs. 2.35 and 2.36, one may conclude that the lifetime method is more appropriate if $Mg_{3.5}FGeO_5$:Mn phosphor is used, especially when T > 650 K. However, if the surfaces of interest are in movement, the lifetime method will lead to important errors due to the increased difficulty of tracking the emitting source. The intensity ratio method would yield better results in this case as variations due to the motion of the surface can be attenuated using the quotient of the two wavelength intensities (Khalid et al. (2010)). As we did not intend to measure surface temperatures

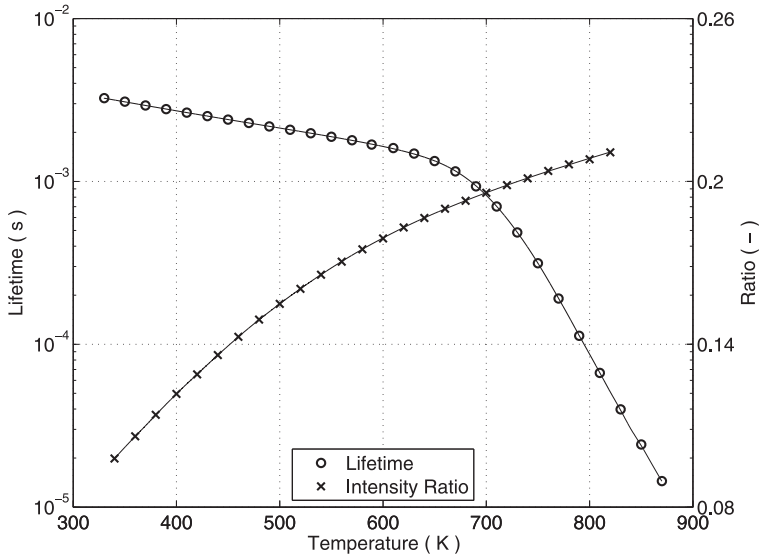

Figure 2.35: *Lifetime and intensity ratio as a function of the temperature for $Mg_{3.5}FGeO_5$:Mn obtained using CMOS high speed cameras. From Fuhrmann et al. (2013).*

of movable objects, we decided to use the lifetime method in our studies.

2.6.3 Choice of the phosphor

In the previous section, the $Mg_{3.5}FGeO_5$:Mn phosphor served as a reference material. However, there is an important number of different phosphors described in the literature that may be interesting for our purpose. The objective of this section is to list the parameters altering the phosphor selection and justify the selected materials. Figure 2.37, from Brübach et al. (2013) combined with data from Allison and Gillies (1997), shows the calibration curves of numerous usual phosphors usually selected for combustion applications. Each phosphor has a specific range of measurable temperatures. It is then necessary to know approximately the temperature of the surface of interest before choosing a phosphor. To illustrate this, a surface temperature T = 1200 K can in principle be measured with Y_2O_3:Eu, YAG:Eu, and $LuPO_4$:Dy phosphors. However, using the $LuPO_4$:Dy is not advisable as the sensitivity is very weak around this temperature. It is also interesting to notice that some phosphors feature very high sensitivities over a wide range of temperatures like LaO_2S_2:Eu and they can be used at different collection wavelengths. Finally, at a given temperature, different phosphors have lifetimes varying from a few milliseconds to a few tens of nanoseconds. While recording a luminescent signal of few tens of nanoseconds requires very specific hardware, lifetimes of the order of a millisecond imply that the measurement repetition rate cannot exceed the kHz. High frequency measurements require high repetition rate laser sources for phosphor excitation

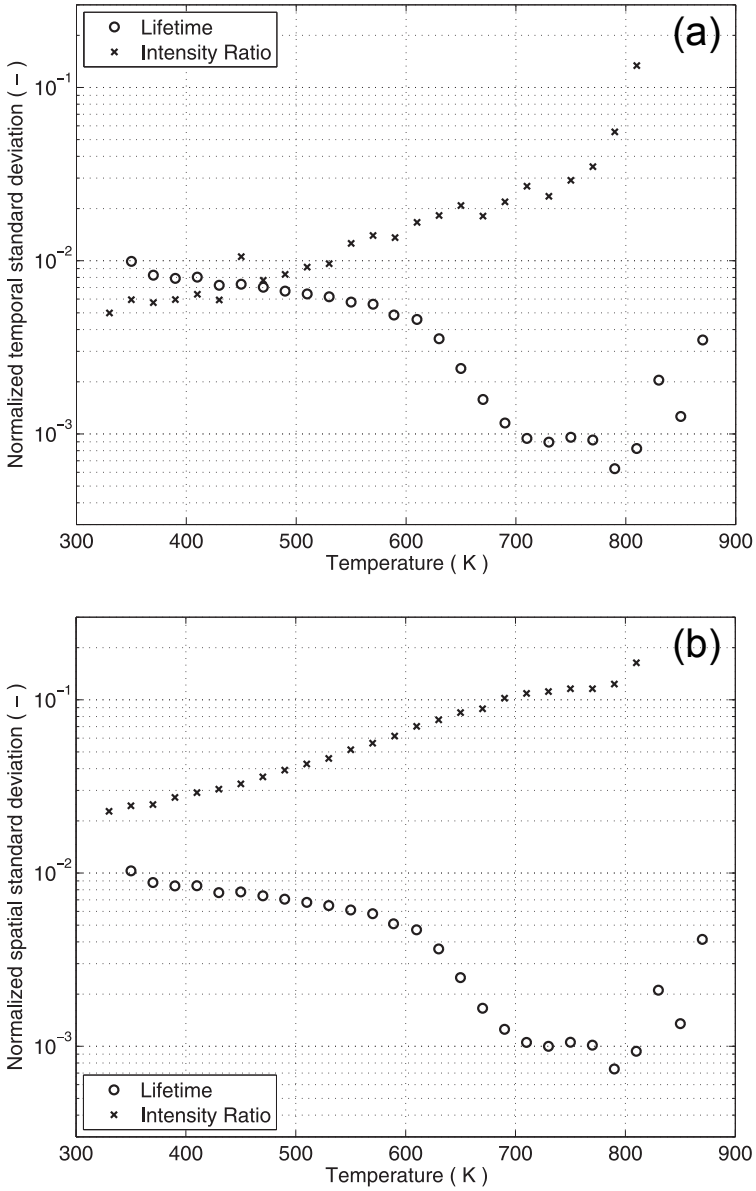

Figure 2.36: *Normalized temporal (a) and spatial (b) standard deviations of the measured temperatures for $Mg_{3.5}FGeO_5$:Mn within an isothermal calibration environment. These data are associated to the data shown in Fig. 2.35. From Fuhrmann et al. (2013).*

and were not planed in our studies. Many LIP setups use detectors enable to resolve phosphorescent decay times down to a few microseconds.

Based on these observations, LaO_2S_2:Eu, $Mg_{3.5}FGeO_5$:Mn, and Y_2O_3:Eu phosphors are well suited materials. Nevertheless, LaO_2S_2:Eu does not sustain tem-

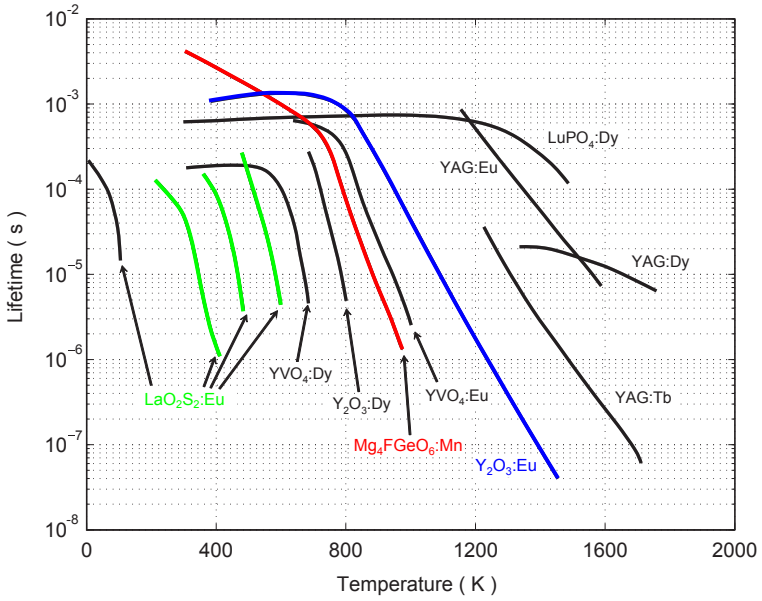

Figure 2.37: *Temperature lifetime characteristics of numerous thermographic phosphors from Brübach et al. (2013) using data of Allison and Gillies (1997).*

peratures exceeding 600 K and must be restricted to very specific cases. The phosphor Y_2O_3:Eu is not easy to use when in contact with burnt gases. Indeed, Fig. 2.38, from Brübach et al. (2007), shows the effect of the composition of the gas surrounding the phosphor on the calibration curve. It is demonstrated that there is a very strong impact of the oxygen concentration on the phosphor lifetime. In a configuration where fresh and burnt gases featuring very different oxygen concentrations can interact with the phosphor, the precision of the temperature measurements is expected to drop severely. For this reason, we decided not to use Y_2O_3:Eu even if the high sensitivity temperature range is very attractive. According to Brübach et al. (2007), LaO_2S_2:Eu and $Mg_{3.5}FGeO_5$:Mn phosphors are not affected by the gaseous environment. Consequently, all experiments realized in our studies use $Mg_{3.5}FGeO_5$:Mn. This material is well suited for surface temperature measurements ranging from T = 300 K to T = 1000 K in a combustion chamber with a high precision.

2.6.4 Film preparation and deposition

The $Mg_{3.5}FGeO_5$:Mn phosphor used in this study was produced by Phosphor Technology Ltd and has the reference EQD25/N-U1. It comes in the form of a micrometric powder (D_{50} = 8 µm), and is therefore not ready to use. The powder must be mixed with a binder to be able to bond the thermographic phosphor to the surface of interest. We use a UV transparent liquid binder (ZYP-HPC) that resists temperatures up to 1773 K. The objective of this section is to present the protocol required to produce a satisfying phosphores-

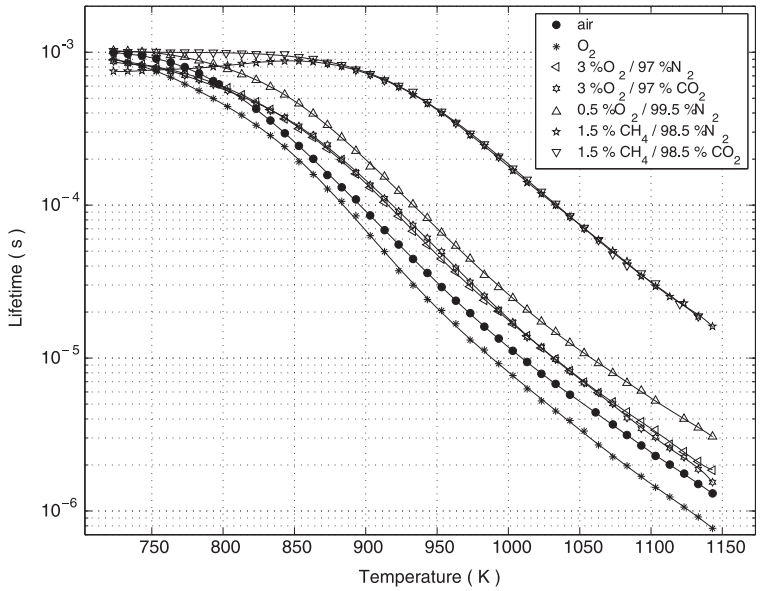

Figure 2.38: *Temperature lifetime characteristics within a reference atmosphere (air) compared to measurements obtained in different mixtures of nitrogen, oxygen, carbon dioxide and methane for Y_2O_3:Eu. From Brübach et al. (2007).*

cent mixture and bond it to the surface where temperature measurements are needed.

Various methods for mixture preparation and bonding exist (Brübach et al. (2013)) but we chose the method that required the minimum investment in terms of purchases and skills development. Therefore, we focused on an air-spraying technique that is suitable for many phosphors and only requires an airbrush (AEROGRAPHE Services, Utopia C05) and few painting skills. The main challenge is then to prepare a mixture that contains a sufficient concentration of phosphor powder (to ensure sufficient luminescence) but a not too high viscosity so that air-spraying is possible. After tests, we fixed the volume ratios of phosphor, binder and dilution water producing a satisfying mixture. We used a dilution water volume corresponding to 10% of the binder volume. Another difficulty concerns the ability to stick this mixture to the surface of interest with good resistance properties to heat transfer and to shear due to the flow. When the mixture must be sprayed on a metallic surface, it is possible to sand blast the surface to improve the grip. However this is not possible on transparent quartz windows that must remain intact after the experiments and after removal of the phosphorescent mixture. The painting procedure is as follows: we first apply a very thin layer of paint using the airbrush and then wait for it to dry. It takes a few minutes at ambient air conditions or few tens of seconds using a hot air blowing device. Next, a second layer is applied and dried. We repeat this procedure until the thickness of the phosphorescent film

is satisfying. The thicker is the film, the higher is the signal intensity. However, this additional painting layer can alter the properties of the surface (emissivity, thermal resistance...), and it is advisable to reduce its thickness as much as possible. In all cases, we tried not to exceed a 100 µm thickness.

2.6.5 LIP setup

The phosphorescent mixture is now laid on the surfaces where temperature measurements are needed. The hardware equipments and the post-processing developments that were realized to measure surface temperatures are described.

2.6.5.1 Hardware

Figure 2.39 shows the absorption and emission spectra of $Mg_{3.5}FGeO_5$:Mn. Absorptivity is high in the UV (A-B) and violet region. It is then possible to excite the phosphor with the third (355 nm) or the fourth (266 nm) harmonic of a Nd:YAG laser. We used a Nd:YAG laser (Continuum, Minilite ML II) operated at 10 Hz for LIP experiments. Figure 2.39 also shows that the maximum phosphorescence intensity is emitted at 660 nm. This wavelength is then used to collect the luminescence signal. A schematic of the LIP setup is presented in Fig. 2.40. The UV laser is focused on the surface of interest using a UV mirror (Melles-Griot, Y4-1025-45P) and a UV spherical lens (Thorlabs, LA4663, f = 1000 mm). These optics are needed to produce a sub-millimeter laser impact on the phosphorescent paint and increase the spatial resolution of the method. The resulting phosphorescent signal is collected by a photomultiplier tube, PMT, (Hamamatsu, R9880U-20) that features a maximum sensibility at 630 nm and has a 0.57 ns typical rise time on a 50 Ω load.

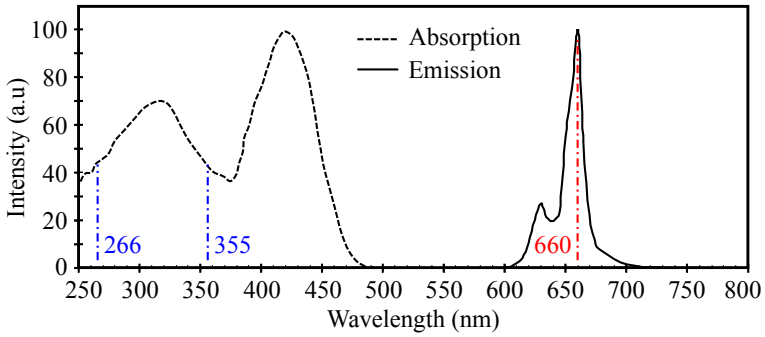

Figure 2.39: *Absorption (dashed line) and emission (solid line) spectra of $Mg_{3.5}FGeO_5$:Mn powders (Phosphor Technology Ltd).*

To prevent interferences from the laser source, a 550 nm longpass filter (Thorlabs, FEL0550) is placed in front of the PMT. A 10 nm bandpass filter centered at 660 nm is put in front of the PMT to select the only wavelength of interest

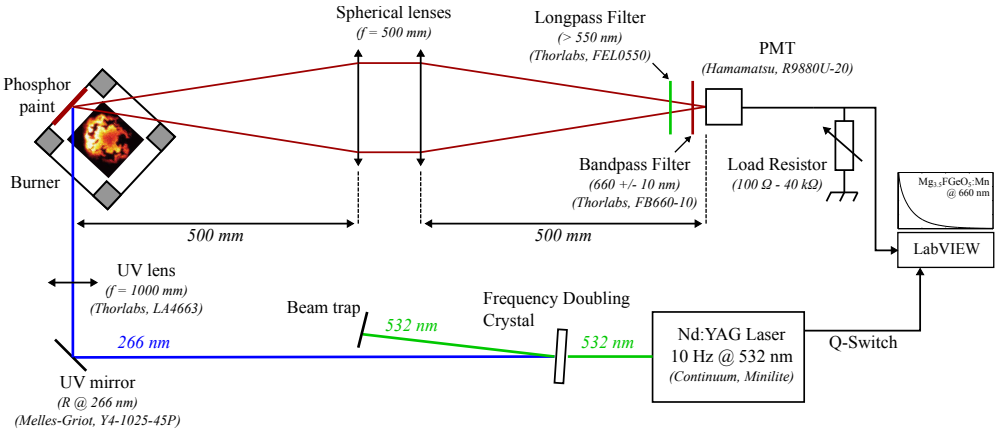

Figure 2.40: *Schematic of the LIP setup used for temperature measurements of the solid surfaces of the combustor.*

of the luminescent signal. Phosphorescence is isotropic and it is not necessary to collect the signal along the surface normal. However, a set of two spherical lenses (Thorlabs, LA1740-A) was first used to focus the PMT on the laser impact to increase the signal to noise ratio. The output PMT signal is proportional to the number of photons collected and gives a very weak current (maximum 0.1 mA). It is then necessary to amplify/convert this current to a sufficiently large voltage (minimum 100 mV). One possible way is to use a high frequency amplifier that provides sufficient output voltage and preserves the PMT rise time. However, the different models tested produced strong electrical noises that degraded the signal too much. Consequently, we settled for a second method based on the use of a passive load resistor. The load is plugged between the PMT output and the ground as shown in Fig. 2.40 and the voltage drop through the load is recorded. This voltage is proportional to the PMT output current and to the resistance of the load. The signal voltage can be increased by increasing the load without additional electrical noise. However, a strong drawback of this method is that the PMT rise time is drasticcaly degraded when the load is increased above 50 Ω. The choice of the optimal load is justified in section 2.6.5.4.

2.6.5.2 Post-processing

When the signal is properly conditioned, it can be recorded and post-processed. The different treatments that were realized are described. The phosphorescent signals are recorded on a computer using a fast acquisition board (National Instruments, PCI-6111, 4 MHz) piloted by the software LabVIEW. Signals were acquired and processed in "real-time" to determine a phosphorescent decay time after each laser pulse, every 100 ms.

Figure 2.41 shows an example of signal acquisition and processing at $T = 290$ K. Figure 2.41a plots the normalized signal intensity as a function of time where $t = 0$ corresponds to the beginning of the laser pulse. Pulses have a temporal Full Width at Half Maximum close to FWHM = 5 ns. The intensity monotonously decays and drops to zero far from the laser pulse. An adjustable low-pass filter is applied on the signal to reduce noise. The phosphorescence signal follows an exponential decay after the laser pulse. However, to prevent eventual disturbances from the laser pulse or from residual light (producing a non-zero baseline) only a fraction of the decaying signal is selected for further analysis. LabVIEW routines were developed to independently select a starting and an ending point for the interrogation window. These boundaries are indicated by percentages of the maximum signal intensity (see Fig. 2.41b). Once an interrogation window is selected, an exponential fit is applied to the signal obeying to Eq. (2.11): $I(t) = I_0 \exp(-t/\tau)$. The value of I_0 is not of interest here as signals are normalized by their maximum value but the decay time τ is easily obtained. To illustrate this procedure, the signal presented in Fig. 2.41c corresponds to an exponential fit with a decay time $\tau = 2.80$ ms. The validity of this regression is evaluated by its coefficient of determination R^2. In the case presented here, the uncertainty on the calculated decay time is better than 0.04%.

2.6.5.3 Effect of the interrogation window

The quality of the fit depends on many parameters. The objective of the following sections is to give example of settings that need to be carefully adjusted for accurate temperature measurements. As explained previously, it is important to select an appropriate time window for regression of the data. Effects of the width of the interrogation window are shown in Fig. 2.42 for the case presented in Fig. 2.41 corresponding to a decay time $\tau = 2.80$ ms. The beginning of the interrogation window was fixed here to 50% of the maximum intensity. The best fit is obtained in this case using a 6 ms interrogation duration while too narrow or too large windows lead to larger errors. The best width approximately corresponds to twice the decay time. This value is retained as a reference for further investigations.

The impact of the starting point is now examined. Figure 2.43 shows the evolution of the calculated decay time τ and its corresponding coefficient of determination R^2 as a function of the starting point of the window, in percentage of the maximum signal intensity. Again, this parameter has a strong influence on the decay time and it is important to choose it carefully. The best fit is obtained here if the window starts at a time corresponding to 60% of the maximum signal intensity. It is then possible to choose the appropriate ending point (also in percentage of the maximum intensity) that would lead

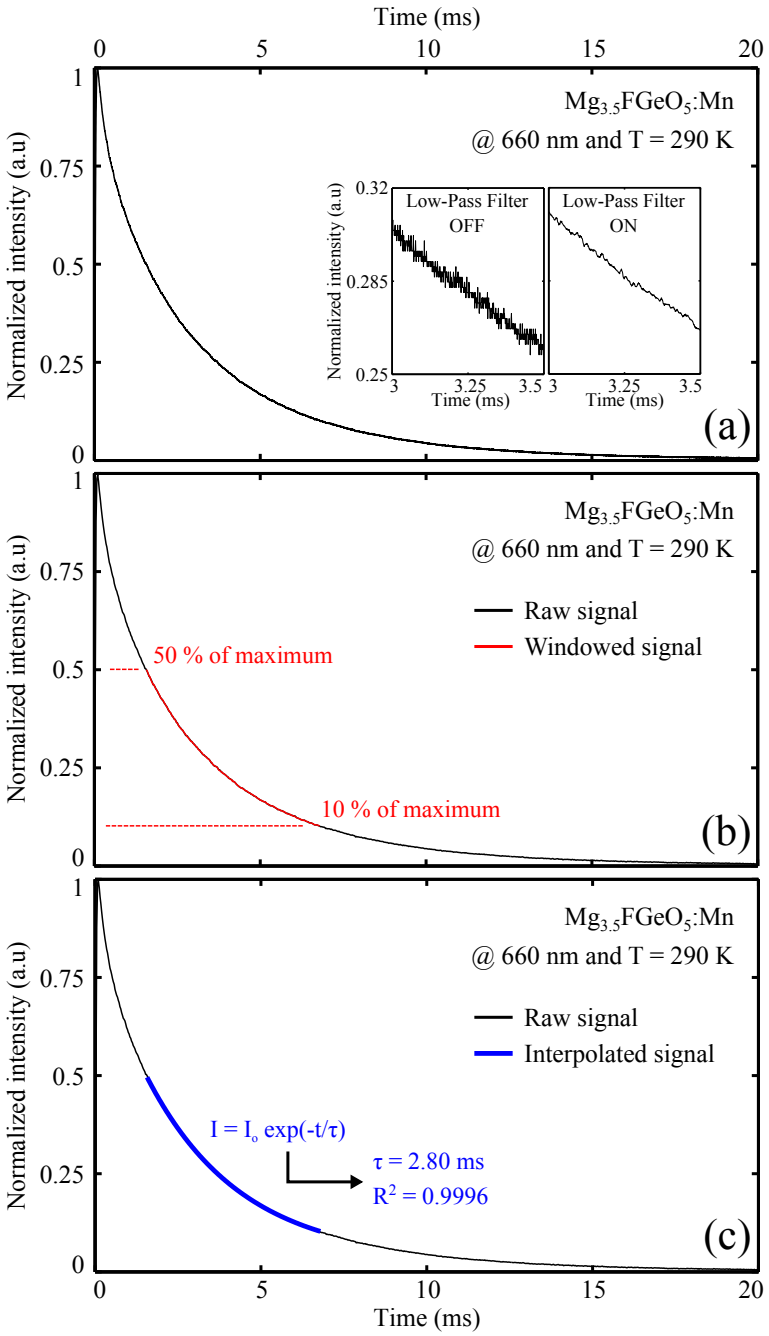

Figure 2.41: *(a) Typical temporally decaying phosphorescent signal at* 660 nm *for* $Mg_{3.5}FGeO_5$*:Mn at* T = 290 K*. The effect of a low-pass filter applied to the signal is also visible. (b) A fraction of the raw signal is extracted to reduce interferences from the laser source and background light. The time window used for data reduction can be modified. (c) Exponential regression of the windowed signal and calculation of a decay time* τ *and a coefficient of determination* R^2 *indicating the quality of the fit.*

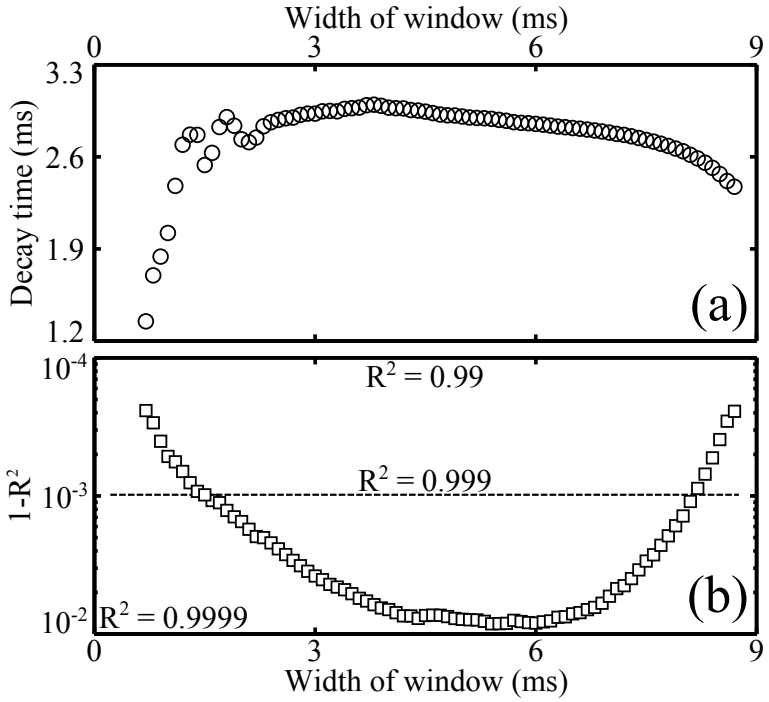

Figure 2.42: *Decay time (a) and coefficient of determination (b) as a function of the width of the window used for the exponential fit for $Mg_{3.5}FGeO_5$:Mn at T = 290 K.*

to a window width equal to twice the decay time (see Fig. 2.42a and b). One finds 8.1% of the maximum intensity for a starting point at 60%. These results were used to select the characteristics of the time windows that will be used for the regression of the phosphorescent signals in all our LIP experiments. This adaptive method has the advantage to be valid on a wide range of decay times and signal intensities because it uses dimensionless values.

2.6.5.4 Effect of the resistor load

As mentioned earlier, we decided to use a passive load resistor to convert the PMT signal to a measurable voltage. However, the optimal PMT rise time is obtained at a R_{load} = 50 Ω load. It is then interesting to study effects of the load on the PMT rise time. Figure 2.44 shows examples of normalized phosphorescence decay signals for $Mg_{3.5}FGeO_5$:Mn at T = 290 K. In these experiments, all parameters remained constant except the resistance of the load that was varied from R_{load} = 100 Ω to R_{load} = 34.8 kΩ. In all cases, the pulse temporal Full Width at Half Maximum is FWHM = 5 ns and the emitted intensity rise time is of the order of a nanosecond and should in principle be independent on the measurement chain. Here the rise time is defined by the time needed to increase from 10% to 90% of the signal maximum intensity. It is clear that increasing R_{load} has a strong impact on the [10% - 90%] rise time has it takes

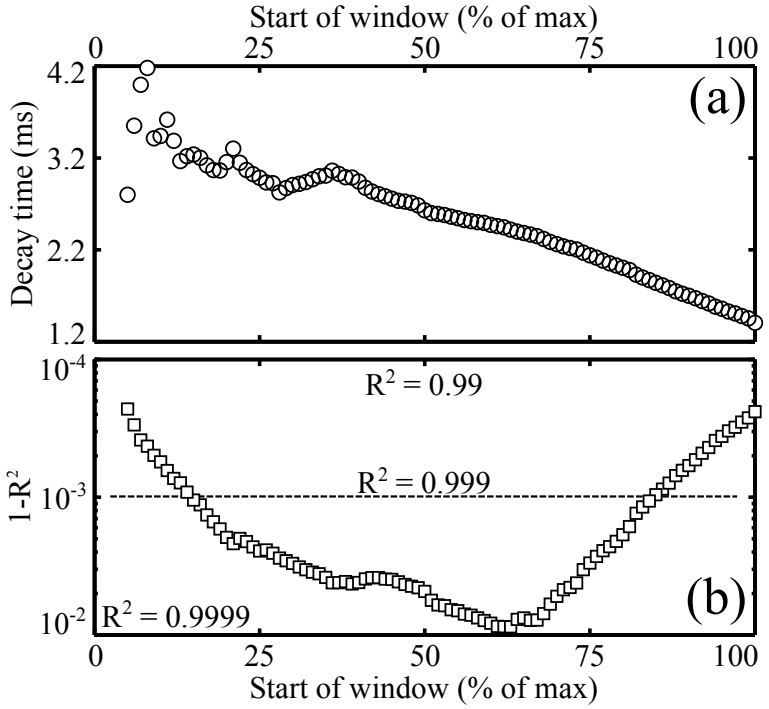

Figure 2.43: *Decay time (a) and coefficient of determination (b) as a function of the starting time of the window used for the exponential fit for* $Mg_{3.5}FGeO_5$*:Mn at* T = 290 K. *The starting time corresponds to the time where the signal level takes a given percentage of its maximum value.*

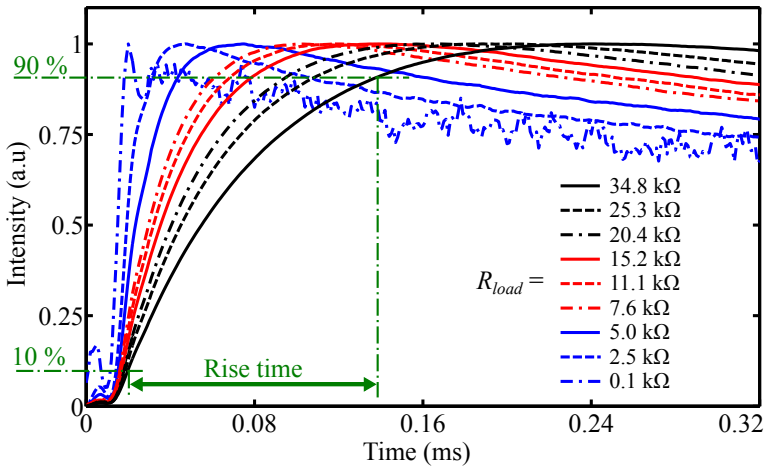

Figure 2.44: *Normalized phosphorescent signals obtained using different load resistors for for $Mg_{3.5}FGeO_5$:Mn at T = 290 K. Effects of the load resistor connected to the detector on its rise time is emphasized.*

a value higher than 100 µs if R_{load} = 34.8 kΩ. Figure 2.45 shows that the rise time linearly increases with the load.

Figure 2.44 also indicates that the signal to noise ratio drasticcaly increases with the load. The reason for that can be found in Fig. 2.46 where it is shown that the output voltage also linearly increases with the load. This is due to Ohm's law: $V = R_{load} \times I$ where V is the potential difference across the load and I is the current through this element. The objective is then to select the highest load that satisfies the following rise time criterion. The rise time must be small compared to the decay time of the phosphorescent signal. In our case, we used a load resistance always lower than 10 kΩ which allows temperature measurements up to T = 750 K using $Mg_{3.5}FGeO_5$:Mn phosphor (Fig. 2.37).

2.6.5.5 Effect of the PMT gain

Another possibility to adjust the signal level is to change the voltage supplied to the PMT, *i.e* the gain. Increasing the gain increases the sensibility of the PMT and increases the signal level, but it also increases the noise level. Thus, this parameter has a strong impact on the calculated decay time and on the temperature measurements. Figure 2.47 shows the evolution of the calculated decay time as a function of the PMT gain. It is demonstrated that modifying the gain alters the decay time. This parameter must be modified carefully during experiments.

Figures 2.42, 2.43, and 2.47 show that the determination of decay times, which are used to deduce temperatures, are a function of numerous parameters. It

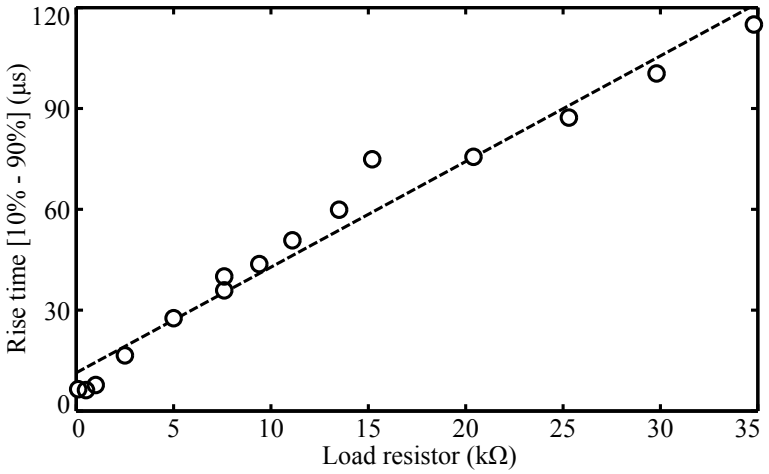

Figure 2.45: *Rise time (10% - 90%) as a function of the load resistor obtained for* $Mg_{3.5}FGeO_5$*:Mn at* T = 290 K.

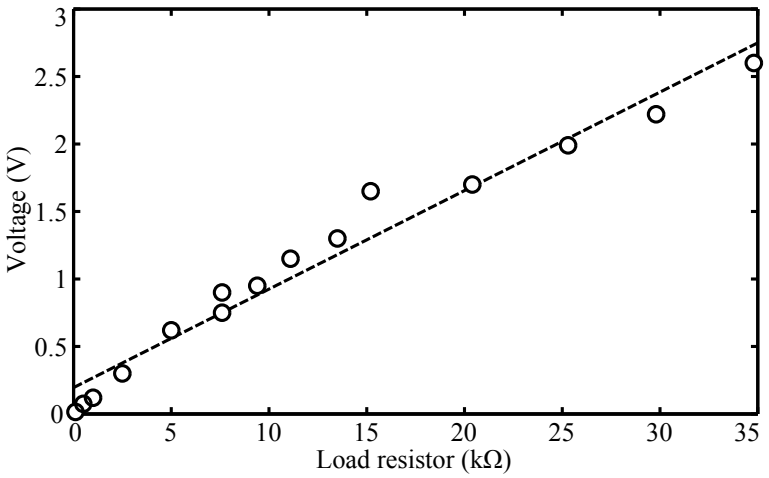

Figure 2.46: *Maximum voltage at the resistor load as a function of the resistance (same as 2.45) obtained for* $Mg_{3.5}FGeO_5$*:Mn at* T = 290 K.

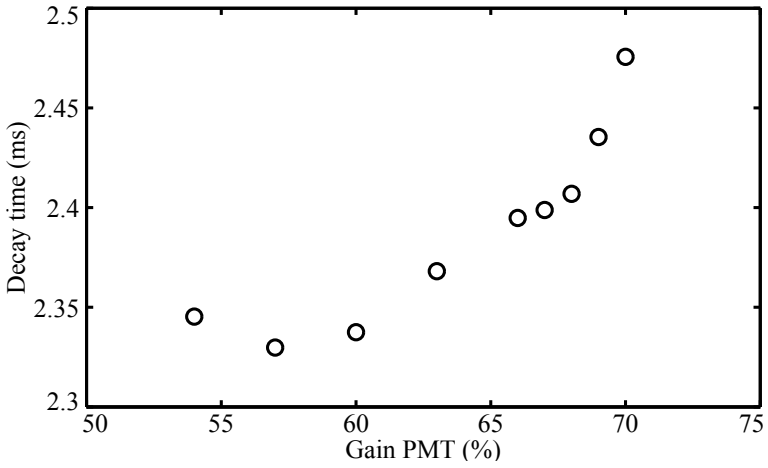

Figure 2.47: *Decay time as a function of the detector gain for $Mg_{3.5}FGeO_5$:Mn at T = 290 K.*

is not recommended to use a calibration curve $\tau = f(T)$ as the ones shown for examples by Fuhrmann et al. (2013) in Fig. 2.35. For that reason, a calibration using the same devices and settings as for temperature measurements in the combustor is necessary before or after experiments within the combustor. The calibration procedure developed in this work is described in the following section.

2.6.6 Calibration

2.6.6.1 LIP calibration procedure

Figure 2.48 shows a schematic of the setup used to calibrate LIP measurements. As explained previously, the devices, settings, and methods used for the calibration should be similar to the ones used for measurements within the combustor. Consequently, the setups in Fig. 2.40 (combustor measurements) and in Fig. 2.48 (calibration) are identical at the exception of one point. For the calibration, the combustor is replaced by a thermocouple (Type K, diameter D = 1 mm) and an adjustable heating device. The heating device is used to vary the temperature of the air surrounding the thermocouple that consequently changes its surface temperature. In our case, the thermocouple is painted with the same phosphorescent mixture as the one used in the combustor to determine surface temperatures reachable by the heating device, from 300 K to 850 K.

The calibration curve is obtained as follows. The heating device is set to its maximum temperature and the thermocouple measures approximately T = 850 K. Then LIP measurements are started at a repetition rate of 10 Hz and the calculated decay times are stored with the temperatures measured by the ther-

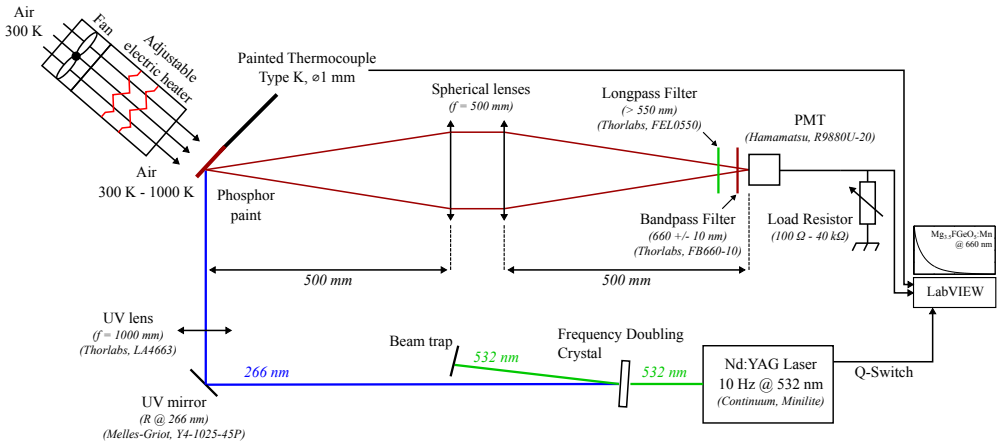

Figure 2.48: *Schematic of the LIP setup used for the calibration of the technique.*

mocouple. Next the temperature of the heating device is progressively reduced to T = 300 K and LIP measurements are continuously repeated at a repetition rate of 10 Hz. At the end, thousands of data pairs (temperature/decay time) are obtained and can be plotted to produce a calibration curve. Figure 2.49 shows an example of one result for $Mg_{3.5}FGeO_5$:Mn at 660 nm and using a 10 kΩ load resistance. This curve is close to the ones found by Fuhrmann et al. (2013) (see Fig. 2.35) and by Allison and Gillies (1997) (see Fig. 2.37). However, it corresponds exactly to the settings that will be used for measurements conducted in the combustor. Slight differences may be observed for $T > 750$ K where the rise time of the PMT at a 10 kΩ load is too close to the measured decay times (see Fig. 2.45). For that reason, this calibration curve will not be used to measure temperatures higher than T = 750 K.

The calibration procedure used here differs from the one generally used. In many cases, the calibration surface (painted with phosphor) is placed in an oven, featuring an optical access for excitation and collection, where temperature is well stabilized and precisely known at steady state. One advantage of this method is that it may be possible to calibrate directly on the object of interest (combustor wall, injector...) as long as it fits in the oven. Moreover, this method is very precise as the temperature within the oven can be controlled with a precision close to one Kelvin. But this method has also two serious drawbacks. First it takes a lot of time as it is necessary to wait for the stabilization of the oven temperature. Secondly, it might be difficult to apply this method without modifying the optical alignment of the setup as the oven cannot always be placed at the same location as the combustor. It is here easier to place a thermocouple where LIP measurements are needed by slightly moving the combustor away. Another advantage is that this alternative method is less time consuming as the thermocouple time response to temperature changes

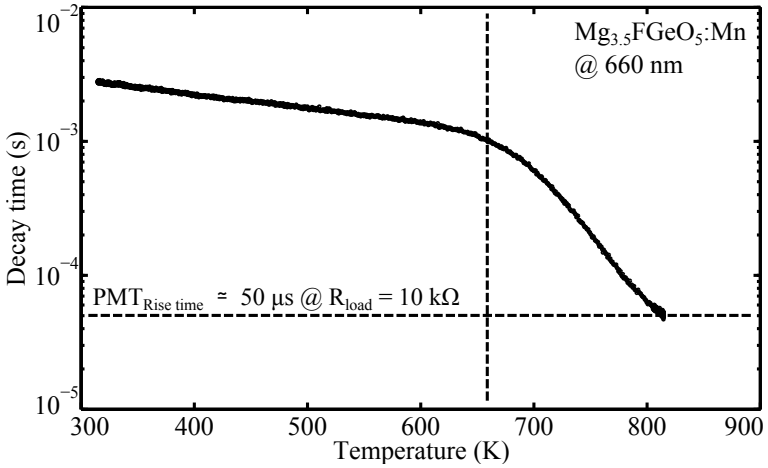

Figure 2.49: *Typical calibration curve giving the evolution of the luminescent decay time as a function of the temperature for $Mg_{3.5}FGeO_5$:Mn at* 660 nm *and using a* 10 kΩ *load resistance.*

is lower than in an oven. However, the temperature is never perfectly stabilized because the thermocouple temperature continuously decreases until it reaches T = 300 K.

2.6.6.2 Effect of the cooling rate

It is then necessary to verify that the temperature measured by the thermocouple corresponds to the one reached at its surface, where LIP measurements are conducted. The cooling rate, expressed in $\mathrm{K \cdot s^{-1}}$, must be sufficiently small compared to the inverse of the thermocouple response time that can also be expressed in $\mathrm{K \cdot s^{-1}}$. As it is difficult to determine precisely this response time, we decided to validate our calibration method by verifying that it is independent of the cooling rate of the thermocouple. Figure 2.50a shows two different calibration curves (between 700 K and 800 K) obtained using two different cooling rates. The first one in black was obtained for a slow cooling rate and the second one plotted in blue was obtained for a fast cooling rate. Figure 2.50b plots the cooling rates as a function of temperature. In the slow case, the thermocouple looses $2\,\mathrm{K \cdot s^{-1}}$. It looses $7\,\mathrm{K \cdot s^{-1}}$ in the fast case. In both cases, calibration curves in Fig. 2.50a collapse on the same curve meaning that they are independent of the cooling rate as long as it does not exceed $7\,\mathrm{K \cdot s^{-1}}$.

2.6.7 Estimation of errors

There is an important number of contributions that affect the uncertainties on surface temperature measurements by LIP. As LIP relies on a calibration step, the accuracy of the technique depends on the care taken during this step. It

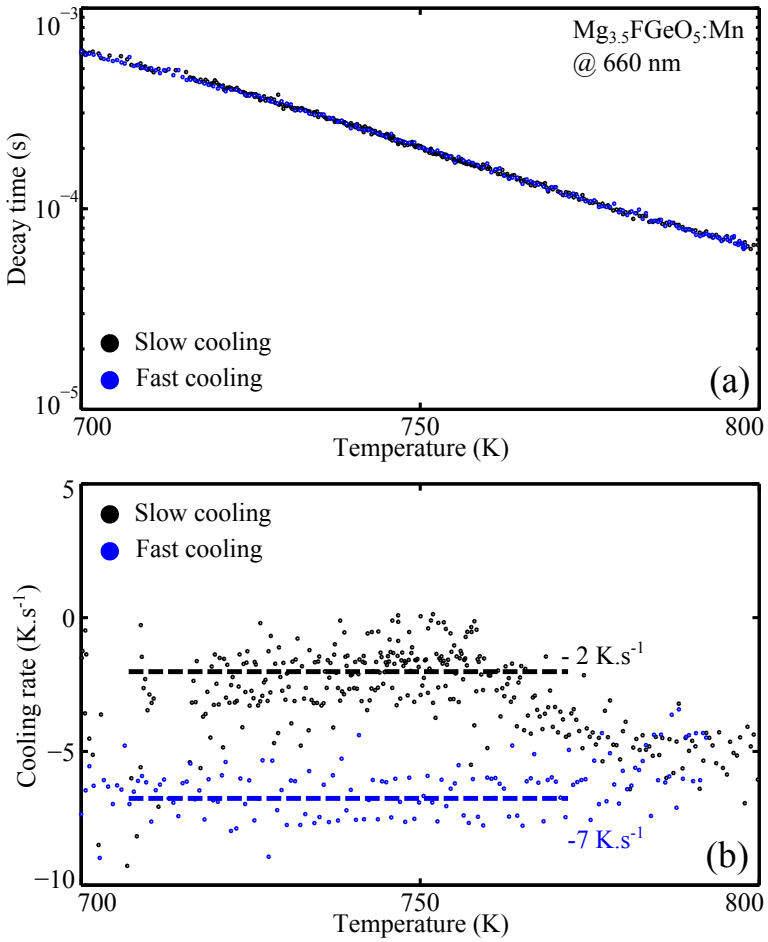

Figure 2.50: *(a) Calibration curves for $Mg_{3.5}FGeO_5$:Mn between* 700 K *and* 800 K *using a "slow" (black) and a "fast" (blue) cooling rate of the painted thermocouple. (b) Cooling rate as a function of the temperature for both experiments used to build the calibration curves visible in (a).*

was already shown in Sec. 2.6.6.2 that one must be careful to use the calibration thermocouple only close to thermal steady-state. An unavoidable source of inaccuracy comes from the static error of the thermocouple measurements. This contribution depends on the thermocouple type and on the temperature range. In our case, the static error for a type K thermocouple is 2.2 K at T = 300 K and 6.0 K at T = 800 K. We consider the inaccuracy due to the reading of the calibration thermocouple acceptable.

The quality of the surface temperature measurement also depends on the precision of the hardware setup. To the leading order, the precision of the technique is directly related to shot-to-shot variations of the measured decay times at a fixed temperature. Values of shot-to-shot fluctuations can be deduced from the calibration curve shown in Fig. 2.49. These values are obtained by measuring the deviation ΔT in Kelvin of the calibration curve for a fixed operating temperature. Values of shot-to-shot fluctuations depend on the temperature range and reach ΔT = 14 K at T = 300 K and ΔT = 3 K at T = 750 K.

By cumulating the contribution of inaccuracies and imprecisions, we evaluated the uncertainties on surface temperature measurements by LIP to ΔT = 17 K at T = 300 K and ΔT = 9 K at T = 750 K. Taking into account a moderate safety coefficient, we say that our setup for LIP using $Mg_{3.5}FGeO_5$:Mn phosphors yields surface temperature measurements with a confidence interval of ΔT = 25 K if 300 K < T < 700 K and with a confidence of ΔT = 13 K if 700 K < T < 800 K.

2.7 Thermocouple measurements (TC)

Temperatures reached by the surfaces of the combustor are measured by LIP. Laser Induced Phosphorescence is an advanced laser-based diagnostics and should be used only if simpler techniques are not suitable. When possible, measurements with thermocouples are preferred. They yield a better precision with a simpler hardware and a reduced effort. In our studies, thermocouples were used, for example, to infer the temperature reached at the surface of one of the four steel bar holding the quartz windows. Type K thermocouples were introduced within these solid elements. Thermocouples are also used for gas temperature measurements. Thermocouples should be used with care to infer the temperature within high-temperature turbulent gaseous flows. They generally have the following disadvantages. They are intrusive, have limited temporal resolution, and are subjected to radiative losses when immersed in high temperature flows.

The wake created behind thermocouples is not an issue in our experiments

because compact thermocouples with a characteristic size of few tens of micrometers are used away from the flame. This value should be compared to the characteristic size of the combustor that is generally larger than tens of centimeters.

The voltage difference between the two wires of a thermocouple is related to the temperature at the wires junction, generally a spherical bead produced when the two wires are welded. Therefore, the temperature measured by the thermocouple is not exactly the gas temperature. Gas and bead temperatures can be safely considered very close under the following conditions. The thermocouple bead needs to be at thermal steady state and it must not exchange heat with distant surfaces through radiative heat transfers.

These two conditions imply that the convective heat flux taking place between the thermocouple bead and the surrounding gas is nul and that the gas and bead temperatures are equal. The objective of this section is to verify under which circumstances thermocouples may be safely used and eventually propose adapted corrections to infer the gas temperature.

2.7.1 The response time of thermocouples

Figure 2.51 shows a simplified model of a spherical thermocouple of diameter D immersed in the burnt gases of a lean CH_4/H_2/air flame. In the case of a spatially isothermal spherical bead and if radiative heat transfers at the bead surface as well as conduction through the wires are neglected, the following expression gives the temperature $T_b(t)$ of a bead immersed in a hot stream of gases as a function of time:

$$\frac{T_b(t) - T}{T_b(0) - T} = \exp\left(-\frac{hS}{\rho_b V C_p^b} t\right) \tag{2.15}$$

where, T is the gas temperature, $T_b(0)$ stands for the bead temperature at initial time $t = 0$, h is the convective heat transfer coefficient at the bead surface, V and S respectively represent the bead volume and surface area, ρ_b is the bead density, C_p^b stands for the bead specific heat capacity, and k_b is the thermal conductivity of the bead. The properties of the bead (ρ_b, C_p^b, k_b) are supposed to be constant and equal to their value at $T_b(0) = 300\,\mathrm{K}$. The thermocouple is immersed in a gas stream of fixed composition represented by the molar fractions X_k of the different species and featuring a velocity u far from the thermocouple. In the following analysis, the gas properties (thermal conductivity k, kinetic viscosity ν, and Prandtl number Pr) are mixture average properties evaluated at the film temperature defined as $T_f = (T + T_b)/2$.

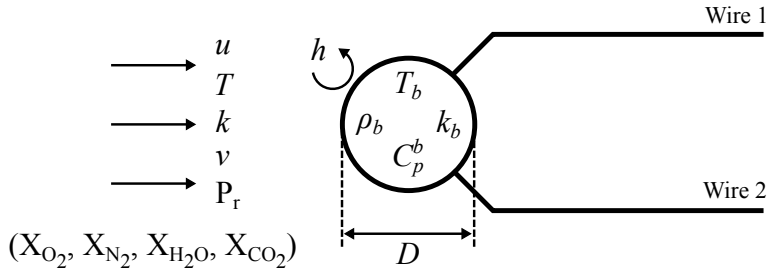

Figure 2.51: *Schematic of a spherical thermocouple of diameter D immersed in a gaseous non-stagnant flow composed of the burnt gases of a lean CH_4/H_2/air flame.*

The characteristic time t_r in Eq. (2.15) takes the following expression:

$$t_r = \frac{\rho_b V C_p^b}{hS} = \frac{\rho_b C_p^b D}{6h} \tag{2.16}$$

We will refer to this time t_r as the thermocouple response time in the following. To the leading order, the thermocouple response time depends on its diameter, its composition, and on the convective heat transfer coefficient. It is then necessary to evaluate this coefficient. The convective heat transfer coefficient h is given by:

$$h = \mathrm{Nu}\, k/D \tag{2.17}$$

where Nu is the Nusselt number. The Nusselt number depends on the flow Reynolds number Re and the mixture Prandtl number Pr and is generally evaluated using empirical correlations (Incropera and Witt (1990)). In the case of a sphere immersed in a flow where Re < 200 and Pr < 250, the correlation from Ranz and Marshall (1952) may be used:

$$\mathrm{Nu} = 2 + 0.6\mathrm{Re}^{\frac{1}{2}}\mathrm{Pr}^{\frac{1}{3}} \tag{2.18}$$

where Re= uD/ν. It is then necessary to calculate the thermal conductivity k, the kinetic viscosity ν, and the Prandtl number Pr that are a function of the film temperature T_f and mixture composition. As in Sec. 2.2, mixture properties are calculated with the same expressions as in the CHEMKIN flame solver (Kee et al. (1992)).

The thermocouple response time depends on the surrounding gas properties and is not an intrinsic property of the device. For that reason, we need to consider the type of gaseous mixtures and flows where the thermocouple will be immersed. Figure 2.52 shows a schematic of our combustion chamber that describes the different zones filled with burnt gases with varying properties.

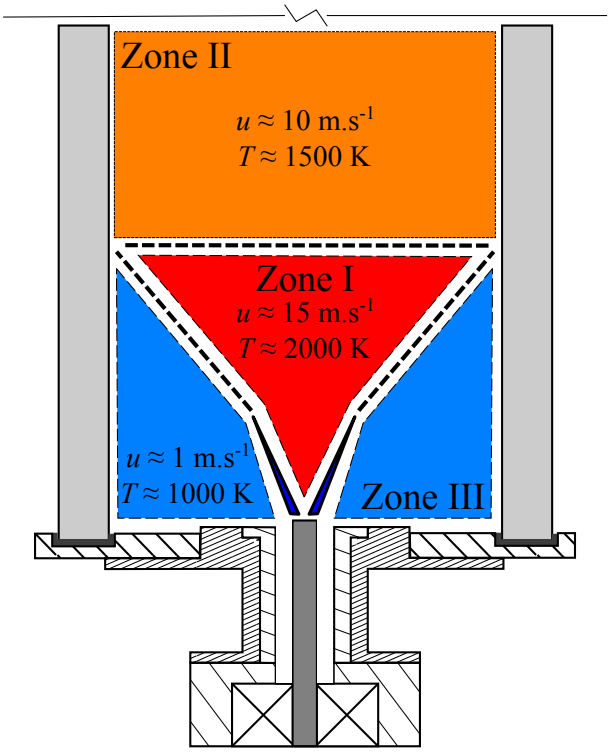

Figure 2.52: *Schematic of the combustion chamber with a flame. This figure describes the different zones filled with burnt gases and featuring different flow velocities and temperatures.*

Closely downstream the flame, the burnt gases are close to the adiabatic flame temperature ($T \simeq 2000$ K) and feature high velocities due to the jet and thermal expansion ($u \simeq 15\ \mathrm{m \cdot s^{-1}}$). Far downstream, heat losses to the combustor peripheral walls cool the burnt gases to a lower value $T \simeq 1500$ K. The velocity is also reduced to $u \simeq 10\ \mathrm{m \cdot s^{-1}}$. Burnt gases in the ORZ (Zone III) recirculate at a lower velocity $u \simeq 1\ \mathrm{m \cdot s^{-1}}$ leading to a long residence time of the flow in the vicinity of cold boundaries. The hot flow in this region features thus a lower gas temperature $T \simeq 1000$ K. These values are only rough estimates and depend on the operating conditions. Selected values will be justified in Secs. 3.1 and 3.3.

As an illustration, we calculated the response time of a thermocouple immersed in the burnt gases of a reference CH_4/H_2/air flame with a thermal power $P = 4$ kW, hydrogen enrichment $X_{H_2}^{fuel} = 0.60$, and equivalence ratio $\phi = 0.7$. The burnt gases composition is computed using the REGATH flame solver (Candel et al. (2011)). The response time is calculated for bead diameters ranging from $D = 10$ µm to $D = 1$ mm. These values roughly correspond to unsheathed fine gage thermocouples available from OMEGA. We use the physical properties of Type R thermocouples (Pt/13%/Rh-Pt, OMEGA, series P13R-00X) that are

mainly composed of platinum. We conducted two sets of calculations. The first set is carried out with a fixed gas temperature $T = 1000$ K but for different velocities ranging from $u = 0.5\ \mathrm{m\,s^{-1}}$ to $u = 16\ \mathrm{m\,s^{-1}}$. A second series of calculations is conducted with a fixed velocity $u = 4\ \mathrm{m\,s^{-1}}$ but for different gas temperatures ranging from $T = 500$ K to $T = 2000$ K.

Figure 2.53a shows in a log/log plot the evolution of the thermocouple response time t_r as a function of its bead diameter D at $T = 1000$ K and for different gas velocities. For a fixed velocity, one can notice that the response time increases rapidly with the bead diameter. A multiplication of the bead diameter by a factor of 10 roughly increases the response time by a factor of 44. There is also an effect of the gas velocity but it is less important. When the gas velocity increases by a factor of 8 the response time only decreases by a factor of 1 to 3 depending on the bead diameter. Figure 2.53b shows in a similar log/log plot the evolution of the convective heat transfer coefficient h as a function of its bead diameter D at $T = 1000$ K and for different gas velocities. Increasing the bead diameter rapidly reduces h, while increasing the velocity slowly increases h.

Figures 2.54a and 2.54b respectively show in a log/log plot the evolution of t_r and h as a function of the bead diameter D when the velocity is fixed to $u = 4\ \mathrm{m \cdot s^{-1}}$ and for different gas temperatures. Increasing the gas temperature increases the convective heat transfer coefficient and shortens the thermocouple response time. To sum up, a given thermocouple immersed in the Zone I in Fig. 2.52 features a response time shorter than if immersed in Zone II. The difference will be even higher in Zone III. In the following, different references of thermocouples from OMEGA featuring different bead diameters are used. For example, we use thermocouples with bead diameters of $D \simeq 50\ \mu\mathrm{m}$ (Thermocouple 1) and up to $D \simeq 1$ mm (Thermocouple 2). In zone I, Thermocouple 1 features a response time close to $t_r = 4$ ms while Thermocouple 2 features a response time close $t_r = 0.7$ s. These durations increase to $t_r = 9$ ms for Thermocouple 1 and to $t_r = 2.2$ s for Thermocouple 2 placed in Zone III. As an illustration, Thermocouple 1 may be used to resolve temporal fluctuations of the temperature in the combustor up to 250 Hz while Thermocouple 2 should be limited to mean value measurements in the gas or measurements in solids where temperature fluctuations have slower time sclaes.

Calculations were based on the hypothesis that the thermocouple has a spatially isothermal spherical bead. The isothermal hypothesis is verified under the condition that the Biot number of the bead is small $\mathrm{Bi} << 1$. The Biot number is a dimensionless quantity that compares the heat transfer resistance inside an object to the heat transfer resistance at the object surface. It is defined by the

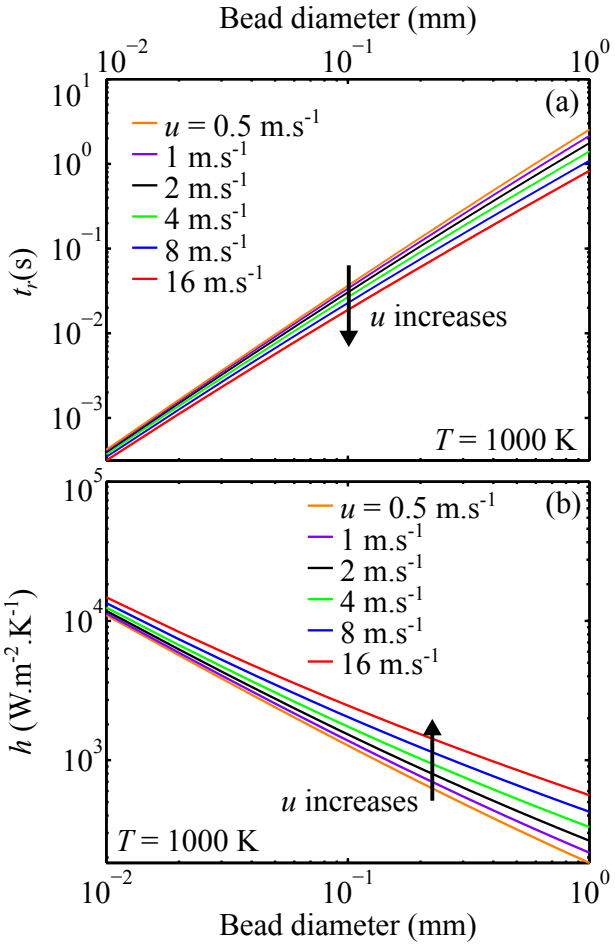

Figure 2.53: *(a) Log/log plot of the evolution of the thermocouple response time t_r as a function of its bead diameter D at T = 1000 K and for different gas velocities. (b) Evolution of the convective heat transfer coefficient h.*

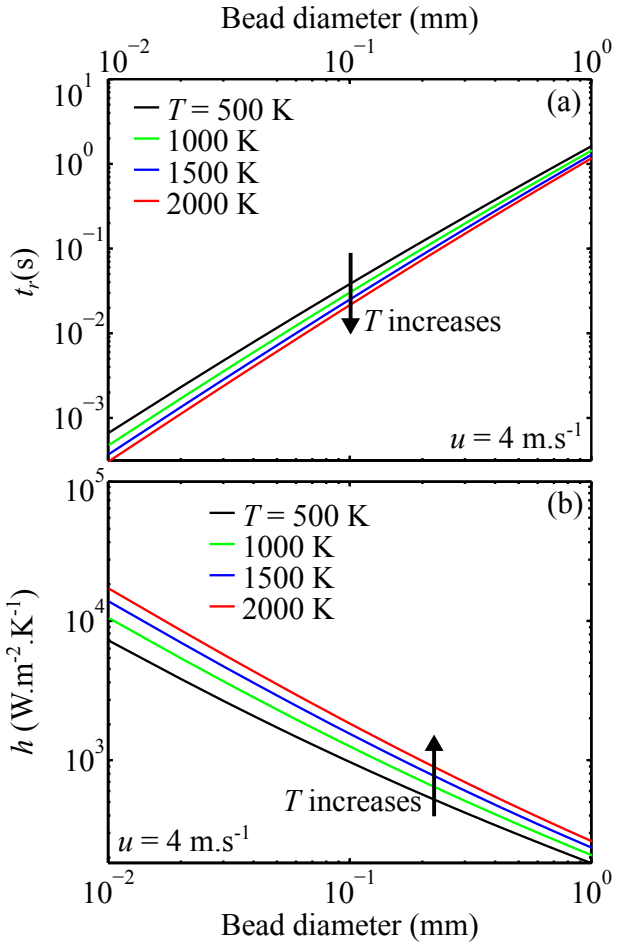

Figure 2.54: *(a) Log/log plot of the evolution of the thermocouple response time t_r as a function of its bead diameter D at $u = 4$ m s^{-1} and for different gas temperatures. (b) Evolution of the convective heat transfer coefficient h.*

following expression:

$$\mathrm{Bi} = \frac{hV}{k_b A} = \frac{hD}{6k_b} \tag{2.19}$$

The maximum Biot number obtained for the response time calculations presented in Figs. 2.53 and 2.54 is Bi = 0.015 << 1. The thermocouple bead can thus be considered spatially isothermal.

The global response time of a temperature measure with a thermocouple also depends on the quality of the signal amplification electronics. Conditioning of the thermocouple signal is realized with a fast (500 Hz bandwidth at −3 dB) voltage amplifier (Meiri, ME26C-TC-ISO), allowing to resolve temporal fluctuations up to 250 Hz. This corresponds to a period of 4 ms which is compatible with the response time of Thermocouple 1 in zone I.

2.7.2 Correction to radiance at the thermocouple surface

Another well known drawback of thermocouples is that measurement must be carefully corrected to radiance when the thermocouple bead is immersed in a high temperature flow. The influence of radiance at the bead surface on the measured temperatures is calculated and it is verified under which circumstances our thermocouple measurements should be corrected to radiance.

At steady state, radiative heat losses from the thermocouple spherical bead are compensated by the convective heat flux from the hot flow around the bead. By assuming that conduction in the thermocouple arms may be neglected, which is in general the case for small wire diameter thermocouples as the ones used in this study (Hindasageri et al. (2013)), one has for steady operation:

$$\Phi_r + \Phi_c = 0 \tag{2.20}$$

where, Φ_r and Φ_c respectively stand for the radiative and convective heat fluxes through the spherical surface of the thermocouple bead. The temperature of the thermocouple bead is lower than the gas temperature of interest. To precisely infer the gas temperature, radiative and convective heat fluxes through this surface need to be taken into account. The convective heat flux is given by:

$$\Phi_c = hS(T - T_b) \tag{2.21}$$

where, h stands for the convective heat transfer coefficient, S denotes the surface area of the spherical bead, and T and T_b respectively denote the gas and

bead temperatures. The heat transfer coefficient is deduced from the empirical correlation due to Ranz and Marshall (1952) as discussed in Sec. 2.7. The radiative heat flux component is given by Incropera and Witt (1990):

$$\Phi_r = \Phi_1^a - \Phi_1^l \tag{2.22}$$

where Φ_1^a and Φ_1^l respectively stand for the arriving and leaving radiative heat fluxes of the bead. These two fluxes need to be determined. The arriving radiative heat flux Φ_1^a is given by:

$$\Phi_1^a = \sum_{k=1}^{n} F_{k1}\Phi_k^l \tag{2.23}$$

In this expression, the subscripts k refer to the n different objects that exchange heat with the bead through radiance and the subscript 1 stands for the bead surface. The coefficient F_{k1} is the shape factor between the surface A_k of the object k and the thermocouple bead surface $A_1 = S$. All necessary shape factors can be derived from geometric calculations and depend on the thermocouple position with respect to the setup. The leaving radiative heat flux Φ_k^l from the object k is given by:

$$\Phi_k^l = A_k\epsilon_k\sigma T_k^4 + (1-\epsilon_k)\Phi_k^a \tag{2.24}$$

where ϵ_k represents the emissivity of the surface of the object k and σ stands for the Stefan-Boltzmann constant. For the wavelengths of interest, the transmissivity of the burnt gases surrounding the thermocouple bead is assumed to be close to unity and is therefore neglected in the expressions yielding the radiative heat flux. The emissivity ϵ_1 of the thermocouple bead at the temperature $T = T_1$ is calculated using the expression proposed by Davisson and Weeks (1924). The other emissivities depend on the temperature and properties of surface k. The gas temperature T is finally deduced from the linear system formed by Eqs. (2.20)-(2.24).

The temperature drop $\Delta T = T - T_b$ van be calculated as a function of the bead diameter D and for different gas velocities u and temperatures T. This analysis is analogue to the one conducted in Sec. 2.7 and is used here to analyze the impact of radiative heat losses at the thermocouple bead at steady state as a function of the zone of interest within the flow (see Fig. 2.52). In this analysis, it is considered that the thermocouple exchanges heat through radiance only with the laboratory walls at $T_2 = 300$ K. This is a strong simplification that leads to an over-estimation of the temperature drop as other eventual heat exchanging objects, like the confinement chamber walls or the injection dump plane, feature higher surface temperatures. It corresponds to the worse case scenario. The wall emissivity is taken equal to $\epsilon_2 = 0.8$, a value which corresponds to usual building materials at $T_2 = 300$ K. Considering only two exchanging objects

(thermocouple bead and laboratory walls), the radiative heat flux Φ_r takes the following expression:

$$\Phi_r = -\frac{\epsilon_1 \epsilon_2 S}{1 - \left(1 - \epsilon_1 \frac{S}{A_2}\right)(1 - \epsilon_2) + \epsilon_1 \epsilon_2 \frac{F_{11}}{F12}} \sigma (T_b^4 - T_2^4) \tag{2.25}$$

As the bead is a spherical convex surface, the form factor $F_{11} = 0$. Moreover, it is safe to assume that the surface area ratio between the bead and the laboratory walls is very small, $S/A_2 << 1$. The radiative heat flux Φ_r can be therefore reduced to:

$$\Phi_r = -\epsilon_1 S \sigma (T_b^4 - T_2^4) \tag{2.26}$$

Equations (2.20), (2.21) and (2.26) are used to calculate the temperature drop $\Delta T = T - T_b$:

$$\Delta T = \frac{\epsilon_1 \sigma}{h} (T_b^4 - T_2^4) \tag{2.27}$$

As the bead temperature is initially unknown, the film temperature T_f is also unknown, but this quantity is needed for the calculation of the gas properties. The bead temperature is then deduced using an iterative process where Eqs. (2.20), (2.21) and (2.26) are solved until the value for T_b converges. Figure 2.55a shows in a log/log plot the evolution of the thermocouple temperature drop ΔT as a function of its bead diameter D when $u = 4$ m s^{-1} and for different gas temperatures. This figure indicates that increasing the bead diameter increases the temperature difference between the bead and the hot gas independently of the gas temperature. For example, increasing the bead diameter by a factor of 10 roughly increases the temperature drop by a factor of 5. One should note that the bead diameter only alters the convective heat transfer coefficient h in Eq. (2.27). Figure 2.55b also shows that the convective heat transfer coefficient decreases with the bead diameter as already found in Figs 2.53b and 2.54b.

Figure 2.55a also shows that the temperature drop increases very rapidly with the gas temperature. For example, doubling the temperature from 1000 K to 2000 K roughly increases the temperature drop by a factor of 11. This is due to the radiative flux that scales with the bead temperature at the power of 4. When immersed in a high temperature fluid, it is advisable to use thermocouples as small as possible to limit perturbations due to radiance.

Figures 2.56a and b show in a log/log plot the evolution of the thermocouple temperature drop ΔT and convective heat transfer coefficient h as a function of the bead diameter D when the gas temperature is fixed to $T = 2000$ K and for different gas velocities. It is clear that the gas velocity has a smaller influence on the temperature drop than the gas temperature. Doubling the velocity roughly decreases the temperature drop by only 10%. The gas temperature

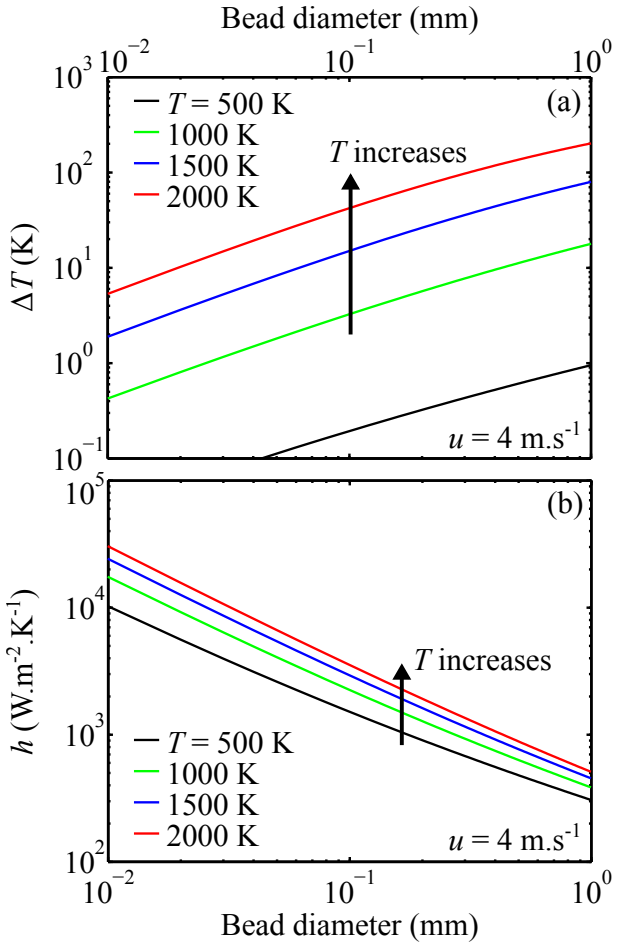

Figure 2.55: *(a) Log/log plot of the evolution of the thermocouple temperature drop ΔT as a function of its bead diameter D when the flow velocity is fixed to $u = 4\ \mathrm{m\ s^{-1}}$ and for different gas temperatures. (b) Evolution of the convective heat transfer coefficient h.*

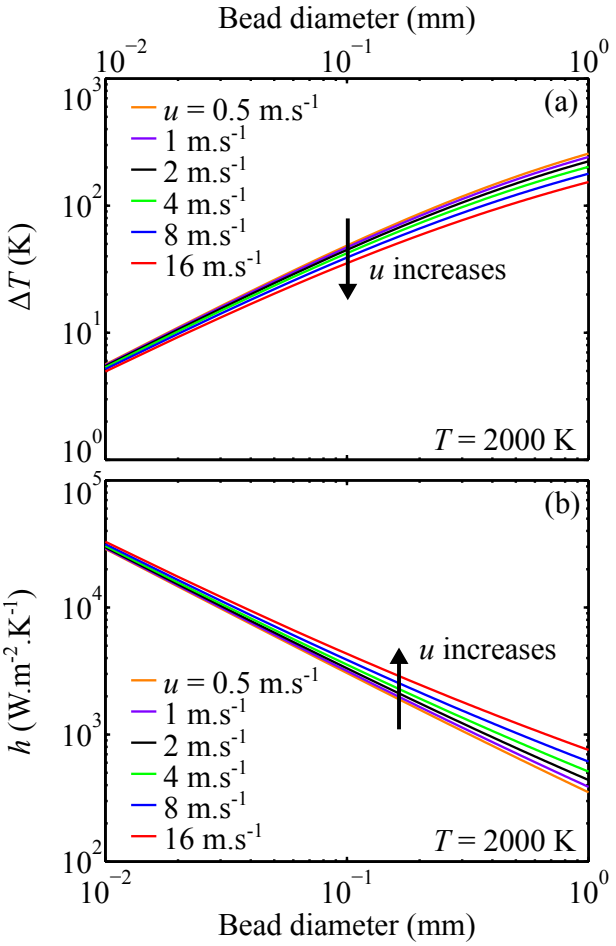

Figure 2.56: *(a) Log/log plot of the evolution of the thermocouple temperature drop ΔT as a function of its bead diameter D when the flow temperature is fixed to T = 2000 K and for different gas velocities. (b) Evolution of the convective heat transfer coefficient h.*

and bead diameter are the main parameters controlling the temperature drop for a thermocouple immersed in a high temperature low Mach flow.

As explained in Sec. 2.7.1, we use thermocouples with bead diameters of $D \simeq 50\,\mu$m (Thermocouple 1) and up to $D \simeq 1$ mm (Thermocouple 2). In zone I in Fig. 2.52, Thermocouple 1 features a temperature drop due to radiance of $\Delta T = 20$ K while Thermocouple 2 features a larger temperature drop of $\Delta T = 155$ K. These temperature drops are reduced to $\Delta T = 8$ K for Thermocouple 1 and to $\Delta T = 64$ K for Thermocouple 2 in Zone III. These temperature drops are further reduced to $\Delta T = 2$ K for Thermocouple 1 and to $\Delta T = 25$ K for Thermocouple 2 in Zone III. Thermocouple 1 may be used to measure the gas temperature in zones II and III without accounting for radiance. Thermo-

couple 2 can be used within zones featuring a temperature lower than T = 800 K where the temperature drop is lower than an acceptable value of ΔT = 10 K over a wide range of gas velocities. Outside these zones, thermocouples may be used but a radiance correction must be applied to the measured temperature values. It is however advisable to use a more detailed geometrical model including more elements of the combustor and the injector if accurate temperature measurements are required.

Conclusion

The different diagnostics used in this work were presented. It includes:

- Laser Doppler Velocimetry (LDV)
- Hot Wire anemometry (HW)
- Flame chemiluminescence
- Planar Hydroxyl Laser Induced Fluorescence (OH-PLIF)
- Particle Imaging Velocimetry (PIV)
- Laser Induced Phosphorescence (LIP)
- Thermocouple measurements (TC)

Several hardware and post-processing developments were analyzed for measurements based on OH-PLIF and LIP. These different diagnostics are used in the following chapters to probe the flow velocity, the gas and combustor wall temperatures, and the flame topology to analyze the stabilization of premixed CH_4/H_2/air swirling flames.

Chapter 3

Experimental setup characterization

The flow in the combustor under non-reactive and reactive conditions is analyzed for one operating condition in order to obtain a deep understanding of its behavior. The flow through the swirlers is analyzed in the first section. In a second stage, the flow within the combustion chamber operated under non-reactive conditions is analyzed using PIV. These characterizations are used to initialize the simulations conducted in a companion work (Mercier (2014)). The thermal behavior of the combustor is analysed by LIP and thermocouple measurements conducted during the thermal transient after ignition and at steady-state. Finally, a reference flame is defined for which detailed measurements were carried out by chemiluminescence, PIV, and OH-PLIF.

3.1 Swirlers characterization

Swirl flows are characterized by a swirl number (Syred and Beér (1974)). For a given injector this number determines the structure of the flow issued from the injector. It is important to know its value. Swirl numbers S presented in this document were determined without considering pressure effects using the following expression (Gupta et al. (1984)):

$$S = \frac{\int_0^{R_i} v_\theta v_z r^2 dr}{R_i \int_0^{R_i} v_z^2 r dr} \tag{3.1}$$

where $R_i = D_i/2$ denotes the injection tube radius, r represents the radial distance to the injector axis and v_z and v_θ respectively stand for the mean axial and azimuthal velocities. The axial and azimuthal velocity profiles needed for the determination of the swirl number can be measured by PIV or LDV and are determined here under non-reactive conditions. Figure 3.1 shows the radial profile of v_z and v_θ 2 mm above the rod tip for a bulk flow velocity $U = 14.0\ \mathrm{m \cdot s^{-1}}$

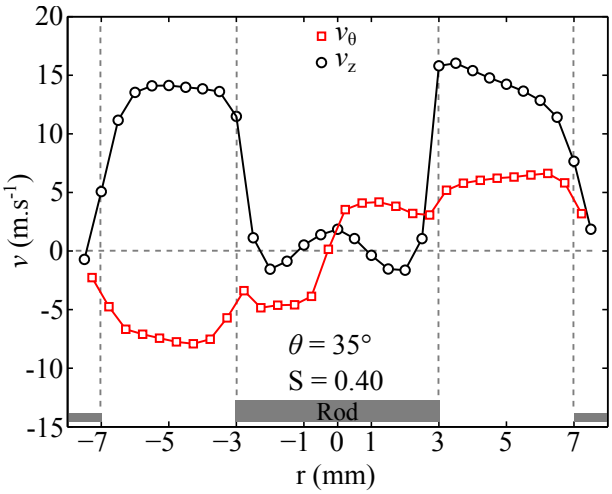

Figure 3.1: *Axial (a) and azimuthal (b) mean velocity components of the swirling jet as a function of the radial distance to the burner axis for a bulk flow velocity* $U = 14.0\ \mathrm{m \cdot s^{-1}}$ *and with the radial swirler featuring a fixed blade angle* $\theta = 35°$*. Measurements were realized by LDV under non-reactive conditions and without quartz tube to confine the flow at 1 mm above the central rod tip. The injector set in configuration A (see Fig. 1.11) is represented in gray to ease visualization.*

when the swirl vane featuring a fixed blade angle of $\theta = 35°$ is installed (see Fig. 1.9 in Chapter 2). In this case LDV was used. The axial velocity profile takes high values in the jet ($3\ \mathrm{mm} < |r| < 7\ \mathrm{mm}$). This profile is slightly asymmetric due to the difficulty to place the vertical rod precisely on the axis of the injector. For $|r| > 7$ mm, the axial velocity is close to zero due to the proximity of the dump plane. For $1\ \mathrm{mm} < |r| < 2.5\ \mathrm{mm}$, the rod tip generates a small recirculation of the flow yielding negative values of the mean axial velocity in this region. The azimuthal velocity profile in the jet between $3\ \mathrm{mm} < |r| < 7\ \mathrm{mm}$ is roughly flat.

These profiles are used to determine the swirl number with Eq. 3.1. One finds, S = 0.4 for the fixed blade angle $\theta = 35°$. Figures 3.2a and b show the mean axial and azimuthal velocity profiles for the swirl vane featuring blades with an adjustable angle and with the injector set in configuration A. The bulk flow velocity is fixed here to $U = 13.3\ \mathrm{m \cdot s^{-1}}$ and results for different blade angles, $\theta_1 = 29°$, $\theta_2 = 30°$, $\theta_3 = 32°$, $\theta_4 = 35°$, and $\theta_5 = 38°$ are plotted. The axial velocity is not affected by the blade angle and increasing the blade angle increases the magnitude of the azimuthal velocity. This leads to an increase in the swirl number S (Eq. 3.1). Table 3.1 summarizes the different swirl numbers obtained by varying the blades angle with the injector set in configuration A. These value range from S = 0.3 to S = 0.4.

Values or the swirl number are not large enough to generate a vortex break-

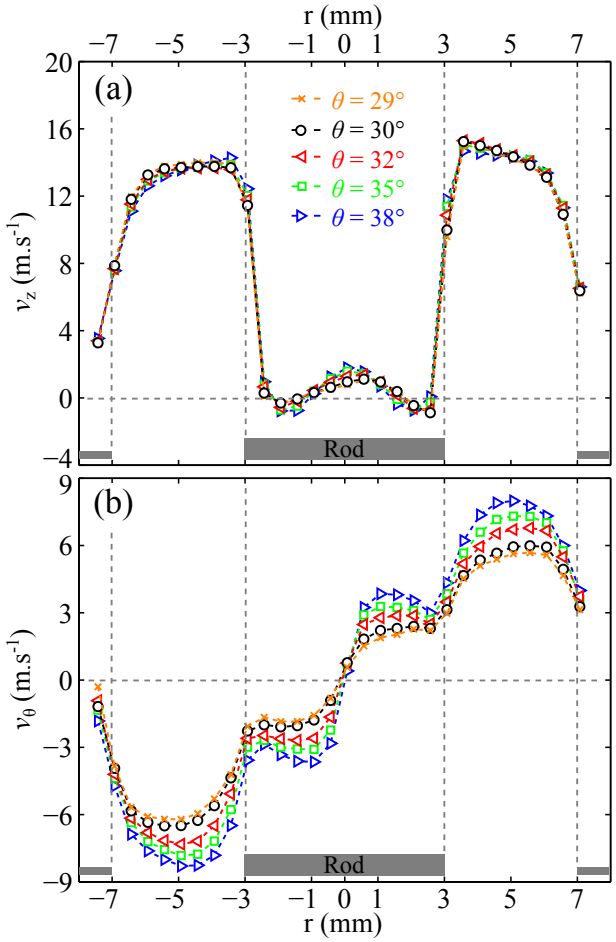

Figure 3.2: *Axial (a) and azimuthal (b) mean velocity components of the swirling jet as a function of the radial distance to the burner axis for a bulk flow velocity* $U = 13.3\ \mathrm{m \cdot s^{-1}}$ *and different blade angles* $\theta_1 = 29°$ ×, $\theta_2 = 30°$ ∘, $\theta_3 = 32°$ ◁, $\theta_4 = 35°$ □ *and* $\theta_5 = 38°$ ▷. *Measurements were realized by LDV under non-reactive conditions and without quartz tube to confine the flow at 1 mm above the central rod tip. The injector set in configuration A (see Fig. 1.11) is represented in gray to ease visualization.*

Table 3.1: *Swirl numbers S measured at the injection tube outlet by varying the blade angle θ and the geometrical configuration of the injector.*

k	1	2	3	4	5	6
S_k	0.30	0.32	0.35	0.37	0.40	0.68
θ_k	29°	30°	32°	35°	38°	61°
$D_i\,(mm)$	14	14	14	14	14	12
$D_r\,(mm)$	6	6	6	6	6	0

down of the flow along the burner axis (Gupta et al. (1984)). Although the apparition of this hydrodynamic instability slightly depends on the flow and injector configurations (Syred and Beér (1974)), it is generally admitted that vortex breakdown occurs for flows featuring swirl numbers larger than $S = 0.6$ (Gupta et al. (1984)). Consequently, we use a central rod, that acts as a bluff body and generates a flow recirculation. This low velocity region helps to stabilize the flames. We say that the flames are rod-stabilized as they are anchored by the central rod tip.

When the central rod is removed, it is necessary to increase the swirl number to $S > 0.6$ to stabilize the flames aerodynamically. This is achieved by increasing the blades angle. Figure 3.3 shows the mean axial and azimuthal velocity profiles at the injector outlet for the swirl vane with a blade angle $\theta_6 = 61°$ and with the injector set in configuration B (Tab. 3.1). In this configuration the central rod is removed but a quartz tube of diameter $D = 50$ mm is also added to confine the flow. In this case, vortex breakdown takes place and an IRZ is created without the help of a bluff-body. The axial velocity measured 2 mm above the injection outlet takes negative values within a recirculating flow when $|r| \leq 2$ mm. The highest axial jet velocities are reached at the extremities of the injection tube. In the jet, the mean azimuthal velocity profile features a solid body rotation. The highest azimuthal velocities are reached for $|r| \simeq 5.5$ mm and the azimuthal velocity nearly linearly decreases with the radial distance and reaches zero for $r = 0$. For this high swirl number, the flames are stabilized aerodynamically.

3.2 Flow field measurements under non-reactive conditions

The velocity field in the combustion chamber is characterized under non-reactive condition for a reference operating condition. These data are used to validate LES calculations carried out in a companion study (Mercier (2014)).

We used PIV to measure the velocity field in the combustion chamber. In this

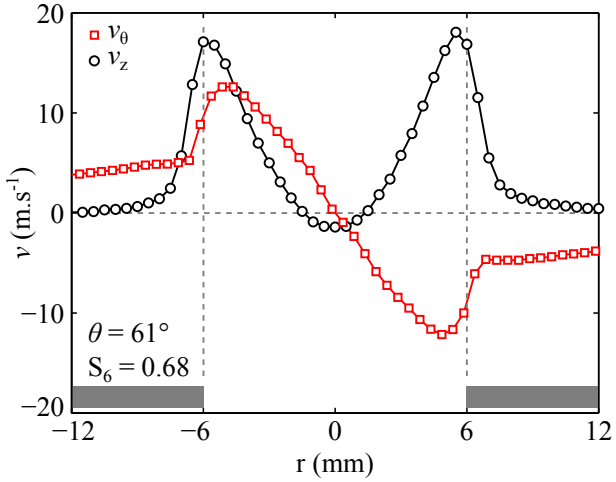

Figure 3.3: *Mean axial ◯ and azimuthal □ velocity components as a function of the radial distance to the burner axis for a swirl number* $S_6 = 0.68$ *(*$\theta_6 = 61°$*) and a bulk flow velocity* $U = 11.0\,\mathrm{m \cdot s^{-1}}$*. Reproduced from Durox et al. (2013). Measurements were realized by LDV under non-reactive conditions with a* 50 mm *diameter quartz tube to confine the flow at* $z = 2$ *mm above the injection nozzle outlet. The injector set in configuration B (see Fig. 1.11) is shown in gray to ease visualization.*

analysis, the combustor is equipped with a square confinement chamber (see Chapter 1). The swirl vane is operated with a fixed blade angle of $\theta = 38°$ and a central rod (see Sec. 3.1). Air is injected at a fixed bulk flow velocity $U = 14.0\,\mathrm{m \cdot s^{-1}}$ yielding a swirl number S = 0.4 measured 2 mm above the rod tip (Fig. 3.1). Oil droplets were used as a seeding agent. Measurements were conducted in 18 longitudinal and 13 transverse planes as shown in Fig. 3.4. This database is then used to infer the 3-D velocity field in a large fraction of the combustion chamber by interpolating the data between different planes. Details on the PIV setup and methods are described in Sec. 2.5.

Figure 3.5 (left column) shows the measured mean axial velocity field in different parallel (X,Z) planes for different positions along the Y axis (Fig. 3.4). Figure 3.5a shows results in the central longitudinal plane when $y = 0$. One can clearly identify the jet of high velocities, the IRZ, and the ORZ. One can also see the radial expansion of the jet due to the swirl imparted to the flow. Mercier (2014) conducted LES simulations of these experiments. Results from these calculations are presented in the right column in Fig. 3.5. The simulations capture well the mean flow topology qualitatively and quantitatively. In particular the correct location and angle of the internal recirculating bubble is well predicted in Figs. 3.5a-b near $z = 6$ mm. The flow field structure at $z = 40$ mm is also well captured except that the swirling jet arms feature a slightly wider angle in the experiments.

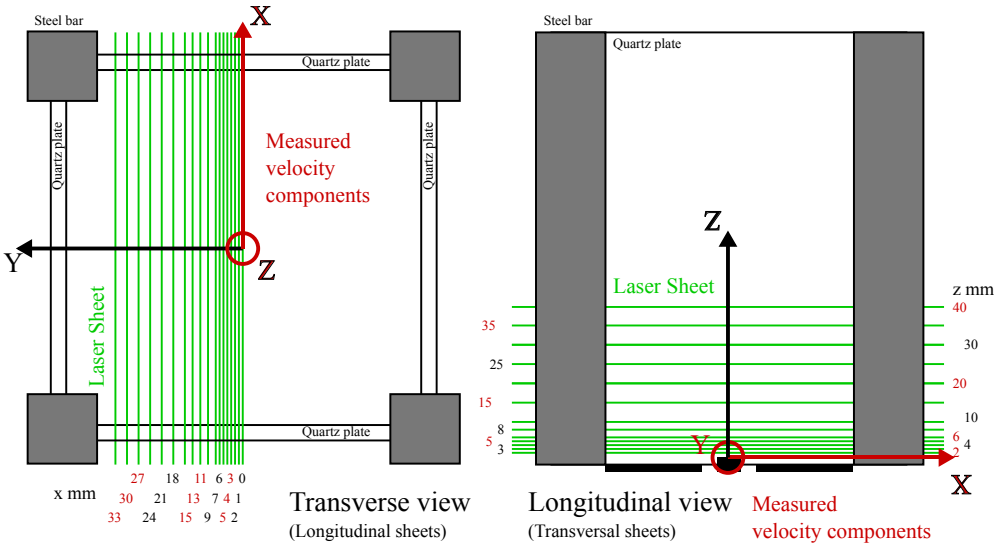

Figure 3.4: *Position of the longitudinal (left) and transverse (right) laser sheets for the PIV experiments conducted under non-reactive conditions.*

It is useful to compare calculated and measured 1-D velocity profiles. Figure 3.6 shows the mean axial velocity in the central longitudinal plane $y = 0$ mm and at different heights z above the rod tip. LES calculations capture well the axial velocity up to $z = 20$ mm. The maximum axial velocity is located in the jet at $|r| = 5$ mm and is $U_z \simeq 15\ \mathrm{m \cdot s^{-1}}$. Above $z = 20$ mm, the agreement remains acceptable but the radial expansion of the flow is slightly underestimated by LES. Further comparisons are conducted by examining the root-mean-square (r.m.s) values of this flow field. These quantities are generally more difficult to capture by LES. Figure 3.7 shows the r.m.s axial velocity corresponding to the mean data plotted in Fig. 3.6. The measured r.m.s fluctuations feature high values for $|z| \simeq 3$ mm and $|z| \simeq 7$ mm that correspond to the positions of the ISL and OSL. The maximum value of the axial r.m.s velocity fluctuations is $U_z^{rms} \simeq 5\ \mathrm{m \cdot s^{-1}}$, which corresponds to 36% of the bulk flow velocity $U = 14\ \mathrm{m \cdot s^{-1}}$. LES predicts the position of these shear layers and the amplitude of the fluctuations. Discrepancies between measurements and simulations increase for $z > 20$ mm where the r.m.s fluctuations are underestimated for $|z| > 10$ mm.

Comparisons are now carried out for the transverse planes. Figure 3.8 shows the mean velocity component U_y in different transverse (X,Y) planes located at different heights z above the rod tip. We see that simulations reasonably capture the velocity profiles of U_y for distances above the rod tip up to $z = 15$ mm. Above this value, simulations overestimate the velocity.

The results presented above were averaged over a large number of realizations. Figure 3.9 (top) shows the evolution of the measured mean and r.m.s axial

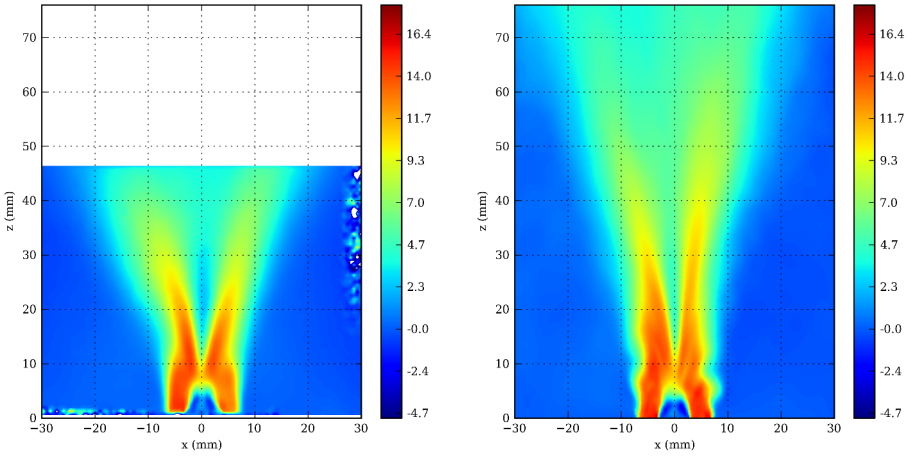

(a) PIV - U_z [m.s^{-1}] - Plane Y = 0 mm (b) LES - $\widetilde{U_z}$ [m.s^{-1}] - Plane Y = 0 mm

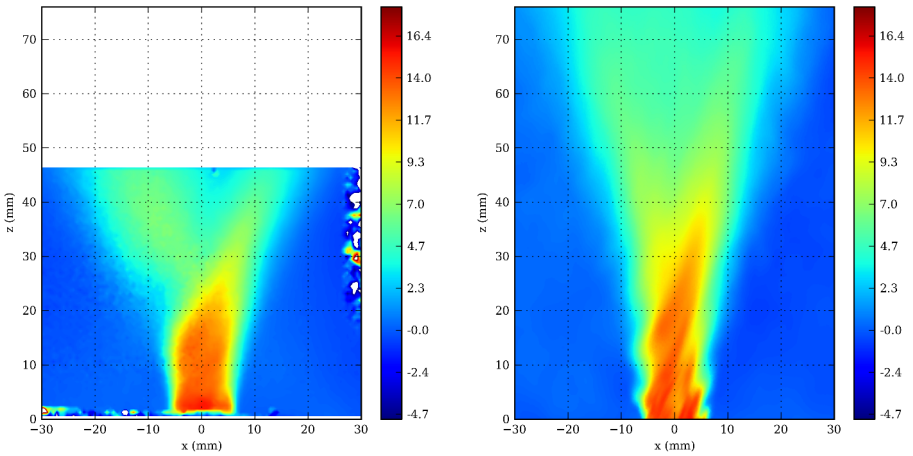

(c) PIV - U_z [m.s^{-1}] - Plane Y = 4 mm (d) LES - $\widetilde{U_z}$ [m.s^{-1}] - Plane Y = 4 mm

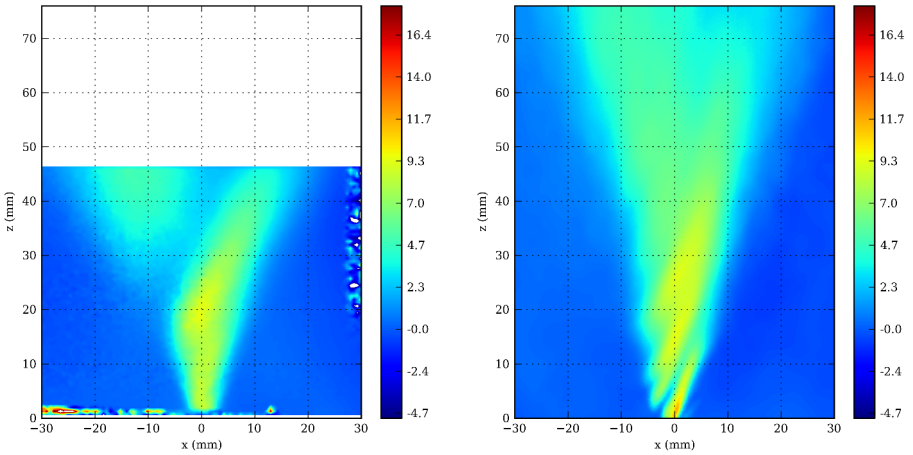

(e) PIV - U_z [m.s^{-1}] - Plane Y = 7 mm (f) LES - $\widetilde{U_z}$ [m.s^{-1}] - Plane Y = 7 mm

Figure 3.5: *2-D cuts of the mean axial velocity U_z in different longitudinal planes from PIV experiments (left) and LES calculations (right) under non-reactive conditions.*

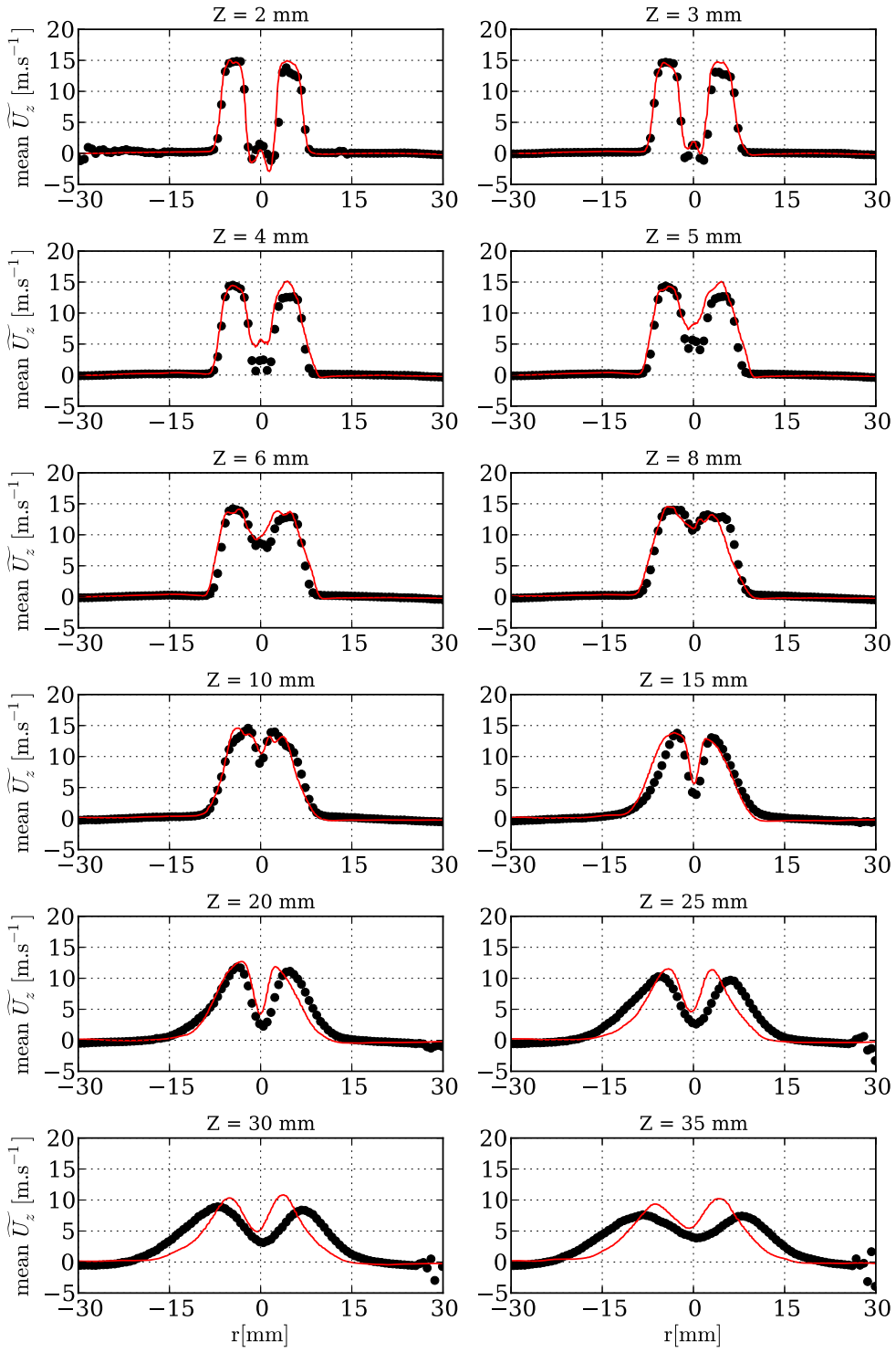

Figure 3.6: *1-D radial mean profiles of the axial velocity component U_z at different heights z above the bluff-body surface in the longitudinal plane $Y = 0$ mm. Red lines and black symbols respectively correspond to LES calculations and PIV measurements.*

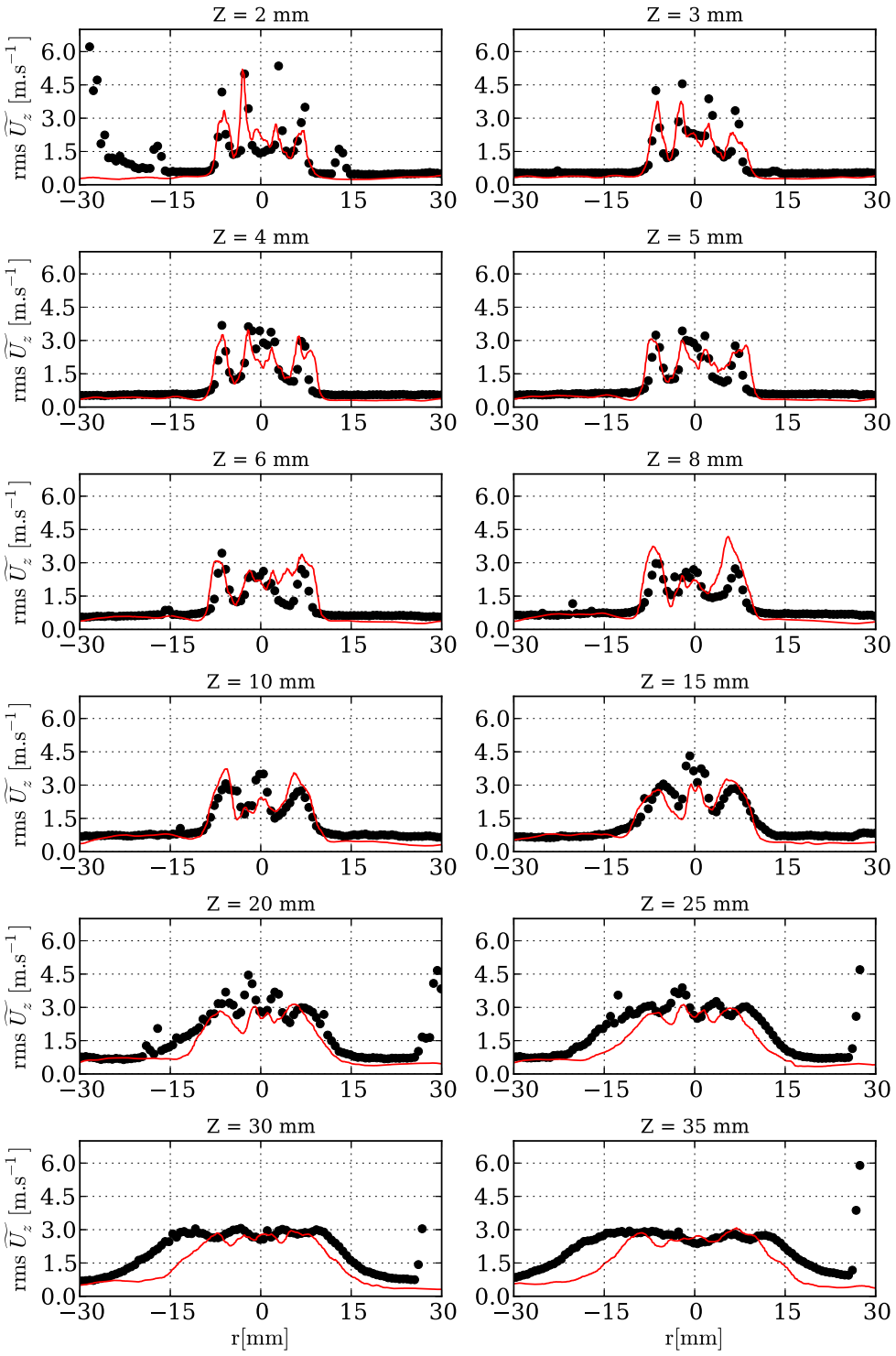

Figure 3.7: *1-D radial r.m.s profiles of the axial velocity component U_z at different heights z above the bluff-body surface in the longitudinal plane $Y = 0$ mm. Red lines and black symbols respectively correspond to LES calculations and PIV measurements.*

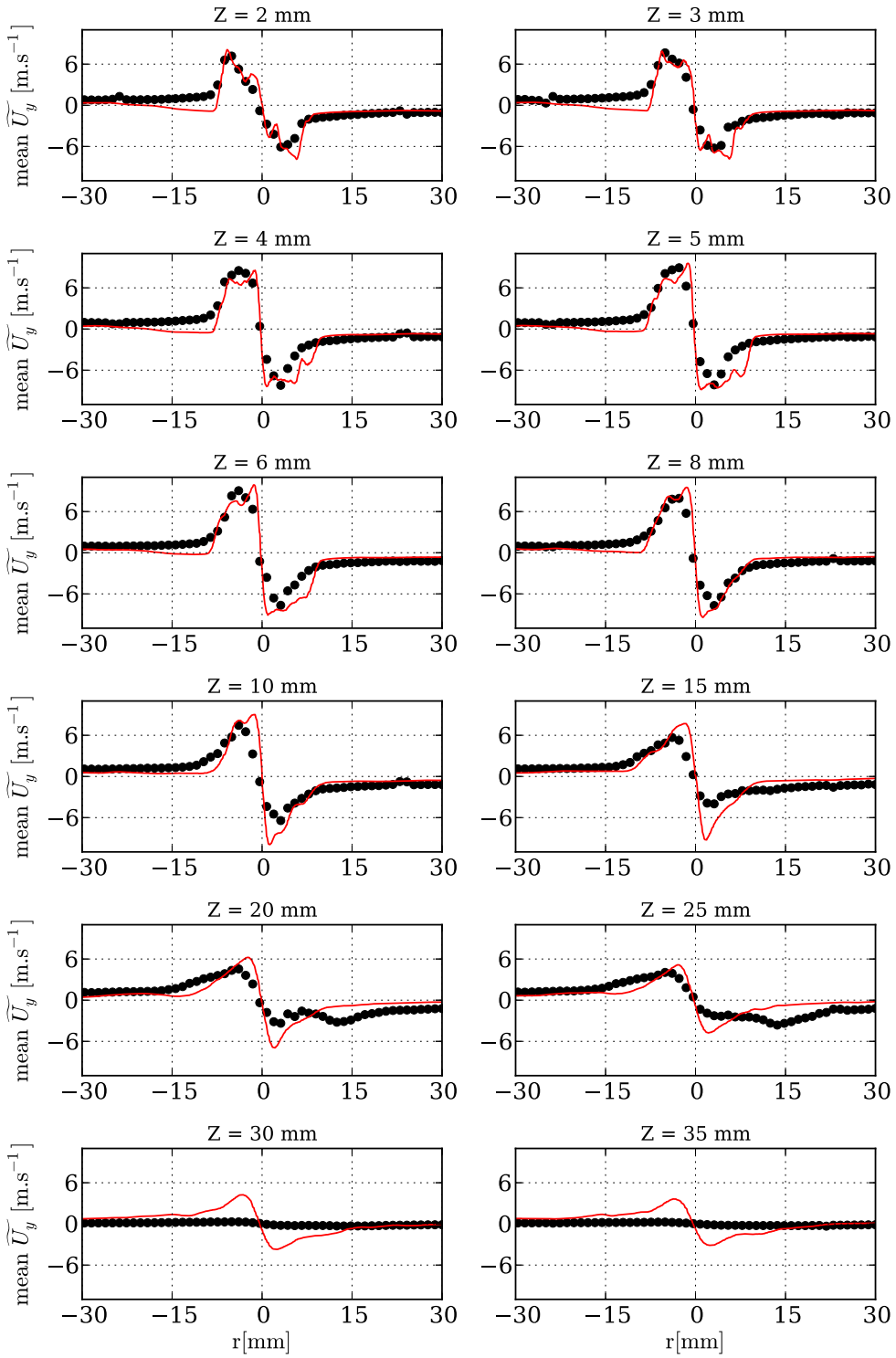

Figure 3.8: *1-D radial mean profiles of the orthoradial velocity component U_y at different heights z above the bluff-body surface in the longitudinal plane $Y = 0$ mm. Red lines and black symbols respectively correspond to LES calculations and PIV measurements.*

velocity at a given position in the ISL as a function of the number of PIV images used to obtain the average mean and r.m.s values for U_z. The statistical convergence of the mean velocity is achieved very rapidly. A 10% accuracy is obtained using less than 50 images. However it takes approximately 400 images to achieve a 10% accuracy on r.m.s values. We used a total of 818 PIV images to obtain the data plotted in Fig. 3.7. This number is large enough to ensure statistical convergence of the mean and r.m.s data in the ISL of the flow. Figure 3.9 (bottom) shows a similar analysis conducted in the OSL of the flow. In this case, 818 PIV images are also sufficient to obtain average quantities which are independent of the number of samples. The ISL and OSL being the two regions featuring the largest velocity fluctuations, it is assumed that the statistical convergence of these quantities is reached in the whole combustor using 818 images.

3.3 Thermal characterization of the combustor

3.3.1 From ignition to steady-state

The topology of swirling flames depends on the thermal state of the combustor that controls the temperature field and heat-fluxes to the boundaries. It is therefore necessary to control or to be able to characterize the thermal state of the combustor before conducting experiments in reacting conditions.

Four different phases may be defined for the operation of a combustor. First, the combustor is not in use and all components feature a temperature close to the ambient temperature. Then comes the ignition of the flame that is followed by a thermal transient during which the different parts of the combustor warm up. After a sufficient time and if operating conditions are unchanged, the temperatures of these different parts reach stable values. This is the steady state. Finally, the flame is blown away and the combustor cools until it reaches the ambient temperature again. During the combustor thermal transient, the temperature field within the chamber and heat fluxes to the boundaries change with time. This may in turn affect flame stabilization. It is then necessary to wait for a sufficient time to reach thermal steady-state before conducting experiments for steady flow operating conditions so that mean and r.m.s values of velocity, temperature, and species concentrations reach their steady state values.

The duration of this thermal transient depends on the combustor geometry and materials and operating conditions. To the leading order, it depends on the mass and heat capacity of the combustor material, the thermal power, and the flame temperature. It is not easy to precisely estimate the time that we must wait after ignition before running experiments. This duration was obtained

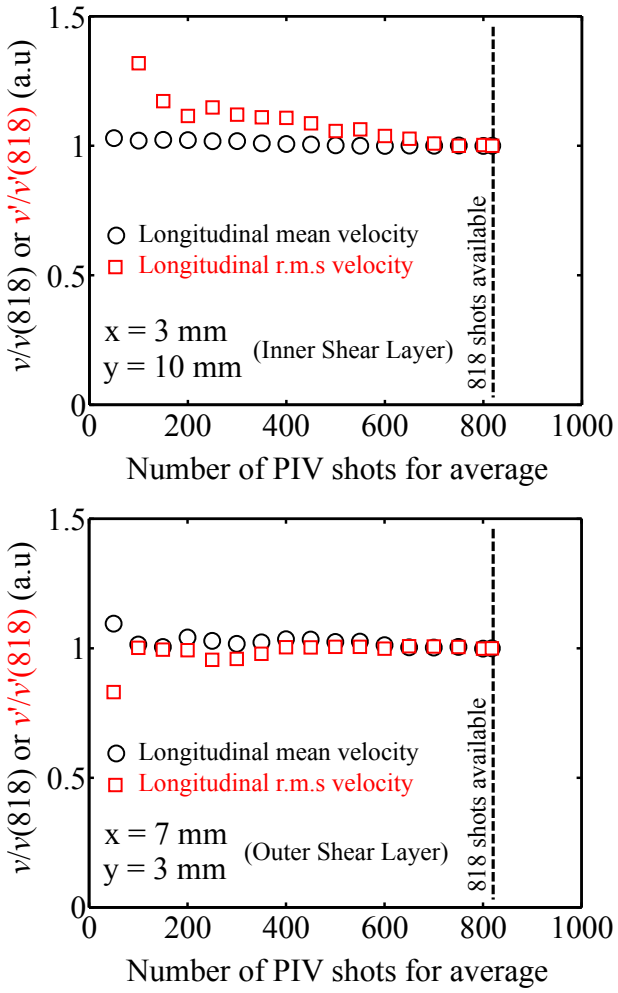

Figure 3.9: *Top: Evolution of the measured mean and r.m.s axial velocities at a given position in the ISL (top) and OSL (bottom) as a function of the number of PIV images used to obtain the average values.*

by recording the temporal evolution of the temperature at different locations within the combustor after ignition. The positions of the different temperature measurements are shown in Fig. 3.10. Temperatures close to the injector rim LIP_1 and on a quartz windows LIP_2 are measured by LIP. Two thermocouples TC_1 and TC_2 are installed at two different heights within a vertical steel bar holding the quartz windows. The gas temperature TC_3 in the ORZ and TC_4 at the outlet of the combustion chamber convergent exhaust are measured by thermocouples.

Figure 3.11 shows the temporal evolution of the temperature reached at different locations in the combustion chamber as a function of time. The instant $t = 0$ min corresponds to the ignition time of a CH_4/H_2/air flame at $P = 4$ kW,

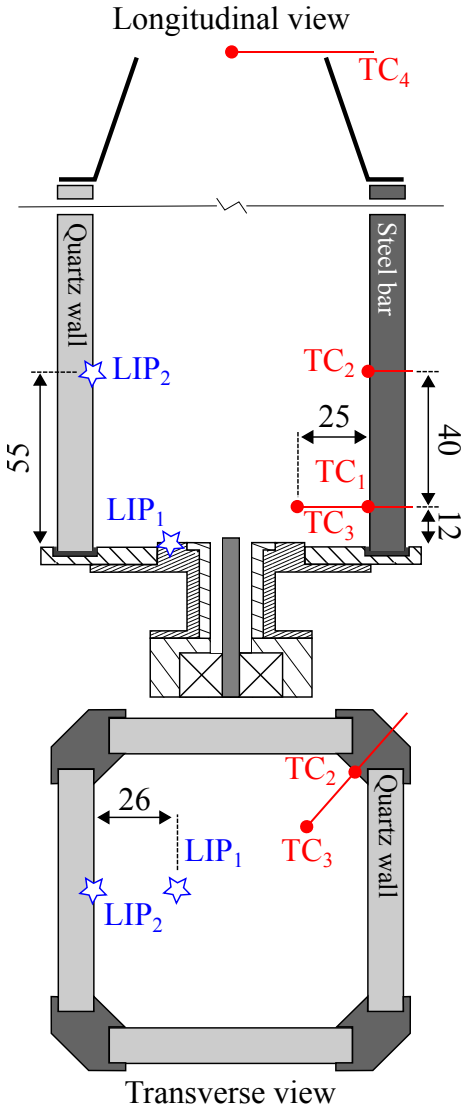

Figure 3.10: *Schematics of the combustor showing the location of LIP and thermocouple TC measurement points.*

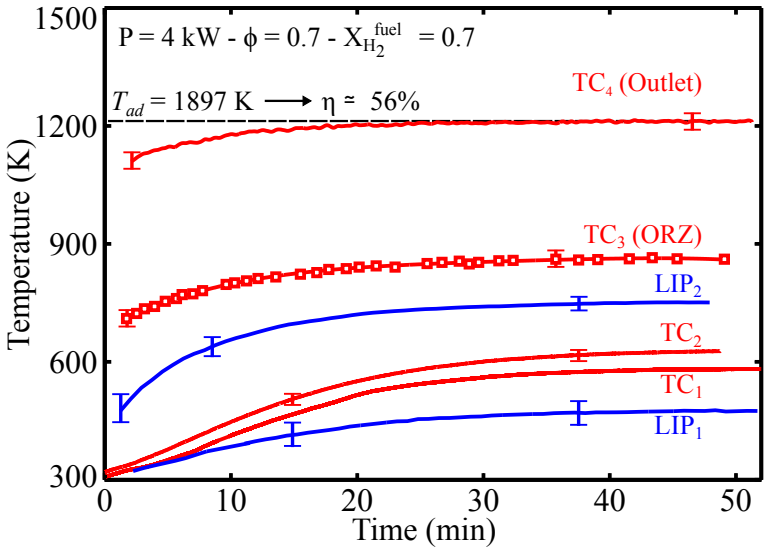

Figure 3.11: *Temporal evolution of temperatures reached at the locations indicated in Fig. 3.10 from ignition ($t = 0$) to steady-state ($t \simeq 45$ min) for a CH_4/H_2/air flame at $P = 4$ kW, $X_{H_2}^{fuel} = 0.70$, and $\phi = 0.7$.*

$X_{H_2}^{fuel}$ = 0.70, and ϕ = 0.7. The surface temperatures increase with time and reach stable values approximately 45 min after ignition. The surface temperatures at steady state depend on the position of the measurement, but they are always much lower than the adiabatic flame temperature T_{ad} = 1897 K. The gas temperatures in the ORZ and in the convergent exhaust also increase with time and they stabilize to constant values 45 min after ignition. It is then necessary to wait for at least 45 min after the ignition to start experiments at thermal steady state of the combustor.

The temperature TC_4 within the burnt gases exhausting the combustor is always lower than the adiabatic flame temperature T_{ad} = 1897 K. This is due to the heat transfers from the hot gases to the combustor walls and to the ambient air surrounding the combustor. It is possible to determine the thermal efficiency of the combustor η using the following expression:

$$\eta = \frac{TC_4 - T_u}{T_{ad} - T_u} \tag{3.2}$$

where $T_u \simeq 300$ K is the temperature of the fresh gases at injection. This efficiency η is a function of time and increases during the thermal transient. It reaches a stable value of $\eta \simeq 0.56$ at steady state after 45 min. This emphasizes the importance of heat losses in our combustor that cannot be considered adiabatic. This expression for η considers that cooled burnt gases have the exact same composition that the equilibrium composition of burnt gases at

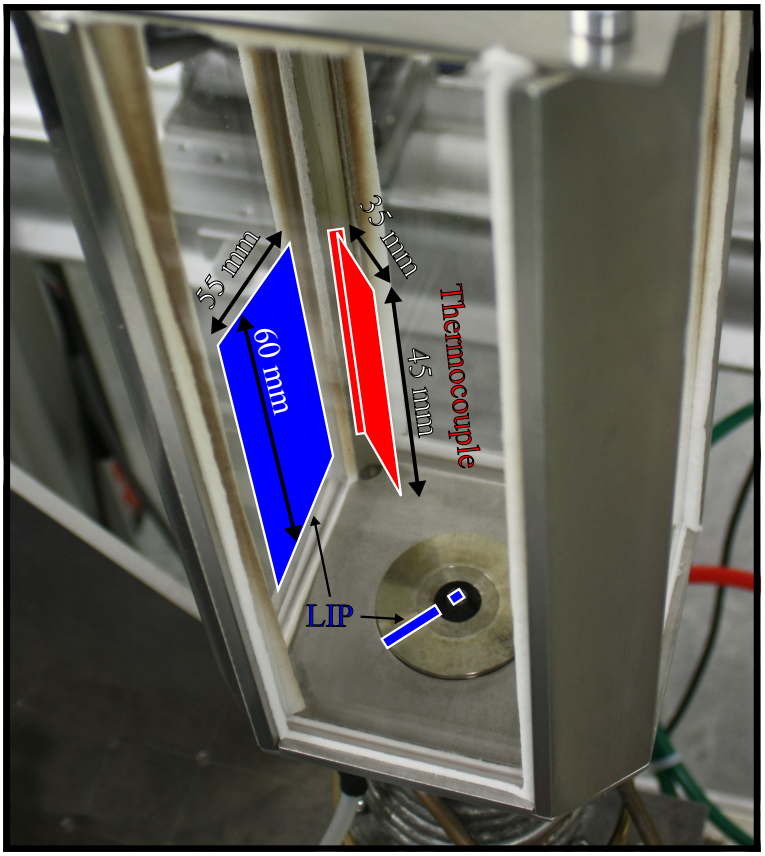

Figure 3.12: *Photograph of the combustion chamber showing the location of temperature measurements for the characterization of thermal boundary conditions of a $CH_4/H_2/air$ flame at $P = 4$ kW, $X_{H_2}^{fuel} = 0.60$, and $\phi = 0.7$.*

T_{ad} = 1897 K. It is therefore a rough approximation of the real thermal efficiency of the combustor.

3.3.2 Characterization at steady-state

Heat losses strongly alter the temperature field in the burnt gases and they are suspected to modify the behaviour of the flames. A deeper analysis of the thermal boundary conditions at steady-state is then conducted. Figure 3.12 shows the position of the temperature measurement points at different combustor wall surfaces and within the burnt gases. Thermal boundary conditions were carefully measured for the $CH_4/H_2/air$ flames at $P = 4$ kW and $\phi = 0.7$ and for two different hydrogen enrichments $X_{H_2}^{fuel} = 0.60$ and $X_{H_2}^{fuel} = 0.70$. We did not notice large differences for these two flames and only results for the flame at $X_{H_2}^{fuel} = 0.60$ are presented in this document.

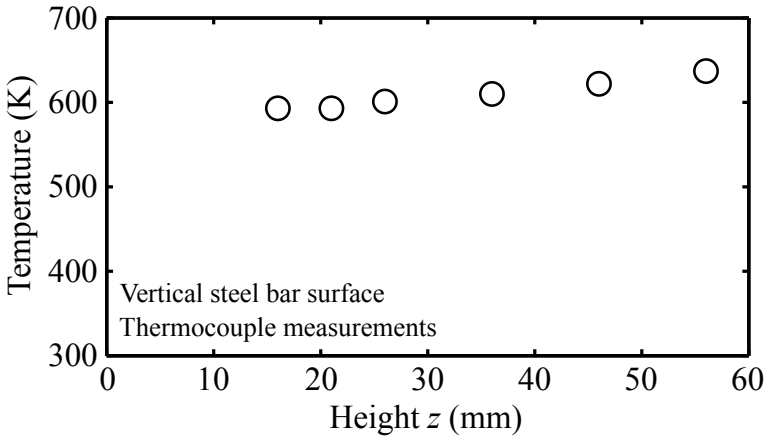

Figure 3.13: *Temperatures, measured with thermocouples located on the surface of a vertical steel bar, as a function of the height z above the rod tip. CH_4/H_2/air flame at P = 4 kW, $X_{H_2}^{fuel}$ = 0.60, and ϕ = 0.7.*

The axial temperature profile at the surface of one of the four vertical steel bars of the combustion chamber is shown in Fig. 3.13. The temperature is only a weak function of the height but it increases nearly linearly from T = 593 K at z = 16 mm to T = 637 K at z = 56 mm with the distance to the dump plate. Figure 3.14 shows the measured radial profile of the temperature at the surface of the injector and along the dump plane. These data were obtained by LIP measurements. The temperature linearly increases with the radial distance for $r > 7$ mm and ranges from T = 435 K at r = 7 mm to T = 516 K at z = 25 mm. The temperature on the rod tip surface is close to T = 500 K ± 50 K. This emphasizes the heat transfer taking place between the flame and the burnt gases filling the IRZ and the central rod tip that is cooled by the high velocity jet of fresh gases. The large uncertainty interval around T = 500 K is due to the large temperature gradient at the tip of the central rod.

Laser Induced Phosphorescence (LIP) was also used to measure the temperature at different positions on the surface of a quartz window. Figure. 3.15a shows the temperature for 30 measurement points regularly distributed over this surface. The wall temperature increases with the distance to the injector and is minimum close to the vertical steel bars featuring lower temperatures. Temperature differences along the X axis can reach ΔT = 27 K. Temperature differences along the Z axis can reach ΔT = 140 K. This figure also shows that the quartz window temperature is not uniform along the X and Z directions. A linear interpolation of these data shows that the temperature field is not perfectly symmetric with respect to the vertical symmetry axis of the window. This is attributed to the swirl motion of the flow. The swirling flow has an azimuthal velocity altering heat transfers to the walls. This analysis demonstrates the impact of swirl on the thermal state of the combustor walls.

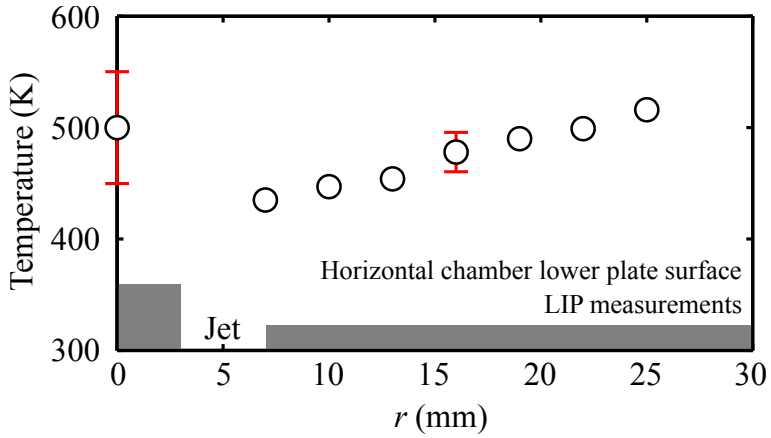

Figure 3.14: *Temperatures, measured by LIP on the dump plate as a function of the radial distance r. $CH_4/H_2/air$ flame at $P = 4$ kW, $X_{H_2}^{fuel} = 0.60$, and $\phi = 0.7$.*

These data were used by Mercier (2014) to compare with RANS and LES simulations. The temperatures in regions where temperatures were not measured are deduced by linear interpolation between the available data. Figure 3.16 shows the thermal boundary conditions that were retained for the simulations. For the sake of simplicity, effects of swirl on thermal boundary conditions (see Fig. 3.15b) were not considered in the simulations. The next step is to verify that the simulations including these thermal boundary conditions yield accurate burnt gas temperatures in the combustion chamber. The burnt gas temperatures measured in the ORZ with six small thermocouples penetrating through a steel bar of the combustion chamber (Fig. 3.12) are compared to calculated temperatures at the same positions in Fig. 3.17 with RANS calculations (ANSYS® Fluent®). RANS was used in this case to obtain rapidly a result and these numerical data were used to initiate more detailed LES calculations. Figure 3.17 shows that the non-adiabatic RANS simulations fed with measured thermal boundary conditions yield the correct temperature field in the ORZ. This allows more sophisticated calculations for the prediction of the flame behavior using LES.

3.4 Measurements on a reference flame

The above thermal analysis was used to infer the thermal behavior of the combustor during the thermal transient and at steady-state. It is now interesting to analyze the flow field of the flame of interest more specifically. Figure 3.18 shows an image of the mean chemiluminescence of the CH_4/H_2/air flame at $P = 4$ kW, $X_{H_2}^{fuel} = 0.60$, and $\phi = 0.7$ after Abel inversion. This flame is sta-

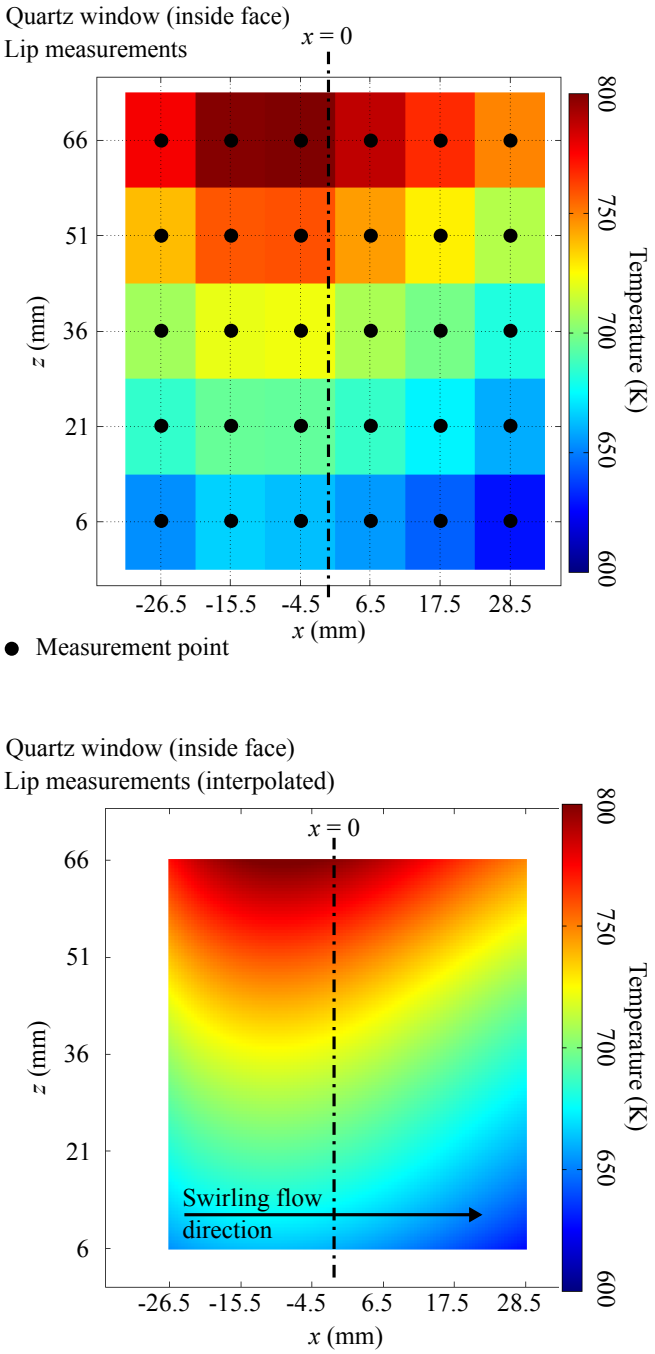

Figure 3.15: *Top: Temperature, measured by LIP at the inner surface of a quartz window of the combustion chamber, of a $CH_4/H_2/air$ flame at $P = 4$ kW, $X_{H_2}^{fuel} = 0.60$, and $\phi = 0.7$. Bottom: Linear interpolation of the data presented above.*

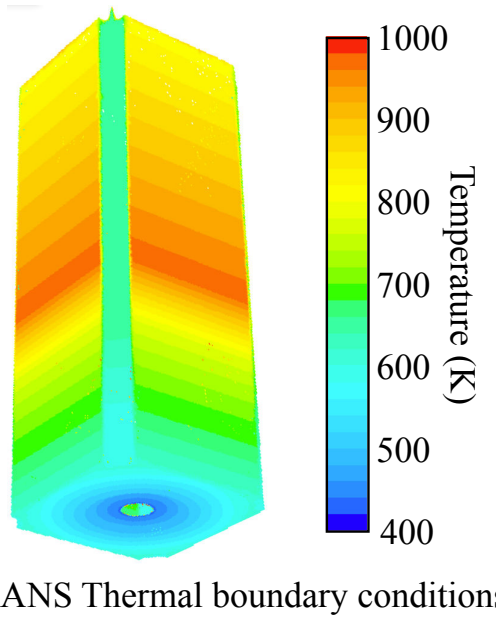

Figure 3.16: *Thermal boundary conditions used for RANS calculations of a CH_4/H_2/air flame at P = 4 kW, $X_{H_2}^{fuel}$ = 0.60, and ϕ = 0.7. These boundary conditions were deduced from measurements made for the same operating conditions.*

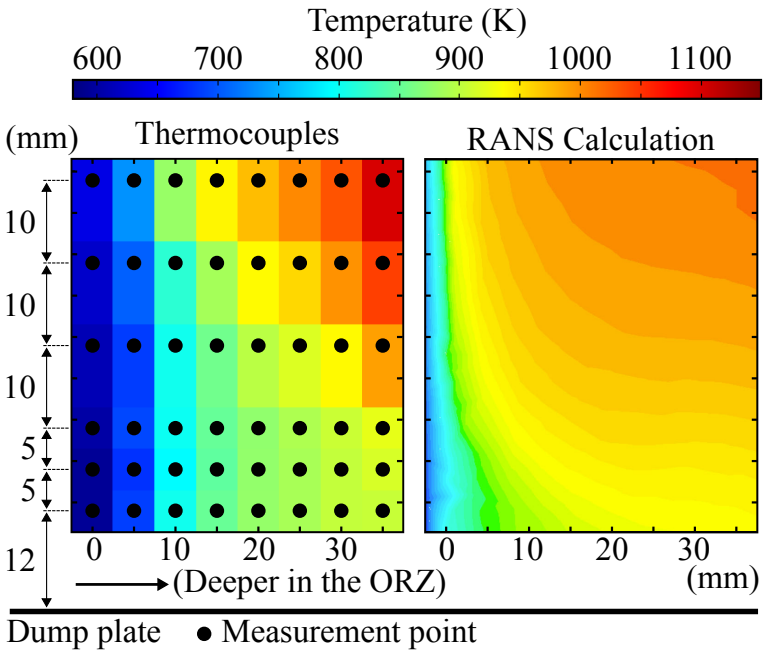

Figure 3.17: *Left: Temperature reached in the burnt gases located in the ORZ, measured by six movable thermocouples. CH_4/H_2/air flame at P = 4 kW, $X_{H_2}^{fuel}$ = 0.60, and ϕ = 0.7. Right: Temperature calculated by RANS at the same positions and for the same operating conditions.*

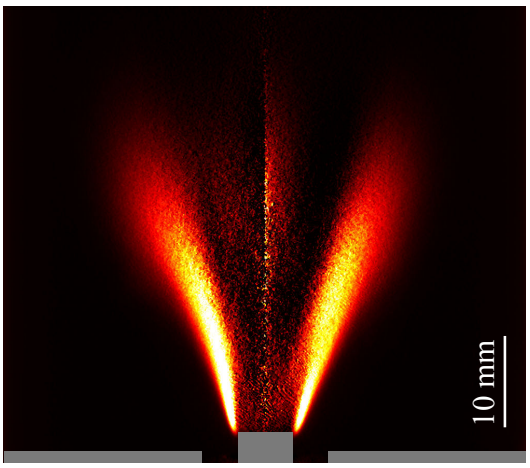

Figure 3.18: *Abel deconvoluted image of the mean OH* chemiluminescence intensity of a CH_4/H_2 flame at $X^f_{H_2}$ = 0.60, ϕ = 0.70, and U = 14.0 m · s^{-1}. Injector set in configuration A.*

bilized within the square combustion chamber when U = 14.0 m · s^{-1} and the injector set in configuration A. The swirl vane has a fixed angle θ = 35°. The swirl number of this flow was measured at the injector outlet without combustion chamber to confine the flow and is S = 0.4. In this case the flame has a V shape and is anchored at the tip of the central rod.

Figure 3.19 shows the radial profiles of mean axial, radial, and azimuthal velocity components measured by PIV when the reacting flow is seeded with solid particles. Axial and radial velocities are shown at different heights above the rod tip z = 2, 6, 10, 16, and 20 mm. Azimuthal velocities were measured at z = 6 mm and 16 mm in transverse planes. For z < 6 mm, the flow features a jet of high velocities (3 mm < $|r|$ < 7 mm) where v_z^{max} = 16.1 m · s^{-1} and an IRZ filled with burnt gases featuring negative axial velocities ($|r|$ < 2 mm) down to v_z = −2.2 m · s^{-1}. Above z = 10 mm, the IRZ of burnt gases ceases as the flow expands in the radial direction. Due to the thermal expansion of the gases, the magnitude of the axial velocity does not decrease when the distance to the rod tip increases. In the same time, the azimuthal velocity decreases with z and the swirl intensity decays with the distance to the rod tip. This phenomenom is well described by Syred and Beér (1974), Gupta et al. (1984), and Ishizuka (1990) and is due to dissipation effects.

OH-PLIF experiments were also carried out in the central (X,Z) longitudinal plane when y = 0. The instantaneous OH-PLIF images shown in Fig. 3.20 indicate that the flame is V shaped. There is no burnt gases signature in the OSL. Instantaneous images are averaged over 1425 shots and the probability of presence of burnt gases is deduced using the method described in Sec. 2.4.

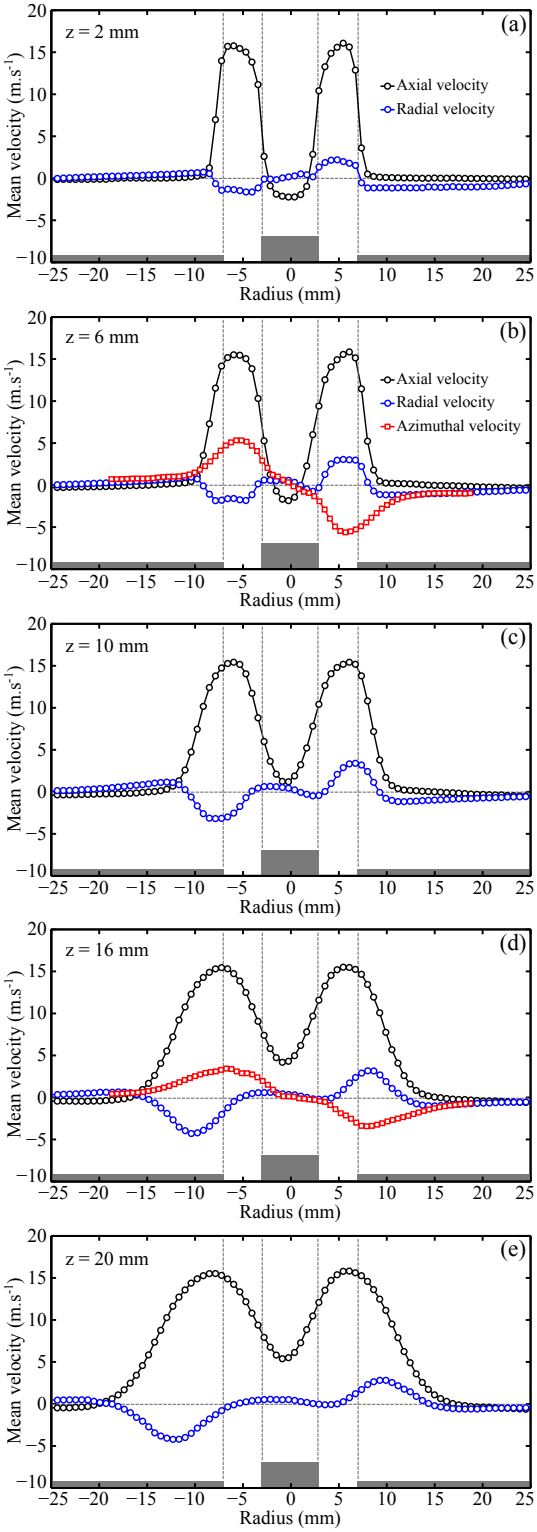

Figure 3.19: *(a)-(e) Mean axial and radial velocities in the longitudinal central plane and at different heights measured by PIV. The azimuthal velocity component, measured by PIV in transverse planes located* 6 mm *and* 16 mm *above the central rod tip, is also shown in (b) and (d).*

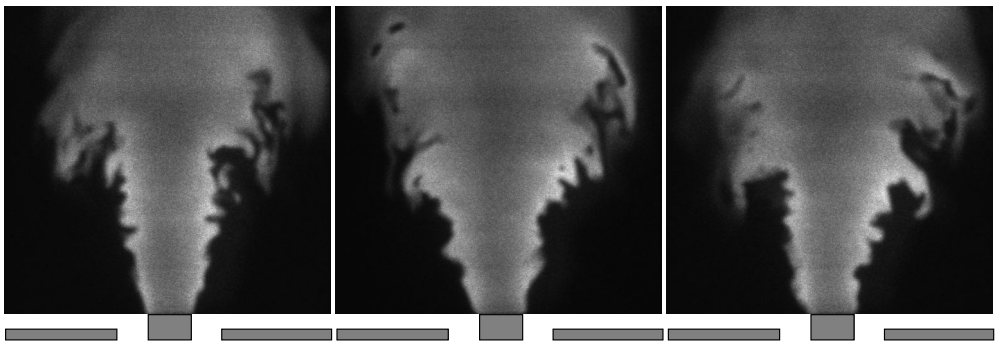

Figure 3.20: *Typical instantaneous OH-PLIF images. CH_4/H_2 flame at $X^f_{H_2} = 0.60$, $\phi = 0.70$, $U = 14.0\ \mathrm{m \cdot s^{-1}}$, and $S = 0.4$. Injector set in configuration A.*

The results, shown in Fig. 3.21, also indicate that the flame is V shaped in average. The burnt gases probability is 1 in the IRZ and fluctuates between 0 and 1 in the region surrounding the ISL. This is due to the fluctuation of the position of the flame front with time as shown in Fig. 3.20. This region featuring a burnt gases probability comprised between 0 and 1 represents the flame brush and is located at the same position as the high intensity region visible in the flame chemiluminescence image shown in Fig. 3.18. The burnt gases probability deduced from Fig. 3.21 is 0 in the ORZ.

This artefact can be explained a follows. Streamlines deduced from PIV measurements are superimposed on this image. These flow patterns clearly show that burnt gases are trapped within the flame brush and are then transported in the ORZ. As a consequence the ORZ must be filled with burnt gases and should therefore yield a probability of 1. This is also confirmed by previous measurements of the temperature taken by the gases within the ORZ (Sec. 3.3). This region is thus filled with burnt gases that are cooled due to heat losses. Figure 3.17 shows that the temperature of the gases in this region is lower than 1100 K. The chemical equilibrium of burnt gases is shifted towards H_2O due to the drop of enthalpy and the OH concentration is drastically reduced (Davidson et al. (1989) and Lam et al. (2013)). The burnt gases probability deduced from OH-PLIF images is falsely attributed to a zero value. Therefore, experiments based on OH-PLIF yield the probability of presence of burnt gases only when they are sufficiently hot.

In this section, the reference flame (CH_4/H_2/air flame at $P = 4$ kW, $X^{\mathrm{fuel}}_{H_2} = 0.60$, and $\phi = 0.7$) was used to characterize the combustor in terms of thermal boundary conditions and give examples of results that may be obtained using PIV and OH-PLIF. These results can now be used to analyse the stabilization of CH_4/H_2/air flames diluted with N_2 or CO_2 in more details.

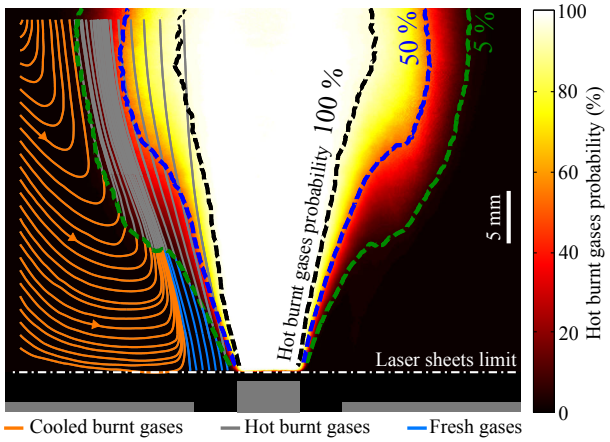

Figure 3.21: *Probability to find hot burnt gases for a CH_4/H_2 flame at $X^f_{H_2}$ = 0.60, ϕ = 0.70, U = 14.0 m · s^{-1}, and S = 0.4. Injector set in configuration A. Three isocontours (5%, 50%, and 100%) of the hot burnt gases probability are shown to ease visualization. Sample streamlines, obtained from PIV measurements in the central longitudinal plane, are also shown on the left side of the image. Streamlines are colored in blue, gray, and orange in the fresh gases, hot burnt gases, and cooled burnt gases.*

The swirl was characterized for two injector configurations A (14 mm annular injector with a 6 mm central rod) and B (12 mm cylindrical injector without the central rod). In configuration A, adjustable blade angles ranging from θ = 29° to θ = 38° were used, yielding swirl numbers varying from S = 0.3 to S = 0.4. In the same configuration, a fixed blade angle θ = 35° was also used, yielding a swirl number S = 0.4. In configuration B, a swirl number S = 0.68 was obtained with a blade angle of θ = 61°.

A reference flame was then analyzed when the injector is set in configuration A with θ = 35° and S = 0.4 for a CH_4/H_2/air mixture with $X^f_{H_2}$ = 0.60, ϕ = 0.70, and U = 14.0 m · s^{-1}.

The flow field in the absence of combustion was characterized by PIV yielding mean and r.m.s values of the 3-D velocity components. Then thermal boundary conditions were characterized during a thermal transient and at steady state by thermocouples and LIP measurements. These data were used to initiate LES calculations of this reference flame in a companion study (Mercier (2014)). The flow field with combustion was also characterized by PIV and radial profiles of mean axial, radial, and azimuthal velocity components were presented. Finally, images of the flame were captured by chemiluminescence and OH-PLIF measurements. These images indicate that the reference flame is V shaped.

Part II

Stabilization of confined premixed CH_4/H_2/air swirling flames

Chapter 4

Analysis of topology transitions of swirled flames interacting with the combustor peripheral wall

The focus of the present chapter is to analyze topological bifurcations of swirled premixed flames impinging the combustion chamber peripheral wall.

Mechanisms controlling flashback of flames along a solid wall are rapidly reviewed in section 4.1. The experimental setup and the diagnostics used to examine V/M flame topology transitions are presented in section 4.2. Structures of V and M stable flames are described in section 4.3 for two configurations of the injector. A typical intermittent regime is also studied at the end of this section where the flame switches alternatively between V and M shapes. A model for delineating the boundary of V to M flame topology bifurcation is proposed in section 4.4. Predictions are compared to measurements in section 4.5 for two different injection systems by varying the swirling rate, combustible mixture injection velocity, equivalence ratio and hydrogen enrichment in the combustible mixture. Results are analyzed in terms of dimensionless products.

4.1 Flashback in the boundary layer of swirled flames

Flashback of laminar flames propagating in tubes is a well characterized phenomenon (Lewis and Von Elbe (1987)). It has been shown that flashback of the flame tip takes place in the boundary layer along a combustor wall when the axial velocity gradient at the wall $g = \partial u/\partial y$ becomes lower than a critical value of the order of S_L/δ_b, where $u(y)$ is the velocity component parallel to the wall, y denotes the normal distance to the wall, S_L indicates the laminar burning velocity and δ_b stands for the quenching distance between the flame tip

and the wall. This model has been extensively used in laminar flows and was also generalized to turbulent configurations by replacing the laminar burning velocity S_L with different expressions for the turbulent flame speed S_T (see for example Khitrin et al. (1965), Syred et al. (2012), Eichler and Sattelmayer (2011)). Recent experiments of Eichler and Sattelmayer (2011) have revealed the strong sensitivity of flashback to the external pressure gradient for flames stabilized in turbulent boundary layers. Direct simulations also indicate that gas expansion strongly modifies the structure of the turbulent boundary layer ahead of the flame front and the shape of turbulent premixed flames in wall boundary layers (Gruber et al. (2012), Gruber et al. (2014)). In many situations, it is however possible to analyze this transition by examining a Karlovitz number Ka= $g\delta_b/S_L$ (Karlovitz et al. (1953)) based on the velocity gradient at the wall g and the quenching distance δ_b. When Ka < Ka_c, where Ka_c denotes a critical value, flashback occurs and the leading edge front of the flame propagates upstream in the boundary layer.

Kurdyumov et al. (2000) and Kurdyumov et al. (2007) analyzed numerically and experimentally transitions to flashback in laminar channel flows for isothermal and adiabatic wall conditions. They showed that in both cases the critical value Ka_c strongly depends on the Lewis number Le of the reactive mixture. Flashback is highly promoted for mixtures featuring small values of the Lewis number as in the case of use of hydrogen. Based on this observation, Syred et al. (2012) recently suggested different solutions to minimize flashback in swirling injectors for burners operated with a range of hydrogen fuel blends. Different mechanisms leading to flashback were identified in turbulent swirling flows. Sommerer et al. (2004) list five possibilities: flashback by autoignition, flashback in the boundary layer, turbulent flame propagation in the core flow, combustion instabilities leading to flashback and flashback induced by vortex breakdown. While flashback along the boundary layer is not the predominant mechanism observed in premixed swirling combustors (Plee and Mellor (1978)), it appears that there are yet no systematic study of effects of swirl on this phenomenon. It also worth noting that studies on flashback generally deal with the flashback of the swirling flame root, *i.e* the leading edge flame element within the swirling flow. The problem which is addressed here is the flashback of the swirling flame tip along the boundary layer of a wall, *i.e* the rear edge of the flame.

For a swirled flame tip impinging a wall, it is reasonable to assume that flashback is *a priori* a function of the combustible mixture Lewis number as for laminar flames and of the swirling rate because it is known that the flame displacement speed in a vortex core strongly depends on the azimuthal velocity component (Ishizuka (2002)). In the experiments conducted in this study, these problems are considered by varying the combustible mixture Lewis number and swirl number.

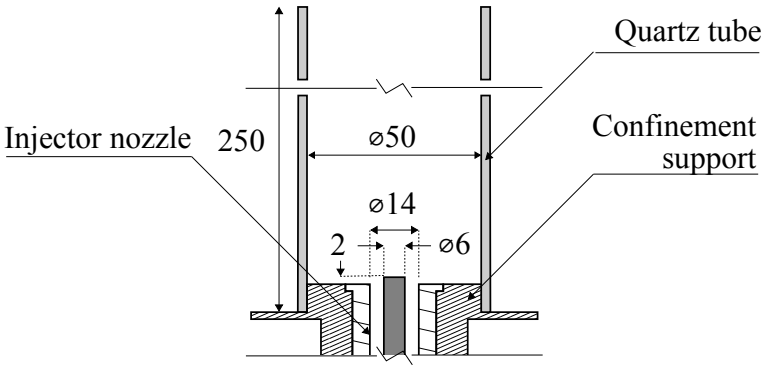

Figure 4.1: *Schematics of the burner equipped with a* 50 mm *diameter cylindrical confinement chamber. Dimensions are in mm.*

4.2 Experimental setup

The test rig used in this chapter is presented in Fig. 4.1. The flames are confined by a quartz tube of 50 mm internal diameter and 250 mm height exhausting to the atmosphere. The flow is put in rotation by the radial swirling vane with movable blades installed at the bottom of the injection tube and shown in Fig. 4.2. A central rod of D_r = 6 mm diameter crossing the swirler helps stabilizing the flames at the injection tube outlet 2 mm above the injection plane. This central element can also be removed to analyze swirled flames stabilized aerodynamically. A schematic of the injection units with (configuration A) and without the central rod (configuration B) is presented in Fig. 1.11. Without central rod, the combustible mixture injection tube is slightly smaller and has a diameter D_i = 12 mm.

Different values of swirl number S can be set using the remote step motor controlling the trailing edge blades angle θ of the swirler. Experiments are conducted for six values of the swirl numbers S corresponding to different blade angles θ presented in Tab. 4.1. For the highest swirling rate, when S_6 = 0.68, it was necessary to remove the central rod and reduce the injection tube diameter to D_i = 12 mm to observe V to M flame shape bifurcations. The flame is in this case aerodynamically stabilized above the injection nozzle. For all other cases, when the swirl number is reduced, the injector was set in configuration A and flames remained anchored on the tip of the central rod.

The hydrogen enrichment in the combustible mixture is expressed by the molar fraction of hydrogen $X_{H_2}^{fuel}$ in the CH_4/H_2 fuel mixture. The Lewis number Le of this mixture is used to characterize effects of fuel composition. V to M flame topology transitions are detected by imaging the flame chemiluminescence with a Pulnix TMC-6 color 752(H)x582(V)-pixels^2 CCD camera operating at a frame rate of 50 images per second without specific interference filters in front of the

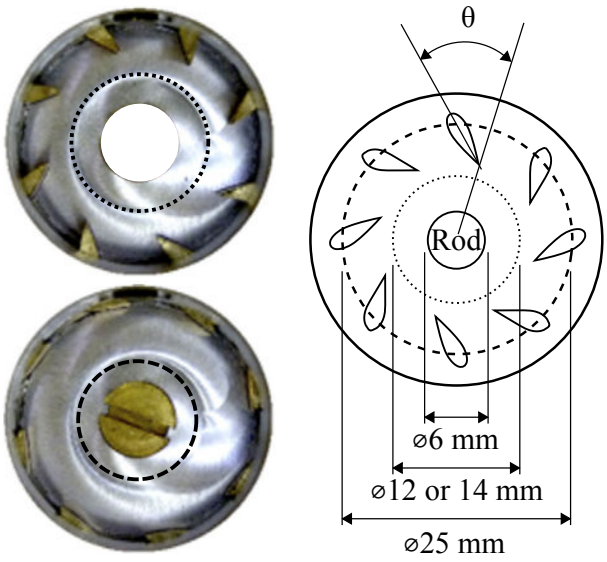

Figure 4.2: *Left: top views of the adjustable swirler for a blade angle θ = 23° (top) and θ = 61° (bottom) (Durox et al. (2013)). The black dotted and dashed circles represent the* 14 mm *(configuration A) and* 12 mm *(configuration B) injection tube diameters respectively. The central hole is crossed by the rod in configuration A and obstructed by a screw in configuration B. Right: Schematic with the main dimensions of the swirler.*

Table 4.1: *Swirl numbers S measured at the injection tube outlet by varying the blade angle θ and the geometrical configuration of the injector.*

k	1	2	3	4	5	6
S_k	0.30	0.32	0.35	0.37	0.40	0.68
θ_k	29°	30°	32°	35°	38°	61°
$D_i\,(mm)$	14	14	14	14	14	12
$D_r\,(mm)$	6	6	6	6	6	0

glass lens of the camera. An additional high speed CMOS camera (FASTCAM ultima APX i^2) is also used for a few operating conditions to characterize intermittent transitions between the flame shapes.

In the absence of combustion and without flame tube, velocity profiles at the outlet of the injection tube were measured by LDV (see Sec. 2.1) for the different swirl numbers indicated in Tab. 4.1 and over a wide range of bulk injection velocities $7\,\mathrm{m\cdot s^{-1}} < U < 25\,\mathrm{m\cdot s^{-1}}$. A PIV system (see Sec. 2.5) is also used to examine the velocity field in an axial plane along the burner symmetry axis with combustion when the flame tube is set in place. Due to the cylindrical flame tube, laser reflections are numerous and disturb visualizations, particularly close to the quartz tube boundaries. It was thus difficult to collect

workable information over the entire flame region. In particular, it was not possible to measure the velocity near the quartz wall.

These measurements are completed by OH-PLIF (see Sec. 2.4) conducted in the same vertical plane to infer the location of the flame and burnt gases in the Outer Recirculation Zone of the flow (ORZ). The laser is tuned to the $Q_1(1)$ transition of the (1,0) band of the $A^2\Sigma$ - $X^2\Pi$ system of OH at 281.91 nm. This line features a strong fluorescence signal for the temperatures of the flames of interest as well as for the lower temperatures reached by the burnt gases in the ORZ. Fluorescence is imaged onto a 512(H)x512(V)-pixels^2 intensified CCD camera (ICCD, Princeton Instruments PIMax) equipped with a 10-nm bandpass filter (2BPA313-88SA-02 Asahi Spectra Co.) centered on 313 nm in addition to a 40-nm bandpass filter (FF01-320/40 Semrock) centered on 320 nm. These filters were used to reduce interferences with the fluorescence signal from the solid surfaces, *i.e* the quartz tube, located close to the flame region. This difficulty cumulated with the numerous laser reflections in the cylindrical cavity led to setting with an important reduction of the available laser energy for OH excitation.

4.3 Structure of V and M flames

The scope of this section is to describe the aerodynamics and flame topologies of typical V and M flames stabilized in the setup with the different injectors. A regime featuring intermittent V and M states is then described using fast imaging.

4.3.1 Swirled flames stabilized by the central rod

Figure 4.3 shows inverse Abel deconvoluted images of typical V and M flames with the injector set in configuration A. These images were obtained by recording the broadband chemiluminescence of the flame with the CCD camera and were averaged over 120 instantaneous snapshots. The hydrogen enrichment $X_{H_2}^{fuel}$ = 0.22 in the CH_4/H_2/air combustible mixture, swirl number S_5 = 0.40 and bulk flow velocity U = 24.5 m $\cdot$ s^{-1} are the same, but the V flame is obtained for an equivalence ratio ϕ = 0.58 and the M flame is observed for ϕ = 0.79.

The V flame is anchored on the central rod tip and features a flame front in the Inner Shear Layer (ISL) between the swirling jet of reactants and the Inner Recirculation Zone (IRZ) filled with burnt gases. The region delineated by the white dashed triangle in the left image in Fig. 4.3 indicates that there is no strong interaction of this V flame with the ORZ. The M flame in the right image in Fig. 4.3 is also stabilized in the wake of the bluff-body, but features a supplemental reaction layer in the Outer Shear Layer (OSL) penetrating the ORZ. As a consequence, the M flame is more compact than the V flame and

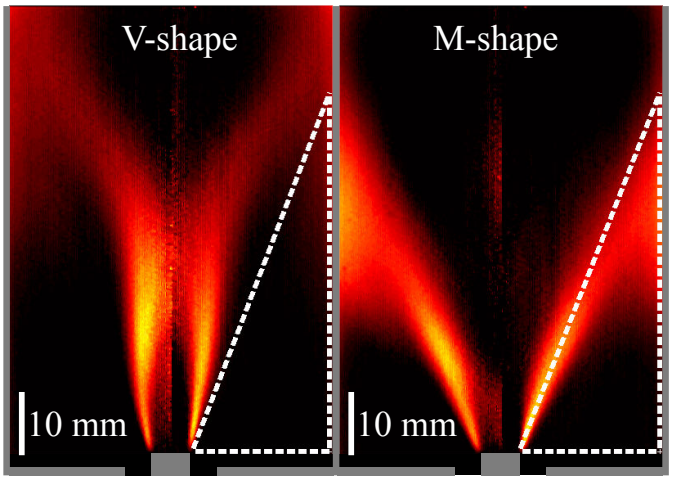

Figure 4.3: *Inverse Abel transformed images of swirled flames stabilized by the central rod (injector in configuration A). Swirl number* $S_5 = 0.40$*, hydrogen enrichment* $X_{H_2}^{fuel} = 0.22$ *and injection bulk velocity* $U = 24.5\ \mathrm{m \cdot s^{-1}}$*. Left : V flame at* $\phi = 0.58$*. Right : M flame at* $\phi = 0.79$*.*

features a wider IRZ but a shorter ORZ as already observed by Wicksall et al. (2005). The flame angle of the reaction layer in the ISL increases thus drastically (with respect to the main flow direction) in the case of an M flame. This observation slightly differs with the simulations presented by Huang and Yang (2004) where the flame angle decreased during the transition from a V to an M flame and also with the simulations presented by Tay Wo Chong et al. (2009) where the transition had no influence on the flame angle in the ISL. It is however worth noting that the geometrical and flow configurations simulated in these studies are also quite different from those investigated here.

The velocity field associated to V to M swirled flames anchored on the central rod is now examined. Figures 4.4a and 4.4b show the trace of the mean velocity field in the axial plane of the burner obtained by averaging over 200 instantaneous PIV measurements conducted under reacting conditions. The conditions explored correspond to a swirl number $S_5 = 0.40$, a hydrogen enrichment $X_{H_2}^{fuel} = 0.09$, and a bulk injection velocity $U = 14.0\ \mathrm{m \cdot s^{-1}}$. The flow field in Fig. 4.4a is associated to a V flame obtained for $\phi = 0.60$. Figure 4.4b shows drastic changes of this flow field when the equivalence ratio is slightly increased to $\phi = 0.64$, all other conditions remaining identical. The flame has in this case an M shape. These operating conditions are different than those presented in Fig. 4.3 to highlight that V and M flame topologies can be found for a wide range of operating conditions.

The different regions of the flow in Fig. 4.4 are indicated by overlaid color contour plots of the velocity. The red contours indicate the structure of the

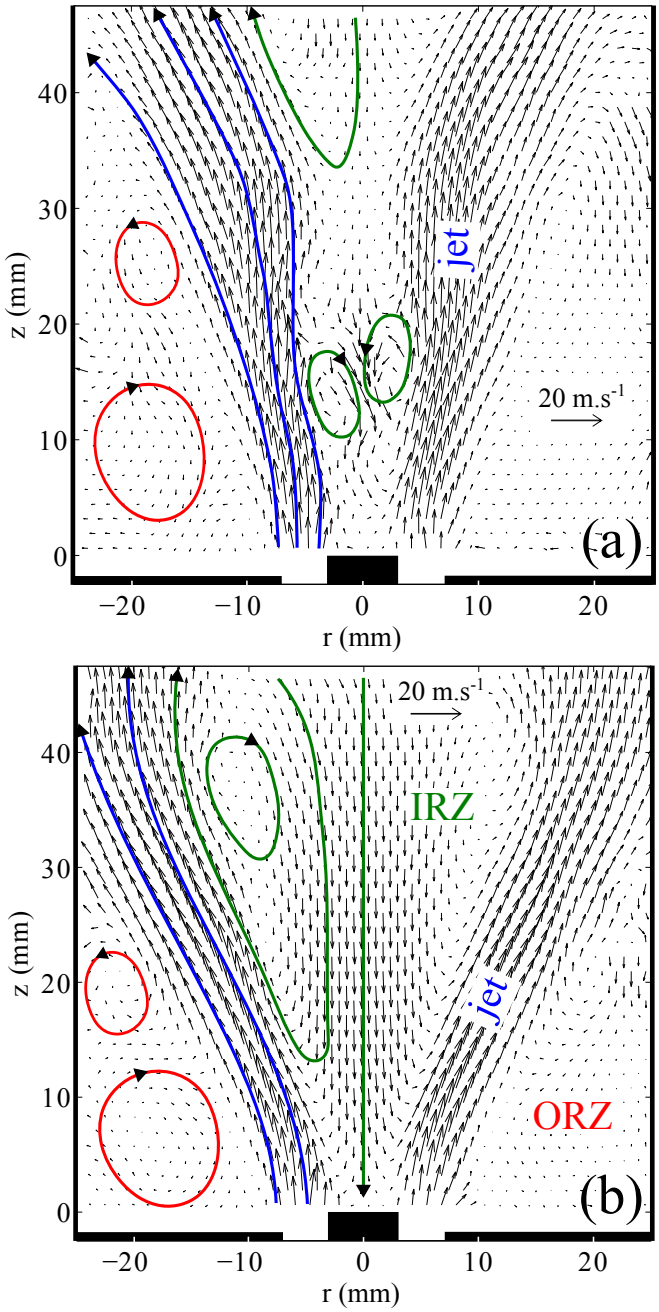

Figure 4.4: *Velocity fields of swirled flames anchored on the central bluff body (injector in configuration A). Swirl number* $S_5 = 0.40$*, hydrogen enrichment* $X_{H_2}^{fuel} = 0.09$*, injection bulk velocity* $U = 14.0\,\mathrm{m \cdot s^{-1}}$*. (a) V flame at* $\phi = 0.60$*. (b) M flame at* $\phi = 0.64$*. Different regions of the flow are colored: jet of reactants (blue), IRZ (green), and ORZ (red). Vector spacing is artificially increased to* 1.27 *mm to clarify the plots. Left and right image boundaries delineate the flame tube made of quartz.*

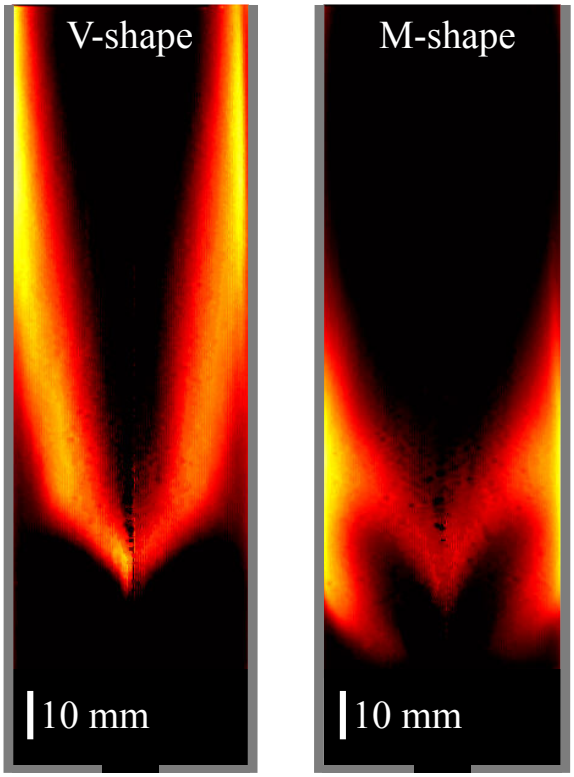

Figure 4.5: *Inverse Abel transformed images of swirled flames stabilized aerodynamically (injector in configuration B). Swirl number* $S_6 = 0.68$*, hydrogen enrichment* $X_{H_2}^{fuel} = 0$*, injection bulk velocity* $U = 13.7\ \mathrm{m \cdot s^{-1}}$*. Left : V flame at* $\phi = 0.53$*. Right : M flame at* $\phi = 0.60$*. The left and right image boundaries correspond to the flame tube in quartz.*

velocity in the ORZ, the blue color is associated to velocity contours of the swirling jet of reactants and the green color shows the structure of the mean flow in the IRZ. Note that these contours do not correspond to streamlines due to the strong azimuthal component of the flow imparted by the swirler. The V and M flames feature both a jet of high velocity, an IRZ, and an ORZ. The shape of the flame strongly modifies the size of the IRZ for about the same flow injection conditions. Its width increases largely in the case of an M flame. The ORZ, that includes two counter-rotating vortices in both cases explored, is also modified and is shortened for the M flame. In both cases, the jet impinges the combustor peripheral wall with relatively high velocities. This is an important feature of the V and M swirled flames investigated in this study. V to M topological transitions of the flame tip will be shown to be controlled by flashback of the flame tip along the boundary layer of the quartz tube.

4.3.2 Swirled flames stabilized aerodynamically

At higher swirling rates, flames can be stabilized aerodynamically away from solid elements of the injector without the help of a central bluff body. This stabilization mode is possible when the swirl number exceeds a certain threshold value associated to a vortex breakdown of the flow along the burner axis (Gupta et al. (1984)). Although the apparition of this hydrodynamic instability slightly depends on the flow and injector configurations (Syred and Beér (1974)), it is generally admitted that flows with swirl numbers larger than $S = 0.6$ feature an IRZ that is favorable to stabilize flames aerodynamically.

Figure 4.5 shows the same type of flame images as in Fig. 4.3 but for the injector set in configuration B. Images have been averaged here over 275 snapshots. These CH_4/air flames are aerodynamically stabilized for a swirl number $S_6 = 0.68$ and a bulk injection velocity $U = 13.7\,\mathrm{m\cdot s^{-1}}$. The leanest flame $\phi = 0.53$ has a V shape and the slightly richer flame at $\phi = 0.60$ takes an M shape as already observed in Fig. 4.3 for another combustible mixture, swirling rate, injector configuration, and bulk flow velocity. The velocity field is not presented for these aerodynamically stabilized swirling flames, but Fig. 4.5 clearly indicates that the swirling jet exhausting the injector impinges the quartz tube with relatively high velocities in both V and M flame cases.

This hierarchy between lean V and M flame topologies is always observed for all geometrical configurations of the injector, combustible mixtures and injection conditions explored. The probability of stabilizing an M flame always increases for lean flames with equivalence ratios closer to unity. Note however that the focus was set in this study on lean flame topologies relatively away from stoichiometry and a systematic study was not carried out for lean flames with equivalence ratios very close to unity or sligthly rich flames.

4.3.3 Flame stabilization in the OSL

Conditions for the stabilization of a reaction layer in the OSL are now examined in more details. Figure 4.6a and b show two examples of instantaneous OH-PLIF images for the M flame described in Fig. 4.4b. The image on the right of the axis in Fig. 4.6b does not correspond to the same instant as the image on the left of the axis in Fig. 4.6a. One notices a strong fluorescence signal close to the region where the high velocity jet interacts with the quartz wall indicating that a flame front is hosted in this region. This reaction layer also extends in the OSL and progresses upstream along the swirling jet of reactants towards the external rim of the injector nozzle. In some cases, this supplemental reaction layer lies very close to the injection rim as in Fig. 4.6b.

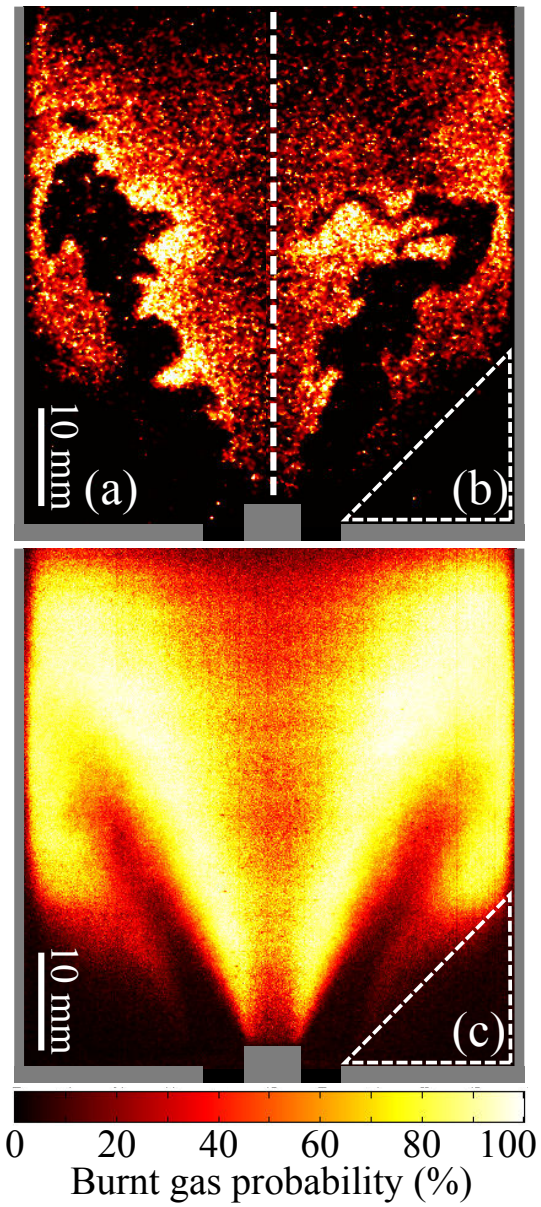

Figure 4.6: *(a)-(b) Examples of instantaneous OH-PLIF images for the M flame described in Fig. 4.4b (injector in configuration A). The image on the right of the axis does not correspond to the same instant as the image on the left of the axis . (c) Average image over 200 binarized OH-PLIF shots yielding the probability of presence of burnt gases. Swirl number* $S_5 = 0.40$*, hydrogen enrichment* $X_{H_2}^{fuel} = 0.09$*, bulk injection velocity* $U = 14.0\ \mathrm{m \cdot s^{-1}}$ *and equivalence ratio* $\phi = 0.64$.

The OH fluorescence signal gives an indication on the flame front location and the burnt gases location at elevated temperatures (Sadanandan et al. (2008), Stöhr et al. (2011)). After binarization of 200 instantaneous OH-PLIF shots, an average image yielding the probability of presence of burnt gases is plotted in Fig. 4.6c. This image clearly highlights the M shape statistically taken by the flame that stabilizes both in the ISL and OSL. One should also note that the zone delimited by the dashed triangle in Figs. 4.6b and 4.6c is filled with burnt gases even if the probability of presence of burnt gases deduced from the exploitation of OH-PLIF images yields a low value. In this zone, the burnt gases recirculate close to the combustor walls as shown in Fig. 4.4 and are cooled due to heat losses. The chemical equilibrium of burnt gases is shifted towards H_2O due to the drop of enthalpy and the OH concentration is drastically reduced (Davidson et al. (1989) and Lam et al. (2013)). Consequently, the OH-PLIF signal drops rapidly, yielding an incorrect indication of the burnt gases probability. Another possible explanation is that the equilibrium is shifted towards H_2O due to heat losses in this region where the residence time of burnt gases is high and the OH concentration is reduced. This phenomenon also yields a lower OH-PLIF signal.

It is difficult to interpret the signal near the flame tip in the instantaneous images in Figs. 4.6a and 4.6b and identify topology transitions with these diagnostics at a limited repetition rate. These transitions are detected using high speed visualizations of the flame chemiluminescence with a high speed CMOS camera. Figure 4.7 shows a typical sequence of the flame topology during the transition from an initially V shape state to a final M shape flame. The conditions explored correspond to a swirl number $S_5 = 0.40$, an hydrogen enrichment $X_{H_2}^{fuel} = 0.28$, a bulk injection velocity $U = 18\,m \cdot s^{-1}$, and an equivalence ratio $\phi = 0.54$. For these flow conditions, the flame takes intermittently V and M shapes without never lasting more than 0.1 s in a specific state.

The region delineated by the white triangle superimposed to the first and last images in Fig. 4.7 represents the boundary of the ORZ for a V shaped flame. This interrogation region is used to easily identify the shape taken by the flame. During the transition, the flame shortens and penetrates within the ORZ in less than 20 ms. At $t = 0$, the flame has a V shape and the reaction takes place outside the region delimited by the triangle. The flame then protrudes progressively within the OSL and reaches its maximum penetration in the OSL after $t = 16$ ms. At $t = 26$ ms, the flame is still well established in the OSL and has an M shape. This situation ceases after a certain duration $t > 26$ ms and the flame takes back its initial V shape. These intermittent transitions take place randomly with time.

These transitions observed for different flow injection conditions, combustible mixtures and swirling rates are analyzed in the next sections with the help of a

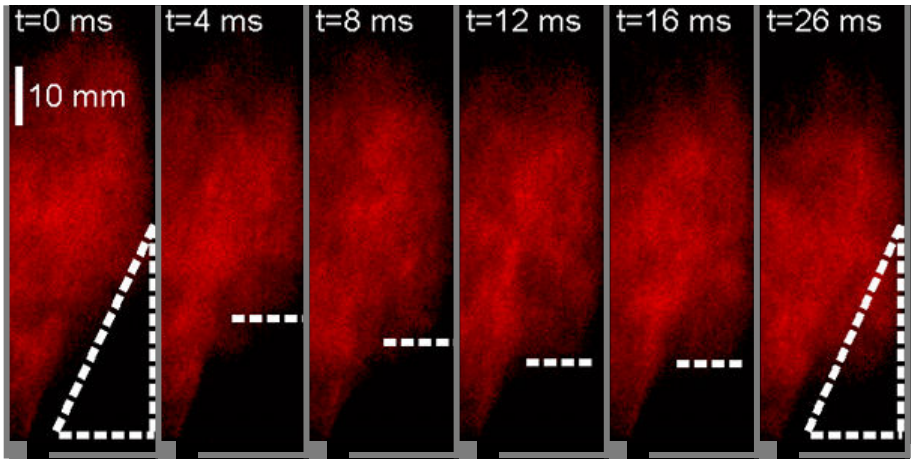

Figure 4.7: *V to M shape transition captured with a high speed CMOS camera. The white triangle delineates approximatively the ORZ boundaries and defines the interrogation zone used in Fig. 4.9. The left and right boundaries in these images respectively correspond to the burner axis and to the quartz tube wall. Swirl number* $S_5 = 0.40$*, hydrogen enrichment* $X_{H_2}^{fuel} = 0.28$*, bulk injection velocity* $U = 18\ \mathrm{m \cdot s^{-1}}$ *and equivalence ratio* $\phi = 0.54$*. Injector set in configuration A.*

scenario based on the flashback of the flame tip protruding along the boundary layer of the peripheral combustion chamber wall.

4.4 Flame topology transition model

It was shown in section 4.1, that the flashback of a flame along a boundary layer may be described by a critical Karlovitz number, which is itself a function of the Lewis number of the combustible mixture. The flashback propensity of a laminar flame in the boundary layer of a wall increases when the Lewis number is reduced as for example when hydrogen is used. It is conjectured here that the transition between V and M flame topologies along the combustor peripheral wall may be described in terms of a critical Karlovitz number Ka_c, function of the mixture Lewis number Le, below which this topological bifurcation takes place. These dimensionless numbers cannot be easily defined in the turbulent flows considered. The objective of this section is to develop a reasonable model to calculate these products.

For inclined laminar flames interacting with a wall, the following expression of the Karlovitz number is retained (Kurdyumov et al. (2000)):

$$\mathrm{Ka}^L = g\delta_b/S_L = \alpha g/S_L^2 \tag{4.1}$$

where g is the axial velocity gradient at the wall, S_L indicates the laminar burning velocity and δ_b stands for the quenching distance that can be replaced

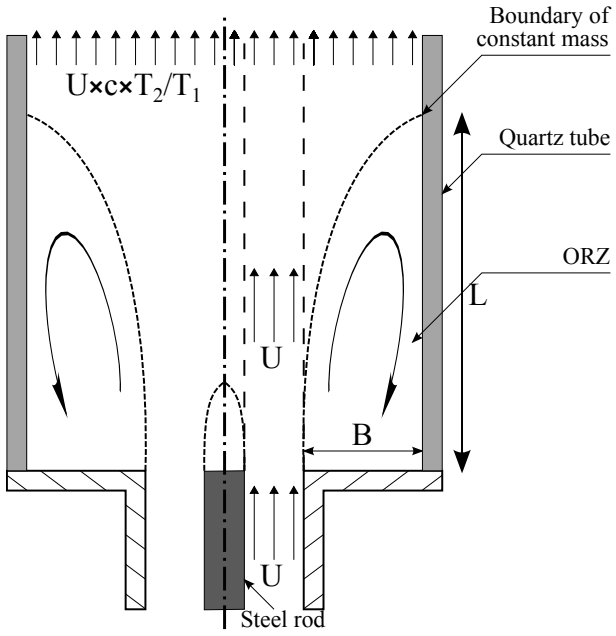

Figure 4.8: *Schematics of the combustion chamber showing the main dimensions of the jet, IRZ, and ORZ. The confinement ratio between the injection tube and combustion chamber cross sections is denoted c. T_1 and T_2 respectively stand for the temperature of fresh gases and burnt gases.*

by the preheat flame thickness $\delta_b \simeq \delta = \alpha/S_L$ where α is the thermal diffusivity of the mixture. This expression may be used as the starting point to build a Karlovitz number for turbulent swirled flames stabilized above the dump plane of the combustor and interacting with the combustion chamber peripheral wall. As already mentioned, it was not possible to measure the velocity field near the wall with PIV. The velocity gradient g at the wall needs thus to be inferred indirectly. This is realized with a global mass balance between the injection tube and the flow in the combustion chamber. The following approximation is used to estimate the velocity gradient g at the flame wall impingement location (see Fig. 4.8):

$$g = U(1 - \mathrm{c})/B \tag{4.2}$$

In this expression, U denotes the bulk flow velocity in the injection tube, c corresponds to the confinement ratio between the injection tube and combustion chamber cross sections and B indicates the width of the backward step. The velocity gradient g at the combustor wall vanishes for very small and large steps ($\lim_{B\to\infty} g = 0$ and $\lim_{B\to 0} g = 0$). In this study, these parameters take the following values, c = 0.064 and B = 18 mm for injector A, and c = 0.058 and B = 19 mm for injector B. The Karlovitz number takes then the form:

$$\mathrm{Ka}^L = \frac{U(1-\mathrm{c})}{B}\frac{\delta_b}{S_L} \tag{4.3}$$

Effects of turbulence were not included in this expression. In the present investigation, the flow rate and swirling strength are varied, so that a turbulent burning rate needs to be considered as well. Assuming that the quenching distance is not drastically altered by turbulence (Poinsot et al. (1993), Bruneaux et al. (1996)), the following expression for the turbulent Karlovitz number Ka^T is retained:

$$\mathrm{Ka}^T = \frac{U(1-\mathrm{c})}{B}\frac{\delta_b}{S_T} = \frac{U(1-\mathrm{c})}{B}\frac{\alpha}{S_L S_T} = g\frac{\alpha}{S_L S_T} \tag{4.4}$$

where S_T is a turbulent flame speed.

Due to difficulties in measuring turbulent flame speeds close to walls, values of S_T are evaluated here from empirical correlations. This quantity is often linked to velocity fluctuations due to the increase in the turbulent diffusivity and flame surface density (Wenzel and Peters (2000), Poinsot and Veynante (2005)). Bradley et al. (1992) have shown that for turbulent flames propagating in closed vessels or for jet flames stabilized on unconfined burners, the turbulent burning velocity S'_T scales as $S_L^{0.6} v'^{0.4}$, where v' stands for the root-mean-square (rms) value of velocity fluctuations. One may find many other correlations linking the turbulent flame speed to turbulent flow properties (Lipatnikov and Chomiak (2005), Driscoll (2008)). These expressions however do not account for the particular structure of swirling flows. It is thus worth examining an alternative correlation taking into account the rotation of the flow.

This problem was examined by Ishizuka (2002) for flames propagating along a vortex axis within cylindrical tubes. He showed that in this case, the turbulent flame speed is mainly a function of the laminar burning velocity and of the azimuthal velocity of the rotating flow $S_T^\theta = [(\rho_u/\rho_b)S_L^2 + {v_{\theta max}^w}^2]^{1/2}$, where ρ_b and ρ_u respectively represent the burnt and unburnt gas densities and $v_{\theta max}^w$ denotes the maximum azimuthal velocity reached by the vortical flow. This expression clearly shows that a turbulent flame in a rotating flow has a flame speed that increases with the azimuthal velocity. This is an important feature that is also observed for swirling flows stabilized at the dump plate of a combustor. When the swirl number increases, the flame generally protrudes deeper upstream within the flow. This alternative correlation for the turbulent flame speed will thus also be used in the next section to analyze the data.

In these expressions, the value used for the thermal diffusivity α is calculated for the mixture composition at the adiabatic flame temperature. The laminar burning velocity S_L is determined by direct simulations of freely propagating adiabatic planar flames with the detailed chemistry mechanism due to Lindstedt (1998) and the internally developed REGATH solver (Candel et al. (2011)). Root-mean-square velocity fluctuations v', needed for the calculations of S'_T, and the maximum azimuthal velocities $v_{\theta max}^w$, needed for the calculation of S_T^θ,

are deduced from LDV measurements at the injection tube outlet under non-reactive conditions and without quartz tube to confine the flow.

As only lean combustible mixtures are considered in this study, with equivalence ratios ϕ ranging from 0.5 to 1.0, the effective Lewis number Le of the mixture is equal to that of the CH_4/H_2 blend, $Le = Le^{fuel}$, which has been modeled by Dinkelacker et al. (2011):

$$\frac{1}{Le^{fuel}} = \frac{X_{CH_4}^{fuel}}{Le_{CH_4}} + \frac{X_{H_2}^{fuel}}{Le_{H_2}} \tag{4.5}$$

where Le_{CH_4} and Le_{H_2} are the methane and hydrogen Lewis numbers in the mixture and $X_{CH_4}^{fuel}$ and $X_{H_2}^{fuel}$ denote the molar fractions of methane and hydrogen in the fuel mixture. Values of the mixture Lewis number were determined with a relative accuracy of 5% corresponding to the accuracy of the mixture preparation with the mass flow controllers. The Karlovitz numbers calculated in this study feature larger uncertainties because of the cumulation of inaccuracies on calculations of the flame speed, thermal diffusivity and velocity gradient g at the wall. The relative accuracy on the Karlovitz numbers determined in this study is better than 10%. To further reduce inaccuracies, all experimental data presented in this study were averaged over three reproducible measurements.

4.5 Analysis of flame shape transitions

4.5.1 Methodology

To simplify comparisons between experiments and model predictions, all critical Karlovitz values Ka_c presented in the following are normalized by the critical value calculated for a reference case defined by a swirl number $S_2 = 0.32$, a Lewis number $Le = 0.75$ and a velocity gradient $g = 689\,s^{-1}$ with the injector set in configuration A. It is thus worth keeping in mind that the values of the critical Karlovitz numbers presented in the following are relative with respect to this reference case. Table 4.2 shows the operating conditions achievable with the experimental setup.

As the Lewis number Le, the Karlovitz number Ka, and the velocity gradient g at the wall are the main parameters that were identified in this study, it has been decided to use these parameters for the combustible mixture preparation and to operate the test rig. This means that the experiments presented below were realized by changing directly the Lewis number Le at fixed Karlovitz Ka number and velocity gradient g, or by changing Ka at fixed Le and g or by changing g at fixed Le and Ka. This method significantly eased the detection of flame topology transitions. When the Lewis number Le, the Karlovitz number Ka and the velocity gradient g of interest are chosen, the mass flow rates of the different species injected are deduced and these data are used to trigger

Table 4.2: *Ranges of explored operating conditions.*

	Parameters of interest		
	Le	Ka	$g\,(\,\mathrm{s}^{-1})$
Min	0.55	0.05	350
Max	0.97	2.5	1300
	Usual parameters		
	$\mathrm{X}_{\mathrm{H_2}}^{\mathrm{fuel}}$	ϕ	$U\,(\,\mathrm{m}\cdot\mathrm{s}^{-1})$
Min	0	0.5	7
Max	0.37	0.9	25

the mass flow controllers. The values for the equivalence ratio ϕ, the hydrogen molar fraction in the fuel $\mathrm{X}_{\mathrm{H_2}}^{\mathrm{fuel}}$ and the bulk injection velocity U are finally automatically reconstructed.

Flame topology charts are presented below. Results are first examined to reveal effects of the Lewis number. Effects of the velocity gradient at the wall and of the swirl number are discussed next.

4.5.2 Effects of the Lewis number

Figure 4.9a shows a typical chart of the flame topologies obtained for the reference swirl number $\mathrm{S_2} = 0.32$ and the reference velocity gradient $g = 689\,\mathrm{s}^{-1}$ when the Lewis number is varied. Shape transitions are found by setting the Karlovitz number to an initial high value and this number is then progressively reduced for a fixed mixture Lewis number. The definition retained for the Karlovitz number is here given by Eq. 4.1. The critical Karlovitz number Ka_c^L, which yields the transition from a V to an M flame, is reached for the flow conditions corresponding to the first flashback event of a flame protruding in the OSL detected by the CCD camera (Fig. 4.7). These experiments are then repeated for combustible mixtures at different Lewis numbers. This yields the upper transition curve with square symbols in Fig. 4.9a. The critical Karlovitz numbers corresponding to an M to V shape transition are also found by repeating the experiments with small initial values of the Karlovitz number, which are then progressively increased for fixed combustible mixture Lewis numbers. This yields the bottom transition curve with circle symbols in Fig. 4.9a. It is worth noting that the mixture equivalence ratio varies between $\phi = 0.53$ and $\phi = 0.69$ to cover the regions plotted in Fig. 4.9a.

This figure shows that the propensity of topology bifurcation increases when the Lewis number of the combustible mixture decreases. It also shows that the Lewis number is an appropriate dimensionless number to examine these transitions. This observation is fully consistent with results obtained for flash-

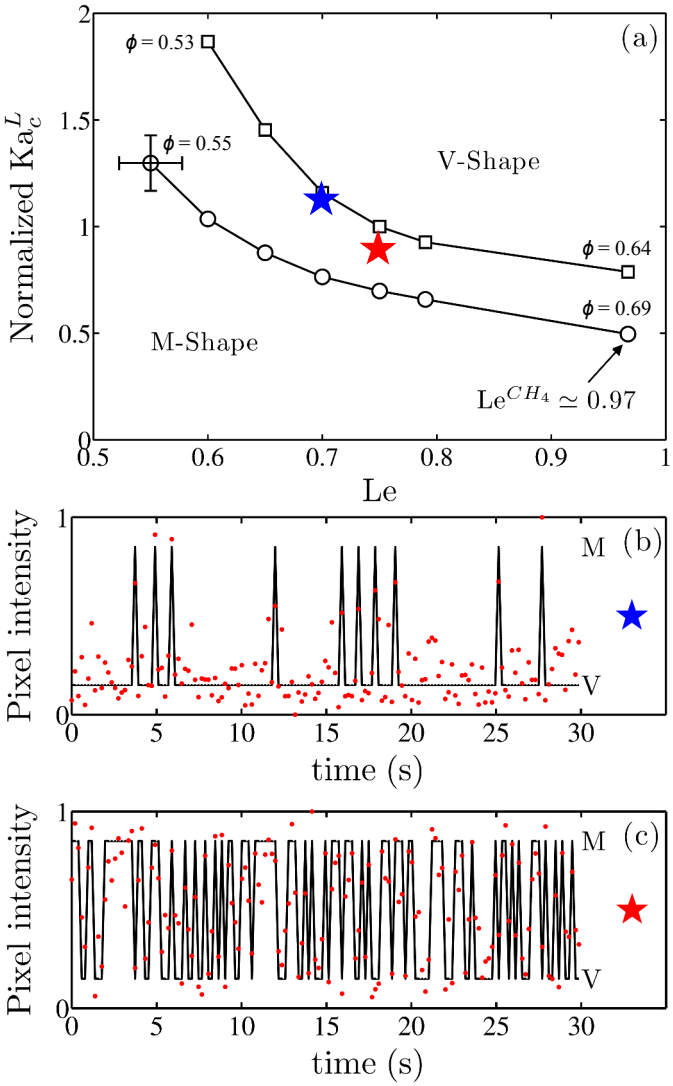

Figure 4.9: *(a) Critical Ka_c^L as a function of Le for $g = 689\,s^{-1}$ and $S_2 = 0.32$ with the injector set in configuration A. V to M shape transitions (square symbols). M to V shape transitions (circle symbols). Blue and red stars indicate operating conditions corresponding to the chronographs presented in (b) and (c) plotting the mean normalized pixel intensity (red dots) in the interrogation zone defined in Fig. 4.7. These graphs give an indication on the shape taken by the flame as a function of time. (b) Results for the blue star operating conditions Le = 0.70, $Ka^L = 1.12$ in (a). (c) Results for the red star operating conditions Le = 0.75, $Ka^L = 0.84$ in (a).*

back of laminar flames along the boundary layer of a wall (Kurdyumov et al. (2000)) and confirms similarities between the topological transitions observed in this study and the flashback of flames along a wall. One can already conclude that the critical Karlovitz number is a function of the mixture Lewis number : Ka_c^L=$\mathrm{Ka}_c^L(\mathrm{Le})$.

For a given Lewis number, a zone separates regions with well defined flame shapes in Fig. 4.9a. V flames are found for large Karlovitz numbers. M flames are found for small Karlovitz numbers. In between these regions, the flame takes intermittently a V or an M shape. This zone is delimited by the two critical Karlovitz boundaries corresponding to V to M shape and M to V shape transitions. Figure 4.9b shows a plot indicating the shape taken by the flame as a function of time for Le= 0.70 and a Karlovitz number slightly below the V to M critical transition value for this combustible mixture (blue star in Fig. 4.9a). The indicator retained to identify the flame shape is the normalized average pixel intensity integrated over the triangle region shown in Figs. 4.3 or 4.7. This flame stabilizes mainly with a V shape, but different flashback events along the peripheral combustion chamber wall occur yielding an M flame state, as for example around times t = 5 s, t = 12 s or t = 25 s. During these short periods, the flame is protruding in the OSL but cannot be stabilized with an M shape for a long duration and transits back to its initial V shape.

Figure 4.9c shows a similar plot for Le = 0.75 and a value of the Karlovitz number lying close to the center of the intermittent zone where the flame state is not well defined (red star in Fig. 4.9a). In this case, the probability to find a V or an M flame is close to 0.5. This value is in agreement with the separation distance between the M to V shape and V to M shape boundaries. In the following, only transitions from V to M flame topologies are characterized.

4.5.3 Effects of the velocity gradient

Experiments at the reference swirl number S_2 = 0.32 are now conducted by varying the injection bulk velocity from U = 8.8 to 19.1 $\mathrm{m \cdot s^{-1}}$ to analyze effects of the velocity gradient g on the previous results. Measurements are carried out for different hydrogen enrichments in the combustible mixture featuring decreasing Lewis numbers Le=0.80, 0.70, 0.60 and for a combustible mixture with pure methane having a Lewis number Le = 0.97. Values of the critical velocity gradient g, corresponding to flow conditions where the V to M flame transition takes place, are plotted as a function of S_L^2/α in Fig. 4.10a for the four combustible mixtures explored. It is first interesting to note that the different curves do not correspond to straight lines. This is in contrast with predictions from Eq. (4.1) that is reproduced here:

$$g = \mathrm{Ka}_c^L(\mathrm{Le}) \times \frac{S_L^2}{\alpha} \tag{4.6}$$

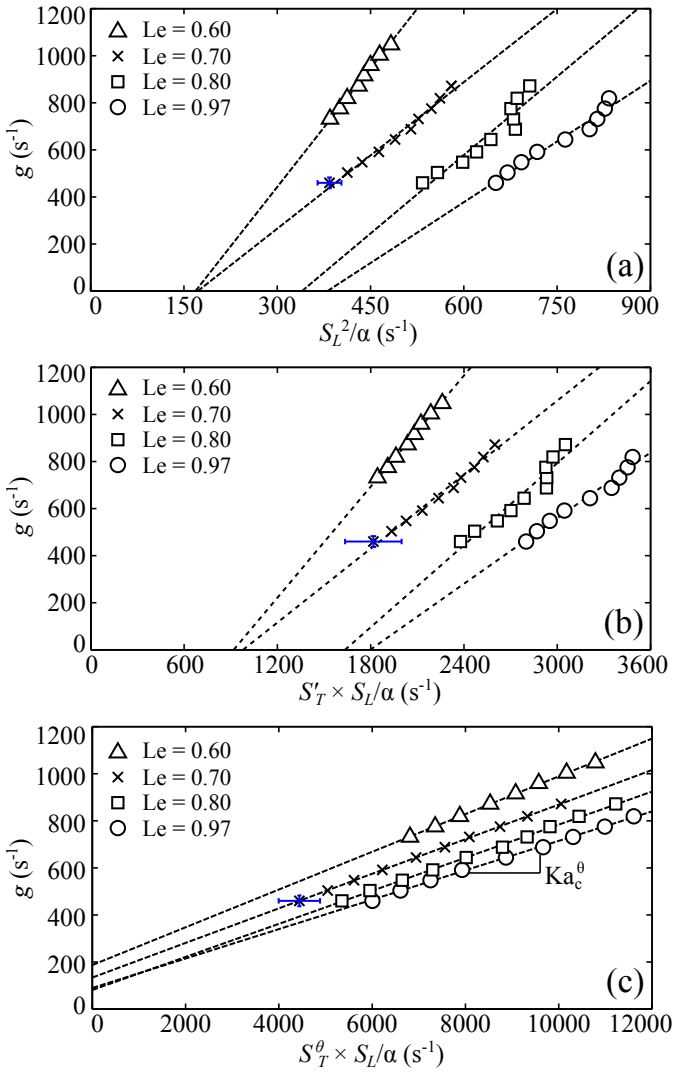

Figure 4.10: *Velocity gradient g at bifurcation as a function of (a) S_L^2/α, (b) $S'_T S_L/\alpha$ and (c) $S_T^\theta S_L/\alpha$ for four different Lewis numbers Le = 0.60 △, 0.70 ×, 0.80 □, and 0.97 ∘ with a swirl number S_2 = 0.32 (injector set in configuration A). Dashed lines show linear regressions of the data. Blue error bars give an indication of uncertainties.*

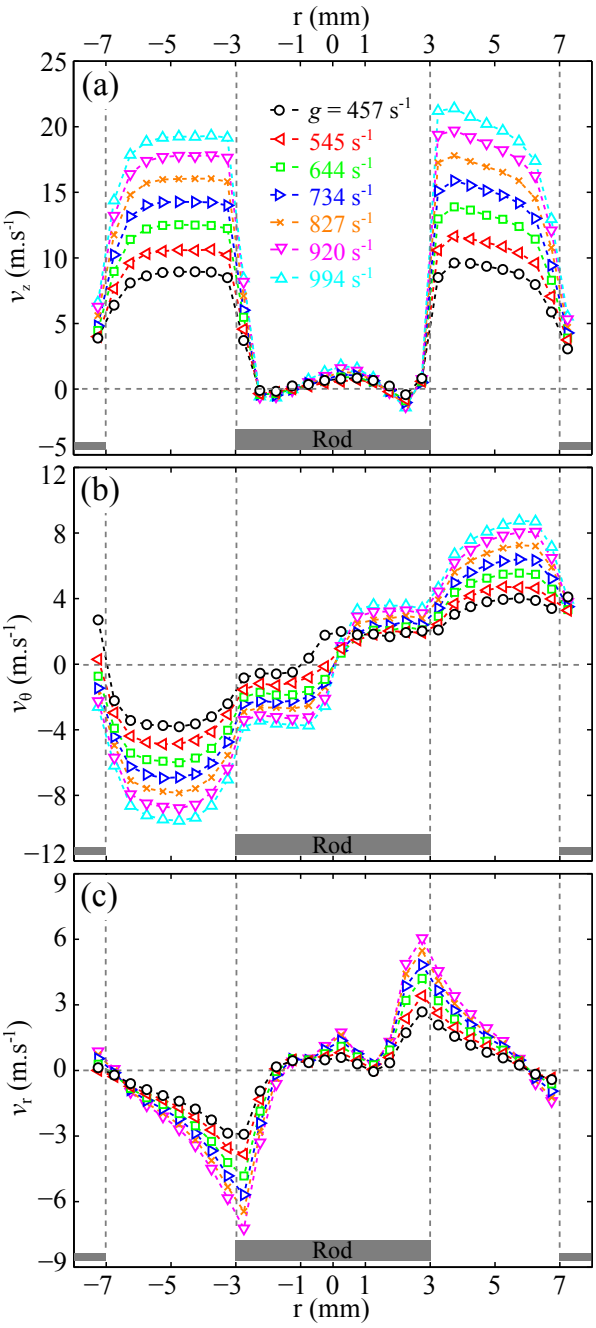

Figure 4.11: *Axial (a), azimuthal (b), and radial (c) mean velocities as a function of the radial distance to the burner axis for a swirl number S_2 = 0.32 (θ_2 = 30°) and for different values of velocity gradients g= 457 ∘, 545 ◁, 644 □, 734 ▷, 827 ×, 920 ▽, and 994 △ s^{-1}. Measurements were realized by LDV at 1 mm above the central rod tip under non-reactive conditions and without quartz tube to confine the flow. The injector set in configuration A is represented in gray to ease reading.*

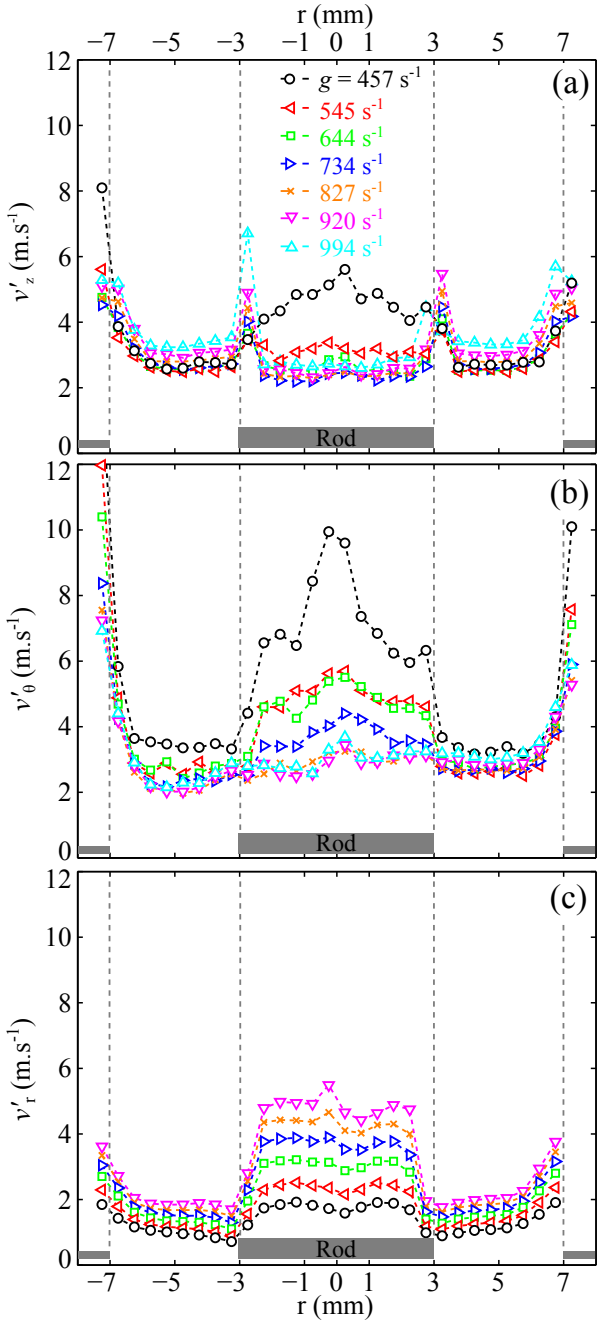

Figure 4.12: *Axial (a), azimuthal (b), and radial (c) rms velocity fluctuations as a function of the radial distance to the burner axis for a swirl number* $S_2 = 0.32$ *(*$\theta_2 = 30°$*) and for different values of velocity gradients* $g =$ *457* ∘, *545* ◁, *644* □, *734* ▷, *827* ×, *920* ▽, *and 994* △ s^{-1}. *Measurements were realized by LDV at 1 mm above the central rod tip under non-reactive conditions and without quartz tube to confine the flow. The injector set in configuration A is represented in gray to ease reading.*

This expression indicates that Ka_c^L should be invariant for a fixed Lewis number Le. Linear regressions of the experimental data intercept the Y-axis in Fig. 4.10a at negative values. The mean value for the four configurations investigated yields $g_0 = -584\ \mathrm{s}^{-1}$ when $S_L^2/\alpha = 0$. The regression correlation factor R^2 of the different linear fits are relatively good ($R^2 = 0.963$ in average), but these results indicate that estimates of the critical transition Karlovitz number based only on laminar flow properties cannot fully capture the V to M flame topology bifurcations observed here at different bulk flow injection conditions.

The swirling flow being turbulent, the flame speed differs from the laminar burning velocity S_L. A correlation for the turbulent flame speed S_T may then be used to replace S_L and estimate the corresponding critical Karlovitz number Ka_c^T where V to M shape transition takes place. As already mentioned, the thermal flame thickness S_L/α is less modified by turbulence (Bruneaux et al. (1996)), it is thus natural to examine results obtained for the critical velocity gradient g as a function of $S_T S_L/\alpha$ (see Eq. (4.4)).

The first type of correlation tested for the turbulent flame speed assumes a link with turbulent fluctuations of the flow field. The one tested here is $S'_T = S_L^{0.6} v'^{0.4}$ (Bradley et al. (1992)). To use this correlation, the root-mean-square (rms) velocity fluctuation level v' needs to be determined. The axial, azimuthal, and radial velocity components were thus measured by LDV at the injection nozzle outlet, 1 mm above the rod tip. Data for the mean quantities are presented in Fig. 4.11 as a function of the radial distance r to the burner axis. Mean axial velocity profiles show a weak IRZ (for $|r| < 3$ mm) in the wake of the central bluff-body. The swirling rate $\mathrm{S}_2 = 0.32$ is here insufficient to induce vortex breakdown ($\mathrm{S}_2 < 0.60$). Due to the difficulty to align the central rod exactly on the axis of the injection tube, velocity profiles feature small asymmetries. It was checked that these asymmetries have a negligible impact on the observed flame transitions. The axial rms velocity profiles plotted in Fig. 4.12a take high values in the ISL and OSL, but feature roughly constant levels in the jet of reactants and in the IRZ. Fluctuations increase in the IRZ at low injection velocities. This phenomenon is emphasized for azimuthal rms velocities shown in Fig. 4.12b.

The rms velocity data in the different directions are now used to calculate the velocity fluctuation $v' = [{v'_z}^2 + {v'_\theta}^2 + {v'_r}^2]^{1/2}$ needed to estimate the turbulent flame speed S'_T, where the axial v'_z, azimuthal v'_θ, and radial v'_r rms velocity fluctuations are first averaged over the injection section between 3 mm $< |r| <$ 7 mm. Results shown in Fig. 4.13a indicate that the axial v'_z and radial v'_r velocity fluctuations averaged over the jet cross section both linearly increase with the velocity gradient g, or equivalently with the injection bulk velocity U. The situation is reversed for the azimuthal velocity fluctuation v'_θ averaged over the injection cross section that decreases linearly with g. As a consequence, the

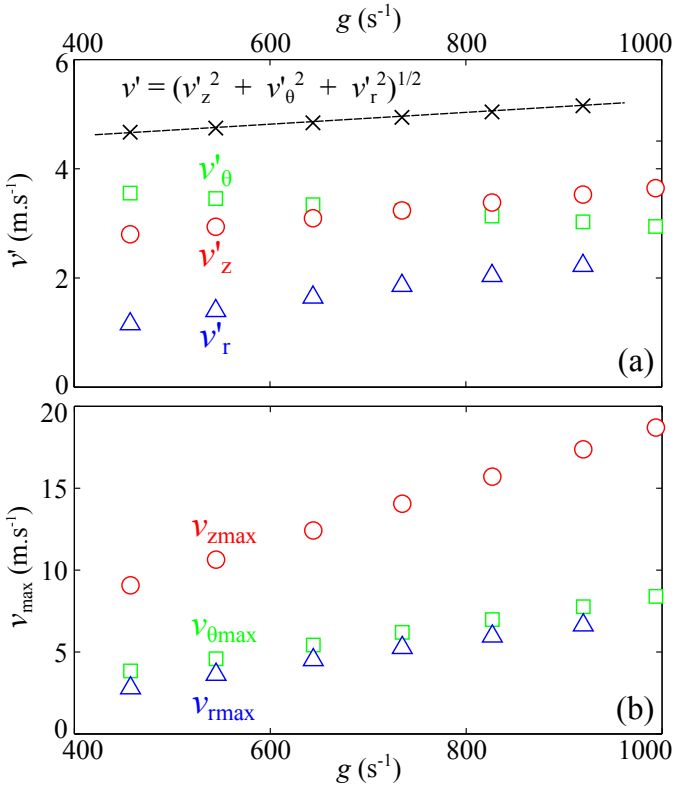

Figure 4.13: *(a) Axial ◯, azimuthal □, and radial △ rms velocity fluctuations averaged over the jet cross section as a function of the velocity gradient g (injector set in configuration A). Black cross symbols × stand for the rms velocity fluctuation level* $v' = [v'^2_z + v'^2_\theta + v'^2_r]^{1/2}$. *(b) Maximum axial ◯, azimuthal □, and radial △ mean velocities as a function of g. Absolute values of azimuthal and radial velocities are plotted to ease comparisons.*

resulting rms value v' only slightly increases with g.

Values for v' can now be used to calculate $S'_T = S_L^{0.6} v'^{0.4}$ and analyze effects of the velocity gradient $g = U(1-c)/B$ on flame topology transitions. Results are plotted in Fig. 4.10b as a function of $S'_T S_L/\alpha$. Linear regressions of the data do not improve compared to results presented in Fig. 4.10a as a function of S_L^2/α obtained by considering a laminar burning velocity. Tests were also conducted for $S_T'^2/\alpha$ and yielded no improvement. One may thus safely conclude that turbulent velocity fluctuations do not participate, at least to the leading order, to the transition of the flame topologies observed along the peripheral combustion chamber wall when the injection velocity U is varied.

Reduction of the data is now attempted with the model proposed by Ishizuka (2002) for the turbulent flame speed $S_T^\theta = [(\rho_u/\rho_b) S_L^2 + {v_{\theta max}^w}^2]^{1/2}$. In this expression, $v_{\theta max}^w$ is the maximum azimuthal velocity of the swirling flow at the location of the flame/wall interaction. As already mentioned, it was not possible to measure the azimuthal velocity component of the swirling flow near the cylindrical tube where the flame tip impinges the wall due to strong reflections of the laser sheet on the quartz tube. Values for $v_{\theta max}^w$ in the flame tube are deduced here from measurements made at the injection tube outlet. The main difference is due to the expansion of the swirling flow between the injection tube and the flame tube cross sections. The maximum azimuthal velocity at the combustor peripheral wall $v_{\theta max}^w$, where the flame tip impinges the quartz tube, is here deduced from the maximum azimuthal velocity $v_{\theta max}$ reached by the flow at the injection tube outlet assuming a solid body rotation (Gupta et al. (1984)): $v_{\theta max}^w R_c = v_{\theta max} R_i$, where R_i and R_c stand for the radius of the injection tube and flame tube respectively. This model is admittedly a rough approximation of reality, but it will be shown to capture the main physics of the problem considered. These data are deduced from the azimuthal velocity profiles plotted in Fig. 4.11b.

The evolution of this maximum azimuthal velocity $v_{\theta max}$ at the injector tube outlet is presented in Fig. 4.13b in addition to the evolution of the maximal axial v_{zmax} and radial v_{rmax} velocity components. The measured critical velocity gradient g is plotted as a function of $S_T^\theta S_L/\alpha$ in Fig. 4.10c. In contrast to the previous correlations tested, the critical velocity gradient g now linearly increases with $S_T^\theta S_L/\alpha$ for the four mixture Lewis numbers tested. The linear regression correlation factor R^2 is now very close to unity ($R^2 = 0.9992$ in average). Data also intercept the Y-axis in Fig. 4.10c with positive values. The mean value $g_0 = 122\ \mathrm{s}^{-1}$ is closer to the origin compared to that found with the previous correlations. These results are also consistent with those presented in Fig. 4.9a as the slope of the linear regressions increases when the Lewis number of the mixture decreases.

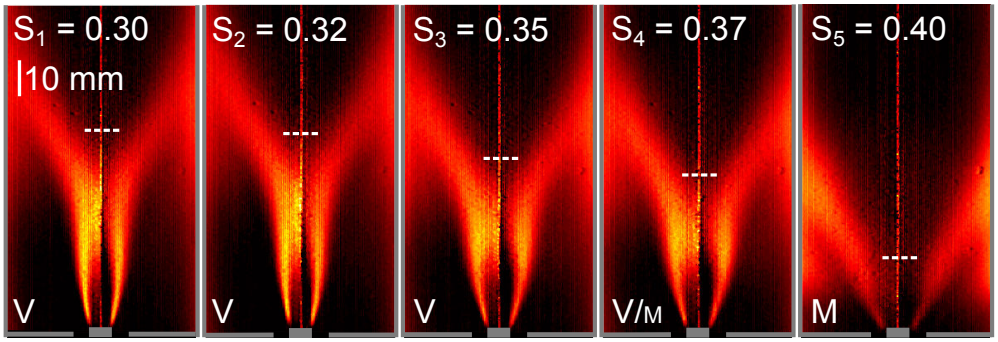

Figure 4.14: *Abel deconvoluted averaged images of the flame chemiluminescence for different swirl numbers S for* $g = 689\ \mathrm{s}^{-1}$ *(*$U = 13.3\ \mathrm{m \cdot s}^{-1}$*),* $Le = 0.75$ *and* $Ka^L = 1.31$ *(injector set in configuration A). The white horizontal dashed lines indicate the flame height on the central axis.*

These results indicate that the azimuthal velocity component of the swirling flow is an important element that needs to be considered to analyze flame tip topology bifurcations, and in particular the transition from V to M swirling flames interacting with the combustor peripheral wall. The model proposed relying on a turbulent flame speed correlated to the azimuthal velocity yields the best agreement with experiments. V to M shape transitions occur in this combustor when:

$$\mathrm{Ka}^{\theta} \leq \mathrm{Ka}_c^{\theta} = (g - g_0)\frac{\alpha}{S_L S_T^{\theta}} \tag{4.7}$$

where g_0 denotes the mean value of the velocity gradient when S_T^{θ} vanishes. This value should be theoretically equal to zero, but experiments yield a small bias $g_0 = 122\ \mathrm{s}^{-1}$. Further experiments also show that this residual velocity gradient g_0 slightly depends on the combustible mixture Lewis number and on the swirling rate, but these effects are not taken into account in the following and g_0 will be considered equal to zero. To further challenge the proposed model, the bifurcation propensity of these swirling flames is examined in the next section by varying the rotation rate imparted to the flow.

4.6 Effects of swirl

Effects of swirl on the flame topology are first examined for low swirl numbers when the flame is anchored on the central rod (configuration A in Fig. 1.11b). The case of aerodynamically stabilized flames with a higher swirl number is then examined (configuration B in Fig. 1.11b).

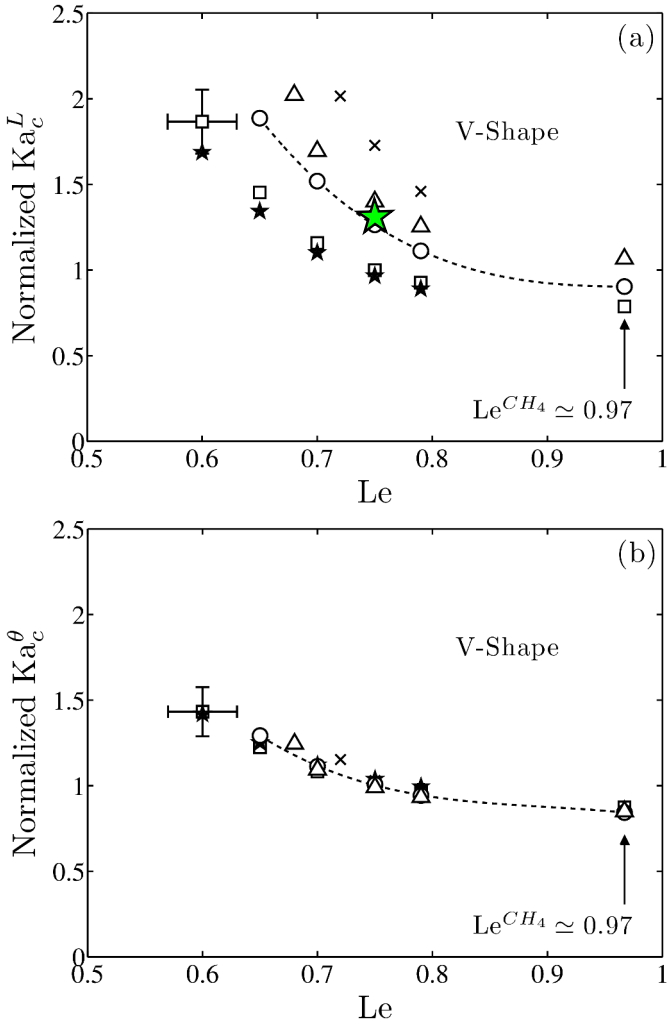

Figure 4.15: *Critical Karlovitz number calculated with (a) laminar flow quantities Ka_c^L and with (b) Eq. (4.7) Ka_c^θ as a function of the combustible mixture Lewis number Le when $g = 689\ s^{-1}$ and for different swirl numbers $S_1 = 0.30$ ⋆, $S_2 = 0.32$ □, $S_3 = 0.35$ ∘, $S_4 = 0.37$ △ and $S_5 = 0.40$ ×. The green star indicates operating conditions for the flame images presented in Fig. 4.14. The injector is set in configuration A.*

4.6.1 Swirled flames anchored on the central rod

Figure 4.14 shows images of the flame chemiluminescence recorded with the CCD camera averaged over 170 snapshots when the swirl number S is varied for a fixed CH_4/H_2/air combustible mixture composition and a fixed velocity gradient $g = 689\ s^{-1}$ corresponding to a bulk injection velocity $U = 13.3\ m \cdot s^{-1}$. The corresponding Lewis and Karlovitz numbers are equal to Le = 0.75 and $Ka^L = 1.31$. This figure clearly indicates that the swirl has a strong impact on the flame topology. For swirl numbers $S < S_4 = 0.37$, the flame features a V shape and takes an M shape for values higher than $S \geq S_5 = 0.40$. In the case of V shaped flames, the IRZ bubble width increases and the flame height measured on the burner axis decreases when the swirl number S increases. For a swirl number $S_4 = 0.37$, the flame lies in the intermittent regime where the shape is not well defined, but with a predominant V shape state. The corresponding mean image results mainly from an accumulation of snapshots where the flame features a V shape, but it also includes several snapshots where the flame has an M shape. This results in a blurred image close to the peripheral wall where it is difficult to precisely determine the boundaries of the flame close to the ORZ. Figure 4.14 confirms that swirl needs to be taken into account to characterize V to M flame topology bifurcations of swirl flames featuring the same combustible mixture and injection conditions.

Figure 4.15a shows the evolution of the critical Karlovitz number Ka_c^L calculated with laminar flow quantities when V to M flame shape transitions take place. This quantity is plotted as a function of the Lewis number of the combustible mixture for different swirl numbers. As already observed in Fig. 4.14, the bifurcation from a V to M flame is promoted when the swirl number increases. This observation holds for a wide range of Lewis numbers in Fig. 4.15a. A family of transition curves is obtained for the different swirl numbers explored. They all follow the same evolution, but the different data do not collapse on the same curve in Fig. 4.15a.

The same data are now plotted in Fig. 4.15b as a function of the critical Karlovitz number Ka_c^θ calculated with Eq. (4.7), where g_0 was set to zero to simplify the problem. The maximum azimuthal velocity $v^w_{\theta max}$ needed for the calculation of Ka_c^θ is deduced from the velocity profiles plotted in Fig. 4.16 assuming a solid body rotation $v^w_{\theta max} R_c = v_{\theta max} R_i$. Raising the swirl number from $S_1 = 0.30$ to $S_5 = 0.40$ increases the maximum azimuthal velocity reached by the flow at the injection tube outlet from $v_{\theta max} = 6.2\ m \cdot s^{-1}$ to $v_{\theta max} = 8.3\ m \cdot s^{-1}$ for the same bulk injection velocity $U = 13.3\ m \cdot s^{-1}$. The axial velocity is not affected by the swirl intensity. Using values deduced for $v^w_{\theta max}$ in Eq. (4.7), the data now fall roughly on the same curve in Fig. 4.15b with a relatively limited dispersion. The model Eq. (4.7) yields thus a reasonable collapse of data gathered for the different swirl numbers explored. This indicates that the

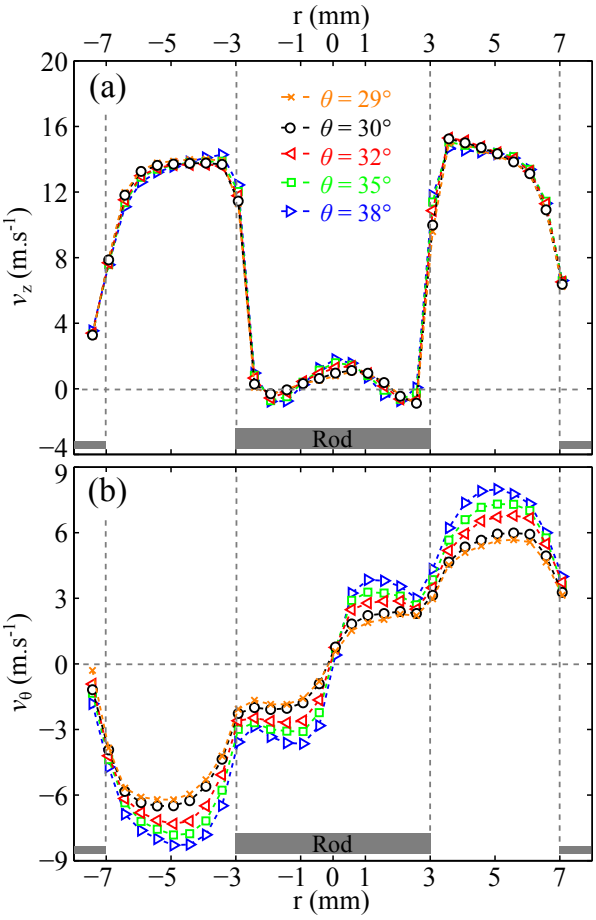

Figure 4.16: *Axial (a) and azimuthal (b) mean velocity components of the swirling jet of reactants as a function of the radial distance to the burner axis for a velocity gradient* $g = 689\,s^{-1}$ *(*$U = 13.3\ \mathrm{m \cdot s^{-1}}$*) and different swirl numbers* $S_1 = 0.30$ ×, $S_2 = 0.32$ ∘, $S_3 = 0.35$ ◁, $S_4 = 0.37$ □ *and* $S_5 = 0.40$ ▷. *Measurements were realized by LDV at 1 mm above the central rod tip under non-reactive conditions and without quartz tube to confine the flow. The injector set in configuration A is represented in gray to ease reading.*

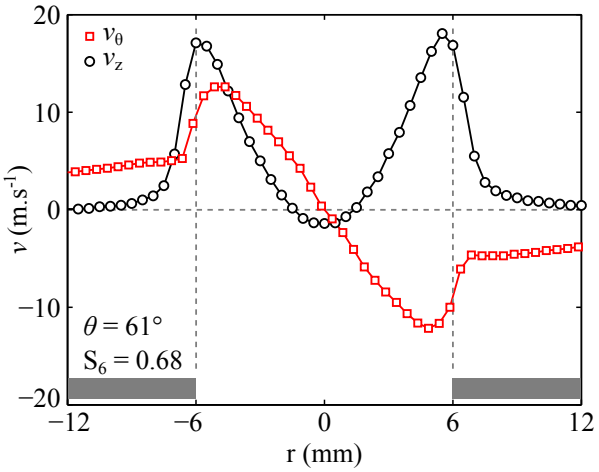

Figure 4.17: *Mean axial ∘ and azimuthal □ velocity components as a function of the radial distance to the burner axis for a swirl number* $S_6 = 0.68$ *(*$\theta_6 = 61°$*) and a velocity gradient* $g = 545\,s^{-1}$ *(*$U = 11.0\,\mathrm{m\cdot s^{-1}}$*). Reproduced from Durox et al. (2013). Measurements were realized by LDV at* $z = 2$ *mm above the injection nozzle outlet under non-reactive conditions with a* 50 mm *diameter quartz tube to confine the flow. The injector set in configuration B is shown in gray to ease reading.*

correlation of Ishizuka (2002) for the turbulent flame speed S_T^θ of vortical flows captures relatively well the physics associated to the stabilization of swirling flames at low to moderate swirl numbers when $S \leq 0.40$.

These experiments further confirm the flashback mechanism taking place along the peripheral wall of the combustor and controlling V to M flame topology transitions. The proposed criterion Eq. (4.7) allows to reproduce the topological bifurcations observed in the setup when the bulk injection velocity is doubled from $U = 8.8$ to $19.1\,\mathrm{m\cdot s^{-1}}$ and for combustible mixtures featuring Lewis numbers within $0.55 \leq \mathrm{Le} \leq 1$. In these experiments, the swirl number featured only limited variations by about 33% from $S = 0.30$ to 0.40 in a configuration where the flame is anchored on a central bluff body when the injector is set in configuration A. The swirling rate is in theses cases relatively low, and it is interesting to examine a situation with a higher swirl.

4.6.2 Swirled flames stabilized aerodynamically

When the swirl number increases and exceeds the value above which vortex breakdown takes place, swirled flames can be stabilized aerodynamically without central bluff body. V to M flame topology transitions are studied in this case when the injector is set in configuration B. This configuration is explored for CH_4/air mixtures at a swirl number $S_6 = 0.68$ (Fig. 4.5).

The velocity $v_{\theta max}^w$ is now deduced from LDV measurements plotted in Fig. 4.17.

It is then possible to plot the critical velocity gradient g corresponding to V to M shape transitions as a function of $S_T^\theta S_L/\alpha$ for the aerodynamically stabilized swirled flames at S_6 = 0.68 and compare the results to those obtained for the reference swirled flames stabilized by a central rod and featuring a lower swirl number S_2 = 0.32. Data obtained for the two swirled flames are not superimposed in Fig. 4.18 (S_2 = 0.32 and S_6 = 0.68 - no dissipation data points). However, experiments conducted at S_6 = 0.68 also yield a linear evolution of the critical velocity gradient. A linear regression of these data intercepts the Y-axis with a similar value as in the case where S_2 = 0.32. The difference between the transition curves for rod stabilized and aerodynamically stabilized swirled flames may be reduced by accounting for dissipation of swirl in the flame tube (Syred and Beér (1974), Gupta et al. (1984)).

In the experiments presented, the swirling jet of the aerodynamically stabilized V flames impinges the combustor peripheral wall at a much higher distance above the injection plane in Fig. 4.5 than the swirled flames stabilized on the central rod presented in Fig. 4.3. This position is located 61 mm above the dump plane in Fig. 4.3 for a rod stabilized swirled V flame and at 90 mm in Fig. 4.5 for the aerodynamically stabilized swirled flame. It is known that the azimuthal velocity of a swirling jet decays with the axial distance to the burner. This is mainly due to dissipation effects. It is generally found that the maximum azimuthal velocity $v_{\theta max}$ decays as $z^{-\beta}$ (Syred and Beér (1974), Gupta et al. (1984), Ishizuka (1990)), where z denotes the axial distance to the injection plane and β is a positive number. This coefficient depends on the flow topology. It takes values ranging between β = 0.5 for a rotating flame in a cylindrical tube (Ishizuka (1990)) and β = 2 for a swirled free jet (Syred and Beér (1974)). In our case, this value is taken equal to unity β = 1 as in Gupta et al. (1984).

With this correction, the azimuthal velocity is reduced by about 32% for a swirled jet impinging the combustor peripheral wall at z = 90 mm compared to a situation where it would impinge the wall at z = 61 mm for the same injection bulk velocity. This difference is taken into account in the calculation of the maximum azimuthal velocity $v_{\theta max}^w$ needed to estimate an appropriate value for S_T^θ at the swirled flame tip impingement location. It allows to directly compare results obtained for the swirled flames stabilized aerodynamically and those found for swirled flames stabilized by a central rod that do not impinge the combustor peripheral wall at the same location.

Using this correction for the maximum azimuthal velocity $v_{\theta max}^w$, data obtained for aerodynamically stabilized swirled flames at S_6 = 0.68 are now superimposed in Fig. 4.18 to the data obtained for rod stabilized swirled flames at S_2 = 0.32. This indicates that the model Eq. (4.7) captures well V to M shape transitions for both swirled flames provided that the value of $v_{\theta max}^w$ at the V flame tip im-

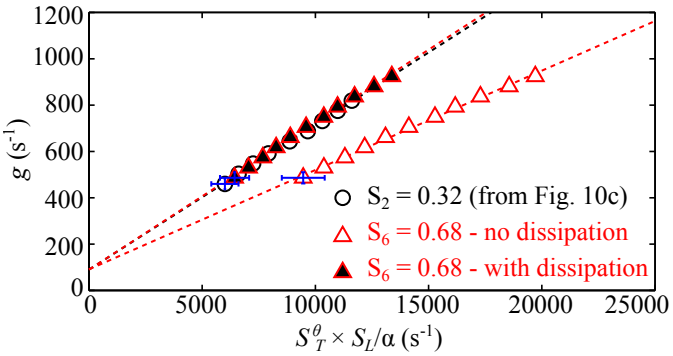

Figure 4.18: *Velocity gradient g corresponding to V to M bifurcations as a function of $S_T^\theta S_L/\alpha$ for the aerodynamically stabilized flames (Le = 0.97, injector set in configuration B, S_6 = 0.68) with (black body triangles) and without (hollow body triangles) accounting for dissipation effects in the flame tube. Values for rod stabilized flames (Le = 0.97, injector set in configuration A, S_2 = 0.32) are represented by black circles. Dashed lines show linear regressions of the data. The blue error bars give an indication of uncertainties.*

pinging the peripheral wall may be estimated adequately. This demonstrates that the model built to characterize shape bifurcations of swirled flames stabilized by a central bluff body with moderate swirl numbers $0.3 \leq S \leq 0.4$ yields also reasonable results for swirl numbers up to S = 0.68 and for aerodynamically stabilized flames.

These results suggest that the mechanisms controlling flame shape transitions are similar for rod stabilized and aerodynamically stabilized swirled flames. For the same operating conditions that the ones investigated in this work, Moeck et al. (2012) reported the presence of a PVC for the aerodynamically stabilized flames with S = 0.68. Rod stabilized flames with $S \leq 0.4$ do not feature a PVC. This demonstrates that the PVC does not influence flame topology bifurcations, at least to the leading order. These results contrast with the observations of Steinberg et al. (2013) and Terhaar et al. (2014). They reported that the sudden V to M shape transition of premixed swirled flames was triggered by the formation of PVC.

4.7 Conclusion

An experimental analysis of V/M flame topology transitions has been carried out for swirled flames interacting with the combustion chamber peripheral wall. It has been demonstrated that the stabilization regimes of V and M flames can be delineated by considering a flashback mechanism of the V flame tip along the boundary layer of the combustor peripheral wall. These different flame topologies are well delimited by considering a diagram of the Karlovitz number

plotted as a function of the combustible Lewis mixture, which is often used to delineate flashback of laminar flames along walls. Transitions between V to M flame topologies take place when the Karlovitz number drops below a critical value Ka_c.

Transition curves between V to M flame topologies and transition curves between M to V flame topologies do not collapse in this diagram and feature an intermediate zone where the mean shape of the flame is not well defined and switches between these two intermittent states. In this region, the probability for a swirled flame to take a V or an M shape increases when the operating conditions are closer to the stable V shape flame region or to the stable M shape flame region respectively.

For a fixed Lewis number of the combustible mixture, the critical Karlovitz number where the V to M flame shape bifurcation takes place was shown to be a function of the swirl. A model for the critical value Ka_c was proposed based on a velocity gradient g calculated with the injection bulk flow velocity U, the laminar flame thickness α/S_L and a turbulent flame speed S_T^θ that is related to the maximum azimuthal velocity $v_{\theta max}$ reached by the swirling jet at the nozzle outlet and to the laminar burning velocity: $\mathrm{Ka}_c \simeq g\alpha/(S_L S_T^\theta)$.

Using this definition of the critical Karlovitz number, it was possible to roughly collapse the data where V to M flame topology transitions take place for different bulk flow injection velocities varying from U = 7 to 25 m·s^{-1}, for lean combustible mixtures with equivalence ratios comprised between ϕ = 0.5 and 0.9 and with Lewis numbers covering the range $0.55 \leq \mathrm{Le} \leq 0.97$. This is valid for bluff body anchored and aerodynamically stabilized swirled flames with swirl numbers comprised between $0.30 \leq \mathrm{S} \leq 0.68$.

It is difficult to provide absolute values of the critical Karlovitz numbers leading to V/M flame topology transitions and only relative values with respect to a reference case were presented in this study. The type of analysis developed in this study may however be used to guide the scaling of injectors and combustion chambers featuring the same flame topologies.

Further work needs to consider heat losses to the combustor peripheral wall as an additional mechanism altering these flame topology transitions. Heat losses to walls are known to delay flashback of laminar flames and were not considered in the present study. It is finally worth recalling that the flashback mechanism identified and analyzed in this study only holds when the swirling jet of reactants impinges the combustion chamber peripheral wall at a relatively high velocity. For combustion chamber featuring a larger cross section or swirled jets with a lower impulsion at the injection nozzle outlet, or any situations where the V flame tip is not directly in contact with the combustion cham-

ber peripheral wall, V/M flame topology transitions are associated to different mechanisms than those described in this chapter.

Chapter 5

Analysis of V to M shape transitions of weakly confined premixed CH_4/H_2/air swirling flames

The objective of this chapter is to improve the knowledge of the physics leading to topology transitions in a swirled combustor when the flame does not interact directly with the combustor peripheral walls. Experiments are conducted for a fixed low swirl number with a flame stabilized by the central rod. Effects of the combustible mixture composition, heat losses, and strain rate are investigated.

The experimental setup used for this investigation, the diagnostics and the flow conditions explored are presented in section 5.1. The impact of the hydrogen enrichment in the fuel blend is analyzed in section 5.2, before considering the influence of the thermal boundaries of the combustor in section 5.3. Finally, the combined effects of heat losses and strain rate are analyzed experimentally and numerically in Sec. 5.4

5.1 Experimental setup

5.1.1 Combustor

The experimental setup used for these experiments is presented in Fig. 5.1. The flow is put in rotation by the radial swirling vane featuring a fixed vanes angle θ = 35°. This yields a swirl number S = 0.4 measured at the outlet of the injector (see Fig. 1.9). A 6 mm diameter central rod installed on the burner axis helps anchoring the flame at the injection unit outlet 2 mm above the dump plane. The flame is stabilized in a squared combustion chamber featuring four quartz windows. One quartz window can also be replaced by a water-cooled

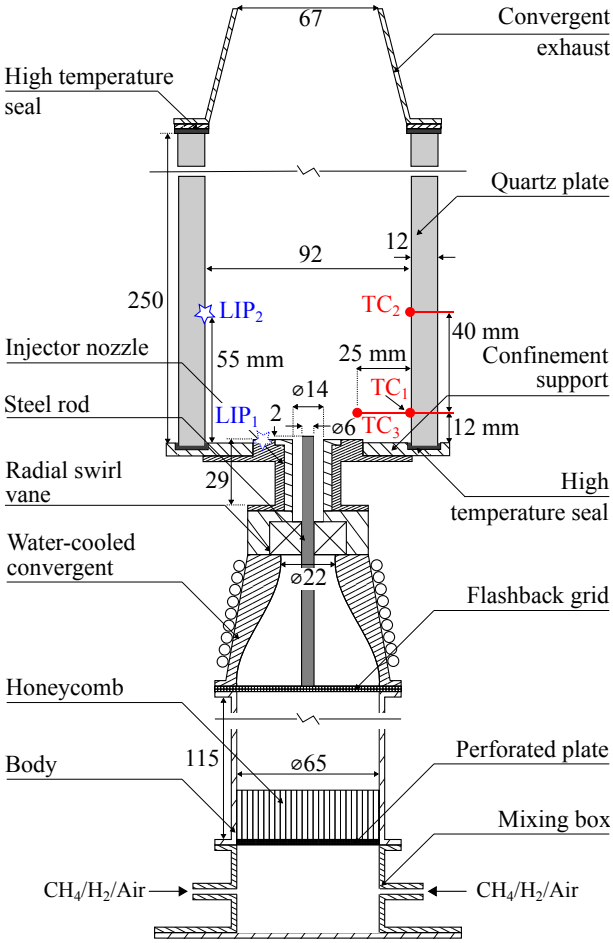

Figure 5.1: *Schematic of the test-rig with the diagnostics. The position of thermocouples is indicated by red circles. Blue stars denote the position of Laser Induced Phosphorescence (LIP) measurements on a quartz window of the chamber and on the injector dump plane.*

stainless-steel wall as shown in Fig. 1.7. This element is used to modify the wall temperature of the combustion chamber by adjusting the water mass flowrate, $\dot{m}_{water}$, through the cooling channels.

The burner is operated here with equivalence ratios $0.70 < \phi < 0.79$ at a constant thermal power of 4 kW. Experiments presented in this chapter were thus conducted at a roughly fixed bulk flow velocity U = 14 m.s^{-1} at the injector outlet.

5.1.2 Diagnostics

Particle Imaging Velocimetry (see Sec. 2.5) is used to characterize the flow under reactive conditions. Longitudinal and transverse planar Laser Induced Fluorescence of the hydroxyl radical (see Sec. 2.4) measurements are carried out to delineate the location of the flame front and burnt gases and infer the shape taken by the flame. The Nd:YAG laser was tuned to excite the $Q_1(6)$ transition of OH at 282.927 nm. Fluorescence was imaged onto a 512(H)x512(V)-pixels^2 ICCD camera (Princeton Instruments, PIMax) equipped with a 40 nm bandpass filter (Semrock, FF01-320/40) centered at 320 nm. Images within transverse planes were recorded off-axis through a quartz wall. The rotation of the plane of sharp focus was achieved using a Scheimpflug adapter. The geometrical distortions induced were corrected during post-processing of the OH-PLIF images.

The chemiluminescence of the flame is also used to infer the shape taken by the flame. Chemiluminescence imaging is realized with an ICCD camera. The chemiluminescence signal is also collected with two PMT recording the light originating from different regions of the flame. These data are used to determine the time resolved flame shape. The first PMT (see Sec. 2.3) records the signal emitted from the entire reaction region and a second PMT probes the signal originating from the OSL as shown in Fig. 5.2. The instantaneous shape of the flame is deduced with a high repetition rate of 20 kHz by comparing the two PMT signals.

Laser Induced Phosphorescence measurements (see Sec. 2.6) are also carried out to determine the temperatures of the quartz walls and of the dump plane of the combustion chamber at different locations. Only one of the four quartz walls is covered with phosphor over its full width and over 1/3 of its height starting from the dump plane. The conductive resistance of this wall is thus weakly altered. Radiative transfers may also be slightly modified due to a decrease in the wall transmittance. OH-PLIF experiments were thus conducted in the presence of the painted wall to take these phenomena into account. In the ORZ, the fluid that is loosing enthalpy by heat transfer to the combustor walls is interacting with the reactive region. The temperature of the burnt gases in the ORZ near

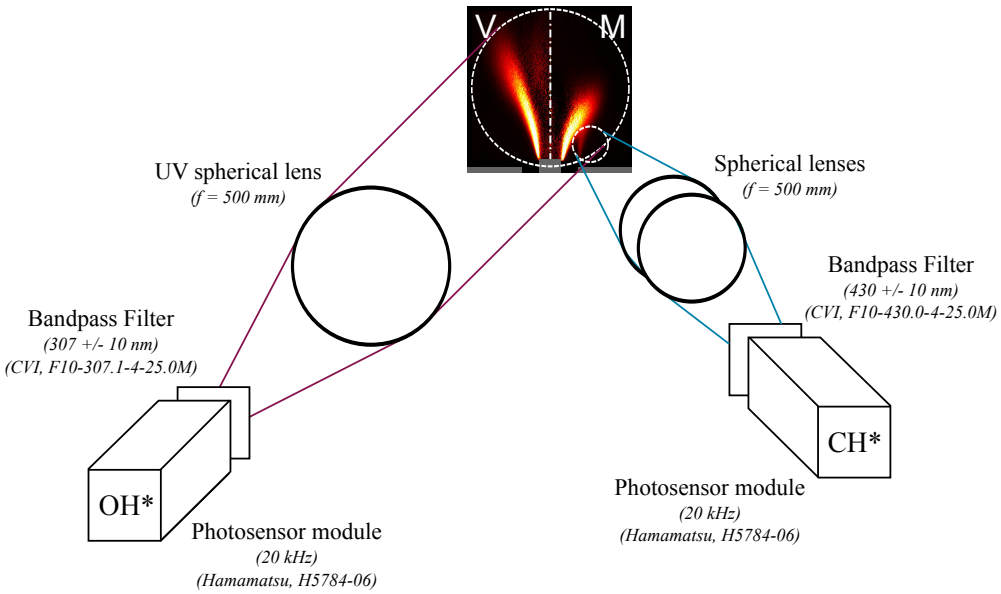

Figure 5.2: *Schematic of the chemiluminescence setup used to infer the time-resolved flame shape.*

the OSL of the swirling jet is measured to characterize its influence on the flame topology. These measurements were realized with thermocouples penetrating the ORZ through one of the four vertical steel bars holding the quartz walls at the corners of the combustion chamber. Two additional 1.5 mm diameter type K thermocouples TC_1 and TC_2 shown in Fig. 5.1 are used to probe the surface temperature of the same steel bar at two different heights.

5.2 Effect of H_2 enrichment

The influence of the hydrogen enrichment on the topology of the flames is demonstrated in Fig. 5.3 by examining the OH^* chemiluminescence distribution in axial planes for $0.55 < X_{H_2}^{fuel} < 0.86$. These images were obtained by accumulating the light over 100 ms. The height of the flame decreases rapidly with hydrogen enrichment. This results from the change in the laminar burning velocity that increases from $S_L = 0.31\ m \cdot s^{-1}$ when $X_{H_2}^{fuel} = 0.55$ and $\phi = 0.70$ to $S_L = 0.66\ m \cdot s^{-1}$ for $X_{H_2}^{fuel} = 0.86$ and $\phi = 0.70$. Secondly, flames with $X_{H_2}^{fuel} < 0.70$ take a V shape while for $X_{H_2}^{fuel} \geq 0.70$, OH^* emission is also detectable in the OSL. The intensity of the signal in the OSL increases with the hydrogen enrichment. A possible explanation is that in many snapshots used to obtain the average images shown in Fig. 5.3, the flame stabilizes with an M shape. However, the signal intensity originating from the OSL is lower than the one in the ISL. Another possibility is that OH^* emission from the flame front located

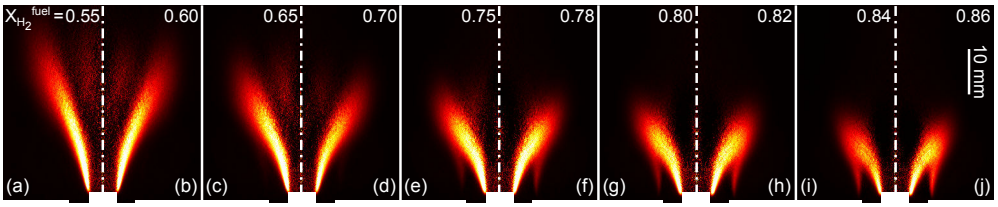

Figure 5.3: *Abel deconvoluted images of the OH* chemiluminescence integrated over* 100 ms *for* $X_{H_2}^{fuel}$ = 0.55, 0.60, 0.65, 0.70, 0.75, 0.78, 0.80, 0.82, 0.84, *and* 0.86. *Only one half of each flame is represented.*

in the OSL is less intense.

Figure 5.4a shows instantaneous OH-PLIF images in the axial and transverse planes for a hydrogen enrichment $X_{H_2}^{fuel}$ = 0.60. The flame is in this case only anchored on the central rod tip and takes a V shape. The flame front lies in the ISL formed between the fresh combustible jet mixture and the IRZ filled with burnt gases. Figures 5.4b to 5.4d show different snapshots of the OH-PLIF signal when the hydrogen concentration is increased to $X_{H_2}^{fuel}$ = 0.70. At this higher hydrogen enrichment, the flame is still anchored on the central rod, but the flame intermittently switches between a V (Fig. 5.4b) and an M shape (Fig. 5.4d). The M flame features an additional reaction front in the OSL comprised between the swirling jet and the ORZ. An intermediate asymmetric state also exists where an additional reaction front protrudes in the OSL, but the reaction does not cover the full azimuthal plane as shown in Fig. 5.4c.

Figure 5.5 maps the probability distribution of the presence of burnt gases obtained by averaging over 1000 instantaneous binarized OH-PLIF images in the transverse plane 5 mm above the central rod tip. Results are examined when the hydrogen concentration increases from $X_{H_2}^{fuel}$ = 0.55 to 0.78. The inner red circle in these images indicates the size of the IRZ in the wake of the central rod. It has a diameter slightly larger than 6 mm that increases with hydrogen enrichment. This region is always filled with burnt gases yielding a probability p = 1. The additional ring appearing in images Fig. 5.5c-f lies in the OSL region that eventually hosts a flame front. The probability of this annular region to be filled with burnt gases increases with the hydrogen enrichment from p = 0.01 for $X_{H_2}^{fuel}$ = 0.55. to p = 0.41 for $X_{H_2}^{fuel}$ = 0.78. These probabilities are smoothly distributed along the azimuthal direction in all transverse cuts explored. It can be concluded that the flame is roughly axisymmetric in average even if the combustion chamber has a square cross section. This is probably the case because the flame lies far away from the combustor walls.

Kim et al. (2010) found that the propensity of a premixed swirling flame to stabilize with an M shape depends on its laminar burning velocity. Figure 5.6

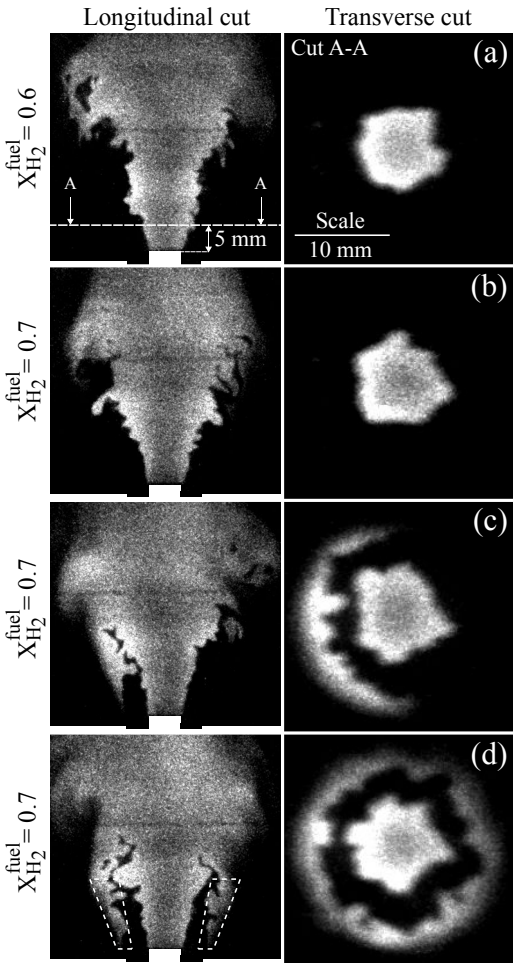

Figure 5.4: *Axial (left) and transverse (right) OH-PLIF snapshots for* $X^{fuel}_{H_2}$ = 0.60 *(a) and* $X^{fuel}_{H_2}$ = 0.70 *((b) (c) (d)). The dashed line in (a) indicates the transverse plane used for measurements* 5 mm *above the central rod tip. Axial and transverse measurements are not synchronized in these images.*

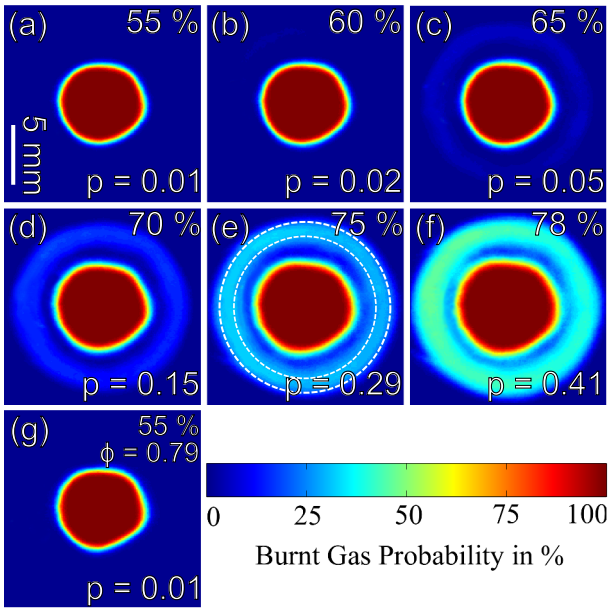

Figure 5.5: *Averages over 1000 binarized transverse OH-PLIF images giving an indication of the presence of unburnt and burnt gases. The probability to stabilize an M shape flame is obtained by average over the annular region delineated by the two dashed circles in (e) and is denoted p. (a)-(f)* $X_{H_2}^{fuel} = 0.55$ *(*$S_L = 0.31\ \mathrm{m \cdot s^{-1}}$*), 0.60, 0.65, 0.70 (*$S_L = 0.42\ \mathrm{m \cdot s^{-1}}$*), 0.75, and 0.78 for* $\phi = 0.70$*. (g)* $X_{H_2}^{fuel} = 0.55$ *and* $\phi = 0.79$ *(*$S_L = 0.42\ \mathrm{m \cdot s^{-1}}$*).*

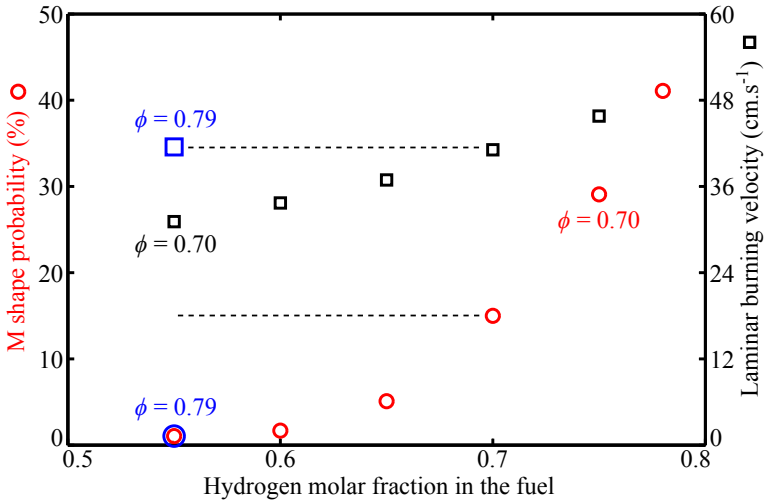

Figure 5.6: *M shape probability measured by OH-PLIF (left axis) and calculated laminar burning velocity S_L (right axis) as a function of the hydrogen enrichment. All flames feature an equivalence ratio $\phi = 0.70$ except one where $\phi = 0.79$ (blue symbols).*

plots the evolution of the M shape probability measured by OH-PLIF and of the calculated laminar burning velocity S_L as a function of the hydrogen enrichment. The M shape probability increases with the laminar burning velocity as observed by Kim et al. (2010). The calculated laminar burning velocity is $S_L = 0.31\ \mathrm{m \cdot s^{-1}}$ for the case $X_{H_2}^{fuel} = 0.55$ and $\phi = 0.70$ shown in Fig. 5.5a. It reaches the same value $S_L = 0.42\ \mathrm{m \cdot s^{-1}}$ for $X_{H_2}^{fuel} = 0.70$ and $\phi = 0.70$ shown in Fig. 5.5d, and for $X_{H_2}^{fuel} = 0.55$ and $\phi = 0.79$ shown in Fig. 5.5g. These results show that two different M shape probabilities can be obtained with the same laminar burning velocity. The laminar burning velocity is then not the main parameter controlling these shape bifurcations.

It is also worth interpreting these results by examining the adiabatic flame temperature reached by these flames featuring the same laminar burning velocity. Hydrogen enrichment moderately modifies the flame temperature compared to changes of the equivalence ratio. In Fig. 5.5g the V flame has a higher temperature $T_{ad} = 2019$ K than in Fig. 5.5d where $T_{ad} = 1899$ K for a configuration where the probability of taking an M shape is higher. These calculations show that the adiabatic flame temperature is also not the main parameter controlling these shape bifurcations. These experiments highlight effects of hydrogen enrichment on the propensity to stabilize an M flame, but it is difficult to explain these patterns with the low repetition rate of the OH-PLIF diagnostic used.

Figure 5.7 shows the temporal evolutions of the OH^* and CH^* emissions captured by the two synchronized PMT. The PMT with the OH^* filter records the light originating from the whole flame and the PMT with the CH^* filter only

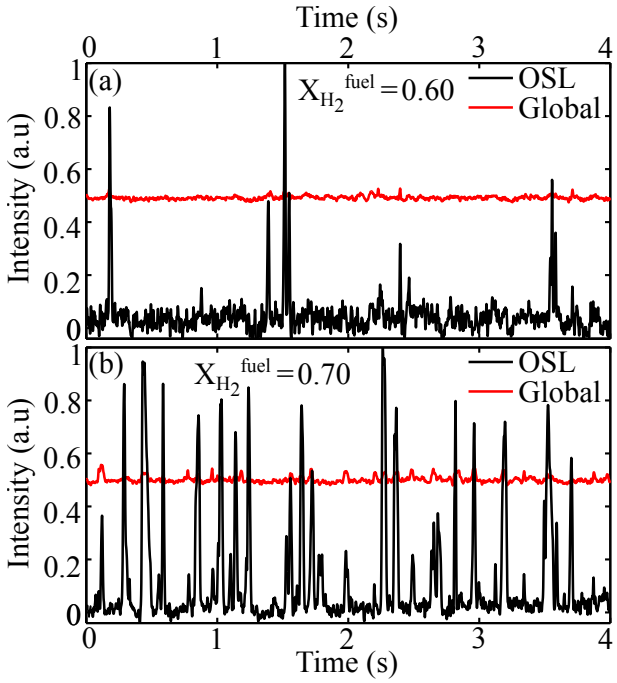

Figure 5.7: *Normalized intensity of the chemiluminescence integrated over the whole flame region (red) and over the OSL region (black) as a function of time for* $X_{H_2}^{fuel} = 0.60$ *(a) and* $X_{H_2}^{fuel} = 0.70$ *(b).*

collects the light emitted from the OSL region as shown in Fig. 5.4. The signal integrated over the entire flame shows a nearly uniform level for both flames at $X_{H_2}^{fuel} = 0.60$ and $X_{H_2}^{fuel} = 0.70$. The light emitted is proportional to the total heat release rate and remains thus roughly constant for fixed injection conditions as explained for example by Palies et al. (2010). The PMT focused on the OSL detects emission peaks eventually emerging from a constant baseline. These peaks reveal the presence of a flame front in the OSL, *i.e.* an M shaped flame. As already observed with OH-PLIF experiments, Fig. 5.7a and b show that M flames are unstable and have a very short lifetime for these flow operating conditions. Moreover, the black peaks appear randomly in Fig. 5.7. A power spectral analysis of these signals did not reveal any particular peak frequency. The flame with $X_{H_2}^{fuel} = 0.70$ features many peaks in Fig. 5.7 and only a few events can be observed at $X_{H_2}^{fuel} = 0.60$. This is in agreement with the previous conclusions based on OH-PLIF experiments. It is possible to calculate the M shape probability as the time ratio $p = t_{peak}/t_{total}$ where t_{peak} stands for the total time during which peaks are detected and t_{total} is the total experiment duration $t_{total} = 48$ s.

Figure 5.8a plots this probability p to stabilize an M flame calculated with the PMT signals as a function of the hydrogen enrichment. It is shown that

p drastically increases with $X_{H_2}^{fuel}$ and ranges from p = 0 to p = 0.81 when the hydrogen enrichment varies from $X_{H_2}^{fuel}$ = 0.50 to $X_{H_2}^{fuel}$ = 0.86. The M shape probabilities calculated with the PMT signals in Fig. 5.8a are in agreement with the probabilities deduced from OH-PLIF experiments in Fig. 5.6. This test confirms that the peaks detected by the PMT correspond to states with M shaped flames. The number of peaks detected first increases with $X_{H_2}^{fuel}$ but it reaches a maximum for $X_{H_2}^{fuel}$ = 0.80 before going down when $X_{H_2}^{fuel}$ is further increased. This implies that the mean duration of the peaks is modified by the hydrogen enrichment. Figure 5.8b confirms that the mean duration of the detected peaks increases from 8 ms to 122 ms when the hydrogen enrichment increases from $X_{H_2}^{fuel}$ = 0.55 to $X_{H_2}^{fuel}$ = 0.86. One can safely conclude that increasing the hydrogen concentration in the fuel blend strongly enhances the stability of eventual flame fronts hosted in the OSL. In addition, Figure 5.8b shows that the mean time lapse between two peaks, indicating the mean time needed before a V flame transits to an M flame, decreases when $X_{H_2}^{fuel}$ increases. To conclude, adding hydrogen to the fuel strongly increases the M shape probability as it promotes V to M shape flame transitions and strengthens the flame front in the OSL of M flames.

5.3 Effect of thermal boundaries

The colored streamlines plotted in Fig. 5.9 indicate that many burnt gas fluid particles in the ORZ interacting with the combustion chamber walls are transported by the flow towards the OSL. The residence time of these fluid particles is deduced from the streamlines plotted in Fig. 5.9. The residence time from the quartz wall to the OSL corresponds roughly to about 40 ms, i.e. twice the time necessary to travel from the image right boundary to the OSL. Note that this residence time, obtained by integration of 2-D velocity fields measured by PIV in the longitudinal plane, does not account for the out of plane velocity component of the flow field induced by swirl and turbulence. However, due to the rotational symmetry of the flame, the expected differences are small. This large residence time indicates that substantial heat transfer takes place between the combustion chamber walls and the ORZ and that cooled combustion products are convected to the OSL. The situation in the ORZ differs from that in the IRZ where the burnt gases mainly recirculate at a temperature closer to the adiabatic flame temperature because of the limited surface area of the central rod (Euler et al. (2014)). Flame fronts stabilized in the OSL are more subjected to extinction due to heat losses in comparison to those lying in the ISL.

It is then interesting to examine the probability to stabilize an M flame as a

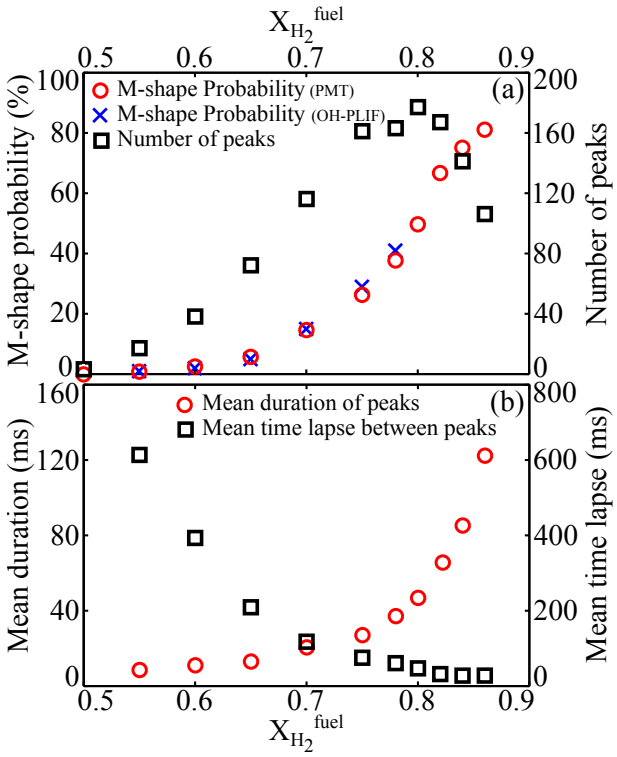

Figure 5.8: *(a) M shape probability p (circle) and number of peaks (square) detected by the PMT corresponding to V/M shape transitions, as a function of the hydrogen enrichment during* 48 s. *Blue crosses show the M shape probability deduced from transverse OH-PLIF measurements. (b) Mean duration of the peaks (circle) and mean time lapse between the peaks (square) detected by the PMT as a function of the hydrogen enrichment.*

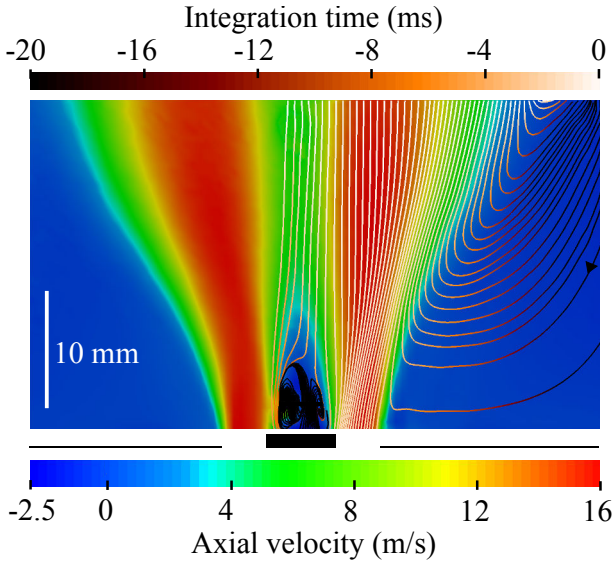

Figure 5.9: *Axial velocity measured by PIV in the axial plane (bottom color bar) for* $X_{H_2}^{fuel} = 0.60$ *and* $\phi = 0.70$. *The dark blue regions delineate the IRZ and ORZ regions with negative velocities. The colored streamlines superimposed show the recirculating flow regions and the integration time (top color bar) gives an indication of the time needed for a fluid particle to escape the measurement area through the image upper boundary. Note that the image limits do not correspond to the combustor boundaries. The central rod and the dump plane locations with respect to the investigated flow region are indicated below.*

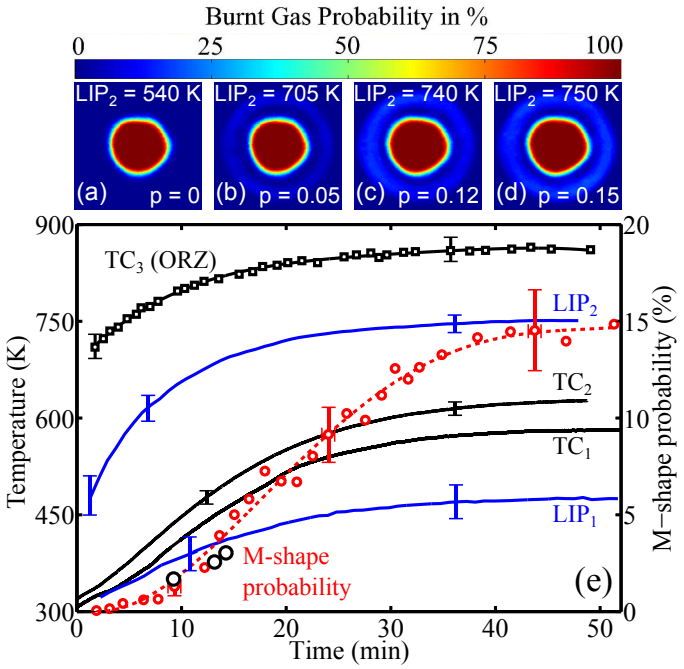

Figure 5.10: *(a)-(d) Averages over 400 instantaneous binarized transverse OH-PLIF images for* $X_{H_2}^{fuel}$ = 0.70 *when the time evolves from ignition to steady state. The temperature reached at* LIP_2 *during OH-PLIF measurements and the corresponding M shape flame probability are indicated. (e) Evolution of the temperature reached at different positions in the combustion chamber with time. Blue and black solid lines respectively stand for LIP and thermocouple surface measurements. Black square symbols represent thermocouple measurements in the ORZ. Red circle symbols show the probability to stabilize an M shape flame as a function of time. Black circle symbols stand for the M shape probability for the experiments with the water-cooled plate.*

function of the surface temperature reached by the combustor walls. This is realized by following the evolution of the shape of the flame with time from ignition to steady state for $X_{H_2}^{fuel}$ = 0.70 and ϕ = 0.70. The wall surface and burnt gas temperatures reached at the five different positions indicated in Fig. 5.1 are recorded as well. Results are presented in Fig. 5.10. The temperature reached at steady state by the inner walls of the chamber strongly depends on the measurement position. LIP_2 and TC_2 measurements yield different temperatures because TC_2 is located on a steel surface away from the combustion region, while LIP_2 is located on a quartz window closer to the flame. As expected, the temperature of the burnt gases in the ORZ and at the chamber walls are below the flame adiabatic temperature. The time needed to reach thermal steady state also slightly varies with the position considered. After 45 min the temperature at point TC_2 featuring the highest thermal inertia reaches a constant value equal to TC_2 = 627 K.

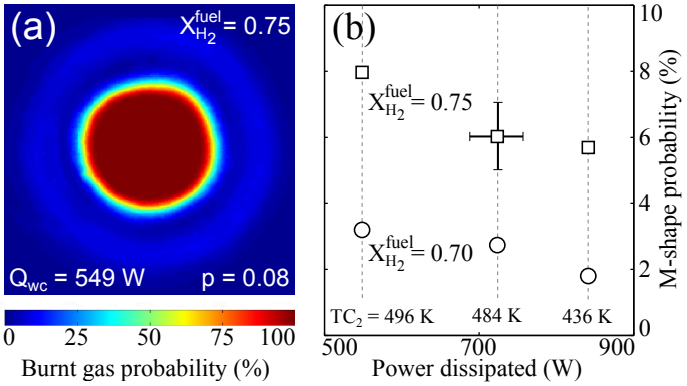

Figure 5.11: *(a) Averages over 1000 instantaneous binarized transverse OH-PLIF images for* $X_{H_2}^{fuel} = 0.75$, $\phi = 0.70$ *and* $\dot{Q}_{wc} = 549$ W *(*$\dot{m}_{wc} = 6.3 \times 10^{-3}$ kg$\cdot$s^{-1}*). (b) M shape probability as a function of the thermal power* $\dot{Q}_{wc}$ *dissipated in the water-cooled wall for* $\phi = 0.70$, $X_{H_2}^{fuel} = 0.70$ *(circle symbols) and* 0.75 *(square symbols).*

The M shape probability is zero shortly after ignition (Fig. 5.10a) due to the relatively low temperature $TC_3 \simeq 710$ K reached by the gases in the ORZ. When the temperature of the chamber walls increases, the temperature in the ORZ raises as well. As a consequence, the probability to stabilize an M flame increases and reaches p = 0.05 when $LIP_2 = 705$ K (Fig. 5.10b). It further increases with time and reaches p = 0.12 when $LIP_2 = 740$ K (Fig. 5.10c). At steady state, after 45 minutes, all temperatures are stabilized. The temperature reached in the ORZ is $TC_3 \simeq 860$ K. The M shape probability remains constant and equal to p = 0.15 in agreement with the value found in Fig. 5.5d. These measurements show the major influence of the thermal boundary conditions of the combustor walls on the shape taken by these swirling flames during ignition and warm-up phases of the test-rig.

Experiments are now carried out at steady state by controlling the temperature of one of the combustor side walls. The quartz window from this wall has been replaced by a stainless steel water cooled plate. The water mass flowrate and temperature difference in this heat exchanger are recorded. The thermal power exchanged through this wall may then be deduced. Figure 5.11a shows an image averaged over 1000 instantaneous binarized transverse OH-PLIF images for $X_{H_2}^{fuel} = 0.75$, $\phi = 0.70$ and a mass flow rate of cooling water $\dot{m}_{water} = 6.3 \times 10^{-3}$ kg$\cdot$s^{-1} in the heat exchanger. The M shape probability is drastically reduced in this new configuration. It drops from p = 0.29, in Fig. 5.5e in the absence of this additional heat exchanger, to p = 0.08 in this new configuration as shown in Fig. 5.11b when the thermal power dissipated through the wall is increased. It is also worth noting that the intensity in the image is homogeneously distributed in the azimuthal plane, indicating that the impact of the water-cooled wall is not strictly limited to the flow region di-

rectly located in front of the heat exchanger. This may be attributed to the swirl motion and turbulence that intensify mixing of burnt gases in the ORZ. Similar behaviors were found for all experiments conducted with this setup. These experiments also indicate that inaccuracies in the knowledge of thermal boundary conditions, even on a restricted surface area of the combustor, may lead to large differences on the observed flame shapes.

Effects of hydrogen enrichment on the M shape probability are plotted in Fig. 5.11b as a function of the thermal power $\dot{Q}_{wc}$ transferred to the heat exchanger. This latter quantity is obtained by measuring the cooling-water temperature increase and mass flow rate. It reaches here successively $\dot{Q}_{wc}$ = 549, 724, and 841 W for the three cases explored and corresponds to approximately 14%, 18% and 21% of the flame thermal power. The temperature reached by TC_2 is also indicated Fig. 5.11b. Increasing heat losses through one of the combustor side walls decreases regularly the probability to stabilize an M flame for experiments conducted at thermal steady state independently of the hydrogen enrichment in the combustible blend. Figure 5.11 also shows that the probabilities found with the water cooled side wall correspond to the values found in Fig. 5.10 during the warm-up phase of the combustor without cooling system, when the combustor temperature TC_2 is the same.

These experiments demonstrate that the temperature reached by the hot gases in the ORZ has a major influence on the shape taken by these swirling flames. Hydrogen enriched CH_4/air mixtures feature extended flammability limits in comparison to CH_4/air mixtures (Giovangigli and Smooke (1987), Giovangigli and Smooke (1989), Ren et al. (2001)). Hydrogen enriched CH_4/air are thus less sensitive to strain rate. The strong influence of the hydrogen enrichment and of the thermal boundary conditions on the M shape probability suggest that the combined effects of strain rate and heat losses in the OSL may be responsible for M to V shape transitions.

5.4 Role of strain rate on extinction

Previous OH-PLIF and PMT experiments revealed that flames stabilized with an M shape are unstable and always transit back to a V shape after a small lapse of time that depends on the hydrogen enrichment in the combustible mixture. The velocity field determined by PIV is used to understand under which circumstances flame fronts can or cannot be stabilized in the OSL region. As it was not possible to stabilize M flames for a long duration with this setup, it was necessary to synchronize PIV experiments with longitudinal OH-PLIF visualizations to associate the two dimensional velocity field to the shape taken by the flame at the same instant. The flame shape is deduced from instanta-

neous OH-PLIF images by examining the mean pixel intensity integrated over the dashed region defined in Fig. 5.4d. These values are then compared to a fixed threshold value to define the shape taken by the flame. This procedure is used to define the shape taken by the flame on its left and right sides. When the integrated intensity is higher than the threshold value, an M shaped flame is detected while the flame has a V shape when the integrated intensity is below the threshold value. Figure 5.12 shows the mean of 1080 binarized OH-PLIF images conditioned to the flame shape. These images give an indication on the probability to find hot burnt gases at a given position within the flow.

We define four cases corresponding to flames taking a V shape at the left (Fig. 5.12a), a V shape at the right (Fig. 5.12b), an M shape at the left (Fig. 5.12c), or an M shape at the right (Fig. 5.12d). Both V and M flames has a reaction layer stabilized in the ISL. In this region, the burnt gases probability is comprised between 0 and 1. This indicates that the instantaneous flame front fluctuates with time in the ISL, yielding a flame brush thickness of a few millimeters. Unlike V shaped flames, M flames host a flame front in the OSL where the burnt gases probability is comprised between 0 and 1. In the OSL of an M flame, the burnt gases probability regularly decreases when the distance to the injector is reduced. This indicates that the flame front lying in the OSL of an M flame is not necessarily anchored at the injector outer rim. This also indicates that cases with a flame front hosted in the OSL that is not connected to the upper flame region are quite improbable. Figs. 5.12e and 5.12f plot the contours of the flow region having a burnt gases probability that differs from zero. These zones differ between V and M flames but the contours of these zones are similar in both cases excepted in the OSL region. In particular, the flame angle in the wake of the bluff-body is not affected by the flame shape. One can safely conclude that the size of the IRZ is not altered by the shape taken by the flame. Moreover, the plume of burnt gases is independent of the flame shape far from the injector.

We now focus on the analysis of the velocity fields in the OSL and ORZ regions. Figures 5.13a and 5.13b show the conditional 2-D mean velocity fields in a longitudinal plane for V and M shaped flames. Due to the rotational symmetry, only the left part of flames is represented. The contour of the hot burnt gases region is superimposed to ease comparison with Fig. 5.12. The velocity fields of both V and M shaped flames feature a jet of high velocity at the injector outlet and a low velocity region defining the ORZ of burnt gases. From a distance, velocity fields show strong similarities for both flame shapes. Differences are highlighted when the two velocity fields are subtracted. In Fig. 5.13c, the modulus of the 2-D velocity field conditioned to the V flame is subtracted to the 2-D velocity field conditioned to the M flame. Regions yielding zero values correspond to regions where the 2-D velocity field is not affected by the shape taken by the flame. Large differences can be observed in the OSL. In

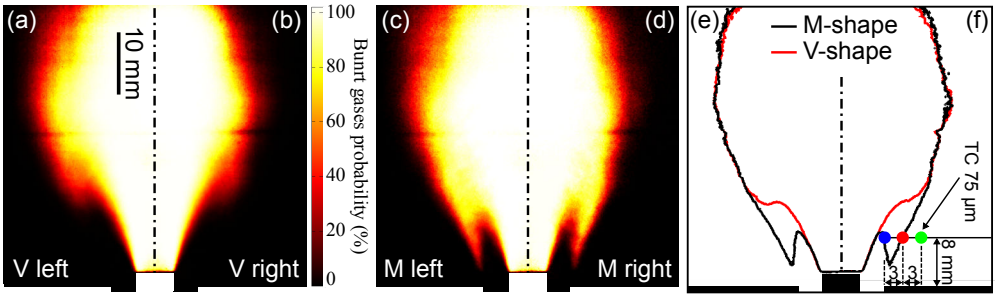

Figure 5.12: *Conditional mean of 1080 binarized longitudinal OH-PLIF images giving the probability of presence of hot burnt gases for the flames featuring a V shape at the left (a), a V shape at the right (b), an M shape at the left (c), and an M shape at the right (d) for* $X_{H_2}^{fuel}$ = 0.70. *(e)-(f) Contour of the zones featuring a non zero probability of hot burnt gases for the mean V (red) and M shape (black) flames. Dots show the position of the* 75 µm *type R thermocouple in the OSL (blue), near the GMLI (red), and in the ORZ (green).*

this region, the flame front, that is only present for M shaped flames, generates thermal expansion and accelerates the flow. The maximum velocity difference reaches $5\,\mathrm{m}\cdot\mathrm{s}^{-1}$ for the case explored. The ORZ is barely modified by this thermal expansion because the velocity difference is close to zero in this region.

It is also interesting to notice that the limit of the ORZ, where the radial velocity changes its sign, corresponds in both cases to the hot burnt gases contour. This contour, that delineates zones with and without OH-PLIF signal, defines the Gas Mixing Layer Interface (GMLI) (Coriton et al. (2013)) where hot burnt gases recently produced by the flame front hosted in the OSL interact with the recirculating burnt gases cooled in the ORZ. In the ORZ, the chemical equilibrium of burnt gases is shifted towards H_2O due to the drop of enthalpy and the OH concentration is drastically reduced (Davidson et al. (1989) and Lam et al. (2013)). Consequently, the OH-PLIF signal drops rapidly. Four zones of interest may then be drawn for M shaped flames: the flame front located in the OSL, the GMLI located few millimeters between the flame front and the ORZ, the hot burnt gases region delimited by the flame front and the GMLI, and the ORZ. These zones can also be defined for instantaneous OH-PLIF images corresponding to M flames. Figure 5.14 shows the temporal evolution of the signal from the PMT collecting the light emitted from the OSL. This figure also plots the temperature in the OSL (a), GMLI (b), and ORZ (c) as a function of time for $X_{H_2}^{fuel}$ = 0.70. The positions of the 75 µm type R thermocouple measuring these temperatures are indicated in Fig. 5.12f. For the thermocouple located in the OSL, *i.e.* close to the flame front of an M flame, the temperature rapidly increases when a V to M transition is detected and reaches values lower but close to the adiabatic flame temperature T_{ad} = 1897 K.

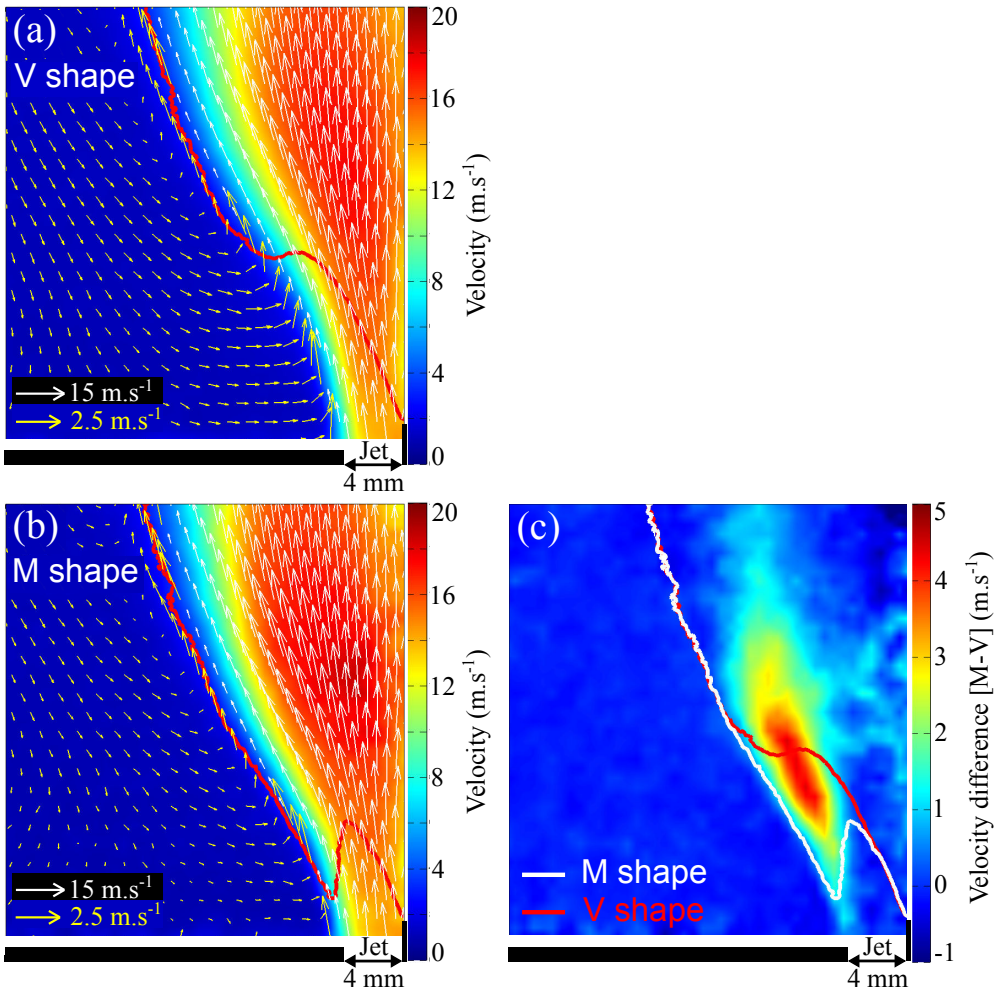

Figure 5.13: *Conditional mean velocity derived from 1080 PIV shots when the flame has a V shape (a) or an M shape (b) for* $X_{H_2}^{fuel} = 0.70$. *The red line shows the limit of the zone featuring a non zero probability of presence of hot burnt gases. (c) Difference of the conditional mean velocity [M shape flame - V shape flame]. The red and white lines respectively show the limit of the zone featuring a non zero probability of presence of hot burnt gases for the mean V and M shaped flames.*

When the thermocouple is placed in the GMLI, the correlation between CH^* emission and temperature peaks persists but the maximum temperature during transition events is drastically reduced. This is attributed to the fast cooling of the burnt gases recently produced in the OSL when they reach the GMLI. Finally, for measurements conducted in the ORZ, the correlation between CH^* emission and the temperature is lost. The thermal expansion of gases is restrained by the ORZ and the heat produced by the flame front located in the OSL does not reach the thermocouple. These observations confirm the conclusions drawn during the analysis of Fig. 5.13c.

In conclusion, Figs. 5.12 to 5.14 indicate that in the case of an M flame, the supplemental flame front hosted in the OSL generates nearly adiabatic burnt gases that cannot fully expand in the post-flame region due to the presence of a counterflow of cooled burnt products in the ORZ. Under these circumstances, it is safe to assume that the latter flame front is submitted to compressive strain. Coriton et al. (2013) studied the effects of strain rate on the interaction of turbulent premixed flames with counterflowing combustion products. They showed that lean $CH_4/O_2/N_2$ turbulent premixed flames may be subjected to localized extinctions for bulk strain rates of the order of few thousands of s^{-1} especially when the counterflowing burnt gases are cooled. Therefore extinctions of the flame elements in the OSL due to high strain rates may explain the M to V shape transitions that we observe. The objective of the following paragraphs is to determine the value of the strain rate reached in our configurations. This value will be compared to the calculated extinction limits for lean CH_4/H_2/air premixed laminar flames.

Figure 5.15a shows an example of instantaneous joint PIV and OH-PLIF experiment. In this example, the flame features an M shape. It is possible to identify the flame front and the GMLI positions from the OH-PLIF image. The situation is comparable to the one studied by Coriton et al. (2013) because a few millimeters thick flame region can clearly be defined between the flame front and the GMLI. However, our configuration is not fully representative of 2-D turbulent premixed flames with counterflowing products. It is not easy to evaluate the effective strain rate based on instantaneous images. We decided to use the conditional mean longitudinal velocity fields to calculate a characteristic value of the strain rate for the M shaped flames investigated. Figure 5.15b shows the mean conditional hot burnt gases probability for the M flame superimposed to streamlines deduced from PIV measurements. The position of the mean flame front and the GMLI are also indicated. The GMLI is located very close to a line where the radial velocity component vanishes ($u = 0$). This difference is lower than 0.5 mm and can be attributed to the PIV spatial resolution and to the threshold value used for the GMLI detection using OH-PLIF images. In the following, we use $u = 0$ to identify the location of the GMLI.

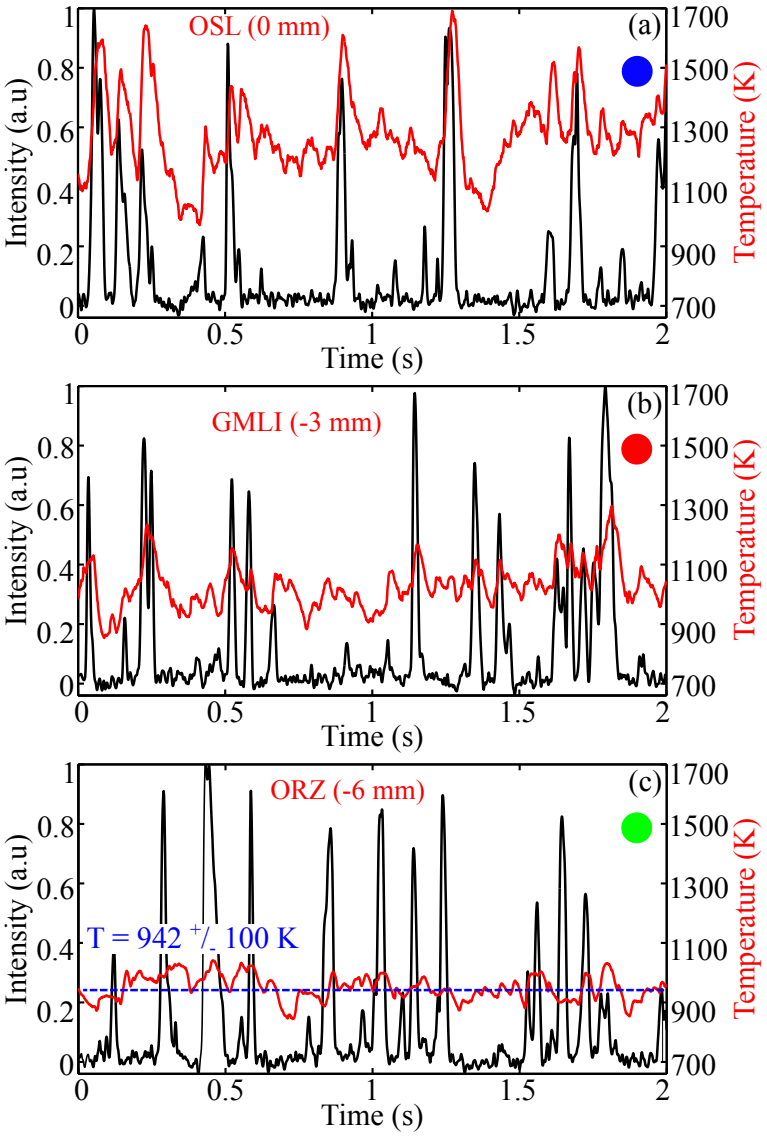

Figure 5.14: *(a) Normalized intensity of the CH* chemiluminescence integrated over the OSL (black) and temperature (red) in the OSL (a), the GMLI (b), and the ORZ (c) as a function of time for* $X_{H_2}^{fuel} = 0.70$.

The mean flame front shown in Fig. 5.15b corresponds to the border of the OH-LIF signal at the fresh reactants jet interface and is nearly vertical. By analogy to 2-D turbulent premixed flames with counterflowing products, the mean compressive strain rate is inferred from the gradient of the radial velocity component along the normal of the flame front. This direction corresponds here to the radial direction as shown by the yellow dashed line in Fig. 5.15b.

In Fig. 5.15b, the distance between the flame front and the GMLI is not constant and increases when the distance from the injector increases. It is useful to define a normalized radius to compare these evolutions at different heights. This normalized radius is set to 0 in the flame front and 1 in the GMLI. Consequently, the physical distance between 0 and 1 is not conserved when the distance from the injector is modified. Figure 5.16 shows the mean radial (a) and axial (b) velocity profiles along the normalized radius of the M flame. Profiles at three different heights are plotted. The abscissa axis is reversed to ease comparison with Fig. 5.15. Due to the swirl imparted to the flow, the radial velocity component u increases with the radial distance r in the jet of fresh gases and reaches a maximum close to the flame front. This maximum velocity reached by the flow depends on the distance to the injector and is lower close to the injector. In the jet, the mean axial velocity v takes a value slightly higher than the bulk flow velocity $U = 14$ m.s^{-1} and decreases close to the OSL. Behind the flame front, the mean radial velocity u linearly decreases and reaches zero in the GMLI. The mean axial velocity v also decreases. It is possible to calculate a strain rate K_b in the burnt gases, which are compressed between the flame front and the GMLI. The strain rate K_b is the slope of the linearly decaying mean radial velocity and is expressed in s^{-1}.

Figure 5.16c plots the evolution of the strain rate K_b measured in these experiments as a function of the axial distance to the rod tip. In all cases, $1300\,\text{s}^{-1} < K_b < 1750\,\text{s}^{-1}$ and a mean value of the strain rate in the burnt gases is $\overline{K_b} = 1500\,\text{s}^{-1}$. This value can be compared to values found in laminar counter-flow simulations. We did not intend here to determine the additional contributions of turbulence to the strain rate (Mastorakos et al. (1995), Kostiuk et al. (1993b)). The mean value found for the strain rate $\overline{K_b}$ is of the same order of magnitude as values of the strain rates found by Coriton et al. (2013) leading to localized extinctions of turbulent premixed $CH_4/O_2/N_2$ flames with counterflowing products. This results confirms that extinction due to strain rate is probably at the origin of M to V shape transitions. However, the combustible mixture of interest in our study differs from that studied by Coriton et al. (2013) because it includes an important concentration of hydrogen and the flame resistance to strain is altered (Wu and Law (1985), Giovangigli and Smooke (1987), Giovangigli and Smooke (1989), Ren et al. (2001), and Guo et al. (2010)). The temperature of the counterflowing products is also not the same. It is necessary to compare the strain rates measured by PIV to extinc-

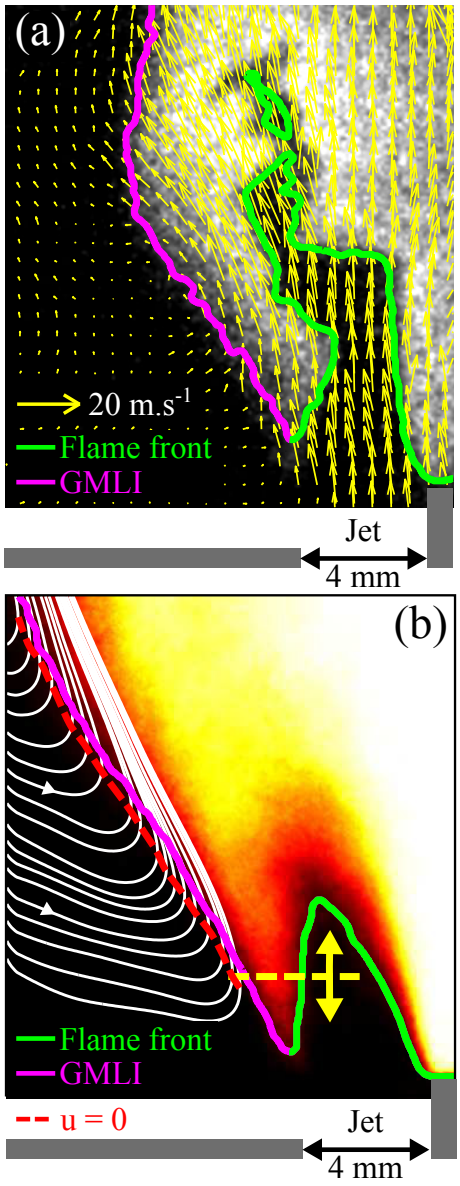

Figure 5.15: *(a) Example of simultaneous OH-PLIF and PIV measurements for* $X_{H_2}^{fuel}$ = 0.70. *The green and pink lines respectively delineate the flame front and the GMLI. (b) Conditional mean of binarized longitudinal OH-PLIF images featuring an M shape. Streamlines extracted from the corresponding conditional mean velocity are superimposed to highlight the ORZ. The contour where the radial velocity reaches* $u = 0$ *is represented by the red dashed line.*

tion limits of lean CH_4/H_2/air mixtures using adequate counterflowing product temperatures. A numerical analysis is proposed in the following to gain further insight into the extinction process leading to M to V shape transition.

5.5 Numerical analysis

A numerical analysis is conducted to better characterize the flame sensitivity to strain rate and to the temperature of counterflowing products within the ORZ. As mentioned previously, focus is made here on the outer flame front only present for M shaped flames. A collection of 2-D strained premixed flames has been computed using the REGATH solver (Candel et al. (2011)). The simulated configuration consists in a 2-D steady isobaric laminar premixed flame stabilized between two counter-flows as shown in Fig. 5.17(a). A CH_4/H_2/air mixture is injected from one side with a constant equivalence ratio ϕ = 0.70 and a constant temperature T_f = 298 K. Three different fuel compositions are considered here to analyze the impact of hydrogen enrichment in the fuel blend: $X_{H_2}^{fuel}$ = 0.60, 0.70, and 0.80. The opposite injector is fed with burnt gases of the same premixture for which a given enthalpy defect is applied. For that purpose, the equilibrium composition of fresh gases at an imposed temperature has been computed for each CH_4/H_2/air mixture composition. The burnt gases temperature varies between the adiabatic flame temperature reached in the absence of heat losses and the minimum temperature set here to 800 K approximately. The temperature range selected for the injection of burnt gases corresponds to the range of measured temperatures of the recirculating burnt gases found in Fig. 5.14.

Results for $X_{H_2}^{fuel}$ = 0.70 are illustrated in Fig. 5.17(b). This figure plots the flame consumption speed S_c as a function of the imposed strain rate K_b in the burnt gases for different temperatures of the counterflowing burnt gases. The consumption speed S_c is computed as:

$$S_c = 1/(\rho^u Y_F^u) \int_{-D/2}^{D/2} \rho \dot{\omega}_{Y_F} dy \tag{5.1}$$

where Y_F denotes the fuel mass fraction $Y_F = Y_{CH_4} + Y_{H_2}$ and the superscript u denote the unburnt gas state. The quantity D is the separation distance between the two burner injectors and y is the axial coordinate along the burner axis as shown in Fig. 5.17(a). The upper curve plotted in Fig. 5.17(b) corresponds to results obtained with counterflowing burnt gases at the adiabatic flame temperature. Each curve located below this reference curve corresponds to results obtained by decreasing the burnt gases temperature with intervals of 50 K. The last point of each curve denotes the maximum strain rate K_b^{max} before flame extinction. Two main regions can be identified in Fig. 5.17(b):

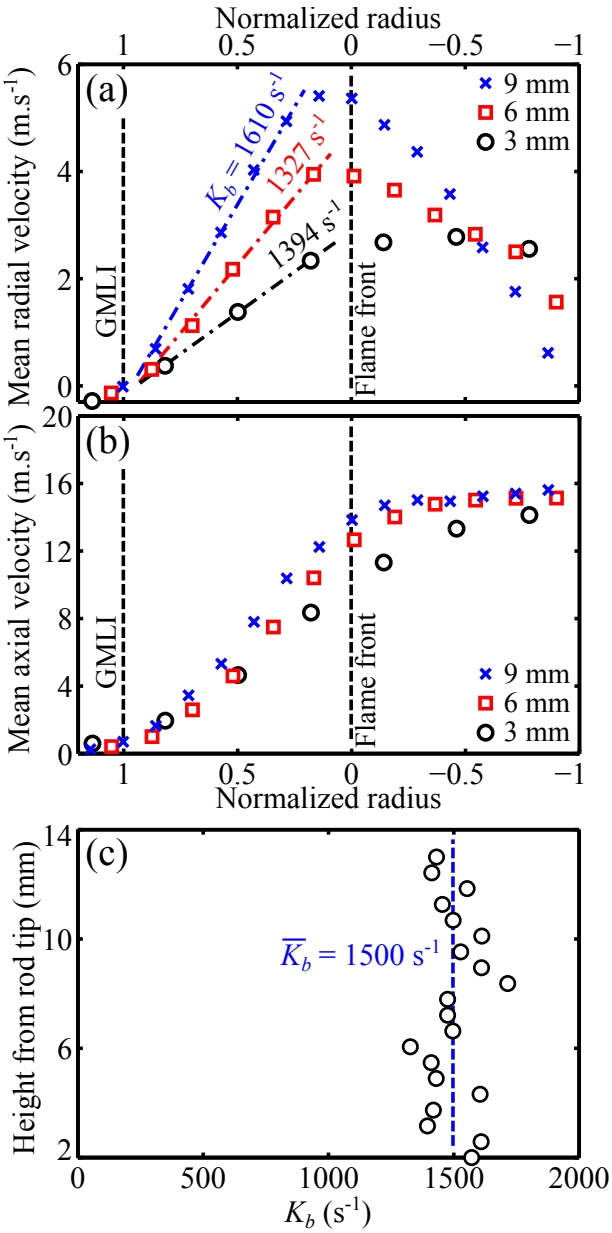

Figure 5.16: *Conditional mean radial (a) and axial (b) velocity for the M flame as a function of the normalized radius for* $X_{H_2}^{fuel}$ = 0.70 *at different heights above the rod tip. The positions 0 and 1 respectively correspond to the flame front and GMLI. The physical distance between 0 and 1 varies with the height above the rod tip. The dashed-dotted lines indicate the linear regressions of the radial velocity between the flame front and the GMLI that are used to determine the strain rates value* K_b*. (c) Measured strain rates* K_b *in the OSL region as a function of the height above the rod tip.*

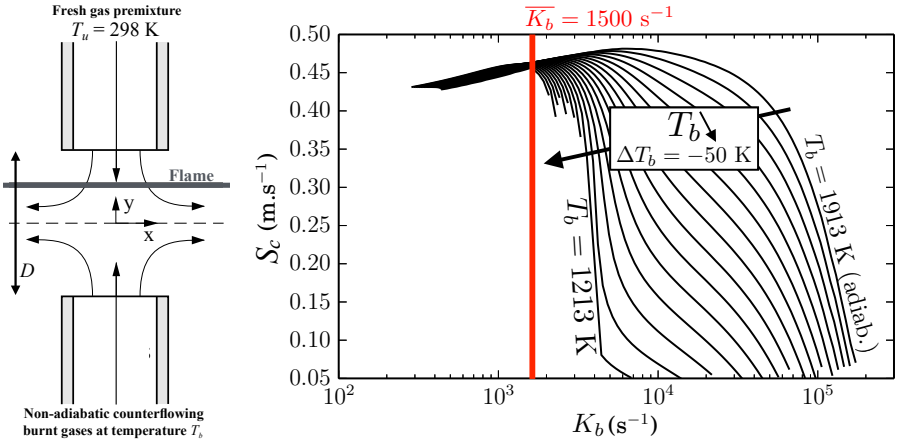

(a) Counterflow flame numerical configuration.

(b) Evolution of the flame consumption speed S_c as a function of the temperature of counterflowing burnt gases T_b and strain rate K_b. The temperature T_b is reduced from the adiabatic flame temperature (T_b = 1913 K) to T_b = 813 K by intervals of 50 K. Results are plotted for $X_{H_2}^{fuel}$ = 0.70.

Figure 5.17: *Numerical analysis of the impact of heat losses and strain rate on the consumption speed of 1-D laminar premixed strained flames.*

1. For strain rates lower than K_b = 1500 s^{-1}, all the curves are approximately superimposed. The strain rate is small enough to avoid that the counterflowing burnt gases modify the flame reaction layer. Therefore, the flame consumption speed does not depend on the level of heat losses seen by the burnt gases. The consequence for the turbulent premixed flames investigated in this work is that when the local strain rate at the outer flame front position is sufficiently low, the turbulent flame front can subsist within the OSL resulting in an M shaped flame.
2. When the strain rate becomes higher than the critical value of about K_b = 1500 s^{-1}, the flame consumption speed becomes a function of the enthalpy defect. For the adiabatic case T_b = 1913 K, the maximum strain rate before flame extinction K_b^{max} is higher than 1.0×10^5 s^{-1}. When heat losses increase, the flame reaction layer gets more and more altered by burnt gases and the extinction strain rate rapidly decreases to reach a value of 6.0×10^3 s^{-1} when T_b = 1213 K. For the range of burnt gases temperatures comprised between T_b = 1913 K and 1213 K, the consumption speed S_c progressively decreases and reaches small values when T_b = 1213 K. When heat losses are sufficiently large, *i.e.* when T_b < 1213 K, the consumption speed S_c drops very sharply and leads to flame extinction.

Figure 5.17(b) also shows the mean strain rate value $\overline{K_b}$ = 1500 s^{-1} deduced

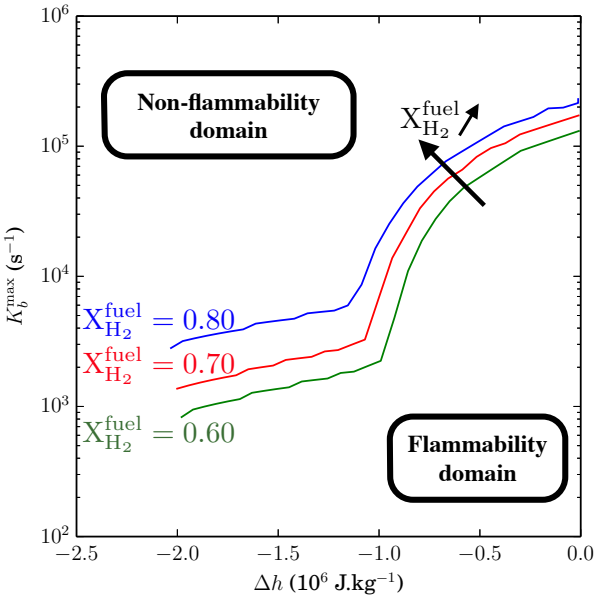

Figure 5.18: *Maximum strain rate $K_b^{\max}$ before flame extinction as a function of the enthalpy defect Δh for three different combustible mixture compositions $X_{H_2}^{fuel}$ = 0.60, 0.70, and 0.80.*

from the experiments in the outer flame front region shown in Fig. 5.16. It is worth noting that the mean temperature measured within the ORZ is equal to $\overline{T}_{ORZ} \simeq 947$ K as shown in Fig. 5.14. The maximum strain rate before flame extinction $K_b^{\max}$ found in these simulations is of the order of magnitude of the measured mean strain rate $\overline{K_b} = 1500\ s^{-1}$. The flow being turbulent, slight variations of the local strain rate around the mean strain rate $\overline{K_b}$ may then lead to sudden extinctions of the outer flame reaction layer stabilized in the OSL. These simulations again confirm that the combination of strain and heat losses is at the origin of extinction of flame elements within the OSL leading to M to V shape transitions.

The impact of the fresh gases composition on flame extinction limit is now analyzed. Figure 5.18 plots the maximum strain rate $K_b^{\max}$ before flame extinction takes place as a function of the enthalpy defect Δh. The enthalpy defect is introduced here to allow the comparison of different mixtures with varying thermochemical properties. The quantity Δh represents the heat lost by the unit mass of mixture due to heat exchange with the combustor walls and is defined as $\Delta h = h_b - h_{ad}$, where h_b is the current sensible plus chemical enthalpy of burnt gases and h_{ad} denotes the enthalpy of adiabatic burnt gases. The flammability domain of the combustible mixture is located below the flame extinction limit. Each curve corresponds to a given fuel composition $X_{H_2}^{fuel}$ = 0.60, 0.70, and 0.80 in Fig. 5.18. Increasing the fraction of H_2 in the fuel

blend $X_{H_2}^{fuel}$ leads to an important modification of the flammability limit, especially if the enthalpy defect is high. The flammability domain widens when $X_{H_2}^{fuel}$ increases showing that the flame front is able to sustain higher strain rates and higher enthalpy defects. This conclusion corroborates the experimental analysis conducted in Sec. 5.2 showing that the M shape probability increases with the fraction of hydrogen in the fuel blend.

5.6 V to M shape flame transition

A mechanism leading to the extinction of the outer flame front of an M flame has been proposed in the previous section. Heat losses in the recirculating burnt gases associated to a sufficiently high strain rate govern the M to V shape transitions. However, the proposed mechanism does not explain the creation of new outer flame fronts leading to V to M shape transition. Two different scenarios can lead to the apparition of a new flame front in the OSL region:

1. Auto-ignition of the injected fresh gases in the GMLI due to the heating by the burnt gases recirculating in the ORZ.
2. Flame propagation from downstream towards the injector outer rim through the OSL.

In order to discriminate which phenomenon is more likely to explain the V to M shape transition, a deductive approach is proposed here. For that purpose, focus is made on operating conditions exhibiting a non-negligible probability to get a V to M shape transition. Therefore, the case $X_{H_2}^{fuel} = 0.70$ is selected to test the auto-ignition scenario. A series of 0-D simulations of autoignition of combustible mixtures has been carried out with the REGATH solver.

The calculations are started with a mixture of fresh gases at $T_u = 298$ K and burnt gases at temperature T_b. The temperature T_b is then varied from the adiabatic flame temperature of the fresh mixture to a temperature of $T_b \simeq 800$ K. The composition of the mixture is determined by a mixing ratio between fresh and burnt gases defined as $\alpha = V_b/(V_b + V_f)$ where V_f and V_b are the volume of fresh and burnt gases respectively. Figure 5.19 shows the computed auto-ignition time τ^i as a function of the burnt gases temperature T_b and the molar dilution ratio α. The colored region represents ignition delays τ^i lower than $\tau^i = 1.0$ s. Above this threshold value, τ^i increases very sharply and auto-ignition cannot occur in the turbulent configurations investigated as the slowest time scale has been estimated to $\tau^{ORZ} \approx 40$ ms (see Sec. 5.3). It can be first noted that the domain where auto-ignition occurs in Fig. 5.19 is small compared to the investigated parameter range. Only high values of dilution ratio $\alpha > 0.65$ allow auto-ignition meaning that a very high turbulent mixing would be necessary to activate combustion chemical reactions.

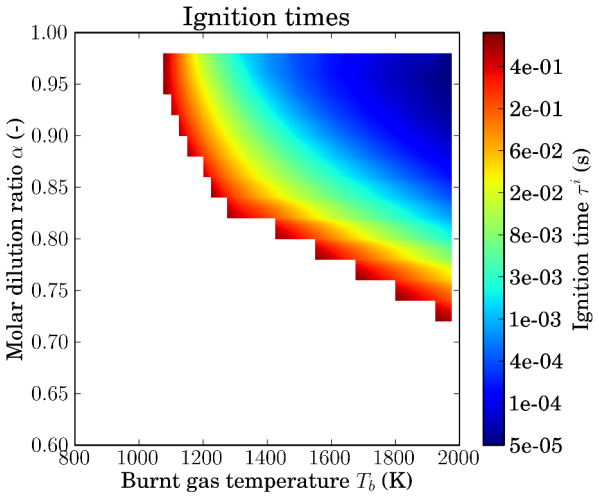

Figure 5.19: *Auto-ignition time τ^i (colormap) as a function of the burnt gases temperature T_b and the molar dilution ratio α between burnt and fresh gases. Results correspond to the case* $X_{H_2}^{fuel} = 0.70$.

Moreover, as shown in Fig. 5.14, the temperature of the burnt gases in the ORZ is almost constant and equal in average to $\overline{T_b} = 947$ K. This value seems to be out of the auto-ignition range even if very high dilution ratios by burnt gases are reached. Consequently, auto-ignition does not seem to be the appropriate mechanism explaining the apparition of the outer flame front leading to V to M flame shape transitions. Turbulent flame front propagation through the OSL remains the only possible explanation for the considered transition mechanism.

Different attempts were made to validate this hypothesis experimentally by capturing a transition event with a camera. Longitudinal OH-PLIF experiments at a repetition rate of 10 Hz were insufficient to observe this transition as only one shot is available during a V to M shape transition. We did not conduct similar experiments at higher repetition rates. We felt that it would be difficult to discriminate auto-ignition events taking place in the lower parts of the OSL and a turbulent flame front propagation starting outside of the laser sheet and crossing the latter as it progresses towards the injector rim due to the swirl motion of the flow. Both situations would lead to the apparition of an isolated reaction zone in the OSL intersected by the laser sheet and lead to the stabilization of an M shape flame. We found similar conclusions when we conducted OH^* chemiluminescence experiments at a 3 kHz repetition rate during V to M shape transition events. In this case, line-of-sight integration of the OH^* signal collected by the camera made any interpretation of the images difficult and it was not possible to conclude on the mechanism leading to V to M shape flame transition.

In addition, Figs. 5.12c-d and 5.15b also show that the probability to find hot burnt gases in the OSL regularly decreases from the flame tip to the injector rim. This means that in regions occupied by the OSL located far from the V flame tip, auto-ignition cannot be the main mechanism leading to V to M shape flame transition. This corroborates previous observations based on 0-D simulations of auto-ignition delays and allows to conclude that the transition from a V to an M shaped flame results from the propagation of a turbulent flame front in the OSL from the V flame tip towards the injector rim.

5.7 Conclusion

Flame shape bifurcations in a confined swirled burner were analyzed with detailed experiments and numerical simulations. It was first shown that increasing the hydrogen enrichment in the combustible mixture raises the probability of the flame to stabilize with an M shape. High hydrogen concentrations in the fuel blend promote transitions from V to M flames and increases the lifetime of M shaped flames.

It was then shown that the shape taken by the flame is controlled by the temperature reached in the outer recirculation zone of the burnt gases within the combustor. These gases being cooled by the combustor side walls, the probability of stabilizing an M flame is very sensitive to the combustion chamber walls temperature. Measurements during thermal transient of the combustor and at steady state confirm the predominant role of the thermal boundary conditions and the associated heat losses in the stabilization of premixed swirling flames.

Using simultaneous PIV and OH-PLIF experiments, we demonstrated that in the case of M flames, the flame front located in the OSL is subjected to high compressive strain rates due to the presence of cooled burnt gases recirculating in the ORZ. The mean value of the strain rate within the hot burnt gases located between the flame front stabilized in the OSL and the GMLI has been evaluated experimentally to $\overline{K_b} \simeq 1500\ \mathrm{s}^{-1}$.

Numerical simulations of laminar CH_4/H_2/air flames counterflowing with non-adiabatic burnt gases were conducted to calculate the flames extinction limits as a function of the hydrogen enrichment in the combustible mixture and the temperature of the counterflowing burnt gases. It was shown that the measured value for the strain rate $\overline{K_b} \simeq 1500\ \mathrm{s}^{-1}$ is lower but very close to the flame extinction limit found in the simulations for the measured burnt gases temperature $\overline{T_b} \simeq 947$ K.

M to V shape transitions were found to be controlled by the extinction of the flame front located in the OSL due to the combined effects of strain rate and

heat losses from the recirculating burnt gases. This mechanism also explains the influence of hydrogen enrichment on the probability to stabilize an M flame. The use of hydrogen extends flammability limits and increase the propensity of the flame to stabilize with an M shape.

Finally, 0-D calculations demonstrated that V to M shape transitions are not likely to be triggered by auto-ignition of the fresh gases within the OSL in contact with burnt gases because the computed auto-ignition delays are in all cases too important in comparison to the slowest flow time scale of the burnt gases recirculating in the ORZ. Transitions from V to M shaped flames are then inferred to be consecutive to turbulent flame propagation from the V flame tip towards the injector outer rim within the OSL.

Capturing this type of behavior is particularly challenging for simulations tools because the turbulent combustion model needs to take into account the cross effects of strain rate and heat losses in order to simulate the correct topology of these flames. The main difficulty resides in the ability of RANS or LES calculations conducted with a turbulent combustion model to capture the sharp drop in the flame consumption speed along the strain rate coordinate that controls extinction of reaction layer elements in contact with non-adiabatic burnt gases. This problem is addressed in the companion work of Mercier (2014).

Chapter 6

Influence of mass flow rate perturbations on the topology of CH_4/H_2/air swirling flames

The stabilization of CH_4/H_2/air swirling flames was analyzed in chapters 4 and 5. The objective of this chapter is to understand effects of unsteadiness on the topology of these flames. The flame response to mass flow rate perturbations at different forcing frequencies and amplitudes is analyzed.

The flame transfer function of a reference CH_4/H_2/air flame is first determined for two different perturbation amplitudes. This transfer function characterizes the frequency response of the flame in terms of heat release rate fluctuations due to incoming flow rate perturbations. These data are then used to select two forcing frequencies and further experiments are conducted using joint OH-PLIF, PIV, and chemiluminescence measurements at these specific forcing frequencies. These experiments reveal large coherent structures synchronized by the acoustic forcing which are interacting with the flame front and burnt gases. These vortical structures are detached from the injector rim during a modulation period and their interaction with the flame and the burnt gases located in the outer recirculation zone is analyzed in details.

Modulation of the flow produces coherent structures of different sizes. The impact of coherent structures that are smaller than the flame length is analyzed. It is shown that these small structures do not influence the shape taken by the reference CH_4/H_2/air flame.

Finally, the response of two CH_4/H_2/air flames, featuring different hydrogen enrichments, to a low frequency and high amplitude flow rate modulation yielding coherent structures larger than the flame length is analyzed. Changes of the mean flame topology resulting from these perturbations are described using

joint OH-PLIF/chemiluminescence measurements. This analysis of the flame dynamics allows a better understanding of the mechanisms driving flame shape transitions without flow modulation.

6.1 Experimental setup

6.1.1 Test rig

The experimental setup presented in Fig. 6.1 is close to that used in chapter 5 for the study of the impact of heat losses and hydrogen enrichment on the shape taken by confined swirling flames.

Velocity perturbations are generated by a loudspeaker located at the bottom of the burner, close to the injection holes of the combustible mixture. The reader is referred to Palies et al. (2010) for more details. The frequency and amplitude of the acoustic modulation are controlled by a Hi-Fi amplifier triggered by a signal synthesizer. Harmonic perturbations with a frequency f varying from 0 Hz (without modulation) to 370 Hz are produced. The amplitude of the resulting velocity perturbations is measured upstream the swirler by a hot wire (see Sec. 2.2). The instantaneous velocity u is recorded as a function of time and the fluctuating component of the velocity u', defined as $u' = u - \bar{u}$, where $\bar{u}$ denotes the mean component of the velocity, is determined by post-processing of the data. In the following, the level of the velocity modulation is characterized by the maximum normalized fluctuating velocity $max(u')/\bar{u}$ also noted $u'/\bar{u}$. It ranges in these experiments from $u'/\bar{u} = 0$ to $u'/\bar{u} = 0.33$.

The hydrogen enrichment in the combustible blend ranges from $X_{H_2}^{fuel} = 0.60$ to $X_{H_2}^{fuel} = 0.78$. The burner is operated here with a fixed equivalence ratio $\phi = 0.7$ and a thermal power of $P = 4\,\text{kW}$. Experiments are conducted at bulk flow velocities close to $U = 14\ \text{m.s}^{-1}$ at the injector outlet.

6.1.2 Diagnostics and methods

The hot wire is introduced in the jet of fresh gases 65 mm upstream the injector outlet and is set to measure the longitudinal velocity component of the flow. This device is calibrated with real gases *i.e* CH_4/H_2/air mixtures as described in chapter 2. The flame frequency response to flow rate modulations is determined by sweeping the forcing frequency of the electrical signal sent to the loudspeaker and recording the flame response to the excitation. For a fixed modulation level controlled by the hot wire, the flame transfer function can be determined for each forcing frequency. When the modulation level is also varied, one records

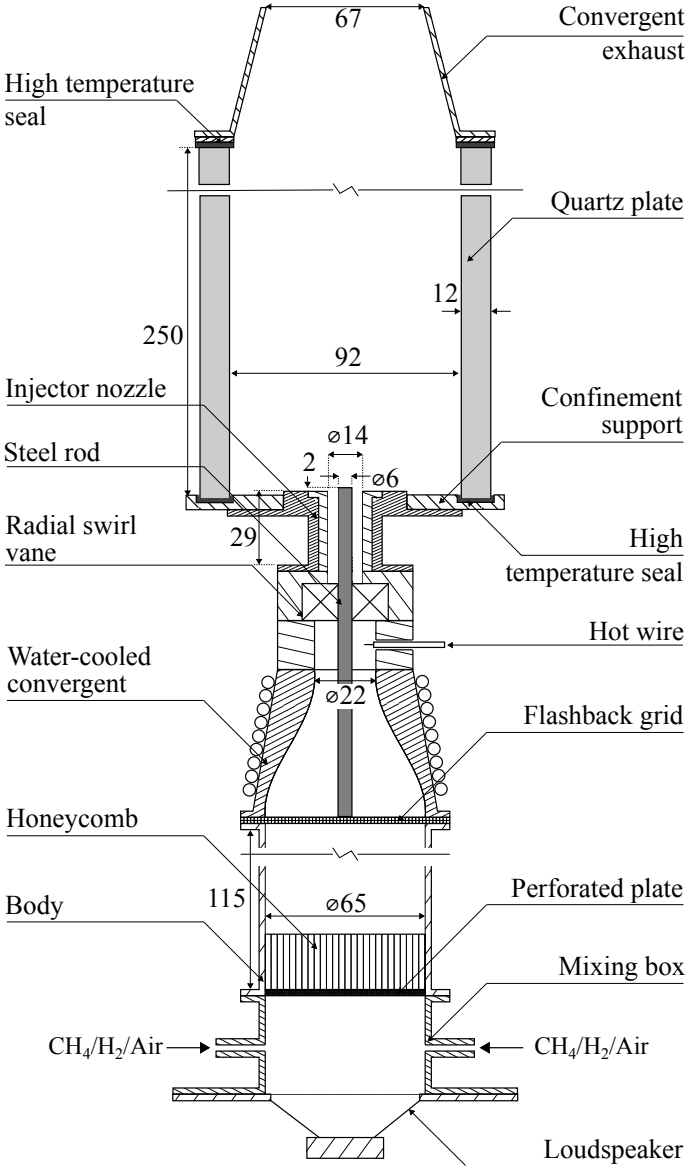

Figure 6.1: *Schematic of the test-rig with the loudspeaker at the bottom.*

the flame describing function defined by Noiray et al. (2008):

$$\mathscr{F}(f, u'/\bar{u}) = \frac{\dot{Q}'/\bar{\dot{Q}}}{u'/\bar{u}} \tag{6.1}$$

where $\dot{Q}'$ and $\bar{\dot{Q}}$ respectively stand for the fluctuating and mean components of the heat release rate and u' and $\bar{u}$ denote the fluctuating and mean velocity signal measured by the hot wire. The heat release rate is deduced from the flame chemiluminescence (Schuller et al. (2002), Palies et al. (2010)):

$$\mathscr{F}(f, u'/\bar{u}) = \frac{\dot{Q}'/\bar{\dot{Q}}}{u'/\bar{u}} \simeq \frac{I'/\bar{I}}{u'/\bar{u}} \tag{6.2}$$

where I represents the intensity of the light emitted by the OH^* chemiluminescence signal integrated over the whole flame region. The signal is collected with a photosensor module (PMT) featuring a 20 kHz bandwidth and a strong spectral response between 200 nm and 600 nm. The PMT is equipped with a 10 nm bandpass filter centered at 307 nm and is used to detect the OH^* global emission from the flame (see Sec. 2.3).

The response of the flame to mass flow rate perturbations was also analyzed at specific forcing frequencies by imaging the OH* chemiluminescence onto a 1024(H)x1024(V)-pixels^2 ICCD camera. The motion of the flame was captured for a selected number of phases during the period of the sinusoidal velocity modulation. Phase average images are obtained by accumulation of images at the same phase of the forcing cycles. The maximum integration time for single shot images was lower than 1/100 of the modulation period. Due to the large expansion of the flow at the injection tube outlet exhausting in the square chamber, the flames are nearly axisymmetric (see chapter 5). They also respond to longitudinal flow perturbations in an axisymmetric fashion. It is then possible to apply an Abel transform to the phase averaged images and infer the OH^* distribution in the central longitudinal plane.

The flow velocity in the central longitudinal plane was also characterized with PIV (see Sec. 2.5) for both unperturbed and perturbed flames. These experiments were conducted at $X_{H_2}^{fuel} = 0.60$ and $\phi = 0.70$ without excitation and with harmonic forcing at 160 Hz and 350 Hz. Five phases were selected in a modulation period and a minimum of 1000 PIV shots were recorded for each phase. A phase average method was again used to obtain a satisfying convergence of the mean flow field. In these PIV experiments, the vector spacing in both directions is equal to 520 µm.

Longitudinal OH-PLIF (see Sec. 2.4) measurements were also carried out to precisely delineate the location of the flame front and the burnt gases. The

laser is tuned to excite the $Q_1(6)$ transition of OH at 282.927 nm. Fluorescence was collected using the same optics and camera than the OH^* chemiluminescence measurements but the gate opening of the ICCD camera is here reduced to 50 ns. Longitudinal PIV and OH-PLIF experiments were conducted simultaneously in order to associate the velocity field to the corresponding shape taken by the flame.

6.2 Flame transfer function

The flame transfer functions of the reference flame $\phi = 0.70$, $X_{H_2}^{fuel} = 0.60$, and $U = 14\ m \cdot s^{-1}$ to incoming velocity fluctuations is determined for two different perturbation levels. Figure 6.2 shows examples of incoming velocity fluctuating signals measured with the hot wire for a harmonic modulation at $f = 350$ Hz and two different perturbation levels $u'/\bar{u} = 0.075$ and $u'/\bar{u} = 0.15$. Instantaneous signals and phase averaged normalized fluctuating velocities are plotted over two periods (blue curve in Fig. 6.2). Blue diamond symbols show the phase averaged normalized fluctuating velocity measured by PIV for five phases in the modulation period. Both measurements collapse on the same values indicating that the two measurement devices are well synchronized. For $u'/\bar{u} = 0.075$, the phase averaged velocity signal has a sinusoidal shape while instantaneous samples feature some dispersion of the data around the sinusoidal response. This is due to turbulent fluctuations of the flow field. When the perturbation level is increased to $u'/\bar{u} = 0.15$, the instantaneous velocity recorded by the hot wire is nearly sinusoidal and collapse onto the phase averaged data.

The normalized fluctuating heat release rate is also plotted as a function of time for the same operating conditions in Figure 6.2. The signal deduced from the summation of the pixel intensities over the ICCD camera chip is superimposed onto the signal deduced from the PMT when the perturbation level is set to $u'/\bar{u} = 0.075$. Both measurements collapse on the same values indicating that the devices are well synchronized and the heat release rate can be inferred from the PMT or from the ICCD camera.

Samples of the heat release rate signals at $u'/\bar{u} = 0.075$ and $u'/\bar{u} = 0.15$ both feature irregularities with respect to a pure harmonic response. This is attributed to the cumulative effects of the flame response to turbulence generated by the flow through the swirler and injection tube. When the signals are phase averaged over 1401 periods, they now both feature a sinusoidal shape with a low harmonic content. These data indicate that the flame response is linear for this forcing frequency $f = 350$ Hz when the perturbation level is lower than $u'/\bar{u} = 0.15$.

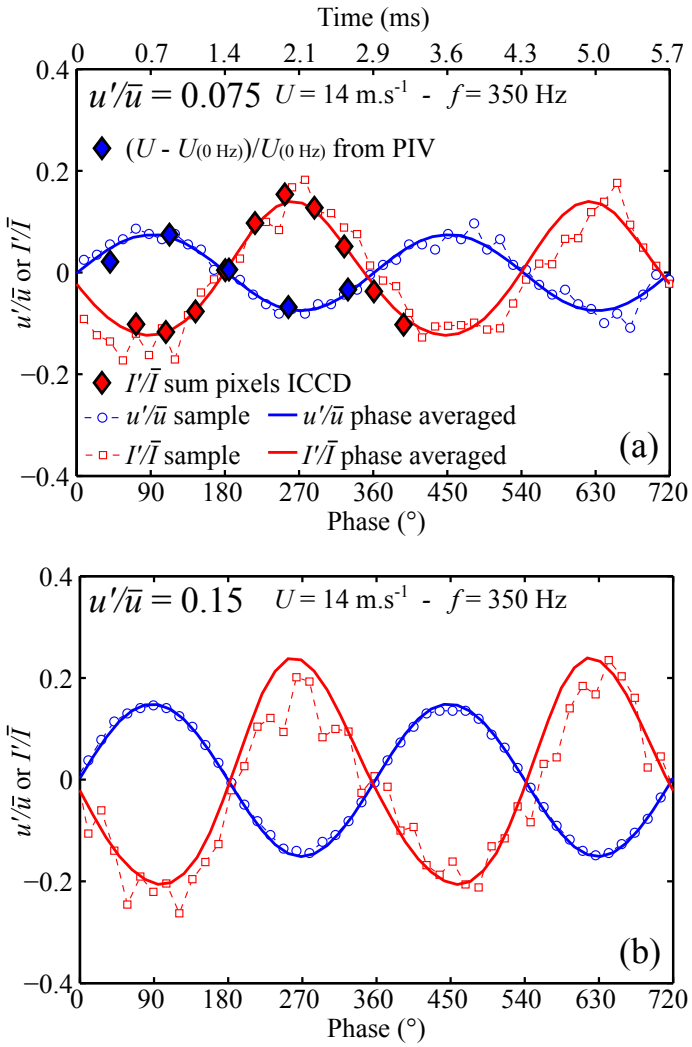

Figure 6.2: *(a) Normalized fluctuating velocity $u'/\bar{u}$ (blue) and light emission $I'/\bar{I}$ (red) as a function of the phase (lower axis) or time (upper axis) in the modulation cycle when the flame at $X_{H_2}^{fuel} = 0.60$, $\phi = 0.70$, and $U = 14\ \mathrm{m \cdot s^{-1}}$ is forced at a frequency $f = 350$ Hz with a perturbation level $u'/\bar{u} = 0.075$. Instantaneous and phase averaged signals are presented. The normalized fluctuating OH^* emission integrated over the ICCD pixel array and phase averaged over more than 500 images is superimposed to the PMT data (red diamonds). The phase averaged normalized fluctuating bulk flow velocity, obtained by integration of the PIV data, is also presented (blue diamonds). (b) Normalized fluctuating velocity $u'/\bar{u}$ (blue) and light emission $I'/\bar{I}$ (red) as a function of the phase (lower axis) or time (upper axis) when $f = 350$ Hz and $u'/\bar{u} = 0.15$.*

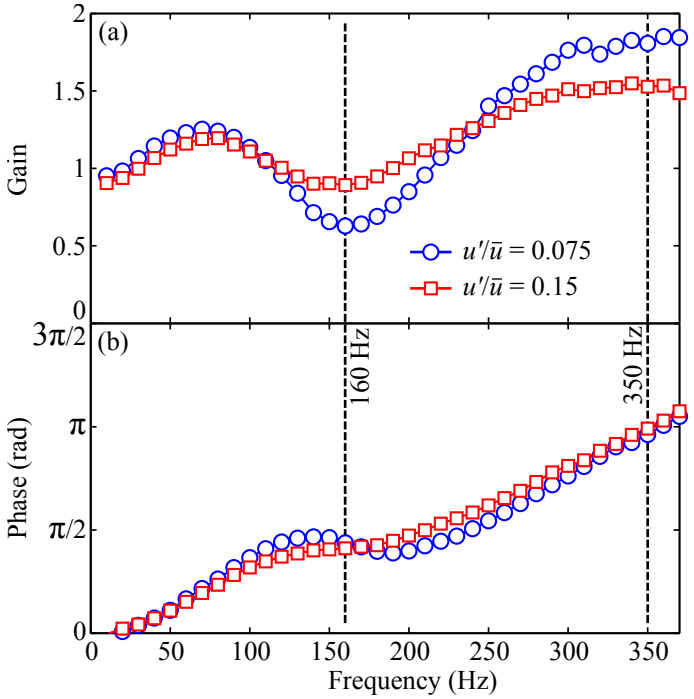

Figure 6.3: *Flame transfer functions deduced from hot wire and PMT measurements for the flame at* $X_{H_2}^{fuel}$ = 0.60, ϕ = 0.70, *and* U = 14 m · s^{-1} *and two different velocity perturbation levels:* $u'/\bar{u}$ = 0.075 *(blue) and* $u'/\bar{u}$ = 0.15 *(red).*

The gain G and phase φ between these two signals, defined by $I'/\bar{I} = Ge^{(i\varphi)}u'/\bar{u}$, can be calculated for these forcing conditions. The gain is G = 1.8 and the phase difference is $\varphi = 0.96\pi$ for a modulation frequency f = 350 Hz and an amplitude $u'/\bar{u}$ = 0.075. In this case the flame response is high as the incoming velocity fluctuations are amplified by the flame (G > 1). One should note that the phase reference is taken at the hot wire position located 65 mm below the central rod tip while the PMT captures the flame chemiluminescence downstream the rod tip. Longitudinal velocity disturbances within the injector propagate at the speed $u_{cv} \simeq U + c$, where U = 14 m · s^{-1} stands for the mean bulk velocity in the injection tube and $c \simeq$ 362 m · s^{-1} is the speed of sound for a CH_4/H_2/air gas mixture at $X_{H_2}^{fuel}$ = 0.60, ϕ = 0.70, and T = 298 K (Wang and Yang (2005), Palies et al. (2010), and Palies et al. (2011)). The time lag corresponding to the time needed for the longitudinal perturbations to reach the injector outlet is then $\tau_{cv} \simeq$ 0.17 ms. This duration corresponds to about 6% of the forcing period at 350 Hz and cannot be neglected (Truffin and Poinsot (2005)). This feature will be considered later to analyze the data.

The flame transfer function (FTF) is obtained by repeating the same experiments for a wide range of modulation frequencies at a fixed forcing amplitude. Figure 6.3 shows the FTF of the flame at $X_{H_2}^{fuel}$ = 0.60, ϕ = 0.70, and

$U = 14\,\mathrm{m}\cdot\mathrm{s}^{-1}$ for modulation frequencies ranging from 10 to 370 Hz and for two different amplitudes $u'/\bar{u} = 0.075$ and $u'/\bar{u} = 0.15$. At 0 Hz, the gain is close to unity (Polifke and Lawn (2007)). From 10 Hz to 70 Hz, the gain increases and reaches a local maximum at 70 Hz for the two forcing levels (G = 1.19 for $u'/\bar{u} = 0.075$ and G = 1.13 for $u'/\bar{u} = 0.15$). From 70 Hz to 160 Hz, the gain decreases and reaches a global minimum at 160 Hz. The global minimum is G = 0.85 for $u'/\bar{u} = 0.015$ and it drops to G = 0.60 for $u'/\bar{u} = 0.075$. Finally, above 160 Hz, the gain increases again and reaches a plateau for 310 Hz $< f <$ 370 Hz. The maximum gain is G = 1.75 for $u'/\bar{u} = 0.075$ and G = 1.46 for $u'/\bar{u} = 0.15$. These features are similar to the ones observed by Palies et al. (2010) for the FTF of lean CH_4/air rod-stabilized swirling flames with a larger swirl number. For $u'/\bar{u} = 0.15$, the local extrema of the gain are observed at the same frequencies as for $u'/\bar{u} = 0.075$ but their values are closer to unity. This type of feature was also observed by Palies et al. (2010), Kim et al. (2010), Komarek and Polifke (2010), and Kim and Hochgreb (2011) in their analysis of the frequency response of swirling flames.

For $u'/\bar{u} = 0.075$, the phase lag increases regularly with the frequency except in the region where the gain features a global minimum close to $f = 160$ Hz. For $f = 0$ to 120 Hz the phase lag increases nearly linearly. The corresponding time lag $\tau = \varphi/(2\pi f)$ is equal to $\tau_1 = 2.22$ ms in this frequency range. For higher frequencies when 200 Hz $< f <$ 370 Hz, the phase lag evolves again linearly with the forcing frequency but with a smaller rate of increase. One can deduce a second time lag $\tau_2 = \varphi/(2\pi f) = 2.02$ ms within this frequency range which is slightly smaller than first one deduced for low forcing frequencies.

It is interesting to compare these two values τ_1 and τ_2 to the time τ_c required by flow perturbations to convect from the injector lip to the flame tip (Durox et al. (2005)). The flame length L is deduced from OH^* flame images with the ICCD camera without acoustic excitation. One finds $L \simeq 28$ mm for these operating conditions. As a rough approximation, perturbations downstream the injector are convected at a speed close to the bulk flow velocity $U \simeq 14\,\mathrm{m}\cdot\mathrm{s}^{-1}$. One then finds $\tau_c \simeq L/U = 2.00$ ms. This value is close to the value found for the time lags τ_1 and τ_2.

For $u'/\bar{u} = 0.15$, the phase lag φ follows the same trend and increases nearly linearly with the modulation frequency. The inflection of the flame response between $f = 120$ and 200 Hz, which corresponds to the region featuring low values of the gain, is less marked than for the lower forcing amplitude $u'/\bar{u} = 0.075$. The FTF presented in Fig. 6.3 reveals two different characteristic frequencies: $f = 160$ Hz and $f = 350$ Hz where the gain G respectively reaches a global minimum and maximum.

6.3 Flame motion

Figure 6.4 shows phase averaged OH^* chemiluminescence images of the flame at $X_{H_2}^{fuel} = 0.60$, $\phi = 0.70$, and $U = 14\ m \cdot s^{-1}$ for ten different phases regularly distributed along a modulation period when the flame is submitted to harmonic flow rate modulations at $f = 160$ Hz and $u'/\bar{u} = 0.12$ (top) and $f = 350$ Hz and $u'/\bar{u} = 0.075$ (bottom). Due to rotational symmetry of the flame response with respect to the burner axis, an Abel transformation is applied to the images at each phase and only the left side of the flames is represented. It has already been verified that the normalized fluctuating heat release rate deduced from the images acquired with the ICCD camera yields the same result as the normalized fluctuating heat release rate deduced from measurements with the PMT. The phase averaged normalized fluctuating heat release rate is derived from ICCD images by summing the pixel intensity over the whole ICCD chip array and then removing the result obtained for the unperturbed flame. This fluctuating signal is finally normalized by the summation of the pixel intensities measured for the unperturbed flame.

The flame response to harmonic velocity modulations at $f = 160$ Hz is shown in Fig. 6.4 (top). When the phase increases from 0° to 180°, the flame brush is progressively stretched along the vertical direction. Integration of the heat release rate over the flame volume shows that the fluctuating heat release rate is above the mean value for this sequence. The maximum flame elongation is reached for $\varphi = 180°$. Between 180° and 360°, the flame tip shortens progressively. Between 72° and 216°, the angle between the flame root and the axial direction increases and the flame tip angle decreases. The situation is reversed between 252° and 36° where the flame root angle decreases with respect to the axial direction and the flame tip angle increases. At the end of the forcing cycle, the flame retrieves its shape at the beginning of the cycle. Except the slight angle modulation at the flame tip and flame root, the global motion of the flame at this forcing frequency is a bulk oscillation with a flame brush that is stretched in the vertical direction when the velocity increases and then compressed axially when the velocity is reduced.

This situation is typical of low frequency modulations when the size of the system does not allow a vortical structure to fully develop at the injector outlet (Durox et al. (2005), Birbaud et al. (2007)). The vortex diameter at this forcing frequency is too large compared to the flame length and cannot fully enroll the flame front. In this case, the flame responds quasi-steadily to the excitation and takes at each phase of the forcing cycle a shape close to the one that it would take within a steady flow at the same injection bulk flow velocity augmented by the fluctuating velocity. It should also be noted that the flame has a V shape for the five phases analyzed during a modulation cycle.

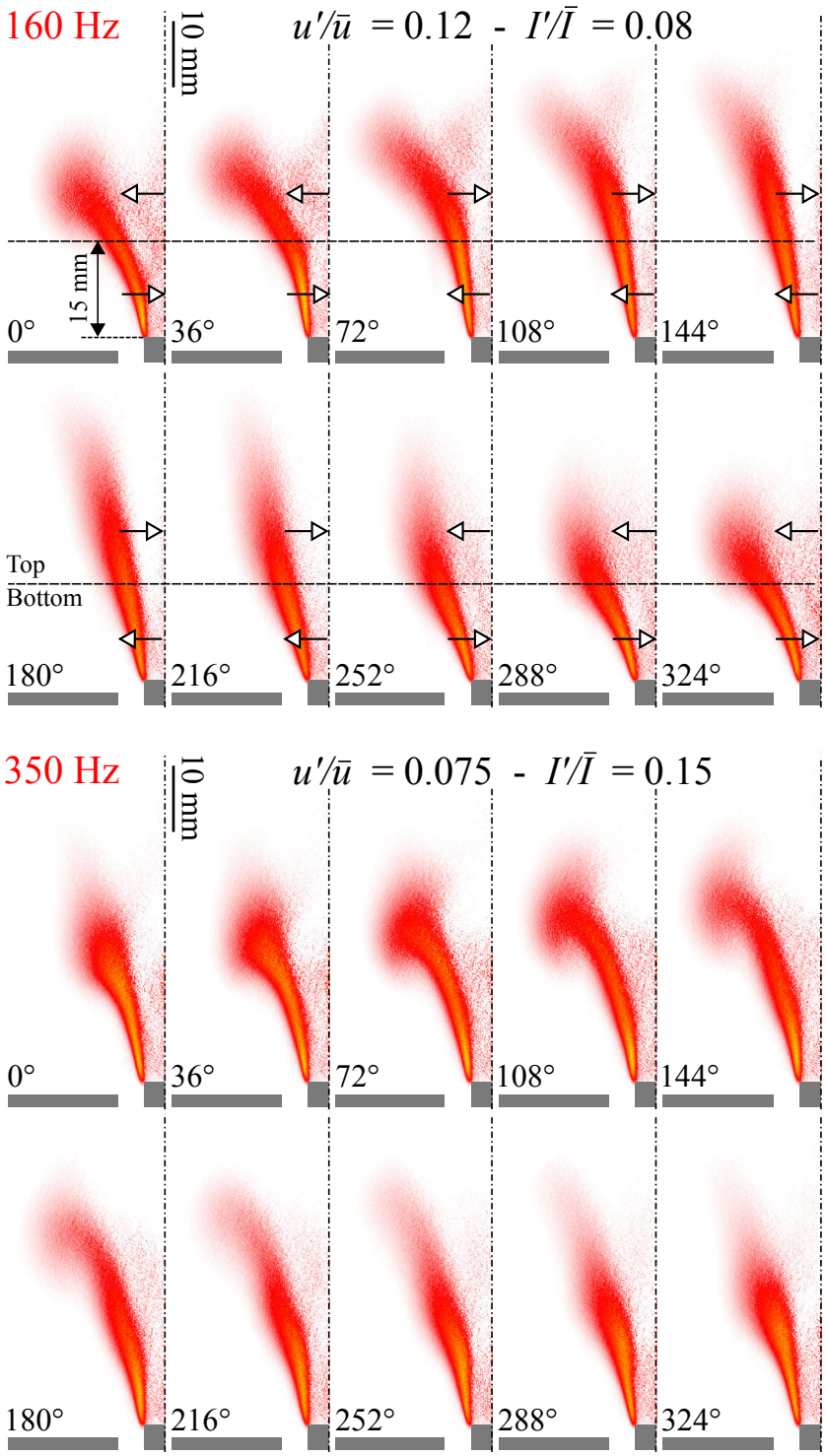

Figure 6.4: *Phase averaged Abel transformed OH* chemiluminescence images of the flame at* $X_{H_2}^{fuel} = 0.60$, $\phi = 0.70$, *and* $U = 14\ \mathrm{m \cdot s^{-1}}$ *forced at a frequency* $f = 160$ *Hz with an amplitude* $u'/\bar{u} = 0.12$ *(top images) and a frequency* $f = 350$ *Hz and an amplitude* $u'/\bar{u} = 0.075$ *(bottom images).*

For a modulation frequency $f = 160$ Hz and a modulation level $u'/\bar{u} = 0.12$, the gain of the flame response reaches a low value $G = 0.66$. This is attributed to large swirl number fluctuations taking place at this specific forcing frequency (Komarek and Polifke (2010), Palies et al. (2010), Palies et al. (2011), and Bunce et al. (2013)). Destructive interferences take place between the heat release rate originating from the upper and lower parts of the flame (Palies et al. (2010)). An analysis of these phenomena leading to reduced fluctuations of the global heat release rate is presented in appendix B.

For a higher modulation frequency $f = 350$ Hz, the situation differs as shown in Fig. 6.4 (bottom). The height of the flame is now only weakly modified during the modulation period, but the resulting heat release rate fluctuation is nearly twice that found for an excitation at $f = 160$ Hz (Fig. 6.4 top). One can identify a large roll-up of the flame brush at the flame tip between $\varphi = 0°$ and 144°, before a rapid extinction at the flame tip between $\varphi = 180°$ and 216°, followed by a progressive compression of the flame brush between $\varphi = 252°$ and 324°. The flame roll-up between $\varphi = 0°$ and 108° corresponds to a positive rate of increase of the fluctuating velocity in Fig. 6.2a leading to the stretching of the flame in the axial direction. Flame tip roll-up leads to large variations of the flame surface during, yielding important fluctuations of the heat release rate (Külsheimer and Büchner (2002), Durox et al. (2005), Balachandran et al. (2005), Kang et al. (2007)). For $f = 350$ Hz and $u'/\bar{u} = 0.075$, the flame also has a V shape for the five phases analyzed during a modulation cycle.

The response of the flame is now examined at a very low forcing frequency. Figure 6.5 (top) shows the flame response to an harmonic velocity modulation at a frequency $f = 44$ Hz and an amplitude $u'/\bar{u} = 0.12$. When the phase increases from 0° to 180°, the flame brush is progressively stretched along the vertical direction but the flame tip is not bent. Between 180° to 360°, the flame tip shortens progressively. As for $f = 160$ Hz, the vortex diameter is too large compared to the flame length and the flame responds quasi-steadily to the excitation. Figure 6.6 shows the normalized fluctuations of the axial velocity measured by the hot wire upstream the swirler when $f = 44$ Hz and the forcing amplitude is increased to $u'/\bar{u} = 0.33$. The phase averaged velocity signal is nearly sinusoidal meaning that the velocity perturbation is still linear at this high modulation amplitude. The phase averaged normalized fluctuating heat release rate is superimposed in Fig. 6.6. Small non-linearities are visible where the negative part of the fluctuation takes place over a shorter period than its positive counterpart (Schuller et al. (2003)). In this case, the gain is close to unity and the phase lag is close to zero.

Figure 6.5 (bottom) shows the flame response to an harmonic velocity modulation at a frequency $f = 44$ Hz and an amplitude $u'/\bar{u} = 0.33$. As for $u'/\bar{u} = 0.12$, the flame responds quasi-steadily to the excitation but the amplitude of the

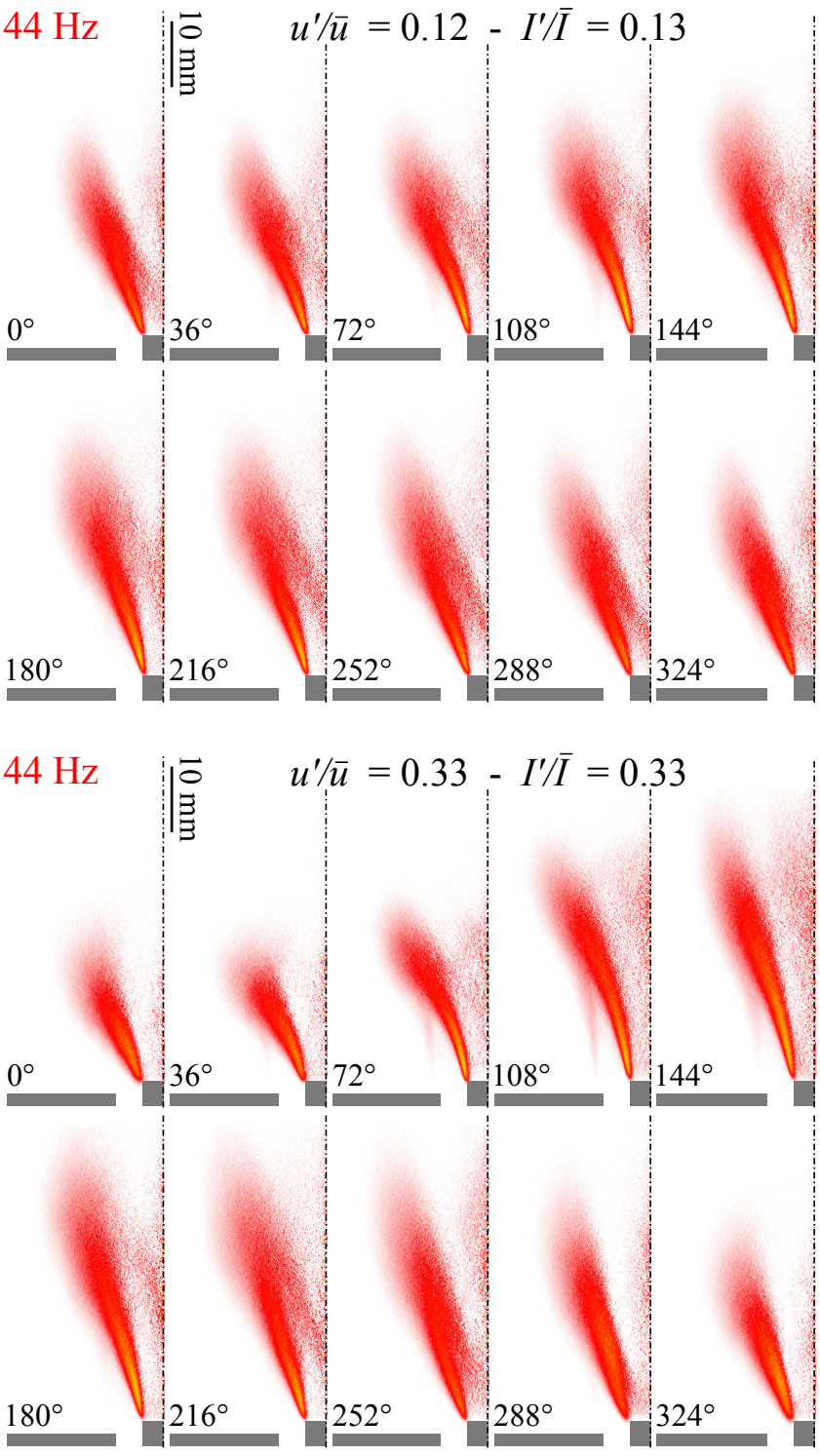

Figure 6.5: *Phase averaged Abel transformed OH* chemiluminescence images of the flame at* $X_{H_2}^{fuel} = 0.60$, $\phi = 0.70$, *and* $U = 14\ \mathrm{m \cdot s^{-1}}$ *forced at* $f = 44$ *Hz and* $u'/\bar{u} = 0.12$ *(top images) and at* $f = 44$ *Hz and* $u'/\bar{u} = 0.33$ *(bottom images).*

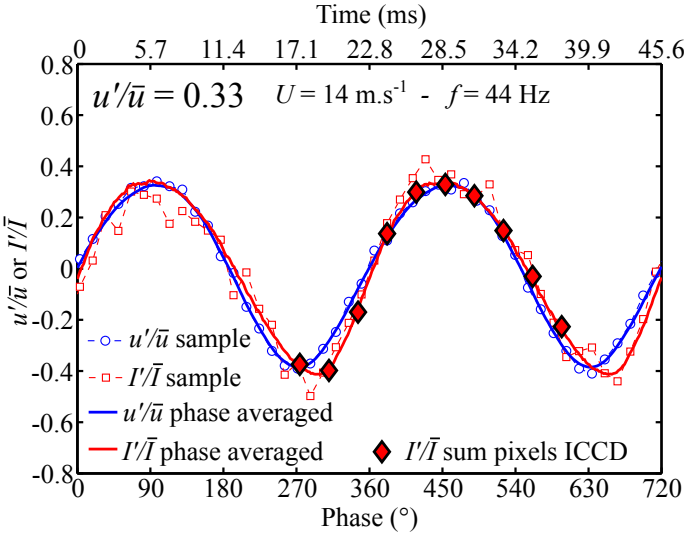

Figure 6.6: *Normalized fluctuating velocity $u'/\bar{u}$ (blue) and light emission $I'/\bar{I}$ (red) as a function of the phase (lower axis) or time (upper axis) when the flame at $X_{H_2}^{fuel} = 0.78$, $\phi = 0.70$, and $U = 14\,\mathrm{m\cdot s^{-1}}$ is forced at a frequency $f = 44$ Hz with a perturbation level $u'/\bar{u} = 0.33$. Instantaneous and phase averaged signals are presented. The normalized fluctuating light emission integrated over the ICCD pixel array is also plotted (red diamonds).*

flame height oscillation is larger. Another difference is that a OH^* chemiluminescence signal is detectable in the Outer Shear Layer (OSL) for the phases $\varphi = 72°$, 108°, and 144°. This means that the flame is not V shaped for these specific phase differences. Mass flow rate perturbations at a low frequency and an high amplitude have an influence on the topology of the reference flame.

It was shown in chapter 4 that, for a fixed hydrogen enrichment in the fuel blend, the probability to stabilize a V shaped flame decreases when the temperature of the burnt gases in the ORZ increases. The objective of the following sections is to analyze under which circumstances mass flow rate perturbations modify the ORZ characteristics and influence the topology of CH_4/H_2/air swirling flames.

6.4 Interactions between vortices and the ORZ

The development of a vortex ring and its interaction with the burnt gases in the ORZ is analyzed using synchronized OH-PLIF/PIV experiments. Figure 6.7 shows the phase averaged velocity field, measured by PIV in a central longitudinal plane, for the reference flame submitted to a modulation at a frequency $f = 350$ Hz and an amplitude $u'/\bar{u} = 0.075$. Results are presented for five phases regularly distributed in a modulation period. The left side of these images shows the 2-D velocity field with vector arrows. This representation is

used to identify the vortical structures. The right side of these images maps the modulus of the velocity field using an adapted colormap. This representation is used to delineate the different regions of the flow to discern the jet of fresh gases, the IRZ, the ISL, the ORZ, and the OSL.

It is first necessary to verify the compatibility of these measurements obtained by PIV downstream the injector with those deduced from hot wire anemometry upstream the swirler. The bulk flow velocity at these two different positions is not the same but their relative fluctuations should be the same (Noiray et al. (2009)). The axial velocity deduced from PIV is first integrated along the radial coordinate 4 mm above the central rod tip for the five phases in the modulation cycle. Then the bulk flow velocity at each phase is deduced. These values are then normalized by the bulk flow velocity measured for the unperturbed flame. The fluctuating component of the bulk flow velocity plotted in Fig.6.2 (blue diamonds) shows that PIV and local hot wire measurements yield the same indications. This allowed to cross check PIV measurements.

Images in the right column in Fig. 6.7 show that the height of the IRZ changes during a modulation period. The swirling jet of high velocity is also modified by the perturbation. It bends and moves from left to right depending on the phase of the forcing cycle. Images in the left column in Fig. 6.7 show that a vortex ring is created near the burner lip and is convected along the OSL in the downstream direction. The size of the vortex increases as it is convected away from the injector rim. At the phase $\varphi = 324°$, two vortices are detected on the same image. A new vortex is generated before the previous one stops interacting with the flame. At $\varphi = 180°$ the rapid extinction of the flame tip shown in Fig. 6.4 indicates that the vortex is detached from the flame tip. The region between $\varphi = 324°$ and $\varphi = 108°$, when the vortex ring fully interacts with the flame tip, corresponds to a positive rate of increase of the fluctuating velocity in Fig. 6.2. Figure 6.7 also shows that a region filled with hot burnt gases (see Sec. 2.4) lies close to the vortex ring for all phases. This zone features a curved shape suggesting that the flame front is trapped by the vortex and is bent (Durox et al. (2005), Balachandran et al. (2005), and Palies et al. (2011)).

Figure 6.8 plots phase averaged chemiluminescence images of the perturbed flame with isocontours of hot burnt gases probability superimposed on the top of it. This figure shows that the curved regions featuring high burnt gases probabilities are larger when the flame brush is bent by the vortex. These interactions indicate that burnt gases that were recently created by the flame front recirculate due to the presence of the vortex. It is interesting to compare the positions of these recirculating pockets of hot burnt gases with the positions of the vortices shown in Fig. 6.7 (left). The center of the recirculating pockets and the center of the vortices are not superimposed in the laboratory frame. It is difficult to further analyze the location of the recirculating pockets with

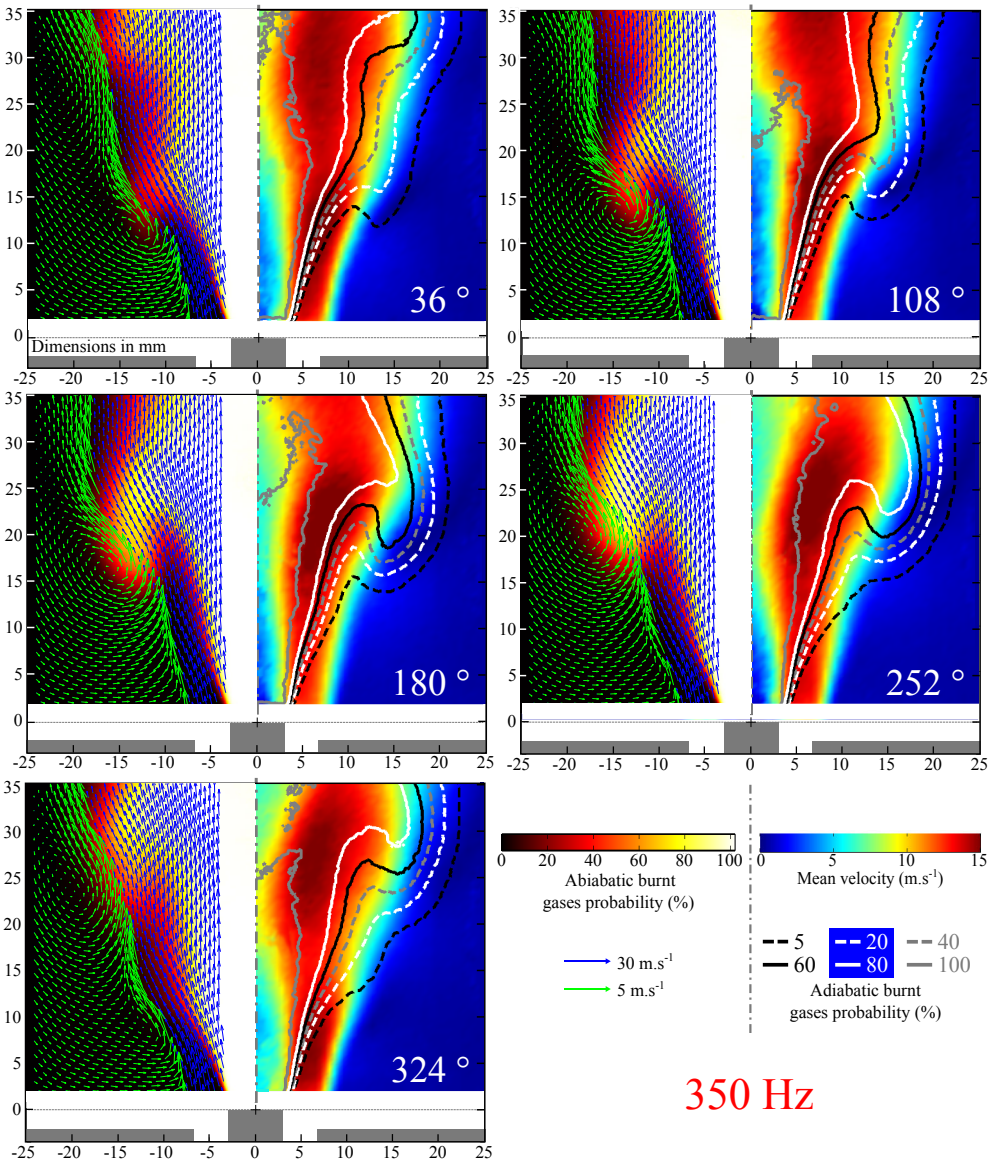

Figure 6.7: *Left side of images: Phase averaged probability to find hot burnt gases for the flame at* $X_{H_2}^{fuel}$ = 0.60, ϕ = 0.70, *and* U = 14 m · s^{-1} *forced at a frequency of* f = *350 Hz with a perturbation level* $u'/\bar{u}$ = 0.075. *The phase averaged mean velocity field in the central longitudinal plane is superimposed. Two different scales are used to ease the visualization of a large range of velocities. Right side of images: modulus of the 2-D phase averaged mean velocity. Different isocontours of the hot burnt gases probability are superimposed.*

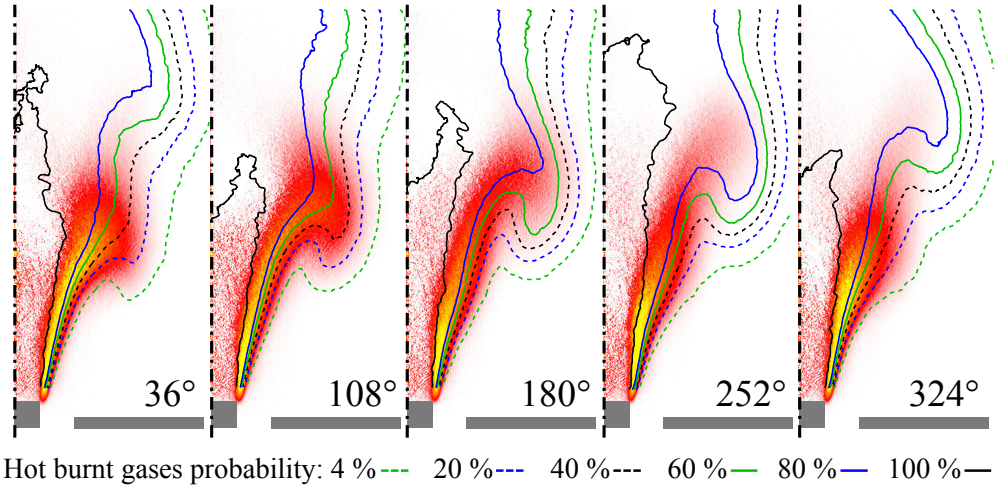

Figure 6.8: *Phase averaged Abel transformed OH* chemiluminescence images of the flame at* $X_{H_2}^{fuel} = 0.60$, $\phi = 0.70$, *and* $U = 14\ \mathrm{m \cdot s^{-1}}$ *forced at a frequency of* $f = 350$ *Hz with a perturbation level* $u'/\bar{u} = 0.075$. *Different isocontours of the hot burnt gases probability are superimposed.*

respect to the vortex rings using these images.

A Galilean decomposition of the flow (Adrian et al. (2000)) may be used to plot the 2-D velocity fields in the vortex frame. This transformation, detailed in appendix C, demonstrates that the center of the burnt gases recirculating pockets coincides with the vortex center in the vortex frame. The envelope of the burnt gases recirculating pockets also corresponds to the vortex envelope. The burnt gases are trapped and recirculate in the vortex. The burnt gases recirculating in the vortex ring interact rapidly with the OSL of the reactants jet and are not convected close to the combustion chamber walls. This situation differs thus from the case without modulation where the burnt gases recirculate in the ORZ and are cooled in the vicinity of the combustion chamber walls (see chapter 5). When a vortex is convected along the OSL, fresh reactants in the OSL of the jet are interacting with burnt gases from the ORZ featuring a temperature closer to the adiabatic flame temperature.

For a modulation frequency $f = 350$ Hz, the size of the vortex ring produced is smaller than the flame length and the recirculating pockets of burnt gases at a temperature close to the adiabatic flame temperature only interact with the OSL close to flame tip. Figure 6.9 shows the phase averaged velocity field, measured by PIV in a central longitudinal plane, for the reference flame submitted to an harmonic modulation of the flow rate at a frequency $f = 160$ Hz and a perturbation level $u'/\bar{u} = 0.12$. The size of the vortex ring created and the associated recirculating hot pockets are larger. It is safe to assume that

the vortex and hot pocket sizes would be even larger for a flow rate modulation at a frequency of f = 44 Hz and an amplitude $u'/\bar{u}$ = 0.33. The recirculation of burnt gases at a temperature close to the adiabatic flame temperature may then interact with the jet of fresh gases in the whole OSL region. These elements explain the modification of the flame topology described in Fig. 6.5 for f = 44 Hz and $u'/\bar{u}$ = 0.33.

6.5 Flame response to high amplitude and low frequency harmonic perturbations

In the absence of external forcing, the reference flame analyzed in the previous sections, that features an hydrogen enrichment in the fuel $X_{H_2}^{fuel}$ = 0.60, has a probability to stabilize with an M shape close to zero (see chapter 5). It is now interesting to analyze the influence of high amplitude and low frequency mass flow rate perturbations on the topology of swirling flames featuring a higher probability to stabilize with an M shape. Two configurations are studied in the following: a flame with $X_{H_2}^{fuel}$ = 0.70, ϕ = 0.70, and U = 14 m · s^{-1} that features a M shape probability p = 0.15 at steady state in the absence of external forcing, and another flame with $X_{H_2}^{fuel}$ = 0.78, ϕ = 0.70, and U = 14 m · s^{-1} that features a higher M shape probability p = 0.42 at steady state without external forcing.

Figure 6.10 (left column) shows phase averaged OH* chemiluminescence images of the flame at $X_{H_2}^{fuel}$ = 0.70 for ten phases regularly distributed during a modulation period when the flow rate is submitted to a modulation at f = 44 Hz and $u'/\bar{u}$ = 0.33. The intensity of the OH* signal in the OSL is strongly modified during the forcing frequency cycle. It increases between φ = 180° and φ = 360° and decreases in the other half of the modulation cycle between φ = 0° and φ = 180°. This intensity is an indicator of the probability to stabilize an M flame (see chapter 5) suggesting that the M shape probability is a function of the phase of the modulation cycle. OH-PLIF experiments yielding the phase averaged hot burnt gases probability are then used to examine this phenomenon in more details.

Figure 6.10 (right column) shows the phase averaged hot burnt gases probability in the central longitudinal plane for the ten phases of interest. The hot burnt gases probability for the unperturbed flame is presented as well at the end of the sequence in Fig. 6.10 (f = 0 Hz). The probability to stabilize an M flame is deduced by integrating the burnt gases probability over the OSL region. Figure 6.11 plots these results as a function of the phase in the forcing period. The M shape probability has a sinusoidal shape and is centered around a value corresponding to the M shape probability found for the unperturbed flame. For phases 108° < φ < 288° the M shape probability is lower than the probability for the unperturbed case. For phases 288° ≤ φ ≤ 108° the probabil-

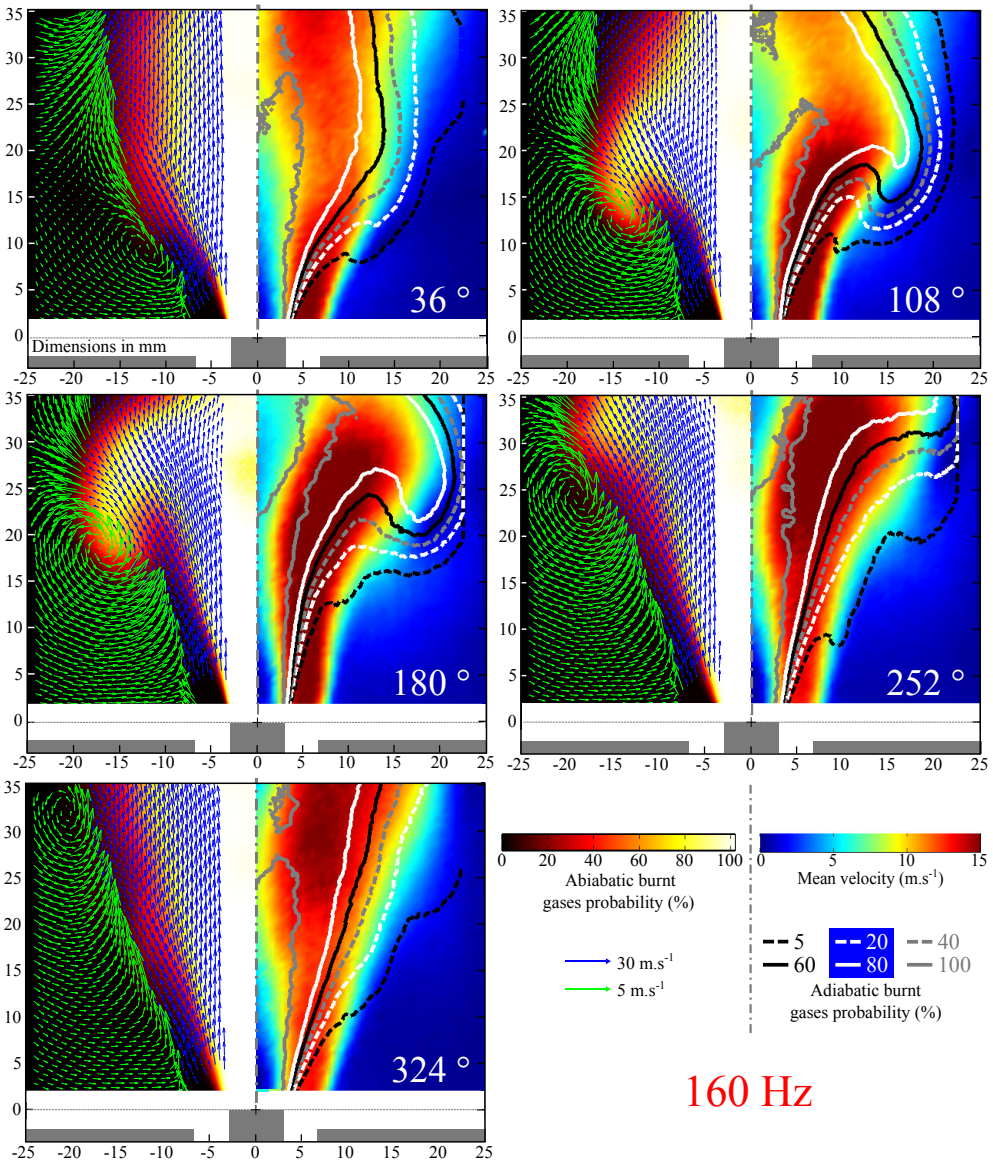

Figure 6.9: *Left side of images: Phase averaged probability to find hot burnt gases for the flame at* $X_{H_2}^{fuel}$ = 0.60, ϕ = 0.70, *and* U = 14 m · s^{-1} *forced at a frequency of* f = *160 Hz with a perturbation level* $u'/\bar{u}$ = 0.12. *The phase averaged mean velocity field in the central longitudinal plane is superimposed. Two different scales are used to ease the visualization of a large range of velocities. Right side of images: modulus of the 2-D phase averaged mean velocity. Different isocontours of the hot burnt gases probability are superimposed.*

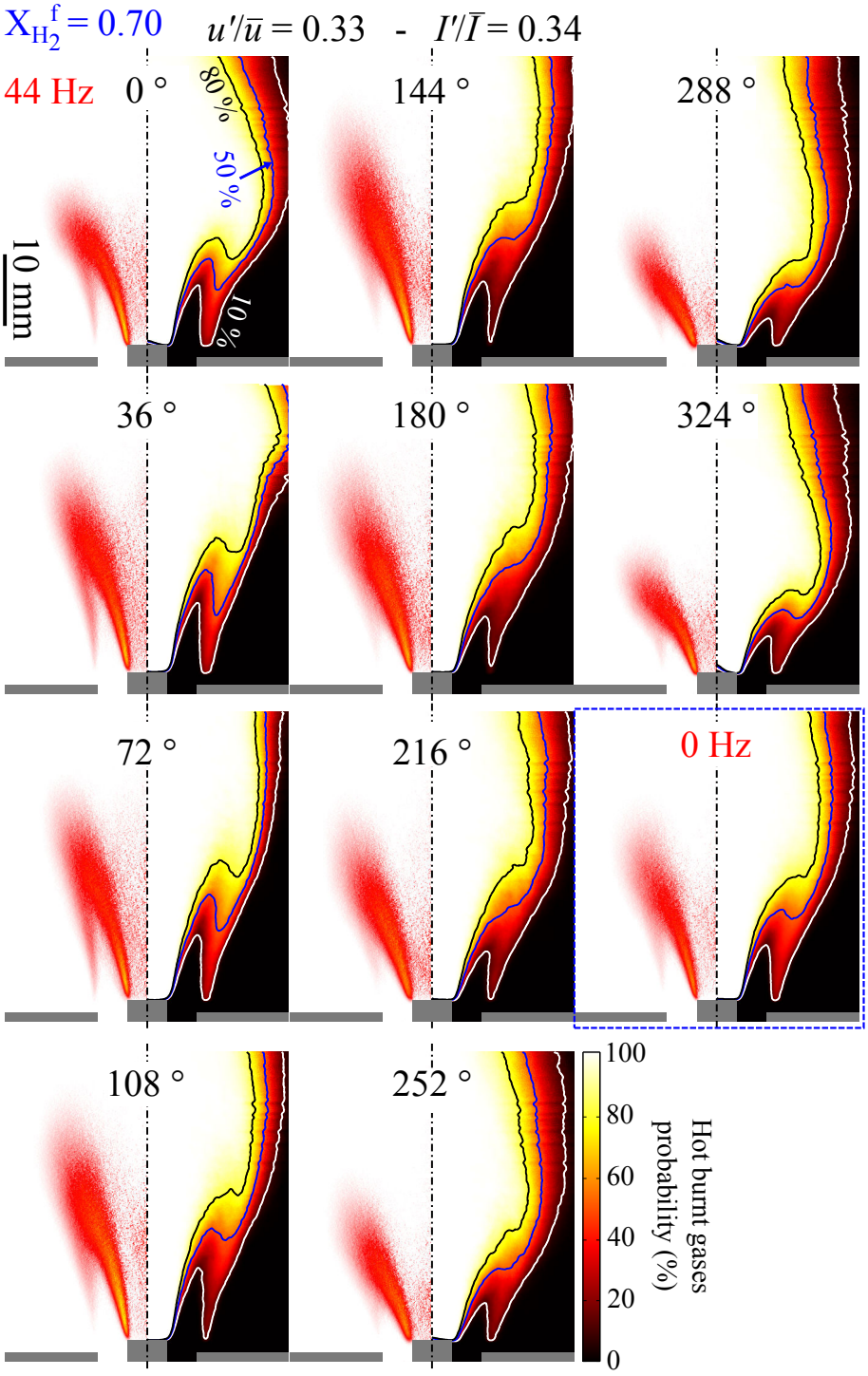

Figure 6.10: *Left side of images: Phase averaged Abel transformed OH* chemiluminescence images of the flame at* $X_{H_2}^{fuel} = 0.70$, $\phi = 0.70$, *and* $U = 14\ \mathrm{m \cdot s^{-1}}$ *forced at a frequency* $f = 44$ *Hz with a perturbation level* $u'/\bar{u} = 0.33$. *Right side of images: Hot burnt gases probability and different isolevels.*

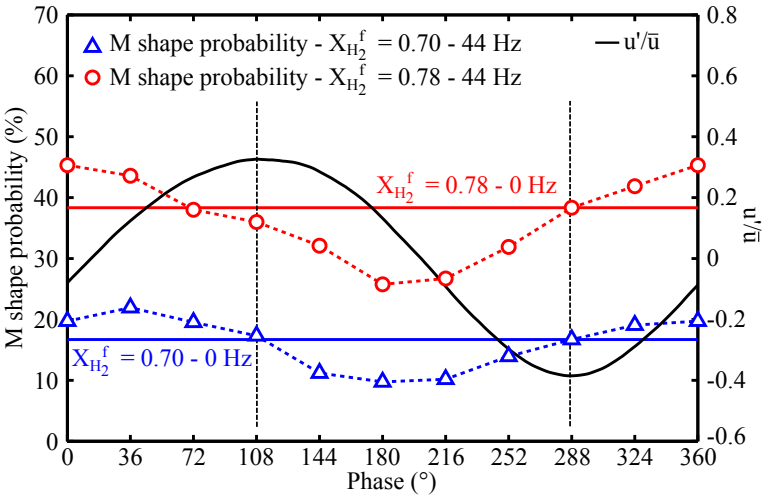

Figure 6.11: *Phase averaged M shape probability for the flames at* $X_{H_2}^{fuel} = 0.70$ *(blue) and* $X_{H_2}^{fuel} = 0.78$ *(red) forced at a frequency* $f = 44$ *Hz with a perturbation level* $u'/\bar{u} = 0.33$. *The normalized fluctuating velocity* $u'/\bar{u}$ *measured by the hot wire in the injection tube (black) is also presented.*

ity to stabilize a reaction layer in the OSL is larger than the probability of the unperturbed flame. This demonstrates that the V/M flame topology is altered by these strong low frequency and high amplitude mass flow rate perturbations.

Figure 6.12 left and right columns show the OH* chemiluminescence and burnt gases probabilities found for the flame at $X_{H_2}^{fuel} = 0.78$ during the same acoustic excitation. Results deduced from these images are plotted in Fig. 6.11. The probability to stabilize an M flame also describes a sinusoidal shape around the value found for the unperturbed flame. The mean M shape probability is also higher than for the flame at $X_{H_2}^{fuel} = 0.70$. The phase averaged normalized fluctuations of the axial velocity measured by the hot wire within the injector are also plotted in Fig. 6.11. For both flames, signals of the fluctuating velocity and the M shape probability are in phase position. The M shape probability is larger than the value obtained for the unperturbed flame when the rate of increase of the axial velocity fluctuation is positive. Conversely, the M shape probability is lower than the value obtained for the unperturbed flame when the rate of increase of the axial velocity is negative. Figures 6.10 and 6.12 also show that higher M shape probabilities are observed when the flame is expanding in the axial direction and lower M shape probabilities are found when the flame is shortening.

It is difficult to know the exact position of the vortex ring created by the flow modulation because the 2-D velocity fields were not measured for these flow forcing conditions. By analogy with mass flow rate perturbations at $f = 350$ Hz

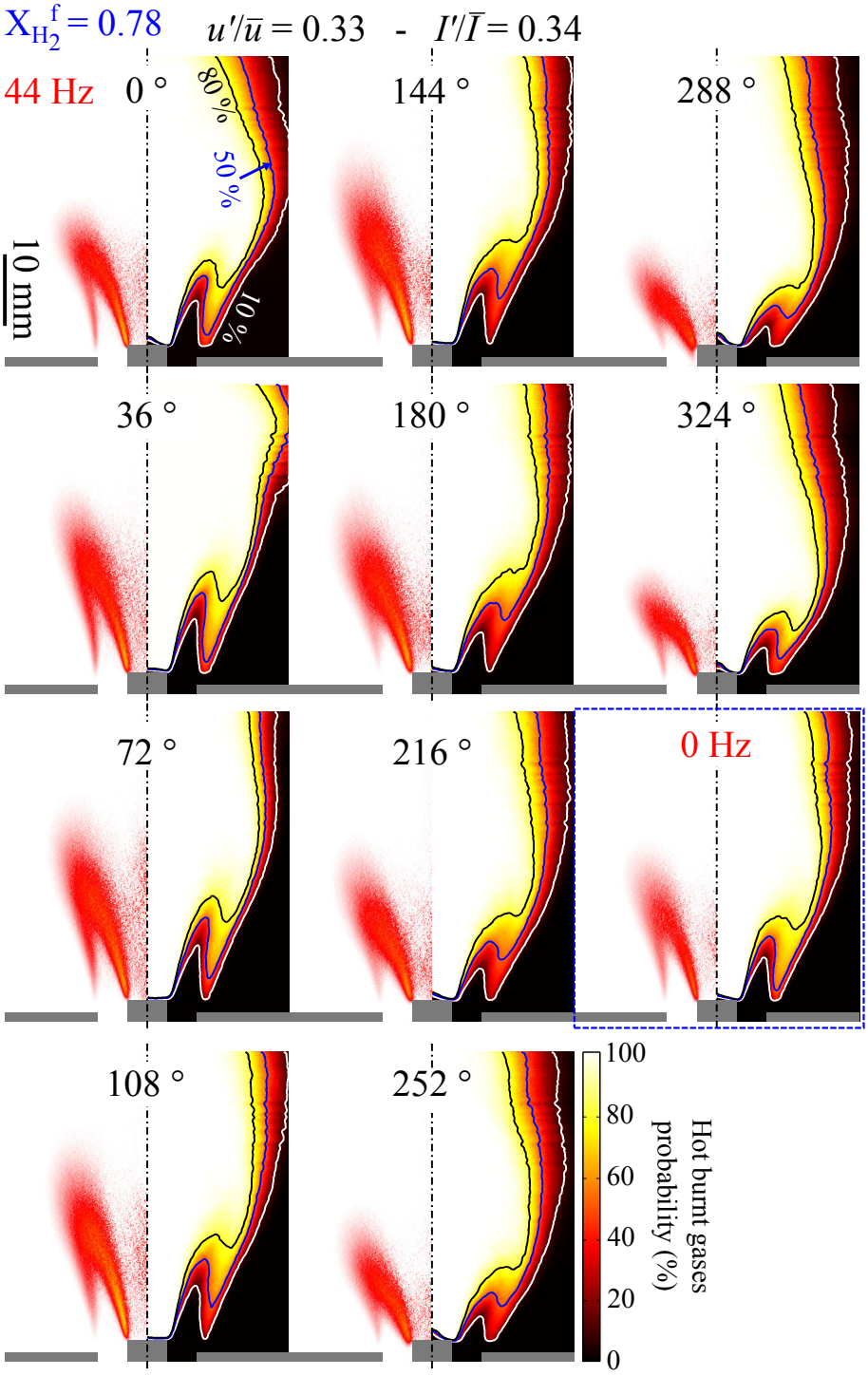

Figure 6.12: *Left side of images: Phase averaged Abel transformed OH* chemiluminescence images of the flame at* $X_{H_2}^{fuel} = 0.78$, $\phi = 0.70$, *and* $U = 14\ \mathrm{m \cdot s^{-1}}$ *forced at a frequency* $f = 44$ *Hz with a perturbation level* $u'/\bar{u} = 0.33$. *Right side of images: Hot burnt gases probability and different isolevels.*

and $u'/\bar{u}$ = 0.075 in Fig. 6.7 and f = 350 Hz and $u'/\bar{u}$ = 0.075 in Fig. 6.9, it is possible to assume that the vortex is convected along the OSL and interacts with the flame front when the rate of increase of the axial velocity fluctuation is positive. The following scenario is then proposed. The probability to stabilize an M flame increases when large vortices are present in the ORZ. The probability to stabilize an M flame decreases when the vortices are detached from the flame tip. In the presence of a vortex in the ORZ, burnt gases are trapped in the vortex and are transported towards the OSL as described in Sec. 6.4. During this interaction, a fraction of the burnt gases recirculate with shorter residence times in the ORZ without entering in contact with the combustor peripheral walls that are subjected to heat losses (see Ch. 5). Consequently, the temperature within the ORZ increases in the presence of a vortex. The resistance of the flame front to compressive strain rate increases and the flame front is less subjected to localized extinctions, yielding a higher M shape probability. This conjecture should be confirmed by additional PIV experiments.

6.6 Conclusions

The influence of mass flow rate perturbations on the topology of CH_4/H_2/air swirling flames was analyzed for different forcing frequencies and perturbation amplitudes. The frequency response was first analyzed for moderate incoming velocity fluctuations when the resulting heat release rate fluctuations respond linearly to the excitation. Our observations confirm previous conclusions drawn by Palies (2010) for the frequency response of CH_4/air swirling flames stabilized with a higher swirl number. These data are used to select characteristic forcing frequencies for which the flame features distinct responses.

Mass flow rate modulations at the frequencies f = 160 Hz and f = 350 Hz produce vortex rings in the OSL featuring a smaller size than the flame length if the perturbation level does not exceed $u'/\bar{u}$ = 0.12. In this situation, the topology is not altered by the perturbations and the flames remain V shaped.

The response of CH_4/H_2/air swirling flames to low frequency and high amplitude mass flow rate perturbations was then analyzed using joint chemiluminescence and OH-PLIF experiments at f = 44 Hz and $u'/\bar{u}$ = 0.33. In this situation, coherent structures with a larger size are created in the OSL. Burnt gases at a temperature close to the adiabatic flame temperature are then trapped in the vortex ring located in the ORZ, are transported towards the OSL, and interact with the jet of fresh gases. The resistance of the flame front to compressive strain rate consequently increases and the probability to stabilize an M flame increases.

Chapter 7

Stabilization of low calorific value flames

Changes of the topology of CH_4/H_2/air swirled flames diluted with N_2 or CO_2 are analyzed in this chapter. A CH_4/H_2/air reference flame defined by $X_{H_2}^{fuel}$ = 0.60, ϕ = 0.70, and P = 4 kW is first described and the molar fraction of the diluent (N_2 or CO_2) is then progressively increased in the combusible mixture to analyze their effects.

The laminar burning velocity S_L and the adiabatic flame temperature T_{ad} of N_2 or CO_2 diluted flames are first examined using 1-D laminar direct simulations with the detailed chemistry mechanism from Lindstedt (1998). These calculations are used to select the operating conditions that will be investigated for the swirled flames. The chemiluminescence signal of the swirled diluted flames is then analyzed. Chemiluminescence images are analyzed to examine effects of dilution on the flame topology and on the intensity of the light emitted by the flame. Results obtained when the diluent composition (N_2 or CO_2) is varied are compared. Finally, temperature measurements are used to characterize the combustor thermal efficiency when the diluent concentration and composition are varied.

7.1 Fundamental properties of N_2/CO_2 diluted flames

It was demonstrated in Sec. 1.1 that the combustion of COG/BFG mixtures can be, in a first step, analyzed using surrogate mixtures of CH_4/H_2/air diluted with N_2 or CO_2 that reproduce the same adiabatic flame temperature and laminar burning velocity. Figure 7.1a shows the evolution of the adiabatic flame temperature of a CH_4/H_2/air flame at $X_{H_2}^{fuel}$ = 0.60, ϕ = 0.7, and U = 14.0 m · s^{-1} when the molar fraction of the diluent in the fuel varies from $X_{diluent}^{fuel}$ = 0 to $X_{diluent}^{fuel}$ = 0.60. In this chapter, the molar fraction of the diluent in the fuel

blend is defined as follows: $X^{fuel}_{diluent} = X_{diluent}/(X_{diluent} + X_{H_2} + X_{CH_4})$ and the diluent is either N_2 or CO_2. Note that this definition does not take into account the N_2 naturally present in the air mixture for the calculation of the molar fractions of the diluent in the combustible mixture $X_{diluent}$ and in the fuel blend $X^{fuel}_{diluent}$. The hydrogen enrichment $X^{fuel}_{H_2}$ is the molar fraction of hydrogen in the CH_4/H_2 mixture and is fixed to $X^{fuel}_{H_2} = X_{H_2}/(X_{H_2}+X_{CH_4}) = 0.60$ in this chapter.

When the molar fraction of diluent in the fuel blend is increased at a fixed equivalence ratio $\phi = 0.7$, the adiabatic flame temperature T_{ad} decreases as shown by the red curves in Fig. 7.1a. A fraction of the heat produced by the oxidation of CH_4 and H_2 is used to heat up the large volume of diluent. For the same molar fraction of diluent in the fuel blend, the adiabatic flame temperature is lower when CO_2 (square symbols in Fig. 7.1a) is used for dilution instead of N_2 (circle symbols). This is due to the thermal capacity per unit of volume for CO_2: $C_p^{CO_2} = 774\ kJ \cdot m^{-3} \cdot K^{-1}$ at $T = 800$ K which is higher than that of N_2 $C_p^{N_2} = 472\ kJ \cdot m^{-3} \cdot K^{-1}$ at $T = 800$ K.

Lean conditions are generally chosen to reduce the flame temperature and limit the production of NOx by the thermal path (Brown (1995)). Figure 7.1a indicates that it is not necessary to operate the combustor at a fixed equivalence ratio as long as the flame temperature is sufficiently low. It is more interesting to dilute the flames at a fixed adiabatic flame temperature T_{ad} and fixed thermal power P because these parameters directly affect the process. Figure 7.1b shows the evolution of the equivalence ratio ϕ when the molar fraction of the diluent in the fuel blend varies from $X^{fuel}_{diluent} = 0$ to $X^{fuel}_{diluent} = 0.60$ at a fixed adiabatic flame temperature $T_{ad} = 1881$ K (black curves). The equivalence ratio increases with the molar fraction of diluent in the fuel blend. For a fixed adiabatic flame temperature and a fixed molar fraction of diluent in the fuel blend the equivalence ratio needs to be fixed to a higher value in the case of CO_2. Note that for $0 \leq X^{fuel}_{diluent} \leq 0.60$, the equivalence ratio always lies below unity $\phi < 1$.

The laminar burning velocity S_L is also an important parameter that alters the stabilization of flames. It is interesting to study the evolution of this parameter for diluted flames. Figure 7.1c shows the evolution of the calculated laminar burning velocity S_L when the molar fraction of the diluent in the fuel varies from $X^{fuel}_{diluent} = 0$ to $X^{fuel}_{diluent} = 0.60$ at a fixed equivalence ratio $\phi = 0,7$ (red curves) or at a fixed adiabatic flame temperature $T_{ad} = 1881$ K (black curves). When the equivalence ratio is fixed, the laminar burning velocity decreases rapidly with the molar fraction of diluent in the fuel blend. The decay is larger for CO_2 than for N_2 diluted flames. The laminar burning velocity is divided by a factor of two when the molar fraction of diluent in the fuel increases from $X_{CO_2} = 0$ to $X_{CO_2} = 0.50$. The laminar burning velocity also decreases when

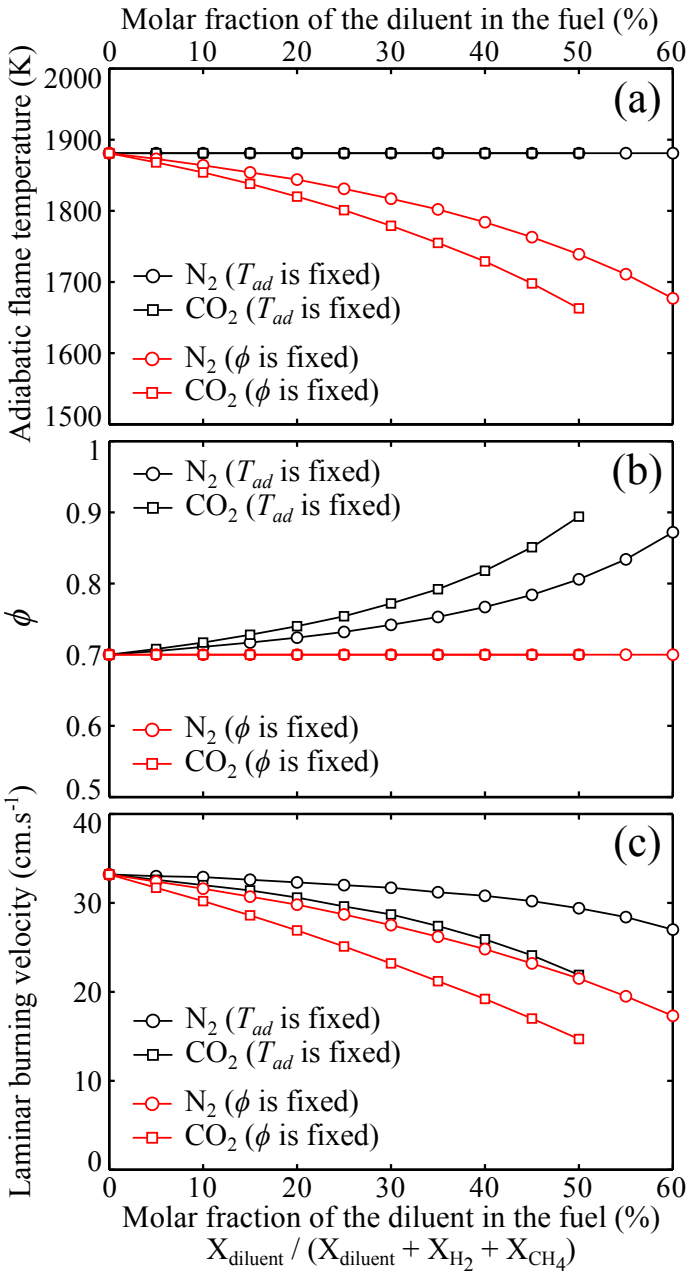

Figure 7.1: *Calculated adiabatic flame temperatures (a), equivalence ratios (b), and laminar burning velocities (c) as a function of the molar fraction of diluent in the fuel* $X_{diluent}^{fuel}$ *for flames at* $X_{H_2}^{fuel}$ = 0.60, ϕ = 0.7, *and* U = 14.0 $\mathrm{m \cdot s^{-1}}$. *Diluent is either* N_2 *(circle symbols) or* CO_2 *(square symbols). Calculations are carried out when the dilution is increased for a fixed equivalence ratio (red symbols) or a fixed adiabatic flame temperature (black symbols). The* N_2 *naturally present in the air mixture is not taken into account in the molar fraction of the diluent in the fuel.*

the molar fraction of diluent increases at a fixed adiabatic flame temperature. The decay is however smaller. As a preliminary conclusion, laminar diluted flames operated at a fixed adiabatic flame temperature are easier to stabilize than flames operated at a fixed equivalence ratio due to their higher laminar burning velocity.

7.2 Chemiluminescence of N_2/CO_2 diluted flames

It is now interesting to analyze the OH* chemiluminescence signal of the swirled diluted flames using an ICCD camera (see Sec. 2.3) with a long exposure time for the two diluents. Figure 7.2 shows the OH^* intensity distribution of the flames for the operating conditions indicated in Fig. 7.1 when the diluent is N_2 and the equivalence ratio is fixed to $\phi = 0.70$, the thermal power is fixed to $P = 4$ kW and the hydrogen enrichment is fixed to $X_{H_2}^{fuel} = 0.60$. An Abel deconvolution is applied on each image and only a half flame is presented due to the rotational symmetry of the configuration. Theses images show that the height of the flame increases with the dilution. This is attributed to the decrease of the laminar burning velocity with the molar fraction of diluent in the combustible mixture as shown in Fig. 7.1c. The shape of the flame is also modified by the dilution. The flame front bends towards the burner axis near the flame tip for the largest dilution ratios. It is also striking that the local OH* intensity in the flame brush rapidly decreases when the molar fraction of diluent increases.

Figure 7.3 plots the evolution of the normalized intensity of the OH* chemiluminescence integrated over the flame region for the flames presented in Fig. 7.2 (red curves with circle symbols). The OH* chemiluminescence globally emitted by the flame decays with the molar fraction of N_2 in the combustible mixture. Hossain and Nakamura (2014) made similar observations in their simulations of the chemiluminescence signal of CH* in CH_4/air flames diluted by N_2 or CO_2. García-Armingol et al. (2014) demonstrated with experiments and simulations that the chemiluminescence intensity from OH^* and CH^* is modified when the flame is diluted by the burnt gases recirculating in the flame front. This was attributed to modifications of the chemical reactions involved in the chemiluminescence process. It was argued that the quenching of excited radicals is altered by the dilution.

Figure 7.4 shows the OH^* chemiluminescence intensity of the flames for the operating conditions shown in Fig. 7.1 when the diluent is CO_2 and the equivalence ratio is fixed to $\phi = 0.70$. Results are similar to those obtained with N_2 in Fig. 7.2. The height of the flame increases with the molar fraction of the diluent while the OH* intensity rapidly decreases. The impact of dilution by CO_2 on the flame height is however more important than for the dilution by N_2 at a

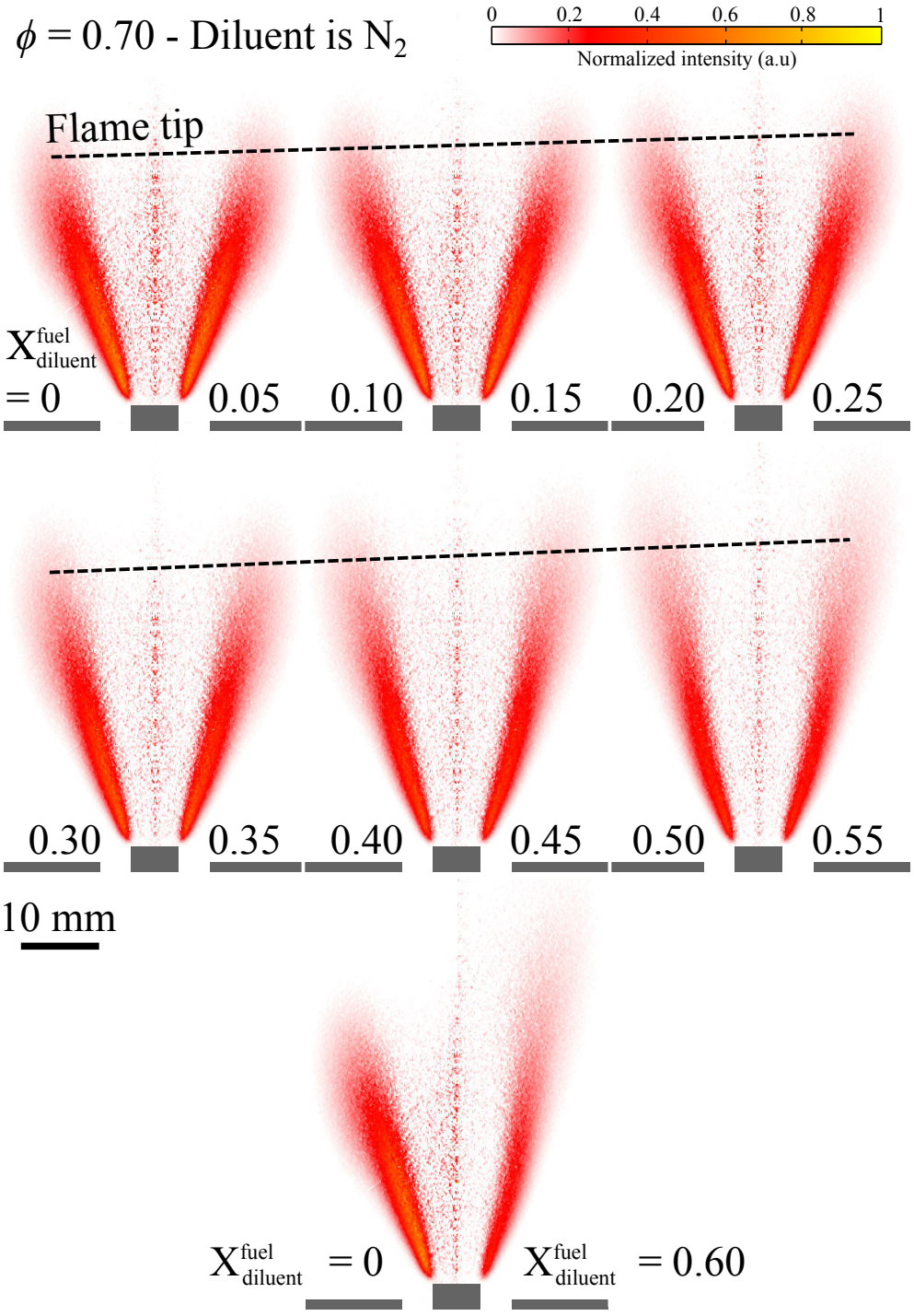

Figure 7.2: *Abel transformed OH* chemiluminescence images of swirled flames when the molar fraction of N_2 in the fuel blend is increased from $X^{fuel}_{diluent} = 0$ to $X^{fuel}_{diluent} = 0.60$ for a fixed equivalence ratio $\phi = 0.70$, thermal power $P = 4$ kW, and H_2 to CH_4 ratio $X^{fuel}_{H_2} = 0.60$.*

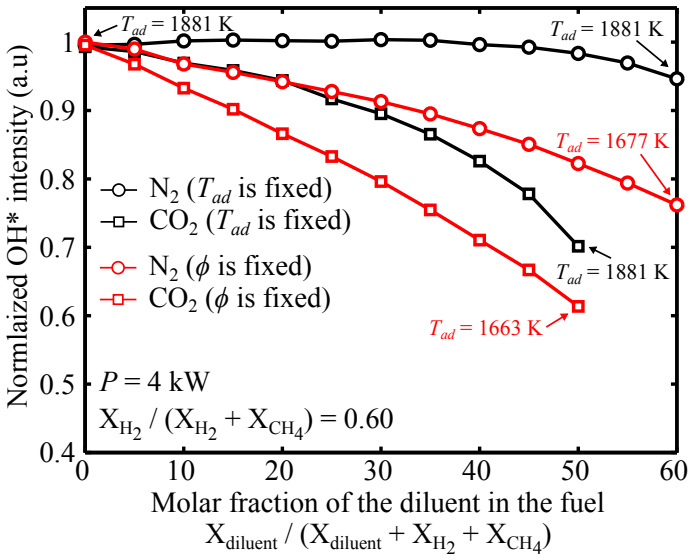

Figure 7.3: *Normalized intensity of the OH* chemiluminescence integrated over the flame region as a function of the molar fraction of diluent in the fuel when* $X_{H_2}^{fuel} = 0.60$ *and* $P = 4$ kW*. Diluent is* N_2 *(circle symbols) or* CO_2 *(square symbols). Experiments are carried out for increasing dilution rates at a fixed equivalence ratio (red curves) or at a fixed adiabatic flame temperature (black curves). The calculated adiabatic flame temperatures are superimposed on the curves for the lowest and largest dilution ratios. The* N_2 *included in the air mixture is not taken into account in the molar fraction of the diluent in the fuel.*

fixed molar fraction of diluent. This is due to the laminar burning velocity that decreases faster when the diluent is CO_2 as shown in Fig. 7.1c. Figure 7.3 also plots the evolution of the normalized intensity of the OH* chemiluminescence integrated over the flame region for the swirled flames presented in Fig. 7.4 (red curves with square symbols). The OH* chemiluminescence intensity globally emitted by the flame decays more rapidly when the diluent is CO_2. This corroborates the numerical results of Hossain and Nakamura (2014) using simulations. The reduction of the OH* chemiluminescence intensity when CH_4/air flames are diluted by CO_2 was also recently reported in the experiments from Gupta et al. (2011) and Lee et al. (2013).

Figures. 7.2 and 7.4 indicate that it is possible to stabilize CH_4/H_2/air swirled flames featuring important dilution ratios of N_2 or CO_2 for a fixed equivalence ratio $\phi = 0.70$, thermal power $P = 4$ kW when the swirl number is set to S = 0.4. Flames with laminar burning velocities ranging from $S_L = 13.8\,\mathrm{cm \cdot s^{-1}}$ to $S_L = 33.2\,\mathrm{cm \cdot s^{-1}}$ are stabilized with the same topology. It is worth noting that the bulk flow velocity in these experiments also slightly increases with the molar fraction of the diluent in the fuel blend and ranges from $U = 14\,\mathrm{m \cdot s^{-1}}$ when $X^{\mathrm{fuel}}_{\mathrm{diluent}} = 0$ to $U = 15.6\,\mathrm{m \cdot s^{-1}}$ when $X^{\mathrm{fuel}}_{\mathrm{diluent}} = 0.50$ when CO_2 is used. The wide range of stability of these diluted flames is due to the presence of the central rod. Flames are anchored in the wake of this bluff-body due to the recirculation of hot burnt gases.

Figures 7.5 and 7.6 show the OH* chemiluminescence distributions and intensities of swirled flames for the operating conditions shown in Fig. 7.1 when the diluent is N_2 or CO_2 and the adiabatic flame temperature is fixed to $T_{ad} = 1881$ K. The thermal power is also fixed to $P = 4$ kW. Again, the flame height increases with dilution but the impact is less important than for the experiments carried out at a fixed equivalence ratio. Dilution with CO_2 has a larger effect on the flame height and luminosity than dilution with N_2 at a fixed adiabatic flame temperature. The evolution of the normalized intensity of the OH* chemiluminescence intensity integrated over the flame region for the flames presented in Figs. 7.5 and 7.6 (black curves) is shown in Fig. 7.3. When N_2 is used as a diluent, the global chemiluminescence intensity is roughly constant up to $X^{\mathrm{fuel}}_{\mathrm{diluent}} = 0.40$ and slightly decreases for $X^{\mathrm{fuel}}_{\mathrm{diluent}} > 0.40$. The local OH* intensity of N_2 diluted flames is lower than for the undiluted case, but the global intensity remains roughly constant due to the increase of the flame volume.

Different studies (Docquier et al. (2000), Higgins et al. (2001), Higgins et al. (2001), Docquier et al. (2002), Hardalupas and Orain (2004), Ballester and García-Armingol (2010)) reported that the intensity of the OH* chemiluminescence increases with the equivalence ratio of lean flames. In our case, the decrease of the OH* chemiluminescence intensity due to dilution is compensated

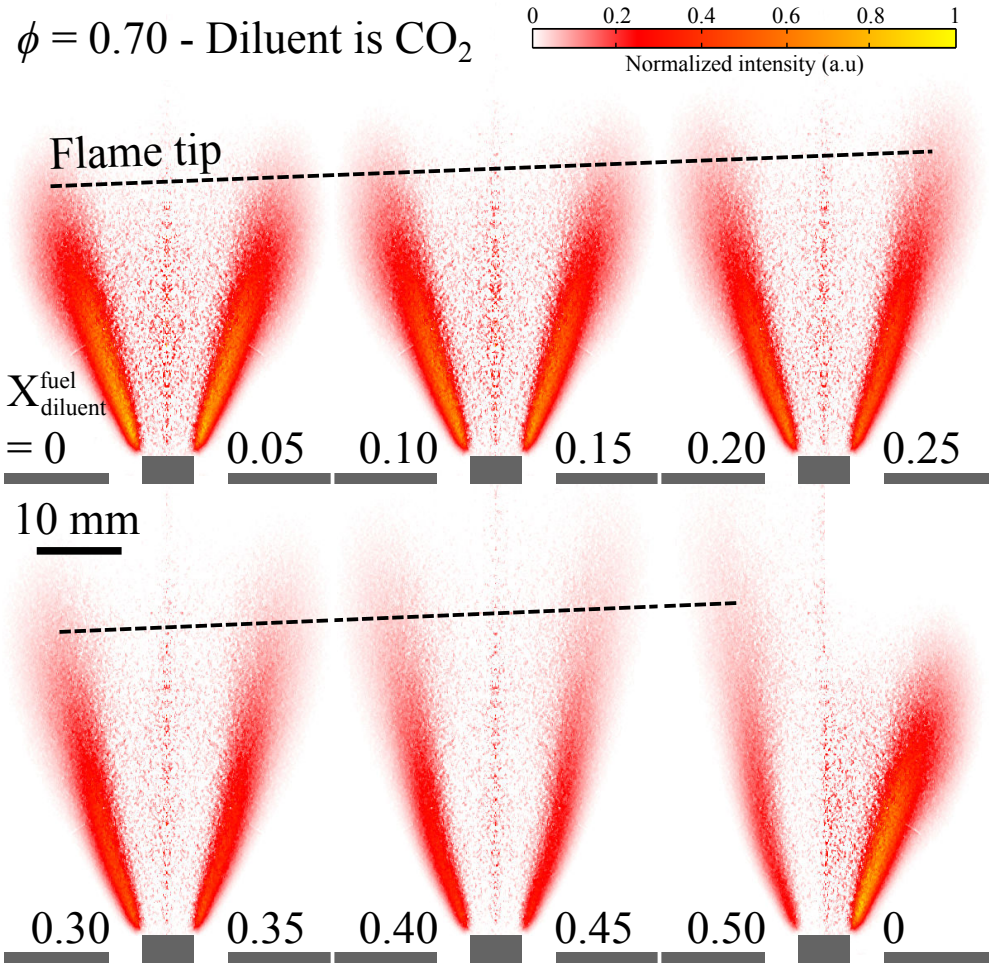

Figure 7.4: *Abel transformed OH^* chemiluminescence images of swirled flames when the molar fraction of CO_2 in the fuel blend is increased from $X^{fuel}_{diluent} = 0$ to $X^{fuel}_{diluent} = 0.60$ for a fixed equivalence ratio $\phi = 0.70$, thermal power $P = 4\,\mathrm{kW}$, and hydrogen enrichment $X^{fuel}_{H_2} = 0.60$.*

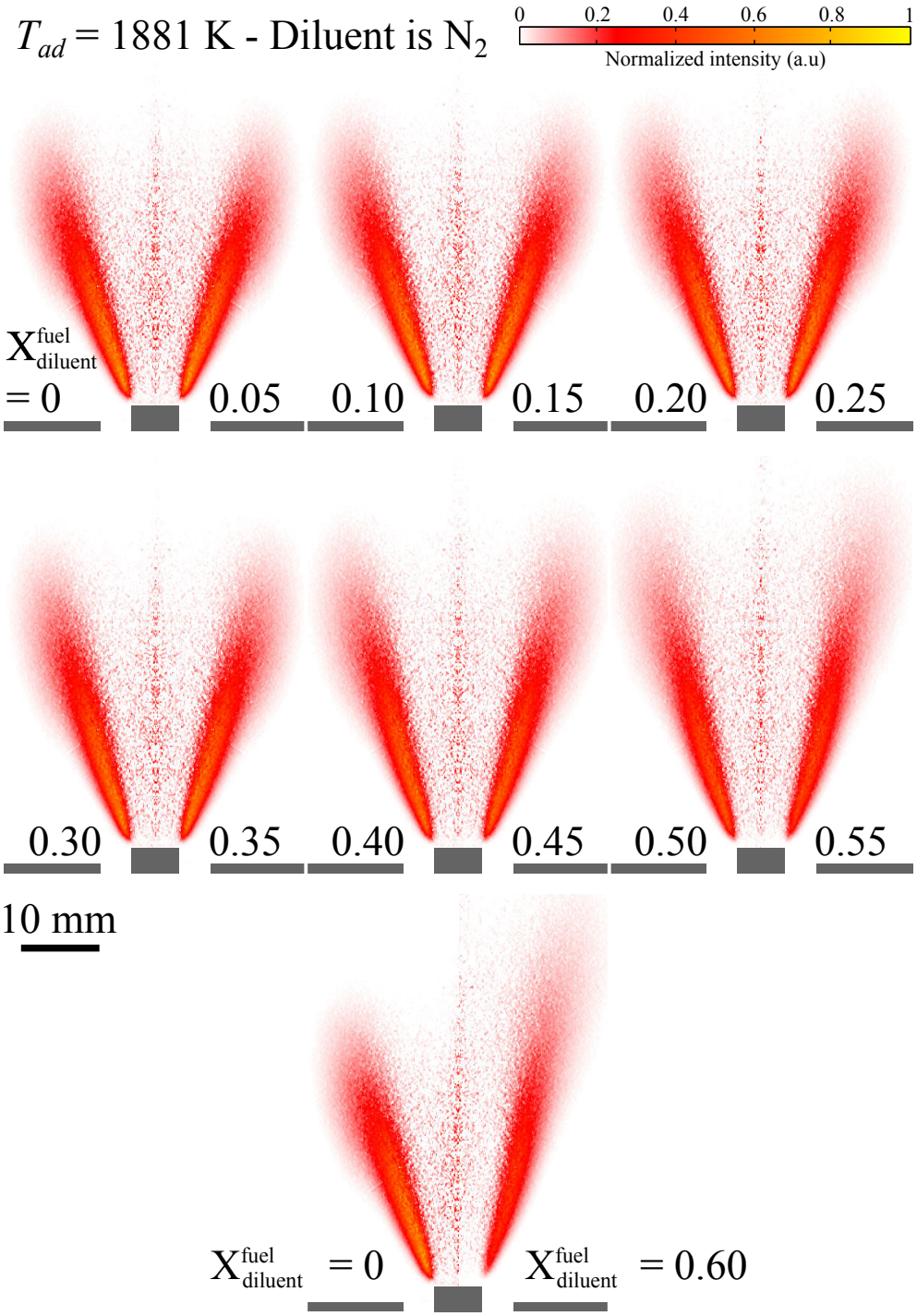

Figure 7.5: *Abel transformed OH* chemiluminescence images of swirled flames when the molar fraction of N_2 in the fuel blend is increased (air not included) from $X^{fuel}_{diluent}$ = 0 to $X^{fuel}_{diluent}$ = 0.60 for a fixed adiabatic flame temperature T_{ad} = 1881 K, thermal power P = 4 kW, and hydrogen enrichment $X^{fuel}_{H_2}$ = 0.60.*

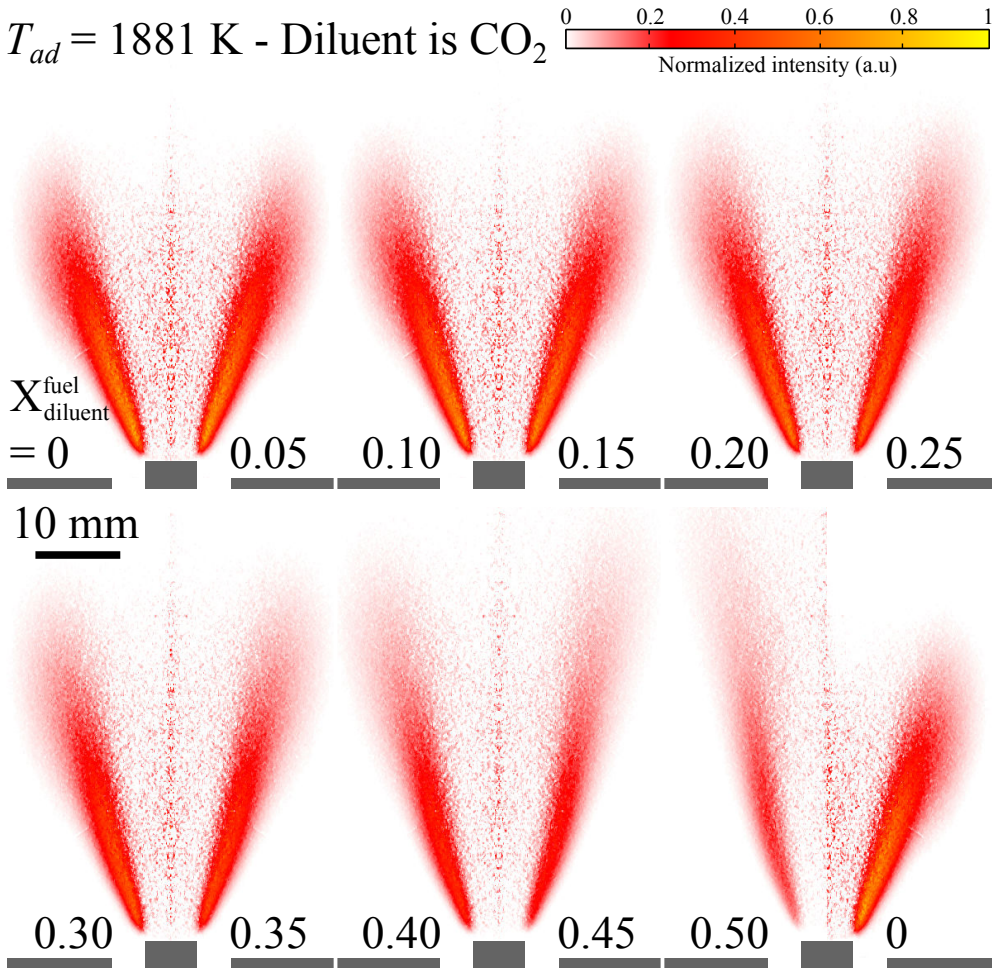

Figure 7.6: *Abel transformed OH* chemiluminescence images of swirled flames when the molar fraction of CO_2 in the fuel blend is increased (air not included) from $X^{fuel}_{diluent}$ = 0 to $X^{fuel}_{diluent}$ = 0.60 for a fixed adiabatic flame temperature T_{ad} = 1881 K, thermal power P = 4 kW, and hydrogen enrichment $X^{fuel}_{H_2}$ = 0.60.*

by the increase of the equivalence ratio of the combustible mixture that was set to operate the system at a fixed adiabatic flame temperature (see Fig. 7.1). When CO_2 is used as a diluent, the decrease in the OH* chemiluminescence intensity due to dilution is larger than for N_2 diluted flames and the increase of the equivalence ratio does not compensate this effect anymore. It is known that increasing the CO_2 concentration in the combustible mixture reduces the concentration of CH in the flames (Guo et al. (2010)). The production of OH^* is then penalized because this excited radical is mainly produced through the formation reaction: $CH + O_2 \longrightarrow OH^* + CO$ (Porter et al. (1967) and Panoutsos et al. (2009)). However, the OH* chemiluminenscence intensity takes higher values for experiments conducted at a fixed adiabatic flame temperature that those carried out at a fixed equivalence ratio.

7.3 Thermal effects of CO_2

The thermal impact of dilution differs when using N_2 or CO_2 due to the difference in the thermal capacities per unit of volume of these molecules. The radiative properties of the burnt gases are also modified when the diluent compositions and concentrations are varied. It was shown in chapter 3 that heat losses need to be taken into account in our combustor because they strongly alter flame stabilization processes as discussed in chapter 5. Because the combustion chamber is made of four transparent quartz walls, the contribution to heat losses due to the thermal radiation of species located in the high temperature burnt gases has to be considered. It is well known that N_2 and CO_2 feature very different radiative properties (Gaydon (1957)) in particular in the IR spectrum. The nature of the diluent affects the thermal efficiency of the combustor because the intensity of the radiative heat losses from the burnt gases is modified.

Stable molecules such as CO_2, H_2O, or CO are generally present in the burnt gases of hydrocarbon flames and radiate in IR spectrum (Gaydon (1957)). Short life radical species present within the flame reaction layer such as OH, CH, or C_2 also emit light in the UV or visible spectrum (Dagusé et al. (1993)). Nitrogen does not participate, at least at the leading order, to radiation (Gaydon (1957) and Guo et al. (2010)). As an illustration, Guiberti et al. (2015) found from joint experiments and simulations that H_2O and CO_2 are responsible for 97% of the radiative heat losses in the burnt gases of the $CH_4/O_2/N_2/H_2O$ rich flames they studied. In their case, H_2O alone is responsible for 63% of the radiative heat losses.

Figure 7.7a plots the temperature measured by the thermocouple TC_4 located at the combustor exhaust (see Fig. 3.10) as a function of the molar fraction of

diluent in the fuel for a swirled flame when $X_{H_2}^{fuel} = 0.60$ and $P = 4$ kW. Results are presented for N_2 (circle symbols) or CO_2 (square symbols) dilution. Experiments are carried out when dilution increases for a fixed equivalence ratio (red curves) or for a fixed adiabatic flame temperature (black curves). In agreement with results presented in chapter 3, the temperature at the combustor exhaust is always lower than the adiabatic flame temperature that ranges from $T_{ad} = 1663$ K when CO_2 is used with $X_{diluent}^{fuel} = 0.50$ and $\phi = 0.70$ to $T_{ad} = 1881$ K without dilution for a mixture at the same equivalence ratio. Figures 7.7a shows that the temperature reached at the combustor exhaust depends on the dilution ratio and on the diluent composition.

When experiments are conducted at a fixed equivalence ratio $\phi = 0.70$, the temperature at the combustor exhaust rapidly decreases with the molar fraction of diluent in the combustible mixture. This is attributed to the drop in the adiabatic flame temperature when the molar fraction of diluent increases as shown in Fig. 7.1a. When experiments are conducted at a fixed adiabatic flame temperature $T_{ad} = 1881$ K, the temperature at the exhaust of the combustor remains roughly constant when N_2 is used as a diluent. It is however striking that the temperature at the exhaust of the combustor decreases with the molar fraction of CO_2 in the reactants mixture when this molecule is used for dilution. When the molar fraction of CO_2 increases in the fresh gases, the molar fraction of CO_2 also increases in the burnt gases. The radiative properties of these combustion products are modified and heat losses due to thermal radiation increase (Guiberti et al. (2015)). This phenomenon does not take place when dilution is realized with N_2 which is inert in terms of thermal radiation (Guo et al. (2010)).

In this situation, the molar fraction of the diluent N_2 increases but the concentrations of air decreases as shown in Fig. 7.1. Dilution with N_2 at a fixed adiabatic flame temperature means that a fraction of O_2 is removed from the combustible mixture and replaced by a similar quantity of N_2. N_2 and O_2 have a comparable behavior in terms of thermal radiation (Gaydon (1957)) and the radiative properties of the burnt gases are not modified by the dilution. A thermocouple located at the surface of a vertical steel bar (see Fig. 3.10) measures an increase of the wall temperature from $TC_2 = 646$ K to $TC_2 = 656$ K when the molar fraction of CO_2 in the combustible mixture increases from $X_{diluent}^{fuel} = 0$ to $X_{diluent}^{fuel} = 0.50$ during these experiments conducted at a fixed adiabatic flame temperature. These measurements corroborate the large modifications of the radiative properties of the burnt gases when N_2 is replaced by CO_2.

Modification of the radiative properties of the burnt gases explains the temperature drop when CO_2 is used for dilution provided that convective heat losses are not altered by this replacement. We calculated the convective heat transfer coefficients for the flow conditions reached close to the combustor peripheral walls (Fig. 2.52) for two burnt gases compositions. The first one corresponds

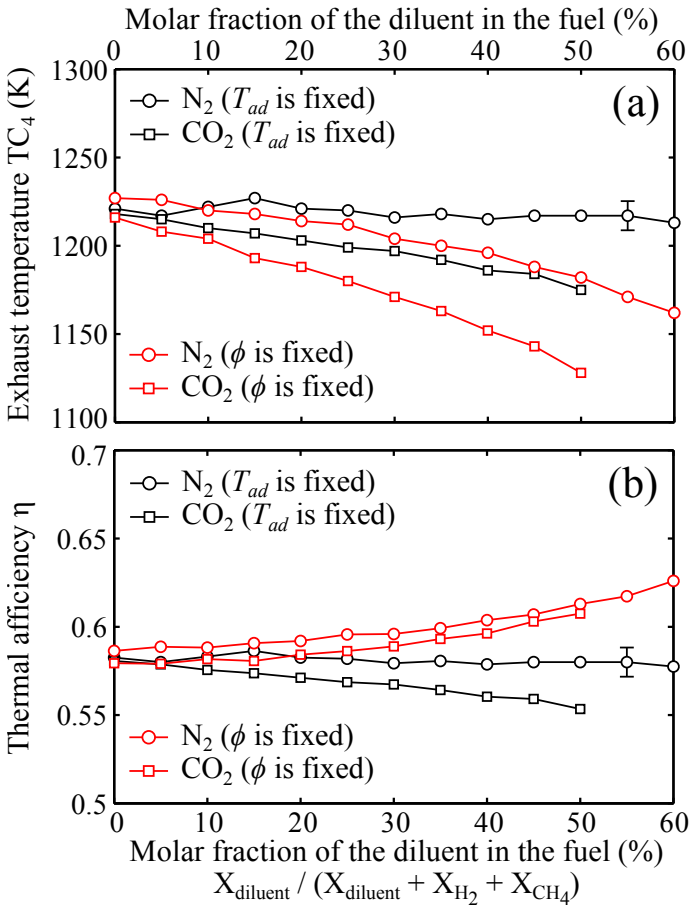

Figure 7.7: *Temperature measured by the thermocouple TC_4 located at the combustor exhaust (a) (see Fig. 3.10) and calculated thermal efficiency η (b) as a function of the molar fraction of diluent in the fuel when $X_{H_2}^{fuel}$ = 0.60 and P = 4 kW. Diluent is N_2 (circle symbols) or CO_2 (square symbols). Experiments are carried out when dilution is increased for a fixed equivalence ratio (red curves) or for a fixed adiabatic flame temperature (black curves).*

to the burnt gases of the flame diluted with N_2 with $X_{H_2}^{fuel} = 0.60$, $P = 4\,kW$, $X_{diluent}^{fuel} = 0.50$, and $T_{ad} = 1881\,K$. The second corresponds to the flame diluted with CO_2 at the same operating conditions. Burnt gases compositions are deduced from 1-D simulations with the REGATH solver. The convective heat transfer coefficients h are calculated with the method described in Sec. 2.7. One finds $h = 11.9\,W \cdot m^{-2} \cdot K^{-1}$ for the N_2 diluted flame and $h = 11.6\,W \cdot m^{-2} \cdot K^{-1}$ for the flame diluted with CO_2. These results indicate that the convective heat transfer is barely affected when N_2 is replaced by CO_2. The small difference may not lead to measurable temperature differences. It is thus safe to conclude that the temperature drop in the burnt gases of the CO_2 diluted flames is due to enhanced radiative heat losses.

Dilution with CO_2 affects the temperature field in the burnt gases and at the surface of the combustion chamber walls. It is interesting to analyze the impact of dilution on the global thermal efficiency of the combustor. An estimation of this efficiency has been proposed in chapter 3 by calculating $\eta = (TC_4 - T_u)/(T_{ad} - T_u)$, where $T_u \simeq 300\,K$ stands for the temperature of the fresh gases in the injector. Figure 7.7b plots the evolution of this quantity η with the molar fraction of diluent in the reactants mixture for the same operating conditions as in Fig. 7.7a. When experiments are conducted at a fixed equivalence ratio, the global efficiency of the combustor increases with the dilution and ranges from $\eta \simeq 0.58$ when $X_{diluent}^{fuel} = 0$ to $\eta \simeq 0.63$ when $X_{diluent}^{fuel} = 0.60$ when N_2 is used. The burnt gases and wall solid temperatures are lower for a high dilution ratio and this penalizes conductive, convective, and radiative heat transfers and reduces heat losses. The thermal efficiency is slightly lower when CO_2 is used as a diluent. Results obtained in this work suggest that this is due to the increased radiative heat losses in this case.

When experiments are conducted at a fixed adiabatic temperature and with N_2 for dilution, the thermal efficiency becomes roughly independent of the dilution ratio. The burnt gases and wall solid temperatures remain here constant when dilution is increased. However, when CO_2 is used as the diluent, the thermal efficiency of the combustor decreases with the molar fraction of diluent in the combustible mixture. It slightly decreases from $\eta \simeq 0.58$ when $X_{diluent}^{fuel} = 0$ to $\eta \simeq 0.55$ when $X_{diluent}^{fuel} = 0.50$. In a combustion chamber featuring transparent peripheral walls, dilution with CO_2 promotes radiative heat losses. These losses penalize to the global thermal efficiency of the combustor. In an opaque combustor, the heat radiated from the burnt gases would lead to an increase of the temperature of the surrounding solid surfaces, including the peripheral walls and the solid load. It is then more difficult to conclude if the global efficiency of the process will reduce or increase. However, it is clear that the temperature field in the combustor will be modified when dilution by N_2 is replaced by CO_2.

7.4 Conclusions

Effects of dilution by N_2 or CO_2 on CH_4/H_2/air swirling flames were analyzed. Experiments were conducted at a fixed H_2 to CH_4 ratio $X_{H_2}^{fuel}$ = 0.60, a fixed thermal power P = 4 kW, and a fixed swirl number S = 0.4.

It was shown that it is possible to stabilize flames featuring high dilution ratios, with a molar fraction of diluent in the fuel up to $X_{diluent}^{fuel}$ = 0.60, when the central rod is installed. However, dilution alters the flame topology and the height of the flames increases with the molar fraction of diluent. This is due to the reduction of the laminar burning velocity when the molar fraction of diluent increases.

Due to its higher thermal capacity per unit of volume, CO_2 as a bigger effect than N_2 on the flame topology for a fixed molar fraction of diluent in the fuel. It is possible to reduce the impact of dilution by conducting experiments at a fixed adiabatic flame temperature instead of operating the system at a fixed equivalence ratio.

It was demonstrated that dilution modifies the global thermal efficiency of the combustor. Increasing the dilution increases the efficiency when experiments are conducted at a fixed equivalence ratio, independently of the diluent nature. This is attributed to the global decay of temperatures in the combustion chamber that penalizes conductive, convective, and radiative heat losses. When the adiabatic flame temperature remains fixed, the thermal efficiency is not modified by dilution with N_2. This efficiency decreases with the dilution ratio when CO_2 is used for dilution, even if the adiabatic flame temperature remains constant. This is due to the thermal radiation of CO_2 in the IR that promotes radiative heat losses.

It was shown in this chapter that the composition and concentration of the diluent modifies the temperature field in a combustion chamber and may consequently alter the efficiency of an industrial process.

Conclusion and recommendations

The stabilization of confined swirling CH_4/H_2/air flames has been investigated experimentally. Focus is made on the analysis of flame topology modifications. Two different situations were considered depending on the level of interaction between the flame and the combustor peripheral walls. In situation A direct flame/wall interactions are considered. In situation B the flame lies far away from the peripheral wall. In both situations, parametric analyses were conducted to identify and sort out the main dimensionless parameters controlling topology bifurcations. The main findings of this work are listed below:

- In the case of direct flame/wall interaction (situation A), it has been shown that transition from a V shaped to an M shaped flame is triggered by flashback of the V flame tip along the boundary layer of the combustor peripheral wall. Critical conditions are reached for the flashback of the V flame tip when a Karlovitz number Ka of the flow exceeds a threshold value.

- A simplified model was developed to predict the critical value of Ka above which transition takes place when the injection bulk flow velocity or the swirl number are varied. It was found that increasing the swirl number helps the stabilization of M flames. For a fixed swirl number and injection bulk flow velocity, flames featuring lower values of the Lewis number of the combustible mixture (obtained by increasing the molar fraction of H_2) are more prone to flashback and are more likely to stabilize with an M shape.

- When the flame does not interact with the combustor peripheral wall (situation B), it has been shown that the Lewis number of the combustible mixture is still an important parameter controlling flame shape transitions. Increasing the molar fraction of H_2 in the fuel helps the stabilization of M flames. In this situation, the impact of H_2 is related to the increased resistance to strain rate of flames featuring large concentrations of H_2. The laminar burning velocity and adiabatic flame temperature

also alter topology transitions, but it was demonstrated that two flames featuring the same laminar burning velocity or the same adiabatic flame temperature do not necessarily have the same probability to stabilize with an M shape.

- Effects of thermal boundary conditions of the combustor solid elements on topological bifurcations were also analyzed. It has been demonstrated that increasing heat losses at the combustor walls, or equivalently decreasing the combustor peripheral wall surface temperatures, decreases the temperature of the burnt gases located in the Outer Recirculation Zone (ORZ) of the swirl flow. This temperature drop in the ORZ penalizes the stabilization of M flames.

- The combined effects of heat losses and strain rate were emphasized with 1-D direct numerical simulations of stretched laminar flames. It has been confirmed that flame extinction limits are reduced when the temperature of the burnt gases decreases. Transitions from an M to a V flame are consecutive to localized extinctions of flame front elements located in the Outer Shear Layer (OSL) of the swirling flow.

- The large impact of heat losses on the stabilization of these swirling flames indicate that the non-adiabaticity of the combustor needs to be taken into account in the numerical simulations. It has also been shown that it is necessary to develop further diagnostics and methods adapted for the measure of thermal boundary conditions in combustors.

The dynamics of CH_4/H_2/air swirling flames submitted to mass flow rate perturbations has also been investigated to analyze effects of unsteadiness on topology changes. It has been found that:

- The flame frequency response of low swirl CH_4/H_2/air flames is very similar to that analyzed by Palies (2010) for the dynamics of CH_4/air flames at a higher swirl number. The role of flame/vortex interactions and of the phase difference between longitudinal and transversal perturbations on the flame transfer function were analyzed in Appendices B and C.

- In the case of flames featuring intermittent fluctuations between V and M states in the absence of external perturbations, incoming flow rate perturbations at low frequency and high amplitude alter the flame topology. In these cases, the probability to stabilize an M flame oscillates around a mean value at the modulation frequency and with an amplitude close to the flow rate modulation amplitude. The mean probability to stabilize an M flame roughly corresponds to the M shape probability of the unperturbed flame.

The stabilization of CH_4/H_2/air flames diluted by N_2 of CO_2 was finally investigated. It was shown that:

- The laminar burning velocity of diluted flames rapidly decreases with the molar fraction of diluent in the fuel blend. This drop of burning velocity is larger when CO_2 is used due to its higher thermal capacity per unit of volume.

- It has been shown that it is possible to dilute flames at a fixed thermal power and adiabatic flame temperature to minimize effects of dilution on flame stabilization.

- Increasing the dilution reduces the local and global OH* chemiluminescence intensity emitted by the flames. Again, effects are more important with CO_2 dilution.

- Due to large differences in the spectroscopic behavior of N_2 and CO_2, it has been found that dilution by CO_2 increases the radiative contribution of burnt gases to heat transfer and modifies the temperature field in the burnt gases and at the combustor solid surfaces.

- For a fixed adiabatic flame temperature, increasing the molar fraction of CO_2 in the fuel blend decreases the burnt gases temperature at the combustor outlet and penalizes the global thermal efficiency of the combustor. Conversely, increasing the dilution at a fixed equivalence ratio decreases the adiabatic flame temperature and increases the global thermal efficiency of the combustor.

- These experiments have demonstrated that the nature and concentration of the diluent have a strong influence on the stabilization of swirl flames, on the temperature field, and more generally on the combustor efficiency.

These studies open new perspectives and can be pursued in various directions:

- It is necessary to account for the combined effects of heat losses and strain rate in the simulations of confined turbulent flames stabilized in shear layers of swirling flows. New combustion models need to be developed to account for the enthalpy defect in the combustion chamber and its effect on turbulent flames. Proper evaluation of the 3-D local strain rate is also fundamental and effects of strain rate on turbulent combustion must be included in new models.

- Another difficulty consists in the implementation of realistic thermal

boundary conditions in the numerical flow solvers. One possibility is to simulate directly heat losses using more complex codes accounting for heat transfer to the solid walls and radiative heat transfer between burnt gases and the combustor solid elements.

- As demonstrated in this thesis, it is also possible to measure the thermal boundary conditions of solid elements and use these data in the simulations. It is then important to improve existing techniques or develop new diagnostics for temperature measurements in the gases but also at the surfaces of the combustor walls. The quality of the predictions from the simulations is directly determined by the accuracy of the thermal boundary condition measurements. In this context, temperature measurements relying on Laser Induced Phosphorescence (LIP) of thermographic phosphors are very promising.

- Individual effects of N_2 and CO_2 as diluents were analyzed in this thesis. It is now necessary to study the combustion of more realistic COG/BFG mixtures which include both N_2 and CO_2 as diluents but also feature large amount of carbon monoxide in addition to methane and hydrogen.

- The stabilization of flames burning these types of mixtures needs to be analyzed in terms of flammability limits to evaluate their propensity for blow-off and flashback. This analysis should be carried out for different combustor geometries and a range of swirl numbers.

- The impact of these parameters on the flame topology is also an interesting topic because methane, COG, and BFG mixtures feature very different Lewis numbers.

- Finally, the influence of the combustible mixture composition on the radiative heat transfers should be addressed due to the large variability of CO_2 and H_2O concentrations in the hot burnt gases.

Appendix A

Schematic diagram of the experimental setup

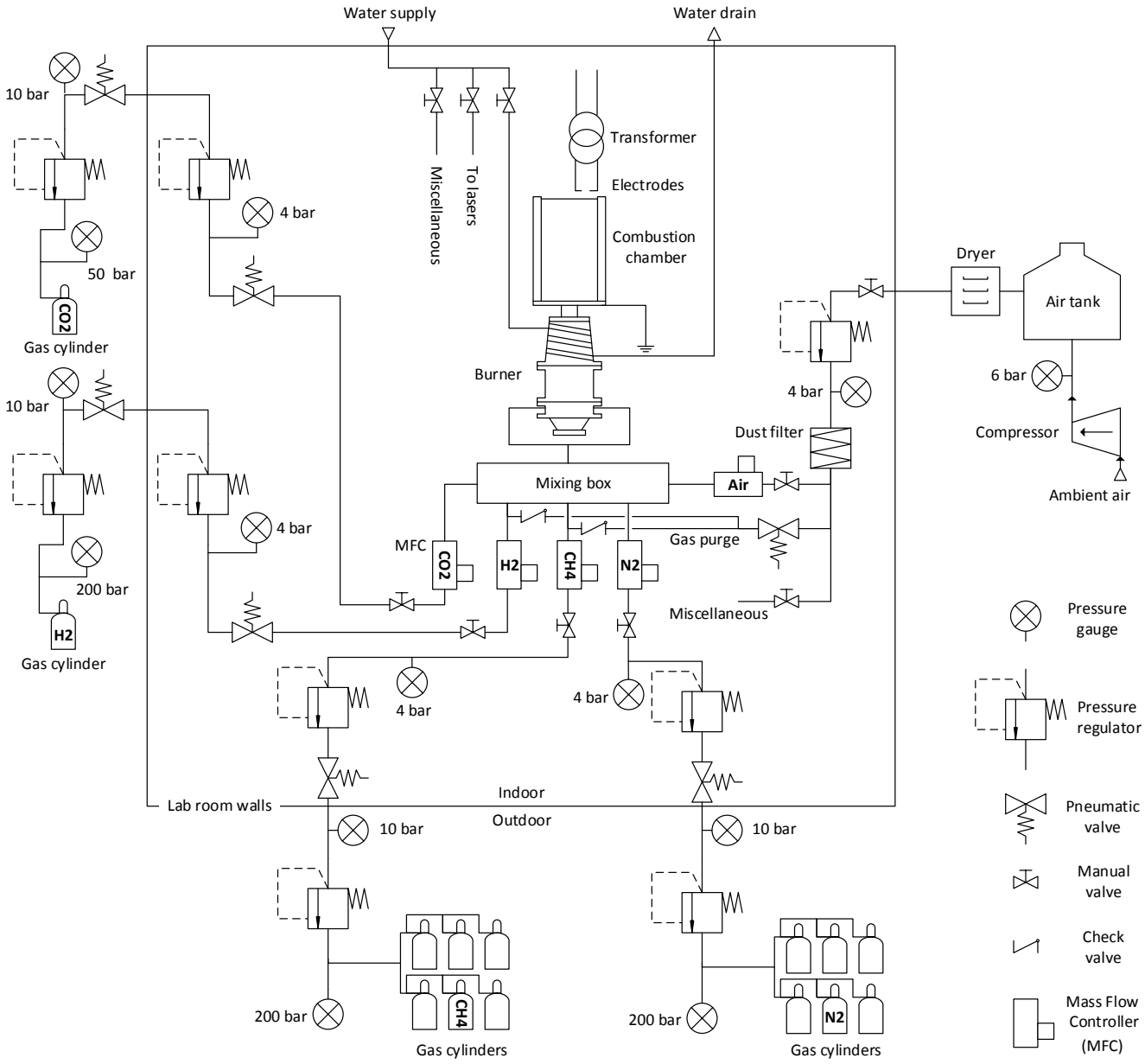
Water supply
Water drain
10 bar
50 bar
CO2
Gas cylinder
4 bar
Miscellaneous
To lasers
Transformer
Electrodes
Combustion chamber
Burner
Dryer
Air tank
6 bar
Compressor
Ambient air
4 bar
Dust filter
10 bar
200 bar
H2
Gas cylinder
4 bar
Mixing box
Air
MFC
CO2
H2
CH4
N2
Gas purge
Miscellaneous
4 bar
4 bar
Lab room walls
Indoor
Outdoor
10 bar
10 bar
200 bar
CH4
Gas cylinders
200 bar
N2
Gas cylinders
Pressure gauge
Pressure regulator
Pneumatic valve
Manual valve
Check valve
Mass Flow Controller (MFC)

Appendix B

Effects of swirl fluctuations

The dynamics of swirling flames is sensitive to the response of the swirler to sound waves. Swirl number fluctuations have been identified in a series of studies for flames stabilized in swirled flows with swirl numbers larger than about $S \geq 0.5$ (Komarek and Polifke (2010), Palies et al. (2010), Palies et al. (2011), and Bunce et al. (2013)). It is interesting to examine if swirl fluctuations also alter the acoustic response of swirled flames before vortex breakdown takes place when the swirl number is not too high.

The swirler submitted to sound waves generate longitudinal and azimuthal flow perturbations downstream in the injection tube (Palies et al. (2011a)). Azimuthal vortical perturbations are detached from the trailing edges of swirler vanes in response to the longitudinal excitation. Closely downstream the swirler, longitudinal and azimuthal perturbations are in phase, but these perturbations are not transported at the same velocity in the injection tube (Palies et al. (2011), Palies et al. (2011a)). Longitudinal disturbances have a velocity $u_{cv}^{z} \simeq U + c \simeq 376\,\mathrm{m \cdot s^{-1}}$ within the injector. Azimuthal perturbations are convected by the mean flow at a lower velocity $u_{cv}^{\theta} \simeq U \simeq 14\,\mathrm{m \cdot s^{-1}}$ in this element. Consequently, the phase difference between longitudinal and azimuthal perturbations changes as the distance from the vanes increases. This mechanism contributes to heat release rate fluctuations (Palies et al. (2011)). If l denotes the distance from the trailing edge of the swirler to the injector outlet, the phase difference $\Delta\varphi$ between azimuthal and longitudinal disturbances at the injector inlet can be written as:

$$\Delta\varphi = \omega\left(\frac{l}{u_{\theta}^{cv}} - \frac{l}{u_{z}^{cv}}\right) \simeq 2\pi f \frac{l}{U} \tag{B.1}$$

because $U << c$. In our experiments, the distance between the trailing edge of the vanes and the injector rim is $l = 45\,\mathrm{mm}$. Longitudinal and azimuthal velocities are in phase at the injector outlet ($\Delta\varphi = 2pi$) for a modulation fre-

quency of f = 322 Hz. A phase difference $\Delta\varphi = \pi$ is obtained for a modulation frequency of f = 161 Hz. These values roughly correspond to the frequencies leading to gain extrema of the FTF as shown in Fig. 6.3. These features have been identified as resulting from swirl number oscillations $S = \overline{S} + S'$ (Palies et al. (2011b)):

$$\frac{\mathrm{S'}}{\overline{S}} = \frac{v'_\theta}{\overline{v_\theta}} - \frac{v'_z}{\overline{v_z}} \tag{B.2}$$

wherev_θ and v_z denote the azimuthal and axial velocity component of the swirling flow at the injector outlet. Predictions from this model are shown in Fig. B.1 where the normalized longitudinal and azimuthal velocity fluctuations are plotted at the injector outlet for the two modulation frequencies f = 161 Hz and f = 322 Hz. The amplitude of the normalized fluctuations is taken equal for both velocity components as shown by Palies et al. (2011a). When a phase difference $\Delta\varphi = \pi$ is set, the relative swirl number fluctuation calculated with Eq. (B.2) shows a large oscillation for f = 161 Hz in Fig. B.1. For a modulation frequency of f = 322 Hz, a phase difference $\Delta\varphi$ = 0 is set. In this case, the swirl number shown in Fig. B.1 does not vary with time. This analysis indicates that the swirled flames studied herein are submitted to different types of flow perturbations at these two modulation frequencies.

Large swirl number fluctuations are suspected for f = 161 Hz. The FTF in Fig. 6.3 features indeed a local minimum of the gain at this forcing frequency. Conversely, when the forcing frequency is set to f = 322 Hz, the swirl number remains constant during the forcing cycle and this corresponds to a high gain of the FTF in Fig. 6.3. These observations are consistent with the descriptions made by Palies et al. (2010) and the mechanisms proposed by Palies et al. (2011). Even if swirl number fluctuations were not measured directly in these experiments, this analysis confirms their presence and their impact on the flame response to acoustic forcing. It is thus interesting to analyze the dynamics of the lower and upper flame brush during the forcing cycle. Figure B.2 shows the phase averaged evolution of the OH* chemiluminescence intensity integrated over the lower part (blue dots), the upper part (green dots), and over the global flame region (red dots) when f = 160 Hz and $u'/\bar{u}$ = 0.12. It is clear that the fluctuating heat release rate originating from the lower and the upper flame regions in Fig. B.2 are in phase opposition for this forcing frequency. This implies that the resulting fluctuation of the heat release rate integrated over the whole flame region remains small. This condition corresponds thus to local minimum of the FTF gain as found in Fig. 6.3. Arrows in Fig. 6.4 (top) show that when the upper part of the flame widens indicating that the flame surface area increases in this region, the size of the lower part reduces and the flame surface area decreases in the lower region. This explains the low gain of the FTF when f = 160 Hz.

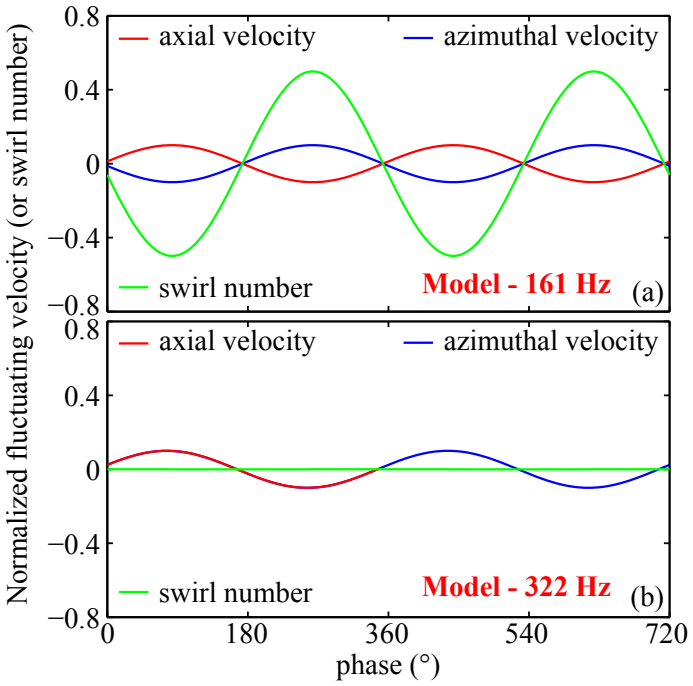

Figure B.1: *Modeled normalized fluctuating axial (red) and azimuthal velocities (blue) as a function of the phase in the acoustic forcing period. The calculated normalized fluctuating swirl number is plotted in green. The amplitudes are set to* $u'/\bar{u} = v'_\theta/\bar{v}_\theta = 0.10$. *(a)* $f = 161$ *Hz, the phase difference between the axial and azimuthal velocity at the injector exit is set to* $\Delta\varphi = \pi$. *(b)* $f = 322$ *Hz, the phase difference between the axial and azimuthal velocity at the injector exit is set to* $\Delta\varphi = 2\pi$.

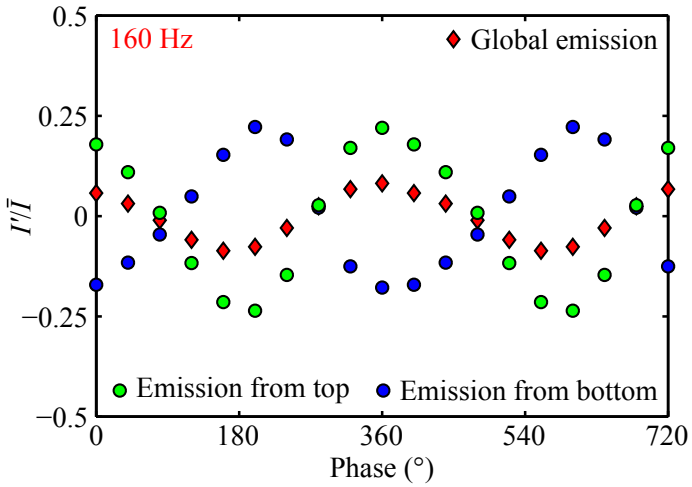

Figure B.2: *Normalized fluctuating light emission $I'/\bar{I}$ integrated over the whole flame region (red diamond), the bottom part of the image (blue circle), and the top part of the image (green circle) as a function of the phase in the modulation cycle when the flame at $X_{H_2}^{fuel} = 0.60$, $\phi = 0.70$, and $U = 14\ \mathrm{m \cdot s^{-1}}$ is forced at a frequency of 160 Hz with incoming velocity perturbations $u'/\bar{u} = 0.012$. The limit between bottom and top images is located 15 mm above the central rod tip (see Fig. 6.4).*

Appendix C

Galilean decomposition of the flow

It is interesting to compare the positions of the recirculating pockets of hot burnt gases to the position of the vortices when the flame is submitted to an acoustic modulation. Results for a flame at $X_{H_2}^{fuel} = 0.60$, $\phi = 0.70$, and $U = 14\ \mathrm{m \cdot s^{-1}}$ forced at $f = 350$ Hz and $u'/\bar{u} = 0.075$ are shown in Fig. 6.7 (left). The center of the recirculating pocket of hit gases and the center of the vortex are not superimposed in Fig. 6.7. It is difficult to correlate the location of the recirculating pocket to the vortex using these images. A Galilean decomposition of the flow (Adrian et al. (2000)) is used to plot the 2-D velocity fields in the vortex frame. For that purpose the convection velocity of the vortices needs to be determined.

Figure C.1 shows the position of the center of the vortices at the different phases of the forcing cycle. The time delay between the different phases is fixed to $\Delta t = 571$ µs. It is possible to plot the trajectory of the vortex during a modulation period and calculate its convection velocity $\mathbf{U_{cv}} = (u_{cv}, v_{cv})$. Except for the first milliseconds after its generation, the vortex follows a straight line and is convected at a constant velocity. The distance between the center point remains the same between successive phases in Fig. C.1. The convection velocity is $U_{cv} = 7.2\ \mathrm{m \cdot s^{-1}}$. This value approximately corresponds to half the injection bulk flow velocity $U = 14\ \mathrm{m \cdot s^{-1}} \simeq 2 \times U_{cv}$. This convection velocity also corresponds to the value measured in the OSL which is approximately the average value between the jet velocity ($U_{jet} \simeq 14\ \mathrm{m \cdot s^{-1}}$) and ORZ velocity($U_{ORZ} \simeq 0\ \mathrm{m \cdot s^{-1}}$). Vortices generated by the acoustic modulation are thus convected along the OSL.

As the trajectory and convection velocity of the vortices are known (see Fig. C.1), it is possible to operate a Galilean decomposition of the flow by removing the vortex convection velocity $\mathbf{U_{cv}}$ from the phase averaged velocity field (u, v)

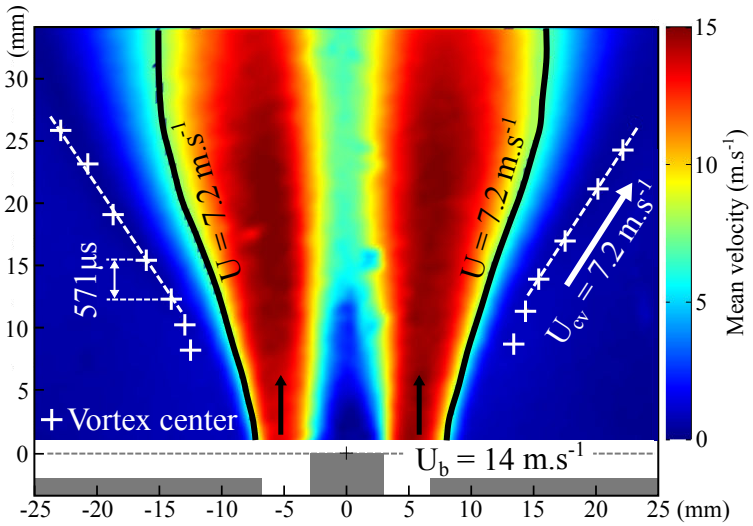

Figure C.1: *Modulus of the 2-D longitudinal mean velocity for the unperturbed flame at* $X_{H_2}^{fuel}$ = 0.60, ϕ = 0.70, *and* U = 14 m · s^{-1}. *The positions of the vortices center for each phase during a forcing cycle at* f = *350 Hz and* $u'/\bar{u}$ = 0.075 *defined in Fig. 6.7 are represented by white crosses.*

(Adrian et al. (2000)). This mathematical operation ($u_{gal} = u - u_{cv}$ and $v_{gal} = v - v_{cv}$) allows to visualize the velocity field in the vortex frame as shown in Fig.C.2 for the five phases of interest. In these images, the center of the burnt gases recirculating pocket coincides with the vortex center. The envelope of the burnt gases recirculating pocket also corresponds to the vortex envelope. These experiments clearly demonstrate that the burnt gases are trapped and recirculate in the vortex.

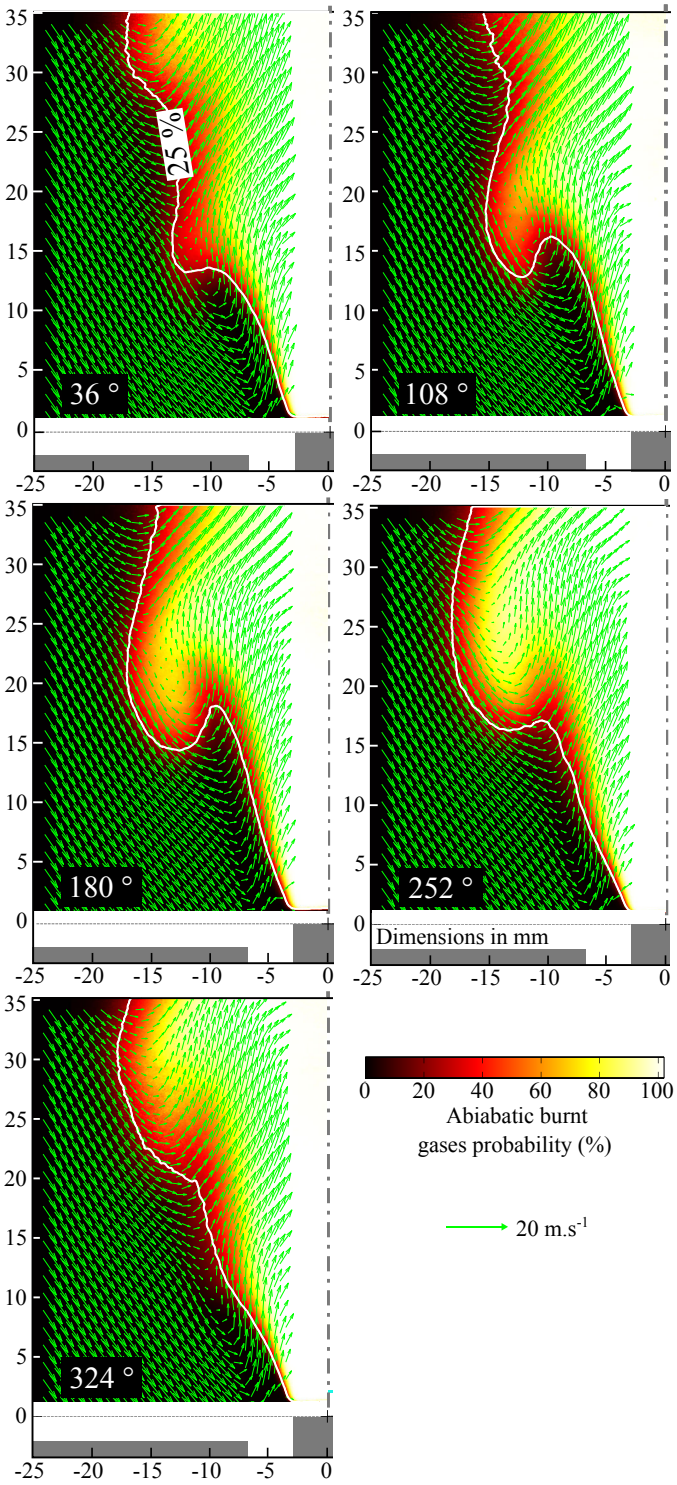

Figure C.2: *Phase averaged probability to find hot burnt gases for the flame at* $X_{H_2}^{fuel} = 0.60$ *and* $\phi = 0.70$ *forced at a frequency* f *= 350 Hz with incoming velocity perturbations* $u'/\bar{u} = 0.075$*. The phase averaged mean velocity field obtained by Galilean decomposition is superimposed.*

References

Adrian, R. J., K. T. Christensen, and Z.-C. Liu (2000). Analysis and interpretation of instantaneous turbulent velocity fields. *Experiments in Fluids 29*(3), 275–290. *(p. 220, 253, 254)*

Allison, S. and G. T. Gillies (1997). Remote thermometry with thermographic phosphors: Instrumentation and applications. *Review of Scientific Instruments 68 (7)*(2615). *(p. 83, 84, 85, 87, 98)*

Arroyo, M. P. and R. K. Hanson (1993, Oct). Absorption measurements of water-vapor concentration, temperature, and line-shape parameters using a tunable ingaasp diode laser. *Applied Optics 32*(30), 6104–6116. *(p. 81)*

Augé, M. (2005). *Développement et exploitation de diagnostics optiques basés sur la fluorescence de radicaux. Application aux moteurs automobiles*. Ph. D. thesis, Ecole Centrale Paris, Laboratoire d'Energétique Moléculaire et Macroscopique Combustion (EM2C) du CNRS et de Laboratoire d'Energétique Moléculaire et Macroscopique, Combustion (EM2C) du CNRS et de l'ECP. *(p. 59, 60, 61)*

Balachandran, R., B. Ayoola, C. Kaminski, A. Dowling, and E. Mastorakos (2005). Experimental investigation of the nonlinear response of turbulent premixed flames to imposed inlet velocity oscillations. *Combustion and Flame 143*(1–2), 37 – 55. *(p. 215, 218)*

Ballester, J. and T. García-Armingol (2010). Diagnostic techniques for the monitoring and control of practical flames. *Progress in Energy and Combustion Science 36*(4), 375 – 411. *(p. 233)*

Ballester, J. M., C. Dopazo, N. Fueyo, M. Hernández, and P. J. Vidal (1997). Investigation of low-nox strategies for natural gas combustion. *Fuel 76*(5), 435 – 446. *(p. 2)*

Beér, J. and N. Chigier (1972). *Combustion Aerodynamics*. London, Applied Science. *(p. 5, 39)*

Birbaud, A. L. (2006). *Dynamique d'intéractions sources des instabilités de combustion*. Ph. D. thesis, Ecole Centrale Paris. *(p. 43)*

Birbaud, A. L., D. Durox, S. Ducruix, and S. Candel (2007). Dynamics of free jets submitted to upstream acoustic modulations. *Physics of Fluids 19*(1), 1–20. *(p. 213)*

Boudy, F. (2012). *Analyse de la dynamique non-linéaire et du contrôle des*

instabilités de combustion fondée sur la "Flame Describing Function" (FDF). Ph. D. thesis, Ecole Centrale Paris. *(p. 43)*

Bourgouin, J.-F., J. Moeck, D. Durox, T. Schuller, and S. Candel (2013). Sensitivity of swirling flows to small changes in the swirler geometry. *Comptes Rendus Mécanique 341*(1–2), 211 – 219. *(p. 40)*

Bouvet, N. (2009). *Experimental and Numerical Studies of the Fundamental Flame Speeds of Methane/Air and Syngas (H_2/CO)/Air Mixtures*. Ph. D. thesis, Université d'Orléans. *(p. 26)*

Bradley, D., A. K. C. Lau, and M. Lawes (1992). Flame stretch rate as a determinant of turbulent burning velocity. *Philosophical transactions of the Royal Society of London series A-Mathematical Physical and Engineering Sciences 338*(1650), 359–387. *(p. 154, 162)*

Bray, K., M. Champion, and P. A. Libby (1991). Premixed flames in stagnating turbulence: Part I. the general formulation for counterflowing streams and gradient models for turbulent transport. *Combustion and Flame 84*(3–4), 391 – 410. *(p. 18)*

Bray, K., M. Champion, and P. A. Libby (1996). Extinction of premixed flames in turbulent counterflowing streams with unequal enthalpies. *Combustion and Flame 107*(1–2), 53 – 64. *(p. 18)*

Brown, D. M. (1995). Combustion control apparatus and method, european patent application No. 0 677 706 A1, 95/42. Technical report, General Electric Company. *(p. 3, 4, 27, 228)*

Brübach, J., A. Dreizler, and J. Janicka (2007). Gas compositional and pressure effects on thermographic phosphor thermometry. *Measurement Science and Technology 18*(3), 764. *(p. 87, 88)*

Brübach, J., C. Pflitsch, A. Dreizler, and B. Atakan (2013). On surface temperature measurements with thermographic phosphors: A review. *Progress in Energy and Combustion Science 39*(1), 37 – 60. *(p. 82, 83, 84, 85, 87, 88)*

Bruneaux, G., K. Akselvoll, T. Poinsot, and J. Ferziger (1996). Flame-wall interaction simulation in a turbulent channel flow. *Combustion and Flame 107*(1–2), 27 – 44. *(p. 154, 162)*

Bruun, H. H. (1995). *Hot-Wire Anemometry, Principles and Signal Analysis*. Oxford University Press Inc, New York. *(p. 45, 47)*

Bunce, N. A., B. D. Quay, and D. A. Santavicca (2013, 10). Interaction between swirl number fluctuations and vortex shedding in a single-nozzle turbulent swirling fully-premixed combustor. *Journal of Engineering for Gas Turbines and Power 136*(2), 021503–021503. *(p. 215, 249)*

Candel, S., D. Durox, T. Schuller, J.-F. Bourgouin, and J. P. Moeck (2014). Dynamics of swirling flames. *Annual Review of Fluid Mechanics 46*(1), 147–173. *(p. 7)*

Candel, S., T. Schmitt, and N. Darabiha (2011). Progress in transcritical combustion: experimentation, modeling and simulation. *Proceedings of 23rd ICDERS, Irvine USA, 2011*. *(p. 27, 53, 104, 154, 197)*

Cattolica, R. (1981). OH rotational temperature from two-line laser-excited fluorescence. *Applied Optics 20*(7), 1156–1166. *(p. 81)*

Cessou, A., C. Maurey, and D. Stepowski (2004). Parametric and statistical investigation of the behavior of a lifted flame over a turbulent free-jet structure. *Combustion and Flame 137*(4), 458 – 477. *(p. 62)*

Cessou, A. and D. Stepowski (1996). Planar laser induced fluorescence measurement of [OH] in the stabilization stage of a spray jet flame. *Combustion Science and Technology 118*(4-6), 361–381. *(p. 59)*

Cetas, T. C. (1978). Practical thermometry with a thermographic camera - calibration, transmittance, and emittance measurements. *Review of Scientific Instruments 49*(2), 245–254. *(p. 81)*

Chanaud, R. C. (1965). Observations of oscillatory motion in certain swirling flows. *Journal of Fluid Mechanics 21*(01), 111–127. *(p. 7)*

Chen, W.-H., M.-R. Lin, T.-S. Leu, and S.-W. Du (2011). An evaluation of hydrogen production from the perspective of using blast furnace gas and coke oven gas as feedstocks. *International Journal of Hydrogen Energy 36*(18), 11727 – 11737. *(p. 25, 26)*

Chomiak, J., J. Longwell, and A. Sarofim (1989). Combustion of low calorific value gases; problems and prospects. *Progress in Energy and Combustion Science 15*(2), 109 – 129. *(p. 26)*

Chterev, I., C. W. Foley, D. Foti, S. Kostka, A. W. Caswell, N. Jiang, A. Lynch, D. R. Noble, S. Menon, J. M. Seitzman, and T. C. Lieuwen (2014). Flame and flow topologies in an annular swirling flow. *Combustion Science and Technology 186*(8), 1041–1074. *(p. 10, 11, 59, 60)*

Coppola, G., B. Coriton, and A. Gomez (2009). Highly turbulent counterflow flames: A laboratory scale benchmark for practical systems. *Combustion and Flame 156*(9), 1834 – 1843. *(p. 18, 59, 60)*

Coriton, B., J. H. Frank, and A. Gomez (2013). Effects of strain rate, turbulence, reactant stoichiometry and heat losses on the interaction of turbulent premixed flames with stoichiometric counterflowing combustion products. *Combustion and Flame 160*(11), 2442 – 2456. *(p. 18, 60, 191, 193, 195)*

Coriton, B., J. H. Frank, A. G. Hsu, M. D. Smooke, and A. Gomez (2011). Effect of quenching of the oxidation layer in highly turbulent counterflow premixed flames. *Proceedings of the Combustion Institute 33*(1), 1647 – 1654. *(p. 18, 59, 60)*

Coriton, B., M. D. Smooke, and A. Gomez (2010). Effect of the composition of the hot product stream in the quasi-steady extinction of strained premixed flames. *Combustion and Flame 157*(11), 2155 – 2164. *(p. 18)*

Croonenbroek, T. (1996). *Diagnostics optiques appliqués aux milieux réactifs (diffusion rayleigh, fluorescence induite par laser, absorption, analyse de la chimiluminescence,...) application aux flammes laminaires étirées à contrre-courant*. Ph. D. thesis, Université Paris 6. *(p. 60)*

Dagusé, T., A. Soufiani, N. Darabiha, and J. Rolon (1993). Structure of diffusion and premixed laminar counterflow flames including molecular radiative transfer. *Combustion, Explosion and Shock Waves 29*(3), 306–311. *(p. 237)*

Daily, J. W. (1997). Laser induced fluorescence spectroscopy in flames. *Progress in Energy and Combustion Science 23*(2), 133 – 199. *(p. 58, 59, 60, 63)*

Davidson, D. F., A. Y. Chang, and R. K. Hanson (1989). Laser photolysis shock tube for combustion kinetics studies. *Symposium (International) on Combustion 22*(1), 1877 – 1885. *(p. 136, 151, 191)*

Davisson, C. and J. R. Weeks (1924, Sep). The relation between the total emissive power of a metal and its electrical resistivity. *Journal of the Optical Society of America 8*(5), 581–602. *(p. 109)*

Devillers, R., G. Bruneaux, and C. Schulz (2008). Development of a two-line OH-laser-induced fluorescence thermometry diagnostics strategy for gas-phase temperature measurements in engines. *Applied Optics 47*(31), 5871–5885. *(p. 81)*

Dinkelacker, F., B. Manickam, and S. Muppala (2011, September). Modelling and simulation of lean premixed turbulent methane/hydrogen/air flames with an effective Lewis number approach. *Combustion and Flame 158*(9), 1742–1749. *(p. 155)*

Döbbeling, K., J. Hellat, and H. Koch (2005, 09). 25 years of BBC/ABB/Alstom lean premix combustion technologies. *Journal of Engineering for Gas Turbines and Power 129*(1), 2–12. *(p. 2)*

Docquier, N., S. Belhalfaoui, F. Lacas, N. Darabiha, and C. Rolon (2000). Experimental and numerical study of chemiluminescence in methane/air high-pressure flames for active control applications. *Proceedings of the Combustion Institute 28*(2), 1765 – 1774. *(p. 233)*

Docquier, N. and S. Candel (2002). Combustion control and sensors: a review. *Progress in Energy and Combustion Science 28*(2), 107 – 150. *(p. 3, 4, 27)*

Docquier, N., F. Lacas, and S. Candel (2002). Closed-loop equivalence ratio control of premixed combustors using spectrally resolved chemiluminescence measurements. *Proceedings of the Combustion Institute 29*(1), 139 – 145. Proceedings of the Combustion Institute. *(p. 233)*

Driscoll, J. F. (2008). Turbulent premixed combustion: Flamelet structure and its effect on turbulent burning velocities. *Progress in Energy and Combustion Science 34*(1), 91 – 134. *(p. 154)*

Ducruix, S. (1999). *Dynamique des intéractions acoustique-combustion.* Ph. D. thesis, Ecole Centrale Paris. *(p. 43)*

Durbin, M. D., M. D. Vangsness, D. R. Ballal, and V. R. Katta (1996). Study of flame stability in a step swirl combustor. *Journal of Engineering for Gas Turbine and Power 118*(2), 308–315. *(p. 10)*

Durox, D., S. Ducruix, and F. Lacas (1999). Flow seeding with an air

nebulizer. *Experiments in Fluids 27*(5), 408–413. *(p. 44, 74)*

Durox, D., J. P. Moeck, J.-F. Bourgouin, P. Morenton, M. Viallon, T. Schuller, and S. Candel (2013). Flame dynamics of a variable swirl number system and instability control. *Combustion and Flame 160*(9), 1729 – 1742. *(p. 9, 14, 15, 40, 41, 119, 144, 169)*

Durox, D., T. Schuller, and S. Candel (2005). Combustion dynamics of inverted conical flames. *Proceedings of the Combustion Institute 30*(2), 1717 – 1724. *(p. 212, 213, 215, 218)*

Eckbreth, A. (1996). *Laser Diagnostics for Combustion Temperature and Species*. Combustion science and technology book series. Taylor & Francis. *(p. 58, 81)*

Edmondson, H. and M. Heap (1970). Blowoff of inverted flames. *Combustion and Flame 14*(2), 191 – 194. *(p. 12)*

Egolfopoulos, F., H. Zhang, and Z. Zhang (1997). Wall effects on the propagation and extinction of steady, strained, laminar premixed flames. *Combustion and Flame 109*(1–2), 237 – 252. *(p. 18)*

Eichler, C. and T. Sattelmayer (2011, November). Premixed flame flashback in wall boundary layers studied by long-distance micro-PIV. *Experiments in Fluids 52*(2), 347–360. *(p. 8, 142)*

Escudié, D. and E. Haddar (1993). Experimental study of a premixed turbulent stagnating flame. *Combustion and Flame 95*(4), 433–435. *(p. 18)*

Escudié, D., E. Haddar, and M. Brun (1999). Influence of strain rate on a premixed turbulent flame stabilized in a stagnating flow. *Experiments in Fluids 27*(6), 533–541. *(p. 18)*

Esquiva-Dano, I., H. Nguyen, and D. Escudié (2001). Influence of a bluff-body's shape on the stabilization regime of non-premixed flames. *Combustion and Flame 127*(4), 2167 – 2180. *(p. 13)*

Euler, M., R. Zhou, S. Hochgreb, and A. Dreizler (2014). Temperature measurements of the bluff body surface of a swirl burner using phosphor thermometry. *Combustion and Flame 161*(11), 2842 – 2848. *(p. 184)*

Francois, I., D. Larrauri, and D. Escudié (1997). Interaction between two premixed laminar V-shaped flame fronts at low Lewis number. *Combustion and Flame 110*(1–2), 14 – 24. *(p. 81)*

Fuhrmann, N., J. Brübach, and A. Dreizler (2013). Phosphor thermometry: A comparison of the luminescence lifetime and the intensity ratio approach. *Proceedings of the Combustion Institute 34*(2), 3611 – 3618. *(p. 85, 86, 97, 98)*

Galley, D., S. Ducruix, F. Lacas, and D. Veynante (2011). Mixing and stabilization study of a partially premixed swirling flame using laser induced fluorescence. *Combustion and Flame 158*(1), 155 – 171. *(p. 39)*

García-Armingol, T., Y. Hardalupas, A. Taylor, and J. Ballester (2014). Effect of local flame properties on chemiluminescence-based stoichiometry measurement. *Experimental Thermal and Fluid Science 53*, 93–103.

(p. 230)

Gaydon, A. (1957). *The Spectroscopy of Flames*. Wiley. *(p. 53, 81, 237, 238)*

Geyer, D., A. Dreizler, J. Janicka, A. Permana, and J. Chen (2005). Finite-rate chemistry effects in turbulent opposed flows: comparison of raman/rayleigh measurements and monte carlo {PDF} simulations. *Proceedings of the Combustion Institute 30*(1), 711 – 718. *(p. 18)*

Gibaud, C., J. A. Snyder, V. Sick, and R. P. Lindstedt (2005). Laser-induced fluorescence measurements and modeling of absolute {CH} concentrations in strained laminar methane/air diffusion flames. *Proceedings of the Combustion Institute 30*(1), 455 – 463. *(p. 27)*

Gicquel, O., L. Vervisch, G. Joncquet, B. Labegorre, and N. Darabiha (2003). Combustion of residual steel gases: laminar flame analysis and turbulent flamelet modeling. *Fuel 82*(8), 983 – 991. *(p. 3)*

Giovangigli, V. and M. Smooke (1987). Calculation of extinction limits for premixed laminar flames in a stagnation point flow. *Journal of Computational Physics 68*(2), 327 – 345. *(p. 16, 189, 195)*

Giovangigli, V. and M. Smooke (1989). Adaptive continuation algorithms with application to combustion problems. *Applied Numerical Mathematics 5*(4), 305 – 331. *(p. 18, 189, 195)*

Glassman, I. (1996a). 6 - diffusion flames. In I. Glassman (Ed.), *Combustion* (Third edition ed.)., pp. 267 – 324. San Diego: Academic Press. *(p. 3)*

Glassman, I. (1996b). 8 - environmental combustion considerations. In I. Glassman (Ed.), *Combustion* (Third edition ed.)., pp. 351 – 433. San Diego: Academic Press. *(p. 3)*

Gruber, A., J. H. Chen, D. Valiev, and C. K. Law (2012, 10). Direct numerical simulation of premixed flame boundary layer flashback in turbulent channel flow. *Journal of Fluid Mechanics 709*, 516–542. *(p. 8, 142)*

Gruber, A., A. Kerstein, D. Valiev, C. Law, H. Kolla, and J. Chen (2014). Modeling of mean flame shape during premixed flame flashback in turbulent boundary layers. *Proceedings of the Combustion Institute (2014), http://dx.doi.org/10.1016/j.proci.2014.06.073*. *(p. 142)*

Guiberti, T. F., C. Garnier, P. Scouflaire, J. Caudal, B. Labegorre, T. Schuller, and N. Darabiha (2015). Experimental and numerical analysis of the impact of radiative heat losses on syngas production from partial oxidation of $CH_4/O_2/N_2/H_2O$ mixtures. *Fuel (Submitted)*. *(p. 237, 238)*

Guo, H., J. Min, C. Galizzi, D. Escudié, and F. Baillot (2010). A numerical study on the effects of CO_2/N_2/Ar addition to air on liftoff of a laminar CH_4/air diffusion flame. *Combustion Science and Technology 182*(11-12), 1549–1563. *(p. 237, 238)*

Guo, H., B. Tayebi, C. Galizzi, and D. Escudié (2010). Burning rates and

surface characteristics of hydrogen-enriched turbulent lean premixed methane–air flames. *International Journal of Hydrogen Energy 35*(20), 11342 – 11348. *(p. 195)*

Gupta, A. K., D. G. Lilley, and N. Syred (1984). *Swirl flows*. Tunbridge Wells, Kent, England, Abacus Press, 488p. *(p. 4, 5, 6, 13, 40, 115, 118, 134, 149, 164, 170)*

Gupta, S. B., B. P. Bihari, M. S. Biruduganti, R. R. Sekar, and J. Zigan (2011). On use of chemiluminescence for combustion metrics in natural gas fired reciprocating engines. *Proceedings of the Combustion Institute 33*(2), 3131 – 3139. *(p. 233)*

Hardalupas, Y. and M. Orain (2004). Local measurements of the time-dependent heat release rate and equivalence ratio using chemiluminescent emission from a flame. *Combustion and Flame 139*(3), 188 – 207. *(p. 233)*

Heeger, C., R. Gordon, M. Tummers, T. Sattelmayer, and A. Dreizler (2010). Experimental analysis of flashback in lean premixed swirling flames: upstream flame propagation. *Experiments in Fluids 49*(4), 853–863. *(p. 8)*

Higgins, B., M. McQuay, F. Lacas, and S. Candel (2001). An experimental study on the effect of pressure and strain rate on CH chemiluminescence of premixed fuel-lean methane/air flames. *Fuel 80*(11), 1583 – 1591. *(p. 233)*

Higgins, B., M. McQuay, F. Lacas, J. Rolon, N. Darabiha, and S. Candel (2001). Systematic measurements of OH chemiluminescence for fuel-lean, high-pressure, premixed, laminar flames. *Fuel 80*(1), 67 – 74. *(p. 233)*

Hilpert, R. (1933). Heat transfer from cylinders. *Forsch. Geb. Ingenieurwesen 4*(215). *(p. 47)*

Hindasageri, V., R. P. Vedula, and S. V. Prabhu (2013). Thermocouple error correction for measuring the flame temperature with determination of emissivity and heat transfer coefficient. *Review of Scientific Instruments 84*(2). *(p. 81, 108)*

Hossain, A. and Y. Nakamura (2014). A numerical study on the ability to predict the heat release rate using CH* chemiluminescence in non-sooting counterflow diffusion flames. *Combustion and Flame 161*(1), 162 – 172. *(p. 230, 233)*

Hsieh, T.-C., W. J. Dahm, and J. F. Driscoll (1998). Scaling laws for NOx emission performance of burners and furnaces from 30 kW to 12 MW. *Combustion and Flame 114*(1–2), 54 – 80. *(p. 2)*

Huang, R. F. and S. C. Yen (2008). Aerodynamic characteristics and thermal structure of nonpremixed reacting swirling wakes at low Reynolds numbers. *Combustion and Flame 155*(4), 539 – 556. *(p. 8)*

Huang, Y. and V. Yang (2004, February). Bifurcation of flame structure in a lean-premixed swirl-stabilized combustor: transition from stable

to unstable flame. *Combustion and Flame 136*(3), 383–389. *(p. 9, 14, 17, 19, 146)*

Huang, Y. and V. Yang (2009). Dynamics and stability of lean-premixed swirl-stabilized combustion. *Progress in Energy and Combustion Science 35*(4), 293 – 364. *(p. 7)*

Hultmark, M. and A. J. Smits (2010). Temperature corrections for constant temperature and constant current hot-wire anemometers. *Measurement Science and Technology 21*(10), 1–4. *(p. 50)*

Incropera, F. P. and D. P. D. Witt (Wiley, 1990). *Fundamentals of heat and mass transfer*. 3th ed. *(p. 45, 47, 52, 103, 109)*

Ishizuka, S. (1990). On the flame propagation in a rotating flow field. *Combustion and Flame 82*(2), 176 – 190. *(p. 134, 170)*

Ishizuka, S. (2002). Flame propagation along a vortex axis. *Progress in Energy and Combustion Science 28*(6), 477 – 542. *(p. 142, 154, 164, 169)*

Juchmann, W., H. Latzel, D. Shin, G. Peiter, T. Dreier, H.-R. Volpp, J. Wolfrum, R. Lindstedt, and K. Leung (1998). Absolute radical concentration measurements and modeling of low-pressure $CH_4/O_2/NO$ flames. *Symposium (International) on Combustion 27*(1), 469 – 476. *(p. 27)*

Kang, D., F. Culick, and A. Ratner (2007). Combustion dynamics of a low-swirl combustor. *Combustion and Flame 151*(3), 412 – 425. *(p. 215)*

Kannuluik, W. G. and E. H. Carman (1951). The temperature dependence of the thermal conductivity of air. *Australian Journal of Scientific Research: Physical Science 4*, 305–314. *(p. 50)*

Kariuki, J., J. R. Dawson, and E. Mastorakos (2012, August). Measurements in turbulent premixed bluff body flames close to blow-off. *Combustion and Flame 159*(8), 2589–2607. *(p. 8, 13)*

Karlovitz, B., D. W. Denniston, D. H. Knapschaefer, and F. E. Wells (1953). Studies on Turbulent flames: A. Flame Propagation Across velocity gradients B. turbulence Measurement in flames. *Proceedings of the Combustion Institute 4*(1), 613–620. *(p. 142)*

Kawamura, T., K. Asato, T. Mazaki, T. Hamaguchi, and H. Kayahara (1979). Explanation of the blowoff of inverted flames by the area-increase concept. *Combustion and Flame 35*(1), 109 – 116. *(p. 12, 13)*

Kee, R. J., G. Dixon-Lewis, J. Warnatz, M. E. Coltrin, and J. A. Miller (1992). A Fortran chemical kinetics package for the analysis of gas phase multicomponent transport properties. Technical report, Sandia Report, SAND86-8246. *(p. 52, 103)*

Ketelheun, A., G. Kuenne, and J. Janicka (2013). Heat transfer modeling in the context of large eddy simulation of premixed combustion with tabulated chemistry. *Flow, Turbulence and Combustion 91*(4), 867–893. *(p. 10)*

Khalid, A. H., K. Kontis, and H.-Z. Behtash (2010). Phosphor thermometry in gas turbines: Consideration factors. *Proceedings of the Institution of Mechanical Engineers, Part G: Journal of Aerospace Engineering 224*(7), 745–755. *(p. 84)*

Khitrin, L., P. Moin, D. Smirnov, and V. Shevchuk (1965). Peculiarities of laminar- and turbulent-flame flashbacks. *Tenth Symposium (International) on Combustion 10*(1), 1285 – 1291. *(p. 142)*

Kim, K. T. and S. Hochgreb (2011, December). The nonlinear heat release response of stratified lean-premixed flames to acoustic velocity oscillations. *Combustion and Flame 158*(12), 2482–2499. *(p. 9, 212)*

Kim, K. T. and S. Hochgreb (2012, May). Effects of Nonuniform Reactant Stoichiometry on Thermoacoustic Instability in a Lean-Premixed Gas Turbine Combustor. *Combustion Science and Technology 184*(5), 608–628. *(p. 10, 14, 15)*

Kim, K. T., J. G. Lee, H. J. Lee, B. D. Quay, and D. A. Santavicca (2010). Characterization of forced flame response of swirl-stabilized turbulent lean-premixed flames in a gas turbine combustor. *Journal of Engineering for Gas Turbines and Power 132*(4), 041502. *(p. 9, 13, 14, 179, 182, 212)*

Komarek, T. and W. Polifke (2010, 03). Impact of swirl fluctuations on the flame response of a perfectly premixed swirl burner. *Journal of Engineering for Gas Turbines and Power 132*(6), 061503–061503. *(p. 212, 215, 249)*

Kostiuk, L., K. Bray, and R. Cheng (1993a). Experimental study of premixed turbulent combustion in opposed streams. part I nonreacting flow field. *Combustion and Flame 92*(4), 377 – 395. *(p. 18)*

Kostiuk, L., K. Bray, and R. Cheng (1993b). Experimental study of premixed turbulent combustion in opposed streams. part II reacting flow field and extinction. *Combustion and Flame 92*(4), 396 – 409. *(p. 18, 195)*

Külsheimer, C. and H. Büchner (2002). Combustion dynamics of turbulent swirling flames. *Combustion and Flame 131*(1), 70–84. *(p. 215)*

Kurdyumov, V., E. Fernández, and A. Liñán (2000, January). Flame flashback and propagation of premixed flames near a wall. *Proceedings of the Combustion Institute 28*(2), 1883–1889. *(p. 8, 142, 152, 158)*

Kurdyumov, V., E. Fernández-Tarrazo, J.-M. Truffaut, J. Quinard, A. Wangher, and G. Searby (2007). Experimental and numerical study of premixed flame flashback. *Proceedings of the Combustion Institute 31*(1), 1275 – 1282. *(p. 142)*

Lam, K.-Y., D. F. Davidson, and R. K. Hanson (2013). A shock tube study of H_2 + OH => H_2O + H using OH laser absorption. *International Journal of Chemical Kinetics 45*(6), 363–373. *(p. 136, 151, 191)*

Law, C., D. Zhu, and G. Yu (1988). Propagation and extinction of stretched premixed flames. *Symposium (International) on Combus-*

tion 21(1), 1419 – 1426. *(p. 18)*

Lee, K., H. Kim, P. Park, S. Yang, and Y. Ko (2013). CO_2 radiation heat loss effects on NOx emissions and combustion instabilities in lean premixed flames. *Fuel 106*(0), 682 – 689. *(p. 233)*

Lewis, B. and G. Von Elbe (1987). *Combustion, flames, and explosions of gases* (3th ed.). New York: Academic Press. *(p. 12, 141)*

Lieuwen, T. C. and V. Yang (2005). *Combustion Instabilities in Gas Turbine Engines: Operational Experience, Fundamental Mechanisms, and Modeling (Progress in Astronautics and Aeronautics)*. American Institute of Aeronautics and Astronautics. *(p. 7)*

Lilley, D. G. (1977, 2012/10/28). Swirl flows in combustion: A review. *AIAA Journal 15*(8), 1063–1078. *(p. 13)*

Lindstedt, P. (1998). Modeling of the chemical complexities of flames. *Proceedings of the Combustion Institute 27*(1), 269–285. *(p. 27, 28, 29, 31, 53, 154, 227)*

Lipatnikov, A. and J. Chomiak (2005). Molecular transport effects on turbulent flame propagation and structure. *Progress in Energy and Combustion Science 31*(1), 1 – 73. *(p. 154)*

Lo, A., A. Cessou, P. Boubert, and P. Vervisch (2014). Space and time analysis of the nanosecond scale discharges in atmospheric pressure air: I. gas temperature and vibrational distribution function of N_2 and O_2. *Journal of Physics D: Applied Physics 47*(11), 115201. *(p. 81)*

Longwell, J., J. Chenevey, W. Clark, and E. Frost (1949). Flame stabilization by baffles in a high velocity gas stream. *Third Symposium on Combustion and Flame, and Explosion Phenomena 3*(1), 40 – 44. *(p. 13)*

Lucca-Negro, O. and T. O'Doherty (2001). Vortex breakdown: a review. *Progress in Energy and Combustion Science 27*(4), 431 – 481. *(p. 5, 13)*

Luque, J. and D. R. Crosley (1999). Lifbase: Database and spectral simulation program (version 1.5). Technical report, SRI International Report MP 99-009. *(p. 54, 60, 61, 62, 64, 67, 68)*

Mallens, R. M. M., B. O. Loijenga, L. P. H. De Goey, and P. J. M. Sonnemansb (1997). Numerical and experimental study of lean M-and V-shaped flames. *Combustion Science and Technology 122*(1-6), 331–344. *(p. 12, 13)*

Mastorakos, E., A. Taylor, and J. Whitelaw (1995). Extinction of turbulent counterflow flames with reactants diluted by hot products. *Combustion and Flame 102*(1–2), 101 – 114. *(p. 8, 18, 195)*

Mathur, S., P. K. Tondo, and S. C. Saxena (1967). Thermal conductivity of binary, ternary and quaternary mixtures of rare gases. *Molecular Physics 12*, 569. *(p. 52)*

Mejia, D. (2014). *Wall-temperature effects on flame response to acoustic oscillations*. Ph. D. thesis, Université de Toulouse. *(p. 50)*

Mercier, R. (2014). *Turbulent combustion modeling for Large Eddy Simulation of industrial combustion chambers*. Ph. D. thesis, Ecole Centrale Paris. *(p. 115, 118, 119, 131, 137, 204)*

Mirat, C. (2015). *Analyse des instabilités de combustion dans des foyers de centrale thermique fonctionnant avec des fiouls liquides*. Ph. D. thesis, Ecole Centrale Paris. *(p. 1)*

Modesto, M. and S. Nebra (2009). Exergoeconomic analysis of the power generation system using blast furnace and coke oven gas in a brazilian steel mill. *Applied Thermal Engineering 29*(11–12), 2127 – 2136. *(p. 25)*

Moeck, J. P., J.-F. Bourgouin, D. Durox, T. Schuller, and S. Candel (2012, AUG). Nonlinear interaction between a precessing vortex core and acoustic oscillations in a turbulent swirling flame. *Combustion and Flame 159*(8), 2650–2668. *(p. 10, 11, 12, 171)*

Nogenmyr, K.-J., H. J. Cao, C. K. Chan, and R. K. Cheng (2013). Effects of confinement on premixed turbulent swirling flame using large eddy simulation. *Combustion Theory and Modelling 17*(6), 1003–1019. *(p. 13)*

Noiray, N. (2007). *Analyse linéaire et non-linéaire des instabilités de combustion, application aux systèmes d'injection multipoints et stratégies de contrôle*. Ph. D. thesis, Ecole Centrale Paris. *(p. 43)*

Noiray, N., D. Durox, T. Schuller, and S. Candel (2008, 11). A unified framework for nonlinear combustion instability analysis based on the flame describing function. *Journal of Fluid Mechanics 615*, 139–167. *(p. 208)*

Noiray, N., D. Durox, T. Schuller, and S. Candel (2009, 2014/12/09). Mode conversion in acoustically modulated confined jets. *AIAA Journal 47*(9), 2053–2062. *(p. 218)*

OMEGA. http : //www.omega.com/Temperature/pdf/irco_chal_p13r_p10r.pdf. *(p. 104, 105)*

Palies, P. (2010). *Dynamique et instabilités de combustion des flammes swirlées*. Ph. D. thesis, Ecole Centrale Paris. *(p. 43, 226, 244)*

Palies, P., D. Durox, T. Schuller, and S. Candel (2010, September). The combined dynamics of swirler and turbulent premixed swirling flames. *Combustion and Flame 157*(9), 1698–1717. *(p. 10, 36, 183, 206, 208, 211, 212, 215, 249, 250)*

Palies, P., D. Durox, T. Schuller, and S. Candel (2011a, 4). Acoustic-convective mode conversion in an aerofoil cascade. *Journal of Fluid Mechanics 672*, 545–569. *(p. 249, 250)*

Palies, P., D. Durox, T. Schuller, and S. Candel (2011b). Experimental study on the effect of swirler geometry and swirl number on flame describing functions. *Combustion Science and Technology 183*(7), 704–717. *(p. 36, 250)*

Palies, P., T. Schuller, D. Durox, L. Y. M. Gicquel, and S. Candel (2011).

Acoustically perturbed turbulent premixed swirling flames. *Physics of Fluids 23*(3), 1–15. *(p. 211, 215, 218, 249, 250)*

Panoutsos, C., Y. Hardalupas, and A. Taylor (2009). Numerical evaluation of equivalence ratio measurement using OH* and CH* chemiluminescence in premixed and non-premixed methane–air flames. *Combustion and Flame 156*(2), 273 – 291. *(p. 27, 237)*

Paubel, X. (2007). *Analyse expérimentale des oxy-flammes turbulentes non-prémélangées de gaz à faible pouvoir calorifique*. Ph. D. thesis, INSA de Rouen. *(p. 3, 26)*

Paubel, X., A. Cessou, D. Honore, L. Vervisch, and R. Tsiava (2007). A flame stability diagram for piloted non-premixed oxycombustion of low calorific residual gases. *Proceedings of the Combustion Institute 31*(2), 3385 – 3392. *(p. 3)*

Plee, S. and A. Mellor (1978). Review of flashback reported in prevaporizing-premixing combustors. *Combustion and Flame 32*(1), 193 – 203. *(p. 142)*

Poinsot, T., D. C. Haworth, and G. Bruneaux (1993, OCT). Direct simulation and modeling of flame-wall interaction for premixed turbulent combustion. *Combustion and Flame 95*(1-2), 118–132. *(p. 154)*

Poinsot, T. and D. Veynante (2005). *Theoretical and Numerical Combustion*. Edwards. *(p. 154)*

Polifke, W. and C. Lawn (2007). On the low-frequency limit of flame transfer functions. *Combustion and Flame 151*(3), 437 – 451. *(p. 212)*

Porter, R., A. Clark, W. Kaskan, and W. Browne (1967). A study of hydrocarbon flames. *Symposium (International) on Combustion 11*(1), 907 – 917. *(p. 237)*

Poularikas, A. D. (2010). *Transforms and Applications Handbook*. CRC Press. *(p. 10, 55, 57)*

Raffel, M., C. E. Willert, S. T. Wereley, and J. Kompenhans (2007). *Particle Image Velocimetry, a practical guide*. Springer-Verlag Berlin Heidelberg. *(p. 69, 70, 73)*

Ranz, W. E. and W. R. Marshall (1952). Evaporation from drops. *Chemical Engineering Progress 48*(141). *(p. 103, 109)*

Ren, J.-Y., W. Qin, F. Egolfopoulos, and T. Tsotsis (2001). Strain-rate effects on hydrogen-enhanced lean premixed combustion. *Combustion and Flame 124*(4), 717 – 720. *(p. 18, 189, 195)*

Sadanandan, R., M. Stöhr, and W. Meier (2008). Simultaneous OH-PLIF and PIV measurements in a gas turbine model combustor. *Applied Physics B 90*(3-4), 609–618. *(p. 6, 60, 151)*

Sainct, F. (2014). *Etude de la réactivité de décharges électriques nanosecondes à la pression atmosphériques dans la vapeur d'eau*. Ph. D. thesis, Ecole Centrale Paris, Laboratoire d'Energétique Moléculaire et Macroscopique Combustion (EM2C) du CNRS et de Laboratoire d'Energétique Moléculaire et Macroscopique, Combustion (EM2C) du

CNRS et de l'ECP. *(p. 60, 61, 62, 63)*

Sanchez, A. L., A. Lepinette, M. Bollig, A. Linan, and B. Lazaro (2000). The reduced kinetic description of lean premixed combustion. *Combustion and Flame 123*, 436–464. *(p. 18)*

Schmitt, P., T. Poinsot, B. Schuermans, and K. P. Geigle (2007, JAN 10). Large-eddy simulation and experimental study of heat transfer, nitric oxide emissions and combustion instability in a swirled turbulent high-pressure burner. *Journal of Fluid Mechanics 570*, 17–46. *(p. 9)*

Schuller, T. (2003). *Mécanismes de couplage dans les interactions acoustique-combustion*. Ph. D. thesis, Ecole Centrale Paris. *(p. 43)*

Schuller, T., D. Durox, and S. Candel (2002). Dynamics of and noise radiated by a perturbed impinging premixed jet flame. *Combustion and Flame 128*(1–2), 88 – 110. *(p. 208)*

Schuller, T., D. Durox, and S. Candel (2003). Self-induced combustion oscillations of laminar premixed flames stabilized on annular burners. *Combustion and Flame 135*(4), 525 – 537. *(p. 13, 215)*

Seo, S. (1999). *Parametric study of lean premixed combustion instability in a pressurized model gas turbine combustor*. Ph. D. thesis, The Penn State University. *(p. 14, 16, 19)*

Shanbhogue, S. J., S. Husain, and T. Lieuwen (2009). Lean blowoff of bluff body stabilized flames: Scaling and dynamics. *Progress in Energy and Combustion Science 35*(1), 98 – 120. *(p. 8)*

Shionoya, S., W. Yen, and H. Yamamoto (2012). *Phosphor Handbook*. The CRC Press laser and optical science and technology series. Taylor & Francis. *(p. 82)*

Sick, V., F. Hildenbrand, and P. Lindstedt (1998). Quantitative laser-based measurements and detailed chemical kinetic modeling of nitric oxide concentrations in methane-air counterflow diffusion flames. *Symposium (International) on Combustion 27*(1), 1401 – 1409. *(p. 27)*

Sommerer, Y., D. Galley, T. Poinsot, S. Ducruix, F. Lacas, and D. Veynante (2004). Large eddy simulation and experimental study of flashback and blow-off in a lean partially premixed swirled burner. *Journal of Turbulence 5*(37), 1–21. *(p. 8, 142)*

Steinberg, A., C. Arndt, and W. Meier (2013). Parametric study of vortex structures and their dynamics in swirl-stabilized combustion. *Proceedings of the Combustion Institute 34*(2), 3117 – 3125. *(p. 7, 171)*

Stepowski, D., A. Cessou, and P. Goix (1994). Flame stabilization and OH fluorescence mapping of the combustion structures in the near field of a spray jet. *Combustion and Flame 99*(3-4), 516 – 522. *(p. 62)*

Stöhr, M., I. Boxx, C. Carter, and W. Meier (2011). Dynamics of lean blowout of a swirl-stabilized flame in a gas turbine model combustor. *Proceedings of the Combustion Institute 33*(2), 2953 – 2960. *(p. 7, 9, 59, 60, 151)*

Stopper, U., M. Aigner, H. Ax, W. Meier, R. Sadanandan, M. Stöhr, and

A. Bonaldo (2010). PIV, 2D-LIF and 1D-Raman measurements of flow field, composition and temperature in premixed gas turbine flames. *Experimental Thermal and Fluid Science 34*(3), 396 – 403. *(p. 2)*

Strozzi, C., J. Sotton, A. Mura, and M. Bellenoue (2009). Characterization of a two-dimensional temperature field within a rapid compression machine using a toluene planar laser-induced fluorescence imaging technique. *Measurement Science and Technology 20*(12), 125403. *(p. 81)*

Sung, C., C. Law, and A. Umemura (1992). On adiabatic stabilization of inverted flames. *Twenty-Fourth Symposium (International) on Combustion 24*(1), 205 – 212. *(p. 12)*

Sutherland, W. (1893). The viscosity of gases and molecular force. *Philisophical Magazine 5*(36), 507–531. *(p. 50)*

Syred, N. (2006). A review of oscillation mechanisms and the role of the precessing vortex core (PVC) in swirl combustion systems. *Progress in Energy and Combustion Science 32*(2), 93 – 161. *(p. 6)*

Syred, N., M. Abdulsada, A. Griffiths, T. O'Doherty, and P. Bowen (2012, January). The effect of hydrogen containing fuel blends upon flashback in swirl burners. *Applied Energy 89*(1), 106–110. *(p. 8, 142)*

Syred, N. and J. Beér (1974). Combustion in swirling flows: A review. *Combustion and Flame 23*(2), 143 – 201. *(p. 13, 115, 118, 134, 149, 170)*

Tay Wo Chong, L., T. Komarek, M. Zellhuber, J. Lenz, C. Hirsch, and W. Polifke (2009). Influence of strain and heat loss on flame stabilization in a non-adiabatic combustor. *Proceedings of the European Combustion Meeting, Vienna, Austria, April 14-17 (2009)*, 1–6. *(p. 16, 18, 146)*

Tea, G., G. Bruneaux, J. Kashdan, and C. Schulz (2011). Unburned gas temperature measurements in a surrogate diesel jet via two-color toluene-lif imaging. *Proceedings of the Combustion Institute 33*(1), 783 – 790. *(p. 81)*

Terhaar, S., K. Oberleithner, and C. O. Paschereit (2014). Impact of steam-dilution on the flame shape and coherent structures in swirl-stabilized combustors. *Combustion Science and Technology 186*(7), 889–911. *(p. 7, 10, 14, 171)*

Treviño, C., S. Donnerhack, and N. Peters (1991). LDA measurements in the premixed V flame stabilized in the wake of a flat plate boundary layer. *Combustion and Flame 85*(3–4), 505 – 510. *(p. 12)*

Truffin, K. and T. Poinsot (2005). Comparison and extension of methods for acoustic identification of burners. *Combustion and Flame 142*(4), 388 – 400. *(p. 211)*

Wang, S. and V. Yang (2005). Unsteady flow evolution in swirl injectors with radial entry. II. external excitations. *Physics of Fluids (1994-present) 17*(4), 1–12. *(p. 211)*

Wenzel, H. and N. Peters (2000). Direct numerical simulation and mod-

eling of kinematic restoration, dissipation and gas expansion effects of premixed flames in homogeneous turbulence. *Combustion Science and Technology 158*(1), 273–297. *(p. 154)*

Wicksall, D., A. Agrawal, R. Schefer, and J. Keller (2005). The interaction of flame and flow field in a lean premixed swirl-stabilized combustor operated on H_2/CH_4/air. *Proceedings of the Combustion Institute 30*, 2875–2883. *(p. 146)*

Wilke, C. R. (1950). A viscosity equation for gas mixtures. *Journal of Chemical Physics 18*, 517. *(p. 52)*

Wu, C. and C. Law (1985). On the determination of laminar flame speeds from stretched flames. *Symposium (International) on Combustion 20*(1), 1941 – 1949. *(p. 18, 195)*

Zukoski, E. E. and F. E. Marble (1956). Experiments concerning the mechanism of flame blowoff from bluff bodies. *Proceedings of the Gas Dynamics Symposium on Aerothermochemistry*, 205–2010. *(p. 13)*